EFFECTS OF MAMMALIAN RIBONUCLEOTIDE REDUCTASE DEREGULATION ON REDOX HOMEOSTASIS AND GENOMIC INTEGRITY

A Dissertation

Presented to the Faculty of the Graduate School

of Cornell University

In Partial Fulfillment of the Requirements for the Degree of

Doctor of Philosophy

by

Minxing Li

May 2013

EFFECTS OF MAMMALIAN RIBONUCLEOTIDE REDUCTASE DEREGULATION ON REDOX HOMEOSTASIS AND GENOMIC INTEGRITY

Minxing Li, Ph. D.

Cornell University 2013

Ribonucleotide reductase catalyzes the rate-limiting step in *de novo* deoxyribonucleoside triphosphate (dNTPs) biosynthesis and is essential for providing balanced dNTP pools for nuclear and mitochondrial genome maintenance. RNR contains two components R1 and R2. R2 generates free radicals that are transferred to R1 and used for catalysis. RNR is tightly regulated through several mechanisms, including the control of R2 expression levels. Broad overexpression of R2 in transgenic mice causes lung neoplasms through a mutagenic mechanism. Because R2 produces free radicals, I hypothesized that R2 deregulation results in mutagenic perturbations of cellular redox status which could contribute to R2-induced tumorigenesis. This dissertation aims to (A) elucidate the effect of RNR deregulation on redox homeostasis and dissect the molecular mechanism of RNR-induced mutagenesis and tumorigenesis, and (B) use RNR mice as a lung tumor model in imaging studies to assess lung tumor growth patterns.

For the first aim, we generated cells that overexpress R2 and showed that this overexpression leads to increased reactive oxygen species (ROS) production. By generating a series of R2 mutants, we subsequently identified the source of R2-induced ROS production. In addition, some R2 mutants showed dominant negative effects by interfering with endogenous RNR, leading to mitochondrial DNA depletion and mitochondrial redox imbalance. These findings indicate the importance of RNR regulation in maintaining cellular ROS levels and suggest the possibility that R2-induced ROS may play a role in mutagenesis.

For the second aim, we adapted an automated algorithm for the measurement of pulmonary nodules on human chest CT scans and used it to measure mouse lung tumors. Euthanized mice were first imaged to optimize scan parameters and refine computational algorithms for tumor volume measurement. Lung tumor-bearing mice were then scanned sequentially for tumor growth rate determination. Findings from this study establish new automated algorithms to measure lung tumor volume in mice and confirm an exponential growth model for murine lung neoplasms.

Together, these studies demonstrate the importance of RNR regulation in maintaining cellular redox homeostasis and genome integrity, and that RNR mice serve as an authentic model of human lung cancer in translational studies.

BIOGRAPHICAL SKETCH

Minxing Li was born on September 9, 1983 in Sichuan, China. In 2001, she graduated from Chongqin High school and entered Sichuan International Studies University to study English Language and Culture. In 2003, she went aboard and started her undergraduate studies in the Department of Biochemistry at the University of Toronto, Ontario, Canada. As an undergraduate, She worked in Dr. Emil Pai's lab at the University of Toronto, where she investigated the interaction between the Fab fragment of human anti-HIV antibody 2F5 and its epitope peptide by X-ray crystallography. In 2007, she graduated with a Bachelor of Science (Honors) degree and came to USA for graduate studies. She joined the Ph.D. program in the field of Biochemistry, Molecular and Cell Biology in the Department of Molecular Biology and Genetics at Cornell University, Ithaca, New York. In 2008, after rotations with Dr. Ailong Ke, Dr. Robert Weiss and Dr. Jeff Pleiss, she joined the Weiss lab and started her thesis project under the guidance of Dr. Robert Weiss. She is studying the effect of ribonucleotide reductase on redox homeostasis and genome maintenance.

ACKNOWLEDGMENTS

I would like to thank my Ph.D. mentor Dr. Robert Weiss for his guidance, support and encouragement throughout my Ph.D. study. During my training in the Weiss lab, he helps me develop experimental, analytical and critical thinking skills, which are essential for my future career as an independent researcher.

I would also like to thank my committee members, Dr. John Schimenti and Dr. Paul Soloway, for their support, encouragement, expertise and advices on my project.

Special thanks also go to the past and present Weiss lab members. Dr. Xia Xu for initiating the RNR and lung cancer project, and for making critical RNR mutants for my study. Dr. Jennifer Page for teaching me important experimental skills and for discussions on the RNR project. Dr. Gabriel Balmus for helping me with experiments and for inspiring suggestions. Aaron Cohen, my undergraduate student, for helping me with my projects. Dr. Stephanie Yazinski, Dr. Kelly Hume, Dr. Amy Lyndaker, Dr. Erin Daugherity, Dr. Nedra Holmes, Pei Xin Lim, Tim Pierpont, Joanna Mleczko, Claire Anderson, Jack Stupinski, and Elizabeth Moore for their help, suggestions and friendship.

I am also very grateful to the collaborators of my study. Dr. Artit Jirapatnakul, Dr. Alberto Biancardi, Dr. Anthony Reeves and Mark Riccio, for their expertise and contributions on the RNR lung tumor model and micro-CT project. Dr. Yimon Aye and Dr. Yuan Fu, for their work and advices on RNR biochemical assays.

Finally, I would like to thank my family and friends. My parents and relatives, for their love, constant support, encouragement and faith in me. My friends, for their accompany, support and encouragement. All these great people help me made it all possible.

TABLE OF CONTENTS

LIST OF FIGURES

LIST OF TABLES

CHAPTER 1 Literature Review

1.1 Importance of deoxyribonucleoside triphosphates (dNTPs)

Accurate DNA replication and repair is essential for the maintenance and growth of an organism. There are many factors that coordinate together to ensure the fidelity of DNA replication and repair. Among these, one important factor is the production of balanced pools of the four deoxyribonucleoside triphosphates (dNTPs), which are building blocks of DNA. All eukaryotes have two genomes, the nuclear and the mitochondrial genomes, both of which need to maintain balanced dNTP pools for genomic integrity (Figure 1.1). The nuclear genome replicates during S phase and requires control of dNTP pool throughout the cell cycle, where the pool expands in S phase and is kept low outside of S phase. On the other hand, the mitochondrial genome replicates independent of the cell cycle and needs continuous supply of dNTPs. All these processes are tightly regulated in cells to fit the purpose of each genome replication (Mathews 2006).

Disturbances in dNTP pools can lead to genomic instability. Usually low dNTP levels can result in impaired DNA replication and repair while high dNTP levels can cause mutagenesis (Figure 1.1). Imbalance in dNTP pools has been linked to multiple human diseases such as cancer, mitochondrial and infectious diseases. dNTP accumulation can lead to increased mutation rate during DNA replication, which can contribute to oncogenesis (Wheeler, Rajagopal et al. 2005). In addition, uncoordinated cell proliferation in cancer development can lead to insufficient nucleotides that cause replication stress and promote genomic instability (Bester, Roniger et al. 2011). Genetic mutations that lead to mitochondrial dNTP alterations can cause mitochondrial diseases characterized by severely depleted mitochondrial DNA (Bester, Roniger et al. 2011). Furthermore, during viral infection, reverse transcriptase lacks a proofreading

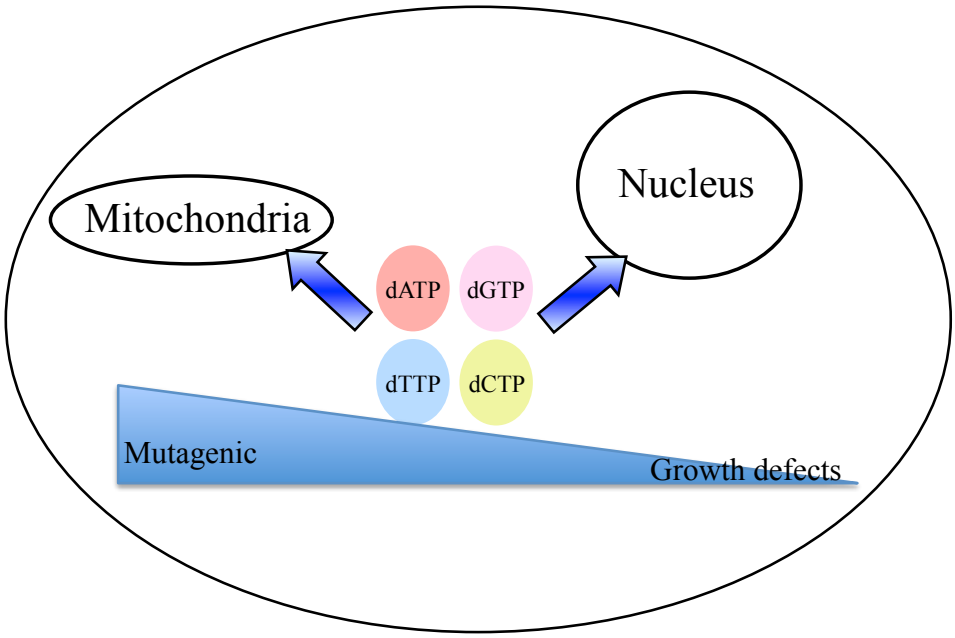

Figure 1.1 Importance of the four dNTPs in genome maintenance. A balanced dNTP pool is essential for both mitochondrial and nuclear genome integrity. Low dNTP levels can lead to growth defects and high dNTP levels are often mutagenic.

activity, and it has been shown that imbalance in dNTPs can lead to increased retroviral mutation rate, leading to viral variants that are drug resistant (Martinez, Vartanian et al. 1994; Vartanian, Meyerhans et al. 1994; Julias and Pathak 1998; Mathews 2006). Recently, it has been shown that SAMHD1, a host protein that restricts HIV infection in myeloid and resting T cells, is a dNTPase that removes the triphosphate from dNTPs, resulting in substrate depletion for viral DNA synthesis and blockage of HIV infection (Baldauf, Pan et al. 2012; Lahouassa, Daddacha et al. 2012). All these examples emphasize the importance of dNTP balance in cells.

1.1.1 dNTP biosynthesis pathways

There are two biosynthetic pathways to synthesize dNTPs: the *de novo* pathway and the salvage pathway. In the *de novo* pathway, ribonucleoside diphosphates (NDPs, Figure1.2) are reduced to corresponding deoxyribonucleoside diphosphates (dNDPs, Figure1.2) by ribonucleotide reductase (RNR). Subsequently, the dNDPs are phosphorylated by nucleoside diphosphate kinases to produce deoxyribonucleoside triphosphates (dNTPs) for DNA replication and repair (Kunz and Kohalmi 1991). This is true for all dNTPs except dTTP. dTTP synthesis uses dUMP as precursor, which is converted to dTMP by dTMP synthase. dTMP is first phosphorylated by dTMP kinase and then nucleoside diphosphate kinase to generate dTTP (Kunz and Kohalmi 1991) (Figure 1.2). In the salvage pathway, deoxyribonucleosides (deoxyribose sugar + nitrogenous base, no phosphate group) are phosphorylated by deoxyribonucleoside kinases to generated corresponding dNTPs (Reichard 1988). Mammalian cells contain four principal salvage enzymes, namely deoxycytidine kinase (dCK), thymidine kinase 1 (TK1), thymidine kinase 2 (TK2) and deoxyguanosine kinase (dGK) (Arner and Eriksson 1995). TK1 and dCK localize to the cytosol and are responsible for making dNTPs for

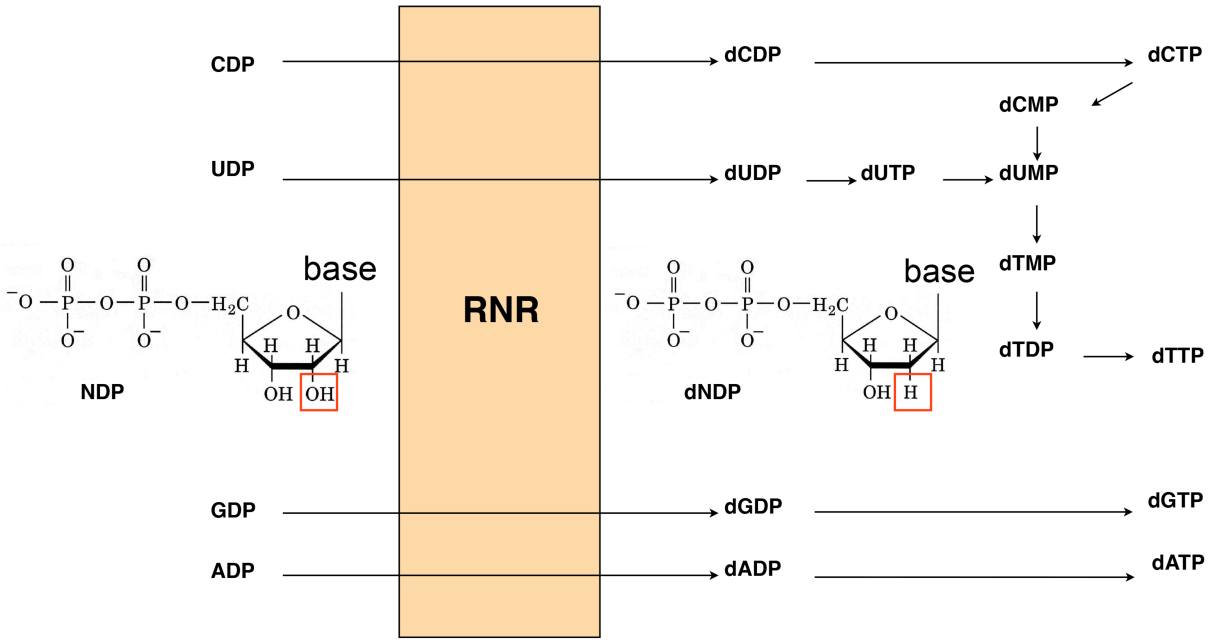

Figure 1.2 RNR and the *de novo* dNTP synthesis. As a single enzyme, RNR is involved in synthesizing all four dNTPs. It catalyzes the reduction of NDP to dNDP, where the 2'-OH is reduced to H. Figure modified from Hofer, Crona *et al.* 2012.

nuclear DNA synthesis. TK1 acts on deoxyuridine and thymidine to make dTTP while dCK primarily works on deoxycytidine, but also deoxyadenosine and deoxyguanosine to make dCTP, dATP and dGTP (Reichard 1988; Arner and Eriksson 1995). dGK and TK2 localize to the mitochondria and responsible for making dNTPs for mitochondrial DNA synthesis. dGK is. involved in making dATP and dGTP while TK2 is involved in making dCTP and dTTP (Arner and Eriksson 1995).

1.1.2 dNTP imbalance and genomic instability

dNTP pool sizes are precisely regulated in cells to maintain genome integrity. During S phase and DNA damage responses, dNTP levels are elevated to facilitate DNA replication and repair. In mammalian cells, the total cellular pool sizes are in the range of 10-100pmoles of each dNTP/million cells in S phase (Rampazzo, Miazzi et al. 2010). Outside of S phase and in non-proliferating cells, dNTP levels are maintained at low levels (about 10-fold lower) for DNA repair and mitochondrial DNA (mtDNA) synthesis (Mathews 2006; Rampazzo, Miazzi et al. 2010).

Loss of normal control of dNTP regulating mechanisms can lead to imbalanced dNTP pools that can cause detrimental effects to cells. Depletion of dNTP pools by inhibition or mutation leads to DNA breaks, mutagenesis and cell death (Reichard 1988). On the other hand, elevated dNTP pools, including balanced expansion of all four dNTPs and unbalanced expansion of a subset of dNTPs, all contribute to increased mutagenesis (Wheeler, Rajagopal et al. 2005; Mathews 2006). Besides the effects on nuclear genome, dNTP alterations can also lead to accumulation of deletions and point mutations in mtDNA and severe mtDNA depletion (Mathews 2006).

In vitro DNA replication studies showed that imbalanced dNTP pools cause enhanced mutagenesis mainly by DNA misinsertion and the next-nucleotide effect (Reichard 1988; Wheeler, Rajagopal et al. 2005). DNA misinsertion can result from competition between dNTPs correctly and incorrectly paired with a template base and increased misincorporation of a nucleotide present in excess is often observed. Next-nucleotide effect refers to the observation that the 3' to 5' proofreading exonuclease activity of DNA polymerase is inhibited by accumulation of a particular dNTP. As a result, DNA chain extension from a mismatch site proceeds before the mismatched nucleotide can be removed (Petruska, Goodman et al. 1988; Perrino and Loeb 1989; Mendelman, Petruska et al. 1990). In addition, it has been shown *in vitro* that dNTP imbalances can stimulate frameshift mutations by correct base-pairing at a slipped structure or misalignment after incorporation of a mismatched nucleotide (Bebenek, Roberts et al. 1992).

In vivo studies also provide evidence on the importance of dNTP pool regulation. dNTP pool bias caused by addition or depletion of deoxyribonucleosides resulted in increased mutation rates of cultured cells (Bradley and Sharkey 1978; Kaufman and Davidson 1979). Furthermore, constitutively high dNTP concentration in yeast arrests cell cycle progression in late G1 phase, affected activation of origins of replication and inhibits the DNA damage checkpoint (Chabes and Stillman 2007).

1.2 Ribonucleotide Reductase

Ribunocleotide Reductase (RNR) is involved in the rate-limiting step of the *de novo* biosynthesis of all four dNTPs. It catalyzes the substitution of the 2' hydroxyl group of a ribonucleoside diphosphate (NDP) with hydrogen, resulting in a deoxyribonucleoside

diphosphate (dNDP). The catalytic mechanism of RNR requires protein radicals. It is an essential enzyme in DNA synthesis and therefore is indispensable for the survival of all living organisms.

1.2.1 RNR enzyme

1.2.1.1 RNR classification

RNR can be grouped into three classes depending on their interaction with oxygen and the way they generate free radicals. Class I RNRs have two non-identical dimeric subunits (R1 and R2). They require oxygen and Fe cofactor for the generation of a stable tyrosyl radical in the R2 subunit. Class II RNRs are isolated as monomers or dimers (R1). They don't have an R2 subunit for radical generation. Rather, they generate radicals directly on R1 by cleaving the cofactor adenosylcobalamin. Class II RNRs don't require oxygen for their function. Class III RNRs contain dimeric R1 subunits and produce glycyl radicals on R1 when a radical SAM protein cleaves S-adenosylmethionine. Class III RNRs are anaerobic enzymes that are inactivated by oxygen. Nevertheless, in all three classes, the radical produced is channeled to a cysteine residue in the catalytic site of the R1 subunit and used for catalysis (Eklund, Uhlin et al. 2001; Nordlund and Reichard 2006; Logan 2011).

1.2.1.2 Overall structure of RNR

Eukaryotes, *E. coli* and DNA viruses have Class I RNR. Class I RNR enzymes have long been believed to have the structure $\alpha_2\beta_2$. However, recent studies proposed that an $\alpha_6\beta_2$ complex may be more physiologically relevant (Rofougaran, Vodnala et al. 2006; Fairman, Wijerathna et al. 2011). The $\alpha 2$ dimer, called protein R1, has the catalytic size and allosteric regulation sites. The $\beta 2$ dimer, called protein R2, harbors di-nuclear iron center that produces a stable tyrosyl radical, which is essential for RNR enzymatic activity (Figure 1.3).

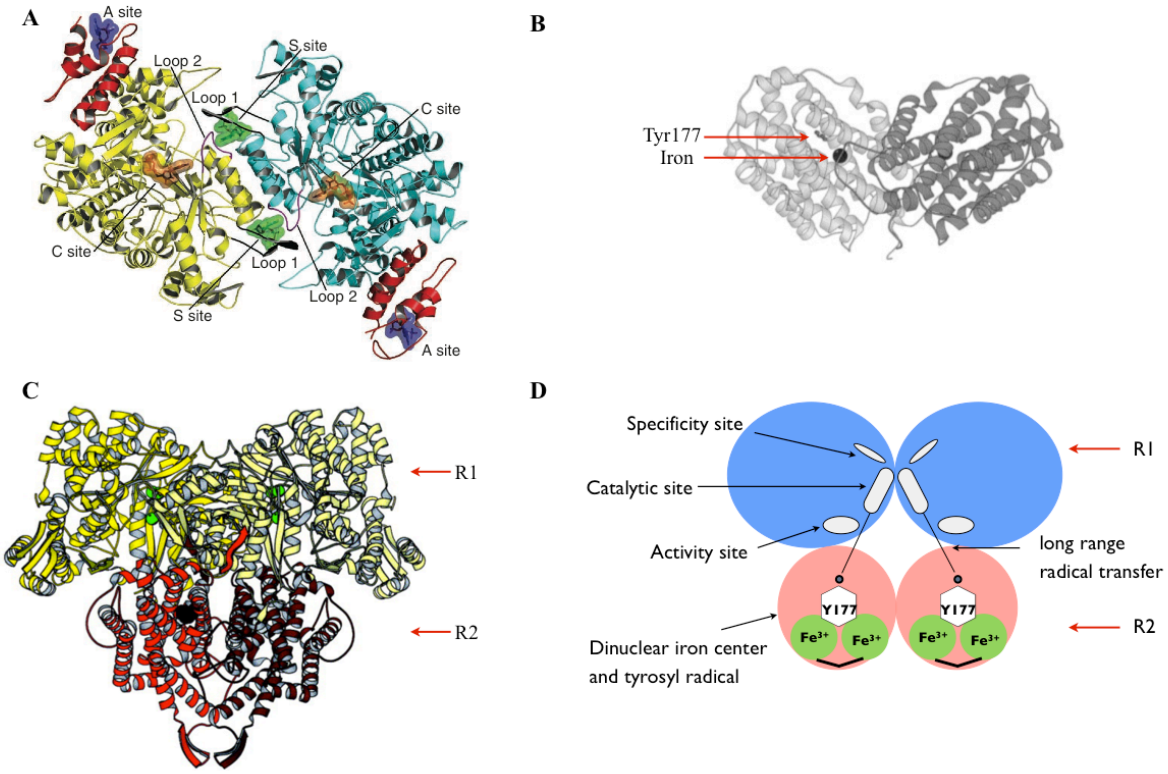

Figure 1.3 Class Ia RNR crystal structures and important sites. (A) Human R1 structure with the activity site (A site, purple, ATP bound), catalytic site (C site, orange, GDP bound) and specificity site (S site, green, TTP bound) shown. Figure from Fairman, Wijerathna *et al.* 2011. (B) Mouse R2 structure with iron atoms shown as dark sphere and the radical harboring tyrosine shown in ball and stick representation. Figure modified from Eklund, Uhlin *et al.* 2001. (C) Model of *E. coli* RNR holoenzyme with R1 dimer positioned on top of the R2 dimer. Figure modified from Eklund, Uhlin *et al.* 2001. (D) Schematic representation of mouse RNR.

Most of the structure and function studies on Class I RNRs have been performed on the *E. coli* enzyme. The crystal structures of the R1 and R2 subunits of *E. coli* have been determined separately (Nordlund, Sjoberg et al. 1990; Uhlin and Eklund 1994). In *E. coli*, the R1 protein dimer has a relative molecular weight of 171Kd (2 x 761 residues). The R1 subunit can be divided into two large domains: the N-terminal domain (~220 residues) and the α/β barrel domain (~480 residues). The catalytic site is located in the center of a deep cleft across the subunit between the N-terminal and barrel domains. Dimerization of R1 are formed by two helices of the α/β barrel from each subunit. The R1 dimer structure is not very stable and both subunits and domains can move with respect to each other, which may form a structural basis for allosteric regulation and catalysis in the subunit (Uhlin and Eklund 1994).

The R2 protein dimer has a relative molecular weight of 87K (2 x 375 residues) in *E. coli*. It is heart shaped and mainly composed of helices (70%). The dinuclear iron center and the tyrosyl radical site are located in the interior of the protein. The R2 dimer is formed mainly by homologous interactions between the helices of each subunit (Nordlund, Sjoberg et al. 1990). C terminus of R2 is important in mediating interactions with R1. Truncated forms of R2 without the last 7 or 30 C-terminal residues cannot bind R1 (Climent, Sjoberg et al. 1992; (Lycksell, Ingemarson et al. 1994).

The only crystal structure of the R1-R2 holoenzyme complex available is from the bacteria *Salmonella typhimurium* (Uppsten, Farnegardh et al. 2006). Instead modeling has been used to generate *E. coli* R1-R2 complexes based on separate structures of the two subunits. R1 dimers are suggested to sit on top of the heart-shaped R2 dimers since the shape of R1 is complementary to this part of the R2 (Uhlin and Eklund 1994). Due to the importance of the R2

C terminus in binding to R1, crystal structures of R1 with the carboxyl end of R2 is also solved. R2 C terminal peptide is shown to bind in a hydrophobic cleft of R1 (Uhlin and Eklund 1994). Mammalian R1 and R2 dimer structures are very similar to those of *E. coli* (Kauppi, Nielsen et al. 1996; Fairman, Wijerathna et al. 2011). As mentioned before, in recent years, it is suggested that eukaryotic R1 forms a hexamer upon dATP or ATP binding and an $\alpha_6\beta_2$ holoenzyme is the functional unit of RNR (Rofougaran, Vodnala et al. 2006; Fairman, Wijerathna et al. 2011).

1.2.1.3 RNR catalytic mechanism

Reduction of NDP to dNDP takes place in the catalytic site of R1 with the involvement of cysteine residues. In the first step of the catalytic cycle, a thiyl radical (C439) is generated by a long-range radical transfer from the tyrosyl radical in R2 (Figure 1.4A; also see 1.2.1.4 for details). This thiyl radical (C439) removes the 3'-H from the ribose ring of the substrate and generates a substrate radical. The substrate radical makes the 2'-OH on the ribose ring less stable, which is protonated by C225 and leaves as H_2O. The resulting radical on the 2' position of the ribose ring is reduced by two cysteine residues, C225 and C462. The excess radical is then transferred to the 3' position of the ribose ring and extracts a hydrogen from C439, generating dNDP and a thiyl radical on C439 (Kolberg, Strand et al. 2004). For a complete turnover, the disulfide bond between C225 and C462 in the active site needs to be reduced. NADPH ultimately provides the reducing power of the catalytic reaction (Kolberg, Strand et al. 2004).

1.2.1.4 RNR iron center and tyrosyl radical formation

Crystal structures of R2 dimer show that each subunit contains an equivalent iron center. The iron atoms are coordinated by 6 charged residues from four helices (two histidines, three glutamic acids and one aspartic acid) (Nordlund, Sjoberg et al. 1990). However, little is known about the incorporation of iron into the R2 subunit, as well as the oxygen activation of the

Figure 1.4 RNR catalytic site and di-nuclear iron center chemistry. (A) RNR catalytic mechanism at the catalytic site in R1. Figure from Eklund, Uhlin *et al.* 2001. (B) RNR di-nuclear iron center oxidation and tyrosyl free radical production in R2. Two important intermediates P and X are shown. Figure modified from Mitic, Clay *et al.* 2007. (Amino acid numbers are based on *E. coli* RNR protein and mammalian RNR acts the same way; the equivalent of Y122 in mouse is Y177).

A

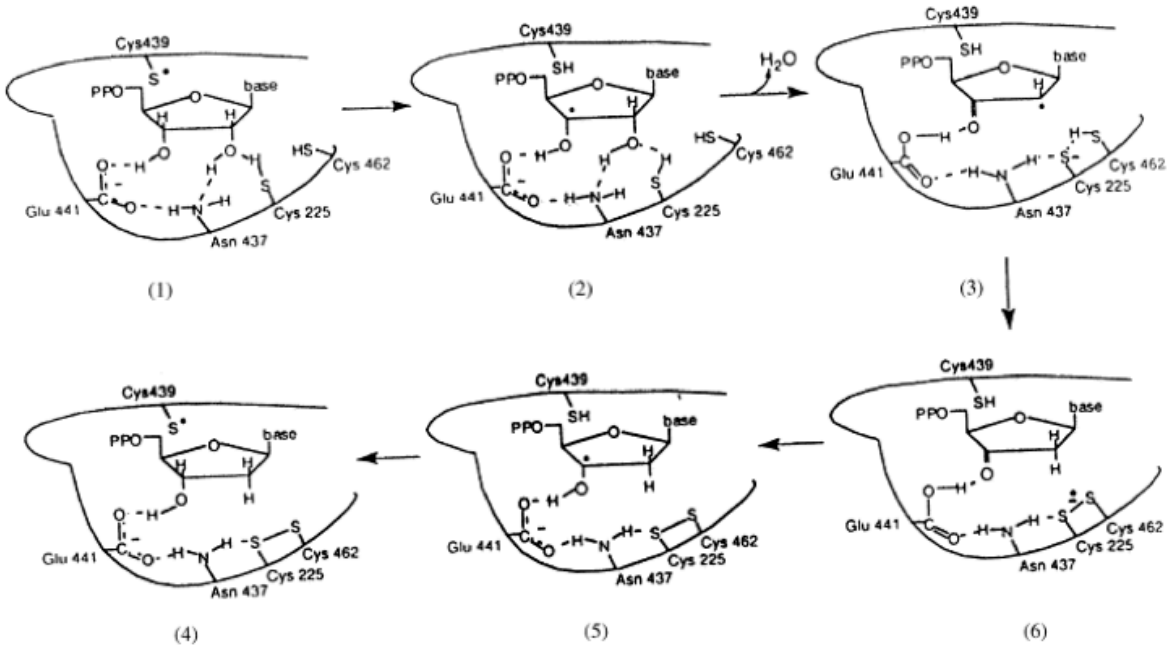
Cys439
PPO
base
Glu 441
Asn 437
Cys 225
Cys 462
H_2O
(1)
(2)
(3)
(4)
(5)
(6)

B

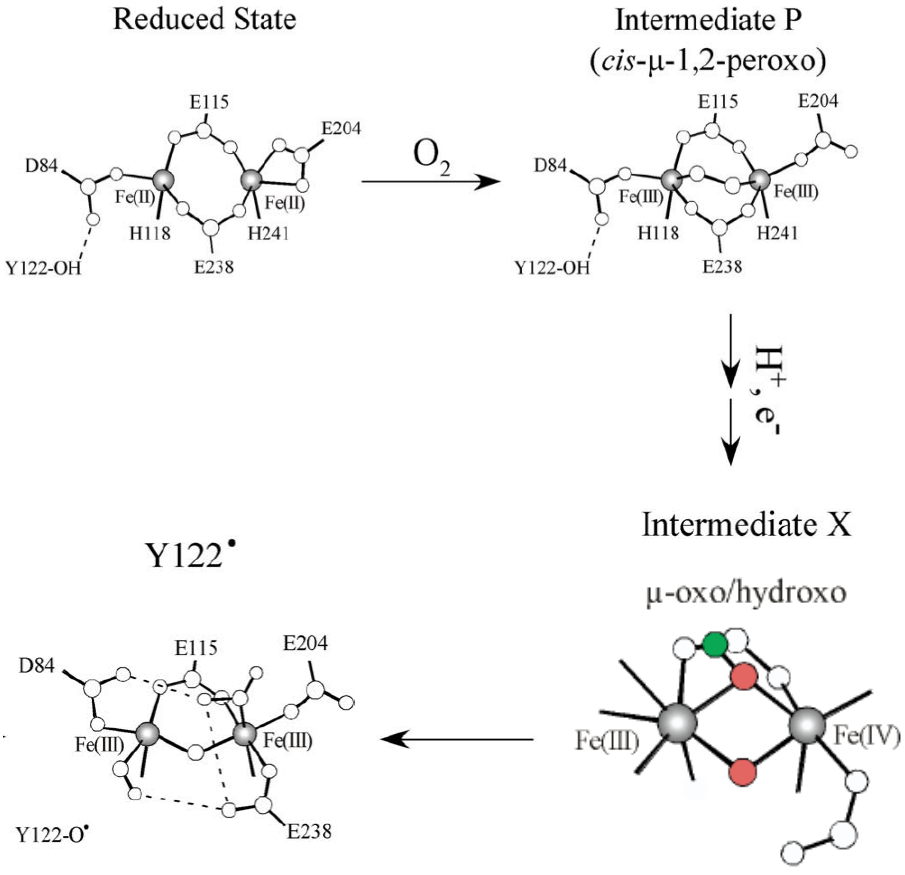
Reduced State
Intermediate P
(*cis*-μ-1,2-peroxo)
E115
E204
D84
Fe(II)
Fe(III)
H118
H241
E238
Y122-OH
O_2
H^+, e^-
Intermediate X
μ-oxo/hydroxo
Fe(IV)
Y122•
Y122-O•

dinuclear iron center *in vivo*. Reconstitution reaction with purified *E. coli* R2 provided some insights into the possible mechanisms. Formation of active R2 starts with the reduced form of R2 where it is bound to two ferrous ions (Fe^{2+}). The reduced form of R2 can initially be formed when two ferrous ions bind to the apo protein or when the active form of R2 is reduced. In the first step of active R2 formation, the ferrous ions are oxidized by molecular oxygen to yield an azide complex. The reaction then goes through a peroxide intermediate P and a μ-oxo/μ-hydroxo $[Fe^{III}(\mu\text{-}O)(\mu\text{-}OH)Fe^{IV}]$ intermediate X. Finally, intermediate X oxidizes a nearby tyrosine residue (Y122 in E. coli and Y177 in mouse) to a stable tyrosyl radical by extracting a hydrogen atom from the phenol oxygen (Figure 1.4B)(Mitic, Clay et al. 2007). The diferrous iron site is oxidized to the diferric form (Fe^{3+}), providing electrons to reduce oxygen to H2O (Eklund, Uhlin et al. 2001; Kolberg, Strand et al. 2004).

1.2.1.5 Mouse R2 iron/radical site

Although *E. coli* R2 serves as a good model in many ways for RNR in higher organisms, a number of significant differences have been observed between *E. coli* and mouse R2s. One striking difference is the stability of the iron center. *E. coli* iron center and tyrosyl radicals are stable at physiological conditions and can perform multiple turnovers of the substrate *in vitro*. However, the iron center in mouse R2 is labile and a continuous supply of Fe^{2+} and oxygen is needed to keep the enzyme fully active (Kolberg, Strand et al. 2004; Strand, Karlsen et al. 2004). Another striking difference is the accessibility of the iron/radical center. Crystal structure comparison shows that the iron/radical site in mouse R2 is accessible to solvent via a narrow hydrophobic channel, while this channel is blocked by an aromatic amino acid (Y209) in *E. coli*. The more open structure around the iron/radical site in mouse R2 explains the higher sensitivity

of this protein towards radical scavengers and inhibitors (Kauppi, Nielsen et al. 1996; Eklund, Uhlin et al. 2001; Kolberg, Strand et al. 2004).

In order to study whether another amino acid may take over the role and enzymatic function of the important tyrosine 177 residue, a series of mouse R2-Y177X mutants have been generated by site-directed mutagenesis, with X representing tryptophan (W), phenylalanine (F), cysteine (C), or histidine (H). R2-Y177W mutant can generate a transient tryptophan radical at the desired position, but does not have catalytic activity. On the other hand, R2-Y177F, R2-Y177C and R2-Y177H mutants can neither generate a radical at the desired site, nor have catalytic activity (Potsch, Lendzian et al. 1999). This suggests strongly that the tyrosyl radical 177 is essential and cannot be replaced by other amino acids.

1.2.1.6 Tyrosyl radical transfer

One striking feature of Class I RNR is its long radical transfer chain. This radical transfer chain connects the essential tyrosyl radical in R2 to the active site thiyl radical in R1. It is proposed that the radical gets to the active site through a coupled electron/proton transfer along a conserved hydrogen-bonded chain, which is about 15 angstrom long (Rova, Adrait et al. 1999). In mouse RNR, the conserved residues His173, Asp266, Trp103 in the R2 subunit and Tyr738, Tyr737, Cys429 in the R1 subunit contribute to the formation of this radical transfer pathway (Rova, Adrait et al. 1999). It has been shown that the tyrosine residue 370 (Y370) in the mouse R2 subunit connects the radical transfer pathway in R2 with the radical transfer pathway in R1. Mutating this tyrosine to phenylalanine (Y370F) renders the RNR enzyme completely inactive (Rova, Adrait et al. 1999).

1.2.2 RNR gene

1.2.2.1 Mouse RNR gene

In eukaryotes, the genes for R1 and R2 are located on separate chromosomes. In mouse, the large subunit R1 is encoded by the gene *Rrm1*, which consists of 19 exons and spans 26kb on chromosome 7. The small subunit R2 is encoded by either the *Rrm2* gene or the *p53R2* gene. The *Rrm2* gene consists of 10 exons and spans 5.9kb on chromosome 12 while the *p53R2* gene consists of 9 exons and spans 37kb on chromosome 15 (Johansson, Hjortsberg et al. 1998; Jordan and Reichard 1998; Tanaka, Arakawa et al. 2000). An enzyme complex of Rrm1 and Rrm2 provides dNTPs for S phase DNA replication and repair in proliferating cells while the Rrm1 and p53R2 complex provides dNTPs for DNA repair in quiescent cells and for mitochondrial DNA replication and repair (Guittet, Hakansson et al. 2001; Pontarin, Ferraro et al. 2007; Pontarin, Ferraro et al. 2012). The *p53R2* gene was originally identified as a p53-inducible gene following DNA damage (Tanaka, Arakawa et al. 2000). At the protein level, mouse p53R2 is 81% identical to mouse Rrm2. Most of the important domains in Rrm2 are conserved in p53R2, including the iron center, the tyrosine radical site and the radical transfer pathway. The major structure difference between Rrm2 and p53R2 is that p53R2 lacks 33 amino-terminal residues including a KEN box that is required for degradation of Rrm2 during mitosis (Nordlund and Reichard 2006). In terms of enzyme activity, it has been shown that mouse p53R2 was about 43% of the specific activity of the mouse Rrm2 when assayed *in vitro* with an excess of mouse Rrm1 protein (Guittet, Hakansson et al. 2001). Human p53R2 is shown to have about 40-70% kinetic activity of that of human Rrm2 *in vitro* (Shao, Zhou et al. 2004; Qiu, Zhou et al. 2006).

1.2.2.2 Yeast RNR gene

In budding yeast, two genes, *RNR1* and *RNR3*, encode separate versions of the R1 subunit, Rnr1 and Rnr3, respectively. Two genes, *RNR2* and *RNR4*, encode two R2-like proteins, Rnr2 and Rnr4, respectively (Nordlund and Reichard 2006). RNR1 and RNR3 shard 80% amino acid sequence identity and both proteins contain the essential catalytic and allosteric regulation sites. The different roles of Rnr1 and Rnr3 are still not very clear. It is believed that all dimeric combinations of the two subunits, Rnr1/Rnr1, Rnr1/Rnr3, and Rnr3/Rnr3 exist. Expression of Rnr1 is essential for cell growth while Rnr3 is not. Under normal conditions, the expression level of Rnr3 is very low; however, Rnr3 expression level is largely induced upon DNA damage (Kolberg, Strand et al. 2004). Rnr2 and Rnr4 form a heterodimer to provide a functional RNR with the large subunit. They only share 47% amino acid sequence identity. Rnr4 lacks essential residues that are involved in iron binding and is therefore not enzymatically active. Rnr4 is demonstrated to have a structural function, where it stabilized the Rnr2 subunit and facilitates iron assembly in Rnr2 (Kolberg, Strand et al. 2004; Nordlund and Reichard 2006; Zhang, Liu et al. 2011).

1.2.3 RNR regulation

The regulation of RNR is complex and multi-faceted, because imbalances in dNTP pools are mutagenic and can interfere with many other aspects of metabolism. There are several important regulatory mechanisms of RNR in cells: allosteric regulation, cell cycle regulation, subcellular localization regulation, small inhibitory protein regulation and iron availability regulation.

1.2.3.1 Allosteric regulation of RNR

Allosteric regulation of RNR allows the enzyme to provide a balanced supply of all four dNTPs and to adapt rapidly to changes in the requirements for dNTPs. Allosteric regulation of RNR involves the binding of effectors to two separate sites in the R1 subunit: the specificity site that regulates substrate specificity and the activity site that regulates the general activity of RNR (Nordlund and Reichard 2006).

The specificity for each of the four substrates is determined by the binding of an allosteric effector to the specificity site: binding of dATP (or ATP) at the specificity site promotes the binding and reduction of the pyrimidines CDP and UDP; binding of dTTP inhibits reduction of CDP and UDP and stimulates reduction of GDP; binding of dGTP inhibits reduction of GDP and stimulates reduction of ADP. Binding of dCTP has no or only a minor effect (Kolberg, Strand et al. 2004). Recently, a collection of yeast strains expressing several single amino acid mutants of the specificity site was generated. These mutants showed imbalanced dNTP pools and increased mutation rates. Depletion of one or a few dNTPs activated the S phase checkpoint; however, when none of the dNTPs was limiting for DNA replication, even extreme and mutagenic dNTP pool imbalances did not activate the S phase checkpoint (Kumar, Viberg et al. 2010).

The overall activity of RNR is controlled by the binding of dATP or ATP to the activity site: ATP binding activates RNR activity while dATP binding inhibits enzyme activity. As a result, dATP has both a stimulatory effect and an inhibitory effect. However, since dATP has a much higher affinity to the specificity site, the inhibitory effect of dATP is only significant at high concentrations of dATP (Kolberg, Strand et al. 2004). It has been reported that mutating the Aspartic acid (D) to asparagine (N) in the activity site, the so-called D57N mutation, resulted in

an RNR enzyme that does not respond to dATP-mediated inhibition. Mammalian lymphoma cells expressing this mutant RNR had around 3- to 10- fold increase in dNTP pools and about 40-fold increase in mutation rate (Weinberg, Ullman et al. 1981; Caras and Martin 1988). When this mutant was expressed in yeast, it resulted in a 1.6-2 fold increase in dNTP pools under normal growth conditions and an 11- to 17-fold increase in dNTP pools during DNA damage. This disruption in dNTP pools also led to a 2- to 3-fold increase in mutation rates (Chabes, Georgieva et al. 2003).

Previous studies have suggested that at physiologically nucleotide concentrations, both active and inactive RNR complexes consists of an R1 hexamer and an R2 dimer (R16-R22) (Rofougaran, Vodnala et al. 2006). Recently, crystal structures of the yeast enzyme with the dATP-induced R1 hexamer has been solved. Site-directed mutagenesis and functional assays showed that hexamerization of R1 is a prerequisite for inhibition by dATP, indicating that dATP-induced R1 oligomerization acts as a mechanism for regulating RNR activity (Fairman, Wijerathna et al. 2011). The same study also showed that ATP binding induces R1 hexamerization and activates RNR activity, suggesting a possible functional $R1_6$-$R2_2$ oligomer at physiologically conditions (Fairman, Wijerathna et al. 2011). Since both ATP and dATP can induce R1 hexamer formation, it is still not clear how dATP acts as an inhibitor while ATP is an activator. This maybe because that ATP and dATP hexamers have different packing arrangements and the conformational changes accompanying dATP hexamerization may lead to the disruption of free-radical transfer to the active site (Fairman, Wijerathna et al. 2011).

1.2.3.2 Cell cycle regulation of RNR

In mammals, RNR activity is highly induced during S phase. R1 and R2 are regulated differently. R1 gene expression during the cell cycle is mainly regulated at the transcriptional

level, with the transcription of *Rrm1* negligible in G_0/G_1 phase and reaches maximum in S phase. The TATA-less promoter of *Rrm1* is recognized by cell cycle specific transcription factors (Johansson, Hjortsberg et al. 1998). However, even if R1 mRNA level fluctuates during the cell cycle, R1 protein shows a constant level throughout the cell cycle due to its long half life (about 15 hours) (Engstrom, Eriksson et al. 1985).

R2 is regulated both transcriptionally and by protein degradation. R2 promoter contains a TATA-box, an upstream activating region and a proximal repressive element that binds E2F4. Similar to R1 regulation, the transcription of *Rrm2* is undetectable in G_0/G_1 phase and peaks in S phase (Chabes, Bjorklund et al. 2004). In contrast to R1 protein, R2 protein correlates with its mRNA level well and has a short half-life of 3 hours (Engstrom, Eriksson et al. 1985). Therefore, R2 level is the rate limiting factor for RNR enzyme activity.

After synthesizing dNTPs for S phase DNA replication and repair, R2 protein is degraded through two ubiquitin ligases that have central roles in cell cycle regulation: the Skip1/Cullin/F-box (SCF) complex and the anaphase-promoting complex (APC) (Chabes, Pfleger et al. 2003; D'Angiolella, Donato et al. 2012). During G_2 phase, R2 protein is recognized by cyclin F, an SCF ubiquitin ligase F-box protein and targeted for degradation. This is achieved by CDK-mediated phosphorylation of R2 on Thr33, which exposes an Rxl motif to cyclin F. After DNA damage, cyclin F is down-regulated in an ATR-dependent manner to allow accumulation of R2 (D'Angiolella, Donato et al. 2012). During mitosis/G_1 phase, R2 is degraded by the Cdh1-APC complex that recognizes a KEN box motif at the N-terminus of R2. Mutating the KEN box motif stabilized R2 during mitosis/G_1 in R2-overexpressing cells (Chabes, Pfleger et al. 2003).

p53R2, the p53 inducible small subunit of RNR, on the other hand, is not cell cycle regulated. It has basal level expression through out the cell cycle and lacks the N-terminal KEN

box required for degradation during mitosis. After DNA damage, p53R2 is induced in a p53-dependent manner. It can substitute for R2 and form an active RNR, providing dNTPs for DNA repair (Tanaka, Arakawa et al. 2000; Guittet, Hakansson et al. 2001; Nordlund and Reichard 2006).

1.2.3.3 Subcellular localization regulation of RNR

RNR subcellular localization is an additional layer of control. In yeast, it is well established that Rnr1 and Rnr3 localize to the cytoplasm while Rnr2 and Rnr4 are in the nucleus. In response to S-phase or DNA damage, Rnr2-Rnr4 complex enters the cytoplasm to bind to Rnr1, forming an active complex. Rnr2 and Rnr4 are anchored in the nucleus by a protein Wtm1. After DNA damage and under replication stress, Wtm1 dissociates from Rnr2 and Rnr4, releasing the subunits to the cytoplasm (Lee and Elledge 2006; Zhang, An et al. 2006). The cytoplasmic Rnr2 and Rnr4 are actively imported to the nucleus by a protein Dif1, which binds directly to the Rnr2-Rnr4 complex. Dif1 is both cell cycle and DNA damage regulated (Lee, Wang et al. 2008; Wu and Huang 2008). Therefore, the nuclear localization of Rnr2 and Rnr4 is achieved by a dynamic balance of Wtm1-mediated nuclear retention and Dif1-mediated nuclear import.

In mammal, the localization of RNR subunits is still controversial. It is largely believed that Rrm1 and Rrm2 localize to the cytoplasm during S phase and synthesized dNTPs are diffused to the nucleus for DNA replication (Engstrom and Rozell 1988; Pontarin, Fijolek et al. 2008). p53R2 was reported to translocate to the nucleus upon DNA damage to facilitate dNTP synthesis at the site of DNA damage (Nakano, Balint et al. 2000; Tanaka, Arakawa et al. 2000). However, a study from a few years ago showed that R1, R2 and p53R2 all localize to the cytoplasm during cell proliferation and after DNA damage (Pontarin, Fijolek et al. 2008). In

recent years, there is increasing evidence showing that R1 and R2 accumulate at the DNA damage site in the nucleus. This accumulation is dependent on the interaction between R1 and the DNA damage response protein Tip60 (Niida, Katsuno et al. 2010; Hu, Yeh et al. 2012). In addition, R2 has been reported to enter the nucleus in G_2 phase to interact with cyclin F and get degraded (D'Angiolella, Donato et al. 2012).

1.2.3.4 Small inhibitory protein regulation of RNR

In yeast, RNR activity is also regulated by the binding of small inhibitory proteins. In *S. cerevisiae*, Sml1, a 104-amino-acid protein, binds to the C terminus of Rnr1 and inhibits its activity (Zhao, Muller et al. 1998; Zhao, Georgieva et al. 2000). Sml1 is regulated by the cell cycle checkpoint proteins Mec1 (homolog of ATM), Rad53 (homolog of CHK2) and Dun1. During S phase and after DNA damage, Mec1 and Rad53 activate Dun1, which directly phosphorylate Sml1, leading to its degradation. At the same time, Dun1 activates the transcriptional induction of RNR genes. The dual function of Dun1 ensures synthesis of sufficient amounts of dNTPs for DNA replication and repair (Zhao and Rothstein 2002). In *S. pombe*, Spd1 binds to Cdc22p (R1 subunit in *S. Pombe*) and inhibits RNR activity (Hakansson, Dahl et al. 2006). So far, no Sml1 homolog or any kind of inhibitory protein of RNR has been identified in mammals.

1.2.3.5 Iron availability regulation of RNR

Iron is an essential cofactor in the class Ia RNRs. A recent study looked at the mechanisms that control RNR function upon Fe deficiency. The authors showed that in budding yeast, during Fe starvation, the R2 subunit is redistributed from the nucleus to the cytoplasm in a manner that is independent of the checkpoint kinases Mec1 and Rad53. Instead, the iron-regulated Cth1/Cth2 mRNA-binding proteins specifically interact with and degrade the mRNA

of an R2 nuclear-anchor protein Wtm1. The decrease in Wtm1 protein levels results in the redistribution of R2 subunit to the cytoplasm, where it assembles with R1 to form active complexes. In addition, Cth1/Cth2 induce downregulation of R2 mRNA levels, leading to a multilayered control of RNR that optimized RNR function to allow DNA synthesis and repair when iron is limited (Sanvisens, Bano et al. 2011).

1.2.4 RNR and DNA damage response

1.2.4.1 RNR and DNA damage response in yeast

All organisms respond to DNA damage in two ways: by cell cycle arrest and by induction of DNA damage repair genes. In yeast, the most abundant DNA damage-inducible genes are those involved in DNA replication, including genes coding for DNA polymerases and subunits of RNR. When DNA synthesis is blocked by agents such as hydroxyurea (HU), or when DNA is damaged by agents such as UV light, transcription of yeast RNR genes, *RNR1*, *RNR2* and *RNR3* are induced. *RNR1* mRNA level shows ~5 fold increase, *RNR2* mRNA shows ~25 fold increase and *RNR3* mRNA is increased about 500 fold (Elledge, Zhou et al. 1993). Later it has been demonstrated that activation of yeast RNR genes in response to DNA damage is through the canonical Mec1/Rad53 DNA damage response pathway, where a downstream kinase Dun1 is activated. Activation of Dun1 has three roles in promoting RNR activity: by activating transcription of RNR genes, by phosphorylating and degrading the RNR inhibitory protein Sml1 and by facilitating cytosolic localization of RNR (Elledge, Zhou et al. 1993; Zhao and Rothstein 2002; Lee and Elledge 2006; Zhang, An et al. 2006). The end result of increased RNR activity is a 6 to 8 fold increase in dNTP levels, which improves organismal survival after DNA damage. In recent years, there is increasing evidence showing that in *E. coli* and yeast, increased dNTP levels after DNA damage allow more efficient translesion synthesis to bypass certain DNA

lesions (Sabouri, Viberg et al. 2008; Gon, Napolitano et al. 2011). It is worth noting that this increase in dNTP pool also leads to higher mutation rates, which may result from reduced fidelity of replicative polymerases and/or activation of error-prone translesion DNA synthesis at elevated dNTP levels (Chabes, Georgieva et al. 2003; Lis, O'Neill et al. 2008; Gon, Napolitano et al. 2011). In addition, it has been proposed that the same mechanisms also result in reduced recombinogenic lesions in yeast strains with increased dNTP levels (Fasullo, Tsaponina et al. 2010).

1.2.4.2 RNR and DNA damage response in mammals

Similar as in yeast, DNA damage in mammals activates the canonical ATM/ATR DNA damage response pathway. Activation of ATM and ATR has two outcomes: recruitment of DNA damage repair proteins including 53BP1 and Brca1 to the site of DNA damage and activation of downstream CHK2/p53 and CHK1 kinases to halt the cell cycle progression. It has long been shown that DNA damage activates mammalian RRM1 and RRM2. Upon treatment of DNA damaging agents such as chlorambucil, RRM1 mRNA level is induced 9 fold while RRM2 mRNA level is induced 13 fold (Hurta and Wright 1992). In addition, upon UV damage, RRM1 promoter is induced up to 3 fold and RRM2 promoter is induced up to 10 fold (Filatov, Bjorklund et al. 1996). It has also been demonstrated that there is S phase/DNA damage-specific stabilization of the R2 protein (Chabes and Thelander 2000).

Recently, it has been shown that RNR activity after DNA damage affects repair pathway choice both in yeast and mammals (Burkhalter, Roberts et al. 2009; Moss, Tinline-Purvis et al. 2010). It is demonstrated that upon ionizing radiation, inhibition of RNR activity in mammalian cells favors non-homologous end joining (NHEJ) while promotion of RNR activity favors homologous recombination (HR) (Burkhalter, Roberts et al. 2009). This is because HR requires

more than 10,000 dNTPs in order to synthesize DNA strand during the pair process (Robert, Vanoli et al. 2011).

The discovery of p53R2, a p53-induced R2 subunit, makes direct connection between DNA damage response and RNR activity, and solves the mystery of DNA damage repair in quiescent cells where the level of Rrm2 is not detectable. In mammals, upon DNA damage, ATM/ATR is activated, which then activates its downstream factor p53. p53 binds directly to the first intron of the *p53R2* gene, activates *p53R2* transcription and expression (Nakano, Balint et al. 2000; Tanaka, Arakawa et al. 2000). p53R2 protein interacts with Rrm1 and forms an active RNR complex to provide dNTPs for DNA damage repair (Guittet, Hakansson et al. 2001; Hakansson, Hofer et al. 2006). Recently, it has also been demonstrated that ATM can directly phosphorylate p53R2 in response to genotoxic stress. This phosphorylation leads to stabilization of p53R2 protein against hyperubiquitination and degradation by the ubiquitin ligase MDM2 and confers resistance to DNA damage (Chang, Zhou et al. 2008). Inhibition of endogenous p53R2 expression in cells that have intact p53-dependent DNA damage checkpoint reduced RNR activity, DNA repair and cell survival after exposure to various genotoxins (Tanaka, Arakawa et al. 2000). Furthermore, cancer cell lines that have p53R2 mutation, which resulted in loss of RNR activity, showed enhanced DNA damage-induced apoptosis (Yamaguchi, Matsuda et al. 2001). p53R2 knout-out mice die by the age of 14 weeks due to severe renal failure. Kidneys from p53R2 null mice showed increased number of apoptotic cells and higher rates of spontaneous mutation. p53R2 null MEFs had severely attenuated dNTP pools under oxidative stress (Kimura, Takeda et al. 2003). When the role of p53R2 in mitochondrial DNA synthesis was detected later (see section 1.2.5), measurement of mitochondrial DNA content in tissues (muscle, kidney and liver) from p53R2 null mice revealed severe mitochondrial DNA depletion

(Bourdon, Minai et al. 2007). All of these results suggest that p53R2 has a pivotal role in maintaining dNTP levels for repair of DNA damage.

Unlike in yeast, even if there is increased RNR activity after DNA damage in mammals, it is still not clear what effects DNA damage has on dNTP pools in mammals (Kunz and Kohalmi 1991). A recent report showed that in non-proliferating cells, there is a slow, 4-fold increase in p53R2 protein expression after DNA damage, which results in a less than 2-fold increase in dNTP pools. This 2-fold increased dNTP pool is only about 5% of the size of the pools in S-phase cells. Moreover, logarithmically growing mammalian cells do not show any major increase in their dNTP pools when p53R2 is activated upon DNA damage (Hakansson, Hofer et al. 2006). This may be due to the possibility that RNR activity and dNTP pools are more strictly regulated in mammals and some undiscovered mechanisms might act on dNTP pools after DNA damage. In addition, in mammals dNTP biosynthesis may also be compartmentalized close to the damage sites during the DNA damage response (Niida, Katsuno et al. 2010) and measurement of total cellular dNTP changes may not be sensitive enough to reflect the local changes.

1.2.5 RNR and mitochondrial DNA synthesis

Mitochondrial DNA (mtDNA) synthesis is not cell cycle regulated. In proliferating cell, there is no difficulty obtaining dNTPs for mitochondrial DNA synthesis since levels of dNTPs are about 20 times higher in S-phase cells than in resting cells (Hakansson, Hofer et al. 2006). dNTPs can be actively transported from the cytoplasm into mitochondria in these growing cells (Mathews and Song 2007). In resting cells, dNTPs for mitochondrial DNA synthesis can come from salvage of deoxyribonucleosides by the salvage pathway enzymes dGK and TK2 that localize in the mitochondria (Mandel, Szargel et al. 2001; Saada, Shaag et al. 2001). Recently, it

has been demonstrated that beside the salvage pathway, p53R2-catalyzed ribonucleotide reduction is required for proper mitochondrial DNA synthesis and DNA repair in resting cells (Bourdon, Minai et al. 2007; Thelander 2007; Pontarin, Ferraro et al. 2012). Over-expression of p53R2 in mice leads to mtDNA depletion in skeletal muscles (Ylikallio, Page et al. 2010). Moreover, mutations in p53R2 have been associated with multiple human mitochondrial diseases that are characterized by severe mtDNA depletion and accumulation of deletions and point mutations in mitochondrial genome (Bourdon, Minai et al. 2007; Kollberg, Darin et al. 2009; Shaibani, Shchelochkov et al. 2009; Tyynismaa, Ylikallio et al. 2009) (more details in section 1.3.3).

1.3 RNR deregulation and genomic instability

Balanced dNTP pools are essential for genomic integrity and organismal survival. As the enzyme that catalyzes the rate-limiting step of de novo dNTP synthesis, RNR is tightly regulated to ensure the fidelity of genome maintenance. It is not surprising to find out that RNR deregulation leads to genomic instability and causes detrimental effects in organisms. For example, RNR deregulation has been shown to be mutagenic in both yeast and mammalian cells (Caras and Martin 1988; Chabes, Georgieva et al. 2003). RNR deregulation can lead to genomic instability through at least two different mechanisms: altered enzyme activity that may result in dNTP pool disruptions and elevated free radical production that may contribute to oxidative stress.

1.3.1 Genomic instability induced by altered enzyme activity

It is not surprising that deregulation of enzymes involved in dNTP biosynthesis often leads to mutagenesis. For example, mutations of two enzymes that are important for dTTP synthesis, TK1 and TMPK, lead to over stabilization of the enzymes and subsequent dTTP

accumulation, which then result in increased spontaneous mutation rates and genomic instability (Ke, Kuo et al. 2005). As a key enzyme in dNTP synthesis, RNR enzyme activity alterations are also mutagenic. Exposure of *E. coli* to UV light increases the expression of RNR, leading to a 1.8- to 3.7-fold increase in all four dNTPs. This increase in dNTP pool is accompanied by increased spontaneous mutagenesis (Gon, Napolitano et al. 2011).

Yeast RNR requires at least 5-10 times higher dATP concentration than mammalian RNR *in vitro* to have feedback inhibition at the activity site (a property called "relaxed dATP feedback inhibition") (Reichard, Eliasson et al. 2000; Domkin, Thelander et al. 2002). Due to this property, in yeast upon DNA damage, there is a 6 to 8 fold increase in dNTP pools. This increase in dNTP pools dramatically improves cell survival, but also leads to increased mutations rates, indicating that altered RNR enzyme activity leads to altered dNTP pool and causes mutagenesis (Chabes, Georgieva et al. 2003). The same paper also showed that an RNR1 mutant, RNR1-D57N, which has a D57N mutation in the allosteric activity site in RNR1 and completely loses dATP feedback inhibition, resulted in an 11- to 17- fold increase in dNTP pools during DNA damage. This disruption in dNTP pool also causes increased mutation rates (Chabes, Georgieva et al. 2003). A recent study created yeast strains with single amino acid substitution in a region of RNR1 that is highly conserved from yeast to humans and is important for the connection between the specificity site and the catalytic site. Yeast stains that express these RNR1 mutants have dNTP pool imbalances, which also correlate with elevated mutation rates. The mutations can be explained by imbalanced dNTP-induced increase in misinsertion, strand misalignment and mismatch extension at the expense of proofreading (Kumar, Abdulovic et al. 2011).

Unlike in yeast, where the connection between RNR enzyme activity alteration and increased mutagenesis is relatively clear, how RNR deregulation leads to mutagenesis in

mammals is not fully understood. A mouse T-lymphosarcoma cell line (S49) was selected by deoxyguanosine and a resistant mutant clone (dGuo-200-1) was identified to have the D57N mutation in the large subunit Rrm1. Same as in yeast, this mutation causes complete loss of dATP feedback inhibition. It has been shown that this cell line has a 2- to 9-fold increase in dNTP pools and over 100-fold increase in spontaneous mutation rates (Ullman, Clift et al. 1980; Weinberg, Ullman et al. 1981; Caras and Martin 1988). A later study cloned the cDNA of Rrm1-D57N and transfected the DNA into Chinese Hamster Ovary (CHO) cells. CHO cells expressing this mutant Rrm1-D57N protein showed around a 15- to 25- fold increase in the frequency of spontaneous mutation; however, no dNTP pool changes was discovered in these cells (Caras and Martin 1988). Another cell line with RNR enzyme activity alterations is a hydroxyurea-resistant, protein Rrm2-overexpressing mouse cell line. These cells have 3-15 times higher RNR enzyme activity than the parent cells. However, the dNTP pools are close to normal (Akerblom, Ehrenberg et al. 1981). In addition, the hydroxyurea-resistant, Rrm2-overexpressing mouse mammary tumor TA 3 cell line had around 40-fold increase in Rrm2 protein level compared to the parent cells, yet didn't show dNTP pool changes compared to the parent cells (Eriksson, Graslund et al. 1984; Chabes and Thelander 2000). Therefore, it is not very clear whether the elevated mutagenesis associated with RNR activity alterations is resulted from dNTP pool perturbations. Failure to detect dNTP pool changes in cells with altered RNR activity could be due to relatively small changes in dNTP pools, which is difficult to measure. Alternatively, a specific interaction of RNR with the machinery of DNA replication or repair may be involved.

The effect of RNR activity alterations in whole organisms such as mice has also been investigated. Simultaneous over-expression of Rrm1 and Rrm2 (or p53R2) subunits in mice leads to imbalanced dNTP pools, where expansion in dATP and dCTP pools and reduction in

dTTP pool were observed. In addition, this over-expression also leads to progressive mitochondrial DNA (mtDNA) depletion in the mouse skeletal muscle (Ylikallio, Page et al. 2010). When the mutant Rrm1-D57N that loses dATP feedback inhibition is simultaneously over-expressed in mice together with either Rrm2 or p53R2, embryonic and postnatal lethality was observed. Skeletal muscles from these mice show dNTP pool perturbations, with 3- to 40-fold increase in dCTP, dTTP and dGTP and 4- to more than 300-fold increase in dATP (J. Page and R. Weiss, unpublished data). This implies that RNR activity alterations in organismal level also cause dNTP pool disturbances, which can have detrimental effects in organisms. The mechanism of how dNTP pool alterations leads to lethality in these mice is still under investigation.

1.3.2 Genomic instability induced by elevated free radical production

The small subunit of RNR, Rrm2, produces free radicals during the catalytic cycle (Kolberg, Strand et al. 2004). Free radicals in cells can interact with critical macromolecules including DNA, proteins and lipids, leading to cell death, mutation and other toxicities (Martin and Barrett 2002). Mouse Rrm2 has a relatively open structure around the free radical producing di-nuclear iron center (Kolberg, Strand et al. 2004). It is possible that the free radicals produced by Rrm2 can interfere with other molecules in cells. It has been shown that recombinant human Rrm2 protein produces excessive reactive oxygen species (ROS) *in vitro* (Xue, Zhou et al. 2006; Liu, Xue et al. 2008). Controversially, in the same paper, p53R2 has been shown to act as an antioxidant *in vitro* (Liu, Xue et al. 2008). However, critical assay conditions including the activity and stability of the two subunits were not provided in the paper, making it hard to compare and conclude the redox properties of these subunits *in vitro*.

Excessive ROS production can cause increased oxidative stress, which leads to DNA damage such as base modifications and DNA strand alterations. Oxygen radicals produce more than 30 different DNA adducts with each potentially mutagenic and contributing to the etiology of cancer (Feig, Reid et al. 1994). Furthermore, Rrm2 has been shown to cooperate with oncogenes including Ras to determine transformation and malignant potential. This activity is independent of ribonucleotide reduction and involves activation of Ras downstream proteins Raf and Rac (Fan, Villegas et al. 1996). Since ROS can activate Ras signaling pathways in cancer, the cooperativity of Rrm2 and Ras could be through ROS production and activation of downstream pathways (Fan, Villegas et al. 1996). Rrm2 and p53R2 overexpressing transgenic mice develop lung neoplasms with frequent G to T transversion mutations in growth regulatory genes. G to T transversions are a signature of oxidative DNA damage, suggesting that R2-induced mutagenesis and tumorigenesis is associated with increased oxidative stress (Xu, Page et al. 2008).

1.3.3 Mitochondrial genome instability induced by p53R2 deregulation

Consistent with a role of Rrm1 and p53R2 in providing dNTPs for DNA repair and mitochondrial DNA synthesis in resting cells, p53R2 knockout mice die at around 14 weeks of age due to severe renal failure (Kimura, Takeda et al. 2003). In addition, multiple tissues in these p53R2 knockout mice showed mitochondrial DNA (mtDNA) depletion (Bourdon, Minai et al. 2007). In humans, nonsense, missense and splice-site mutations and in-frame deletions of the p53R2 gene have been shown to result in mitochondrial DNA depletion syndrome (MDS), where the patients only had 1-4% residual mtDNA in muscle and are not viable (Bourdon, Minai et al. 2007; Kollberg, Darin et al. 2009). Mitochondrial neurogastrointestinal encephalopathy (MNGIE) is a progressive neurodegenerative disorder. Patients with this disease often have

around 12% residual mtDNA and two missense mutations in p53R2 that affects p53R2 and Rrm1 interaction and enzyme activity have been identified to contribute to this disease (Shaibani, Shchelochkov et al. 2009). Another mitochondrial disorder called autosomal-dominant progressive external ophthalmoplegia (adPEO) is characterized by accumulation of multiple mtDNA deletions in postmitotic tissues. A group of patients with this disease have a nonsense mutation in p53R2 that results in a protein with truncation of the C-terminus essential for the interaction with Rrm1 (Tyynismaa, Ylikallio et al. 2009). All these findings suggest that the de novo dNTP synthesis pathway mediated by RNR is essential to maintain not nuclear, but also mitochondrial genome integrity.

1.4 RNR and cancer

Tumor cells are fast proliferating and thus require large amount of dNTPs. Early evidence in the 1970s already showed that in a series of slow and fast growing rat hepatomas, RNR activity correlated well with tumor growth rate. Differences of 200-fold in enzyme activity were observed between the very fast and the slow growing tumors (Elford, Freese et al. 1970). The importance of RNR in DNA synthesis and repair has made it an important target for anticancer and antivirus agents a long time ago. For example, in the 1980s, marked increase in dNTP pools was identified in cancer cells and anticancer chemotherapy targeting nucleotide metabolism was investigated (Weber 1980). However, the role RNR plays in tumorigenesis is still not very well understood.

1.4.1 Rrm1 suppresses tumorigenesis in early stage tumor development

It is generally believed that the large subunit of RNR, Rrm1, acts as a tumor suppressor. It has been shown that Rrm1 over-expression in RAS-transformed mouse cells led to reduced transforming activity and marked suppression of tumorigenicity and lung metastases *in vivo*

(Fan, Huang et al. 1997). In addition, Rrm1 over-expression in human and mouse lung cancer cell lines induced PTEN expression, suppressed migration, invasion, metastasis formation, and increased survival in a mouse model (Gautam, Li et al. 2003). Rrm1 transgenic mice showed significantly suppressed lung tumor formation induced by the carcinogen urethane and it is proposed that this tumor suppressor activity is mediated through efficient DNA damage repair (Gautam and Bepler 2006). In contrast, Rrm1 transgenic mice from a different group showed comparable spontaneously lung tumor incidence as wild type control (Xu, Page et al. 2008). In human patients with non-small cell lung cancer (NSCLC) and treated with surgery already, high levels of Rrm1 expression are associated with longer life span and later disease recurrence than patients with low levels (Bepler, Sharma et al. 2004). It has been demonstrated that Rrm1 protein in NSCLC is nuclear and highly correlates with expression of a nuclear excision repair protein ERCC1. Co-expression of these two proteins is significantly associated with disease-free and overall survival, especially in a group of patients who underwent lung cancer surgery at early stages (Zheng, Chen et al. 2007).

1.4.2 R2 promotes tumorigenesis

Rrm2 has been shown to play a direct role in determining malignant potential through cooperating with oncogenes. Expression of Rrm2 in mouse cells leads to increased focus formation and anchorage-independent growth in cooperation with a variety of oncogenes including ras, myc and src (Fan, Villegas et al. 1996; Fan, Villegas et al. 1998). Human carcinoma cells that have higher Rrm2 expression level demonstrated higher invasive potential *in vitro* (Zhou, Tsai et al. 1998). These cells also showed decreased thrombspondin-1 and increased VEGF production, suggesting a role of Rrm2 in tumor angiogenesis (Zhang, Hu et al. 2009). *In vivo* study with Rrm2 over-expressing transgenic mice showed significantly increased lung

tumorigenesis, with the tumors histopathologically resemble human papillary adenocarcinomas and often have mutations in the *K-ras* proto-oncogene. When combined with defects in DNA mismatch repair pathway, these Rrm2 over-expressing mice showed synergistically increased mutagenesis and carcinogenesis, providing strong evidence for Rrm2 as a tumor promoter through a mutagenic mechanism (Xu, Page et al. 2008).

In humans, Rrm2 expression level is associated with breast tumor grade, suggesting a role of RNR in supporting rapid cell division of high-grade tumors (Ma, Salunga et al. 2003). Overexpression of Rrm2 has also been observed in patients with gastric cancer, ovarian cancer, bladder cancer and colorectal cancer (Morikawa, Hino et al. 2010; Morikawa, Maeda et al. 2010; Liu, Zhang et al. 2012; Lu, Feng et al. 2012; Wang, Lu et al. 2012). There is evidence showing that up-regulated Rrm2 expression in colorectal cancer cell lines is mediated by the oncogene KRAS (Yoshida, Tsunoda et al. 2011). In addition, Rrm2 overexpression induces cellular invasiveness in a pancreatic cancer cell line in a NF-κB-dependent manner (Fan, Villegas et al. 1996).

The role of p53R2 in mutagenesis and tumorigenesis is controversial. Based on the p53-induced nature of p53R2 expression and its role in DNA damage repair, it is proposed that p53R2 has tumor suppressor activity (Tanaka, Arakawa et al. 2000). p53R2 has been shown to have antioxidant activity *in vitro* (Xue, Zhou et al. 2006). Under genotoxic stress, p53R2 can facilitate p21 accumulation and G_1 arrest, which may help with DNA damage repair and prevention of mutation accumulation (Xue, Zhou et al. 2007). In human, p53R2 is negatively related to metastasis of colon adenocarcinoma samples (Liu, Zhou et al. 2006). Higher levels of p53R2 expression suppress invasiveness of cancer cells and are correlated with markedly better

survival in colorectal cancer patients (Liu, Lai et al. 2011). Tumor suppressor activity of p53R2 may be due to its role in DNA repair and regulation of the redox state in cells.

On the other hand, there are several reports on p53R2 as a tumor promoter. p53R2 overexpressing cells have increased mutation frequency and p53R2 overexpression in mice induced lung tumor development (Xu, Page et al. 2008). In humans, p53R2 expression is correlated with melanoma malignancy, oral carcinogenesis, esophageal squamous cell carcinoma and non-small cell lung cancer (Yanamoto, Kawasaki et al. 2003; Okumura, Natsugoe et al. 2006; Uramoto, Sugio et al. 2006; Yanamoto, Kawasaki et al. 2009; Matsushita, Ikeda et al. 2012). In addition, a couple of polymorphisms in the gene encoding p53R2, RRM2B, have been identified and associated with cancer-susceptibility (Smeds, Kumar et al. 2001; Deng, Xie et al. 2005).

Both Rrm2 and p53R2 subunits require oxygen to generate tyrosyl radicals for proper RNR function. As a result, cellular oxygen levels can affect free radical production and RNR activity, where hypoxia leads to decreased free radicals and reoxygenation leads to increased free radicals (Reichard and Ehrenberg 1983; Probst, Schiffer et al. 1989). It has been shown that upon re-oxygenation after exposure to moderate hypoxia, cancer cells with higher levels of R2 resume DNA replication and S phase progression faster than cells with normal levels of R2 (Graff, Amellem et al. 2002). As a result, cells are given less time for DNA damage recognition and repair, which could contribute to mutagenesis. Since cancer cells undergo cycles of hypoxia and reoxygenation (Bristow and Hill 2008), this may provide a possible explanation of the correlation between R2 levels and tumor malignancy (Fan, Villegas et al. 1996; Fan, Villegas et al. 1998).

1.4.3 RNR expression in human cancer studies

Recent advances in molecular biology, including genomics and proteomics, have provided a fantastic opportunity for researchers to look at human cancer samples at a molecular level (Rhodes, Yu et al. 2004). RNR gene expression in human cancers has been studied using the ONCOMINE database and summarized in Figure 1.5. *RRM2* is among the top 10% highly expressed genes in 73 out of 168 cancer vs. normal sample analyses. These include bladder cancer, brain and CNS cancer, breast cancer, colorectal cancer, liver cancer, lung cancer and sarcoma. *RRM1* is among the top 10% highly expressed genes in 30 out of 170 studies. Cancer types include brain and CNS cancer, lung cancer and sarcoma. *RRM2B* (the gene enconding p53R2 in humans) is only found in 5 out of 90 studies with top 10% over-expression. In addition, both *RRM2* and *RRM1* are also shown to have reduced expression in a few cancers.

RNR gene copy number changes are also analyzed using the TCGA database (Figure 1.6). *RRM2* showed amplifications in a few cancer types including breast, ovarian, prostate and uterine. This is consistent with the ONCOMINE data where *RRM2* gene expression is increased in breast, ovarian and prostate cancers. Increased copy number and gene expression of *RRM2* correlate well with Rrm2 protein as a tumor promoter. *RRM1* showed copy number changes in small percentages across a few cancer types. It is amplified in sarcoma samples, which is consistent with increased *RRM1* gene expression in sarcoma samples based on ONCOMINE data. On the other hand, it is lost in a small percentage of glioblastoma cases, which disagrees with its increased expression in brain cancer based on ONCOMINE data. This reflects the complex role Rrm1 plays in tumorigenesis. It can act as a tumor suppressor initially, but later may become important for tumor maintenance. *RRM2B* amplification is associated with more

Figure 1.5 Bar graph showing RNR expression in human cancers. In general, RNR gene overexpression is associated with different cancer types. *RRM2* is among the top 10% highly expressed genes in 73 out of 168 analyses, *RRM1* is among the top 10% in 30 out of 170 studies and *RRM2B* (encoding p53R2) is among the top 10% in 5 out of 96 cases. In addition, *RRM2* is among the top 10% under expressed genes in 7 out of 168 studies and *RRM1* is among the top 10% in 6 out of 170 studies. The expression level of the *c-Myc* proto-oncogene is shown as a comparison. *c-Myc* is among the top 10% highly expressed genes in 40 out of 174 analyses and among the top 10% under expressed genes in 17 out of 174 studies. Data are retrieved from the ONCOMINE cancer gene expression database (version 4.4.3, search done on 12/5/12).

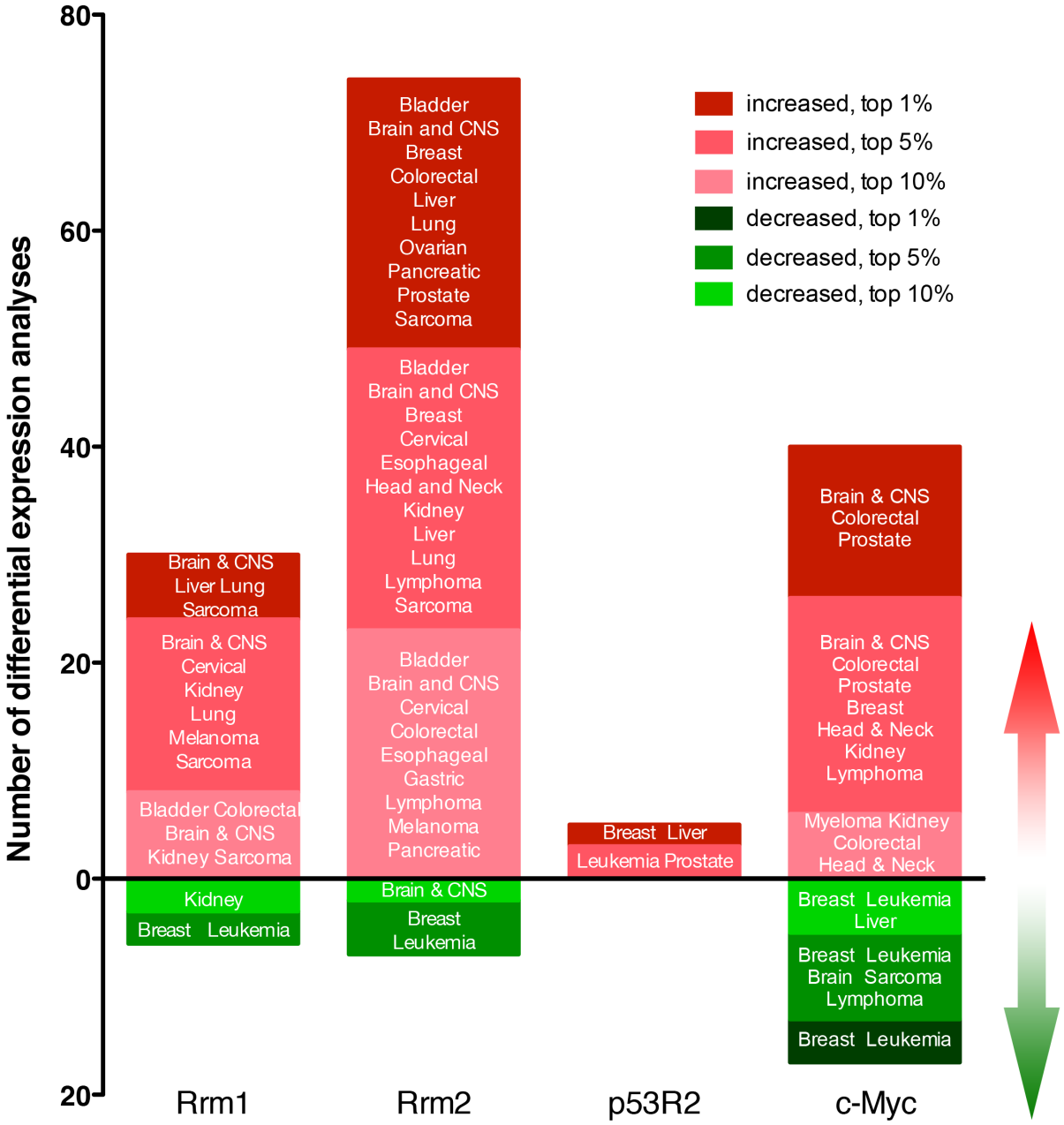
Number of differential expression analyses
80
60
40
20
0
20
increased, top 1%
increased, top 5%
increased, top 10%
decreased, top 1%
decreased, top 5%
decreased, top 10%
Brain & CNS
Liver Lung
Sarcoma
Brain & CNS
Cervical
Kidney
Lung
Melanoma
Sarcoma
Bladder Colorectal
Brain & CNS
Kidney Sarcoma
Kidney
Breast Leukemia
Bladder
Brain and CNS
Breast
Colorectal
Liver
Lung
Ovarian
Pancreatic
Prostate
Sarcoma
Bladder
Brain and CNS
Breast
Cervical
Esophageal
Head and Neck
Kidney
Liver
Lung
Lymphoma
Sarcoma
Bladder
Brain and CNS
Cervical
Colorectal
Esophageal
Gastric
Lymphoma
Melanoma
Pancreatic
Brain & CNS
Breast
Leukemia
Breast Liver
Leukemia Prostate
Brain & CNS
Colorectal
Prostate
Brain & CNS
Colorectal
Prostate
Breast
Head & Neck
Kidney
Lymphoma
Myeloma Kidney
Colorectal
Head & Neck
Breast Leukemia
Liver
Breast Leukemia
Brain Sarcoma
Lymphoma
Breast Leukemia
Rrm1
Rrm2
p53R2
c-Myc

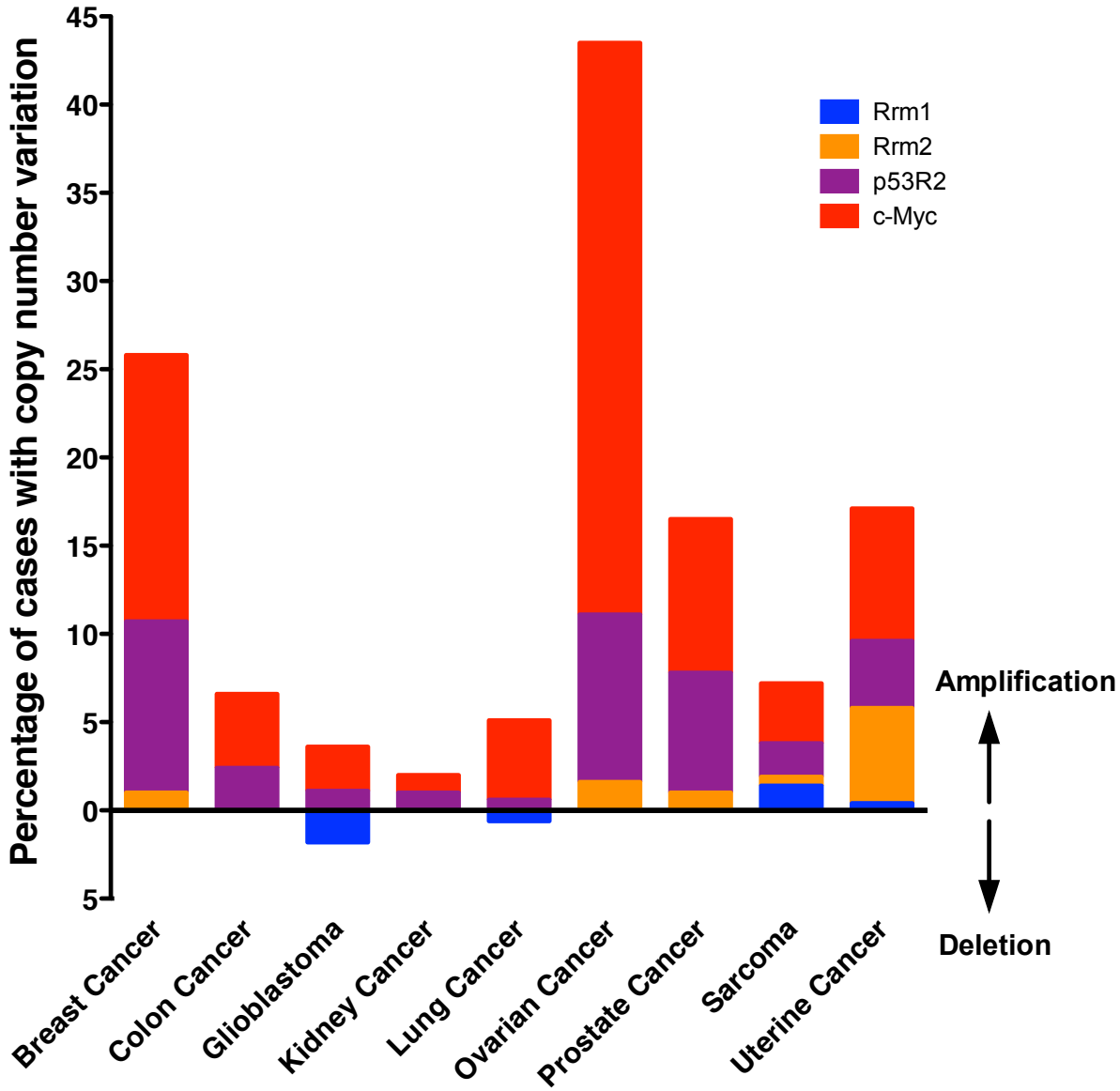

Figure 1.6 Bar graph showing RNR copy number variations in human cancers. In general, RNR copy number variations are associated with different cancer types. *RRM2* is amplified in a small percentage of sarcoma, breast, ovarian and uterine cancers. *RRM1* is amplified in a small percentage of sarcoma and uterine cancer. Its copy number is decreased in glioblastoma and lung cancer. *p53R2* is amplified in a wide range of cancers including breast, colon, glioblastoma, kidney, lung, ovarian, prostate, sarcoma and uterine cancers. However, most of these amplifications are together with *c-Myc* amplification. Data are retrieved from the TCGA database (search done on 12/5/12).

cancer types and occurs at higher percentages for each cancer type. This is partially because *RRM2B* (8q22.3) is located close to the oncogene c-myc (8q24) on the chromosome and majority of *RRM2B* amplification is accompanied with c-myc amplification in these cancers. Further analysis reveals that *RRM2B* amplification is observed in breast cancer, colon cancer, glioblastoma, ovarian cancer, prostate cancer and uterine cancer at small percentages independent of c-myc amplification. This correlates well with its increased expression in breast and prostate cancers in ONCOMINE data and supports p53R2 protein as a tumor promoter.

1.4.4 RNR and cancer therapy

The key role of RNR in DNA synthesis and cell growth has made it an important target for anticancer therapy. Increased RNR expression has been associated with malignant transformation and tumor cell growth (Shao, Zhou et al. 2006). Efforts for new RNR inhibitors have been made in basic and translational research. RNR inhibitors can be divided into different categories based on different criteria.

1.4.4.1 Rrm1 inhibition

Rrm1 can be inhibited at the protein level or RNA level. The general concept of Rrm1 protein inhibition is inactivating Rrm1 protein by interfering with the active site or inducing allosteric malfunction by nucleoside analogs (Shao, Zhou et al. 2006). Gemcitabine (2', 2'-dfluoro-2'-deoxycytidine, dFdC) is a well known deoxycytidine analog with antitumor activity against a wide variety of cancers. It is approved as the single treatment for advanced pancreatic cancer and for combination therapy against non-small cell lung cancer, breast cancer and ovarian cancer (Wong, Soo et al. 2009; Bennett, Tomlinson et al. 2012). Gemcitabine is metabolized intracellularly by deoxycytidine kinase (dCK) and other enzymes to produce gemcitabine diphosphate (dFdCDP) and gemcitabine triphosphate (dFdCTP) (Bouffard, Laliberte et al. 1993;

Shao, Zhou et al. 2006). dFdCDP inhibits RNR by interacting with the active site and results in loss of RNR catalytic activity (Heinemann, Xu et al. 1990). Clofarabine (CIF) is another commonly used Rrm1 protein inhibitor and has been used to treat leukemia (Shao, Zhou et al. 2006). It is a deoxyadenosine analog and binds to the activity site of Rrm1 at a higher affinity than the allosteric inhibitor dATP, thus giving a powerful RNR allosteric inhibition (Xie and Plunkett 1995; Xie and Plunkett 1996). Recently, it has been shown that CIF binds to the activity site of Rrm1 and targets human RNR by converting the large Rrm1 subunit into persistent hexamers *in vitro* and *in vivo*, providing the first evidence that an external ligand can perturb Rrm1 function by interfering with its oligomeric state (Aye and Stubbe 2011; Aye, Brignole et al. 2012)

In the last decade, Rrm1 has been identified as the key molecule in determining the efficacy of gemcitabine. Overexpression of Rrm1 has been reported in gemcitabine-resistant cancer cells both *in vitro* and *in vivo* (Davidson, Ma et al. 2004; Bergman, Eijk et al. 2005; Jordheim, Guittet et al. 2005; Bepler, Kusmartseva et al. 2006). In human cancer patients, high level of Rrm1 expression has been correlated with poor response to gemcitabine (Ceppi, Volante et al. 2006; Nakahira, Nakamori et al. 2007; Ohtaka, Kohya et al. 2008; Akita, Zheng et al. 2009; Reynolds, Obasaju et al. 2009; Jordheim, Seve et al. 2011; Rodriguez, Boni et al. 2011; Gong, Zhang et al. 2012). As a result, efforts have been made on individualized chemotherapy based on Rrm1 gene expression level in patients with advanced NSCLC (Simon, Sharma et al. 2007). In addition, Rrm1-specific small interfering RNA (siRNA) has been explored as a way to downregulate the expression of Rrm1 protein in tumor cells to overcome gemcitabine resistance (Wonganan, Chung et al. 2012).

1.4.4.2 R2 inhibition

R2 inhibitors target the small subunits Rrm2 and p53R2 by interfering with the iron center and tyrosyl radical production (Shao, Zhou et al. 2006). Hydroxyurea, a radical scavenger that inactivates RNR by directly quenching the tyrosyl radical in R2, has been used for cancer therapy for decades (Lassmann, Thelander et al. 1992). The limitation of hydroxyurea is the development of resistance. Overexpression of R2 and mutations in R2 have been shown to confer resistance to hydroxyurea (Zhou, Hsu et al. 1995; Jiang, Zhang et al. 2004; Sneeden and Loeb 2004).

Iron is a well-known growth factor and also an essential co-factor for RNR function. Therefore, iron chelators can be used to inhibit RNR activity and in the treatment of cancer (Buss, Greene et al. 2004). Triapine (3-AP) is an iron chelator and RNR inhibitor that is currently in phase II clinical trials for cancer chemotherapy (Nutting, van Herpen et al. 2009; Traynor, Lee et al. 2010; Ocean, Christos et al. 2011). It is demonstrated that Triapine forms complexes with iron and the Triapine-Fe(II) complex is a potent reductant that rapidly quenches the tyrosal radical in R2, rendering RNR inactive (Aye, Long et al. 2012).

Recently, there are also advances in targeting R2 by RNA interference. Delivery of siRNA against R2 by nanoparticles or by retroviruses has been shown to suppress tumor growth in head and neck cancer and pancreatic cancer (Duxbury, Ito et al. 2004; Rahman, Amin et al. 2012).

1.5 Summary

RNR's critical role in dNTP biosynthesis has made it an essential enzyme for organismal survival. It is well known that dNTP pool perturbation can cause detrimental effects in cells including DNA replication inhibition, growth impairment, genomic instability, mutagenesis and

tumorigenesis. Therefore, RNR activity is tightly regulated in cells to ensure a balance in dNTP pools. Over the past few decades, RNR has been actively studied by many groups to understand its structure, mechanisms of function, regulation, disease association and drug targeting potential. Several aspects of RNR including its regulation, role in DNA damage response and mutagenesis is relatively well understood in yeast. In mammals, there are still quite a few unanswered questions regarding RNR. Important questions we are asking are: what are the cellular and physiological consequences when RNR is deregulated? Does disabling different regulatory mechanisms of RNR lead to different outcomes? What are the underlying mechanisms for these different outcomes?

Previous research in the lab has shown that disabling RNR cell cycle regulation by over-expressing R2 in cells leads to increased mutagenesis and in mice leads to lung tumor development. The first part of this dissertation investigated the molecular mechanism of R2-induced tumorigenesis. The effect of R2 over-expression on cellular redox homeostasis and mitochondrial function has been studied. A possible role of reactive oxygen species (ROS) in R2-induced mutagenesis and tumorigenesis is suggested. The second part of this dissertation used R2 overexpressing mice as a lung tumor model and developed micro-computed tomography (micro-CT) techniques to measure lung tumor growth rates. Exponential lung tumor growth in mice has been revealed by this study using automated tumor measurement algorithm.

Although R2 over-expression leads to tumorigenesis, over-expression of the large R1 subunit or a mutant form of R1 that abolishes the allosteric feedback inhibition of RNR (R1-D57N), does not lead to pathological phenotypes in mice. However, combining overexpression of R1-D57N and R2 in mice leads to synthetic lethality. The supplementary part of this dissertation characterized the stage of lethality and examined the underlying mechanism of the

cause of death. Simultaneous deregulation of the R1 and R2 subunits leads to dramatic changes in dNTP pools and results in embryonic and postnatal lethality.

CHAPTER 2 Ribonucleotide Reductase Deregulation Leads to Increased Reactive Oxygen Species Production and Mitochondrial Dysfunction

2.1 Abstract

Ribonucleotide reductase (RNR) catalyzes the rate-limiting step in *de novo* nucleotide biosynthesis and is essential for maintaining genome integrity. RNR deregulation has been shown to cause dNTP pool imbalances, which can be mutagenic. However, as an enzyme that produces and utilizes free radicals for its function, the effect of RNR deregulation on redox homeostasis in cells is not fully understood. In this study, we show that overexpression of the free radical producing R2 subunit of RNR leads to increased levels of cellular reactive oxygen species (ROS). This increased ROS requires the di-nuclear iron center of R2 and is not affected by the disruption of the free radical transfer pathway, which transfers the free radicals in R2 to the R1 subunit of RNR for catalysis. Instead, R2 mutants with defective free radical transfer are shown to interfere with endogenous RNR function, leading to mitochondrial DNA depletion and disruption of mitochondrial ROS homeostasis. These results demonstrate the importance of RNR regulation in maintaining mitochondrial genome integrity, as well as cellular and mitochondrial redox balance. Importantly, this study suggests a potential role for R2-induced ROS production in mutagenesis and tumorigenesis.

2.2 Introduction

Ribonucleotide reductase (RNR) is a key enzyme in *de novo* deoxyribonucleotide triphosphate (dNTP) synthesis, where ribonucleoside diphosphate (NDP) is reduced to deoxyribonucleoside diphosphate (dNDP), which is further phosphorylated to dNTP and used in DNA synthesis (Eklund, Uhlin et al. 2001). Eukaryotic RNR enzyme belongs to the class Ia family, where it is composed of two nonidentical dimeric subunits R1 and R2. The large R1 subunit harbors the catalytic site and two allosteric regulation sites. It is encoded by the gene *RRM1* in mammals. The small R2 subunit contains the di-nuclear iron center where free radicals are generated and transferred to the catalytic site and used for catalysis. R2 can be encoded by the gene *RRM2* or *RRM2B* in mammals (Nordlund and Reichard 2006). Rrm1 and Rrm2 complex is responsible for making dNTPs in proliferating cells. p53R2 can substitute Rrm2 and form an active enzyme with Rrm1. It is initially identified as the downstream target of the tumor suppressor p53 whose expression is highly induced upon DNA damage (Nakano, Balint et al. 2000; Tanaka, Arakawa et al. 2000; Guittet, Hakansson et al. 2001; Hakansson, Hofer et al. 2006). In recent years, p53R2 is shown to be expressed at low levels independent of the cell cycle and provide dNTPs for mitochondrial genome maintenance (Pontarin, Ferraro et al. 2007; Pontarin, Ferraro et al. 2012).

Since a balanced dNTP pool is essential for genome integrity, RNR activity is highly regulated in cells (Mathews 2006; Nordlund and Reichard 2006). One primary regulation of RNR is through the cell cycle where the transcription of Rrm1 and Rrm2 is not detectable in G_0-G_1 phase, but peaks in S-phase cells (Eriksson, Graslund et al. 1984; Mann, Musgrove et al. 1988; Bjorklund, Skog et al. 1990). Due to the long half-life of Rrm1, its protein level remains constant throughout the cell cycle while Rrm2 protein correlates well with its mRNA level.

Rrm2 protein peaks in S phase and is degraded in G_2 and late mitosis by the ubiquitin ligases Skp1-Cul1-F-box (SCF) and anaphase promoting complex (APC), respectively (Eriksson, Graslund et al. 1984; Chabes and Thelander 2000; Chabes, Pfleger et al. 2003; D'Angiolella, Donato et al. 2012). As a result, RNR enzyme activity is partially regulated by the availability of Rrm2. Disruption of RNR cell cycle regulation by constitutively over-expressing Rrm2 in cells leads to increased mutation frequency and in mice leads to lung tumorigenesis. These lung tumors resemble human papillary adenocarcinoma and often have mutations in the *K-ras* proto-oncogene (Xu, Page et al. 2008). Rrm2 promotes tumorigenesis through a mutagenic mechanism, which could be due to increased RNR activity and dNTP alterations, or increased free radical production and oxidative stress. Since the lung tumors in Rrm2 overexpressing mice have mutations that are characteristic of oxidative DNA damage, this suggests a potential role of oxidative stress in Rrm2 induced mutagenesis and tumorigenesis (Xu, Page et al. 2008).

RNR catalytic cycle starts with free radical production in R2. The di-ferrous iron center (Fe(II)Fe(II)) in R2 is oxidized by O_2 and through a series of intermediate stages, a di-ferric iron center (Fe(III)Fe(III)) and a stable tyrosyl radical (Y177) are produced. The di-nuclear iron center is located within a four-helix bundle (Nordlund and Eklund 1995) and is coordinated by side chains from six charged residues (Glu/Asp/His) from the four helices (Nordlund, Sjoberg et al. 1990; Strand, Karlsen et al. 2004). Y177 radical is transferred to the catalytic site in R1 through a long-range radical transfer pathway consisting of amino acids that can form hydrogen bonds. Tyrosine 370 (Y370) is an essential residue in this pathway where it connects the radical transfer in R2 with that in R1 (Rova, Adrait et al. 1999; Eklund, Uhlin et al. 2001; Kolberg, Strand et al. 2004). It is located on the C-terminus of R2, which is essential for interacting with R1 (Climent, Sjoberg et al. 1992; Lycksell, Ingemarson et al. 1994). Mutating these two tyrosine

residues to non-hydrolysable phenylalanine in recombinant R2 proteins renders RNR enzymatically inactive *in vitro*, indicating the importance of free radicals in RNR function (Potsch, Lendzian et al. 1999; Rova, Adrait et al. 1999).

When studying the role of RNR in genome integrity, a major focus is on the relationship between RNR-induced dNTP pool alterations and mutagenesis. Due to the free radical producing nature of R2, deregulation of this protein could also result in perturbations of cellular redox homeostasis. However, the effect of R2 deregulation on the redox status in cells is not well characterized. Reactive oxygen species (ROS) in cells can lead to oxidative stress with elevated levels of oxidative DNA lesions (8-oxoG), resulting in mutagenesis and tumorigenesis (Valko, Rhodes et al. 2006). Liu et al. showed that human recombinant R2 protein leads to increased ROS production *in vitro* while p53R2 acts as an antioxidant (Liu, Xue et al. 2008). Moreover, mutation signature in R2-induced lung tumors is indicative of oxidative DNA damage (G to T transversions due to 8-oxoG incorporation into DNA), suggesting an association between R2-induced tumorigenesis and elevated ROS, which could potentially result from R2 deregulation.

Furthermore, RNR is important in mitochondrial DNA (mtDNA) synthesis. Mutations in p53R2 has been linked to mtDNA depletion in human diseases ((Bourdon, Minai et al. 2007; Kollberg, Darin et al. 2009; Shaibani, Shchelochkov et al. 2009; Tyynismaa, Ylikallio et al. 2009). Rrm2 over-expression has also been shown to cause mtDNA depletion in mouse skeletal muscles (Ylikallio, Page et al. 2010). As a major source of ROS production in cells, mitochondria function is tightly related to its redox status (Murphy 2009). Therefore, it is worth investigating whether mtDNA depletion under these conditions can lead to disruption of mitochondrial ROS homeostasis.

In this study, we looked closely at the effect of R2 deregulation on cellular and mitochondrial redox homeostasis. We showed that R2 overexpression leads to increased ROS production in cells and that di-nuclear iron center is the source of R2-induced ROS. Two R2 mutants that are defective for free radical transfer had dominant negative effect in cells by interfering with endogenous Rrm1, leading to mtDNA depletion and mild increase in mitochondrial ROS. Our results provide insights into the effect of RNR on redox homeostasis, emphasize the importance of RNR regulation in cellular function and suggest a potential role of ROS production in R2-induced mutagenesis.

2.3 Materials and methods

2.3.1 Plasmids

Mammalian expression plasmids encoding *RRM1*, *RRM2* and *RRM2B (p53R2)* were previously constructed in the pCaggs expression vector (Xu, Page et al. 2008). All primers used for making Rrm2 mutants in this study are listed in Table 2.1. pCaggs-Rrm2-Fe6 was made using a QuikChange® Lightning Site-Directed Mutagenesis Kit (Agilent Technologies) using primers (A), (B), (C) and (D). pCaggs-Rrm2-Y177F and pCaggs-Rrm2-Y370F were made using overlap extension PCR (Ho, Hunt et al. 1989). The two universal primers used are primers (I) and (J). The primers harboring corresponding mutations were (E) and (F) for Y177F and (G) and (H) for Y370F.

pCaggs-Rrm2-Δ7 and pCaggs-Rrm2-Y370F-Δ7 were made using primers (K) and (L) and pCaggs-Rrm2-Δ20 was made using primers (K) and (M). pCaggs-Rrm2-Y177F-Δ7 and -Δ20 were generated by subcloning. pCaggs-Rrm2-Y177F, pCaggs-Rrm2-Δ7 and pCaggs-Rrm2-Δ20 plasmids were digested with ClaI and XbaI. The smaller insert piece from Rrm2-Y177F was

Table 2.1 Primer sequences used for making Rrm2 mutants.

Mutant	Template	Primer
Rrm2-Fe6	Rrm2	(A) Forward: 5'GCCTTTGCCGCCGTAG**C**AGGAATCTTCTTTTTC3'
		(B) Forward: 5'CTATGGCTTCCAAATTGCCATGG**C**AAACATA**GC**C
		TCTGAAATGTACAGTCTCCTTA3'
		(C) Forward: 5'CTTATTAGCAGAGAC**C**GGGTTTA**GC**CTGTGACTTTGCCTA3'
		(D) Forward: 5'CTTTCTTTGCAGCGAGT**C**TGGCATAGTCAATGAGAA3'
Rrm2-Y177F	Rrm2	(E) Forward: 5'GGAAAACATACACTCTGAAATGT**T**CAGTCTCCTTATTGACACTTAC3'
		(F) Reverse: 5'GTAAGTGTCAATAAGGAGACTG**A**ACATTTCAGAGTGTATGTTTTCC3'
Rrm2-Y370F	Rrm2	(G) Forward: 5'TTGAGAAGCGAGTAGGCGAGT**T**TCAGAGGATGG3'
		(H) Reverse: 5'CCATCCTCTGA**A**ACTCGCCTACTCGCTTCTCAA3'
		(I) Forward: 5'AAACTCGAGCCATGCTCTCCGTCCGCACCCC3'
		(J) Reverse: 5'AGAGCTCGAGTTAGAAGTCAGCATCCAAGGT3'
Rrm2-Δ7	Rrm2	(K) Forward: 5'AAACTCGAGCCATGCTCTCCGTCCGCACCCC3'
		(L) Reverse: 5'GAGCTCGAGTTAAGAGTTCTCTGTCGAATT3'
Rrm2-Δ20	Rrm2	(K) Forward: 5'AAACTCGAGCCATGCTCTCCGTCCGCACCCC3'
		(M) Reverse: 5'GAGCTCGAGTTAATACTCGCCTACTCGCTT3'
Rrm2-Y370F-Δ7	Rrm2-Y370F	(K) Forward: 5'AAACTCGAGCCATGCTCTCCGTCCGCACCCC3'
		(L) Reverse: 5'GAGCTCGAGTTAAGAGTTCTCTGTCGAATT3'
Rrm2-T33A	Rrm2	(O) Forward: 5'CTGACAAGGAGAAC**G**CGCCCCCGACTCTC3'

ligated to the larger backbone pieces from Rrm2-Δ7 and Rrm2-Δ20.

pCaggs-Rrm2-T33A was made using a QuikChange® Lightning Site-Directed Mutagenesis Kit with primer (O). pCaggs-Rrm2-T33A-Y177F, pCaggs-Rrm2-T33A-Y370F and pCagss-Rrm2-T33A-Fe6 were generated by subcloning. pCaggs-Rrm2-T33A plasmid was digested by XbaI and EcoRV to release the insert with T33A mutation, which was ligated to the backbones from pCaggs-Rrm2-T33A-Y177F, pCaggs-Rrm2-T33A-Y370F and pCagss-Rrm2-T33A-Fe6 upon XbaI and EcoRV digestion.

All mutant constructs were confirmed by DNA sequencing.

Bacterial expression plasmids encoding Rrm2, Rrm2-Fe6, Rrm2-Y177F, Rrm2-Y370F, Rrm2-Δ7 and Rrm2-Δ20 were constructed in the pGEX-6P-2 GST-fusion protein expression vector (Kaelin, Krek et al. 1992). pCaggs plasmids encoding Rrm2, Rrm2-Fe6, Rrm2-Y177F, Rrm2-Y370F, Rrm2-Δ7 and Rrm2-Δ20 were digested by Xho1 to generate the desired Rrm2 wild type and mutant inserts, which were then cloned into Xho1 digested pGEX-6P-2 backbone.

2.3.2 RNR overexpressing cell lines

Mouse 3T3 fibroblast cells expressing empty pCaggs vector, pCagss-Rrm1, pCaggs-Rrm2 and pCaggs-p53R2 were generated previously (Xu, Page et al. 2008). 3T3 cells expressing Rrm2-Y177F, Rrm2-Y370F, Rrm2-Fe6, Rrm2-Δ7, Rrm2-Δ20, Rrm2-Y177F-Δ7, Rrm2-Y177F-Δ20 and Rrm2-Y370F-Δ7 were generated by transfecting corresponding plasmids together with PGK-puro plasmid into 3T3 cells using FuGENE6 transfection reagent (Roche Diagnostics Co., Mannheim, Germany). Transfected 3T3 cells were cultured in standard culture media (Dulbeco's Modification of Eagles Medium supplemented with 10% bovine calf serum, 1.0mM L-glutamine, 0.1mM MEM non-essential amino acids, 100μg/ml streptomycin sulfate, 100U/ml penicillin). 48 hours after transfection, standard media was replaced by selection media

containing 1.25μg/ml puromycin, which was changed every 2 days. After 10-14 days, puromycin-resistant colonies were pooled together and expanded for further analysis and experiments. Puromycin-resistant cells were always kept in selection media.

2.3.3 Bacterial culture and lysates

pGEX-Rrm2, Rrm2-Fe6, Rrm2-Y177F, Rrm2-Y370F, Rrm2-Δ7 and Rrm2-Δ20 plasmids were transformed into XA90 competent cells and colonies were picked for bacterial culture (LB and Amp). Expression of GST-fused Rrm2 wild type and mutant proteins were induced by IPTG. Bacteria were collected and resuspended in lysis buffer (50mM Tris-HCl pH 8.0, 120mM NaCl, 50mM EDTA, 1% Triton X-100 and 3mg/ml lysozyme) supplemented with 1x proteinase inhibitor (2μg/ml leupeptin, 2μg/ml apropinin and 20μg/ml PMSF). Cells were lysed in lysis buffer by two freeze and thaw cycles.

2.3.4 Western blot and pull-down assay

Rrm2 overexpressing 3T3 and U2OS cells were collected and lysed in RIPA buffer (50mM Tris-HCl pH 8.0, 1% Nonidet P-40, 0.5% sodium deoxycholate, 0.1% sodium dodecyl sulfate, 150mM sodium chloride, 50mM sodium fluoride) supplemented with 1x proteinase inhibitor (2μg/ml leupeptin, 2μg/ml apropinin and 20μg/ml PMSF) and 1x phosphatase inhibitor (400μM sodium orthovanadate). Protein lysates were separated on 10% polyacrylamide gel and transferred to PVDF membrane. Antibodies used were goat anti-R2 (sc-115, Santa Cruz Biotechnology) and mouse anti-α-tubulin (Sigma).

In pull-down assay, bacterial lysates expressing Rrm2 wild type and mutants were incubated with Glutathione Sepharose beads (Amersham Biosciences) for 2-4hrs. Human embryonic kidney 293 cell lysates were added to GST-protein bound beads and incubated for 2-

4hrs. Beads were washed with NETN buffer (20mM Tris-HCl pH 8.0, 10mM NaCl, 1mM EDTA and 0.5% NP-40) and loaded on 10% polyacrylamide gel. Proteins were transferred to PVDF membrane and detected by mouse anti-R1 (AD203, Bio Med Tek).

2.3.5 ROS measurement

Total cellular ROS was measured by dihydroethidium (DHE) staining (Life Technologies). Cells were grown on glass coverslips at a density of 10^5 cells/3ml for 24hrs and stained with 5μM DHE in standard culture media at 37°C for 20min. Cells were then subjected to confocal imaging using a Zeiss LSM 510 Meta confocal microscope (excitation 405nm and emission 530nm). Fluorescence intensity of cells was quantified by Image J.

Mitochondrial ROS was measured by MitoSox Red staining (Life Technologies). Cells were grown on glass coverslips at a density of 10^5 cells/3ml for 24hrs and stained with 5μM MitoSox Red in standard culture media at 37°C for 20min. MitoSox Red containing media was replaced by normal standard media after 20min and cells were incubated in standard media for another 20min. Cells were then subjected to confocal imaging using a Zeiss LSM 510 Meta confocal microscope (excitation 514nm and emission 575nm). Fluorescence intensity of cells was quantified by Image J.

All Statistics was performed by JMP.

2.3.6 Genomic DNA extraction and qPCR

Rrm2 expressing 3T3 cells were collected in cold PBS and digested overnight at 50°C in digestion buffer (100mM NaCl, 10mM Tris-HCl pH 8.0, 25mM EDTA pH 8.0, 0.5% SDS and freshly added 0.1mg/ml proteinase K). 50μg/ml of RNase A was added to the digestion mixture the next day and incubated at 50°C for 1hr. The mixture was then subjected to phenol

chloroform extraction and ethanol precipitation. DNA was resuspended in nanopure water and concentration was measured by NanoDrop.

5ng of genomic DNA was used in qPCR assay. Mitochondrial encoded cytochrome C oxidase I (mt-COI) was amplified by the following primers:

Forward: 5'TGCTAGCCGCAGGCATTACT3'

Reverse: 5'CGGGATCAAAGAAAGTTGTGTTT3'

Nuclear encoded GAPDH was amplified by the following primers:

Forward: 5'GCCTTCCGTGTTCCTACC3'

Reverse: 5'CCTCAGTGTAGCCCAAGATG3'

qPCR reactions were performed using Applied Biosystems 7500 Fast Real-Time PCR thermocycler under the following conditions: 50°C for 2min, 95°C for 10min, 95°C for 15sec (40x) and 60°C for 1min.

2.3.7 Total cellular dNTP measurement

RNR expressing 3T3 cells (10^6 total) were cultured on 10cm tissue culture dish and 5 x 10^5 cells were collected 24hr after. Total cellular dNTPs were extracted and measured as previously described (Sherman and Fyfe 1989; Ferraro, Franzolin et al. 2010). Briefly, cells were resuspended in 100µl of cold 0.4N perchloric acid and incubated on ice for 20min. After centrifugation at 14,000g for 1min, the supernatant was collected and neutralized with 100µl of 0.5N trioctylamine (Sigma) in 1,1,2-fluorotrichloromethane (Sigma). Samples were votexed briefly and centrifuged at 14,000g for 2min and the upper aqueous phase was snap-frozen in liquid N_2 and stored at -80°C until dNTP measurements were performed.

Ribonucleoside levels in samples were first measured as described (Kochanowski, Blanchard et al. 2006; Ylikallio, Page et al. 2010) to assess dNTP extraction quality using a

Shimadzu HPLC system. Samples were separated on a Supelco LC-18T column in 30mM KH_2PO_4 and 10mM tetrabutylammonium hydrogen sulfate, pH 6.5 mixed with methanol (buffer A= 91.7% salt solution and 8.3% methanol; buffer B=71.6% salt solution and 28.4% methanol) over a 40min time period. The elution gradient was as follows: 0-100%B for 0-24min, 1min at 100%B and 100-0%B for 25-30min at a flow rate of 1ml/min. Samples with >80% ATP were used for subsequent dNTP measurements as reported (Ferraro, Franzolin et al. 2010; Ylikallio, Page et al. 2010). Briefly, 50µl reaction mixtures were prepared and incubated for 1hr. The 50µl reaction mixture contains 10µl cellular dNTP extract to be measured together with 40mM Tris-HCl, pH7.4, 10mM $MgCl_2$, 5mM dithiothreitol, 0.25µM oligonucleotide, 1.5µg RNase A, 0.25µM labeled dATP (or labeled dTTP for the dATP assay) and DNA polymerase. For dATP and dTTP assays, 0.02 units and 0.025 units of Klenow enzyme (Fermentas) were used respectively and incubated at 37°C. For dGTP and dTTP assays, 0.2µl homemade Tag were used and incubated at 48°C. After 1hr incubation, 30µl reaction mixture was removed and spotted onto Whatman DE81 paper discs. Discs were washed three times in 5% Na_2HPO_4 and once each in dH_2O and 95% EtOH. Discs were dried and counted on a Beckman Coulter LS6500 scintillation counter. Standard curves were prepared using concentrated stocks of pure individual dNTPs (Fermentas).

2.3.8 Electron Paramagnetic Resonance (EPR) assay and free tyrosyl radical measurement

Rrm2 expressing 3T3 cells were cultured, collected in EPR buffer (50mM Hepes pH7.6 and 5% glycerol) and transferred to a 3.8mm thin wall quartz EPR tube (Wilmad-LabGlass). The tube was spun down at 500xg for 5min at 4°C. Supernatant was removed and the remaining ~200µl of packed cells were rapidly (<5s) frozen stepwise: first in methanol that had been pre-

chilled over dry ice at ~ -70°C, followed by liquid N_2. EPR instrument settings were as following: sweep time, 61 second; time constant, 0.163 seconds; modulation frequency 100kHz, modulation amplitude 1.0G; microwave power, 25dB (0.6325mW). Spectra data were acquired at 50K for 70 scans.

2.3.9 RNR enzyme activity assay

Rrm2 expressing 3T3 cells were cultured and collected in ice-cold activity assay buffer (50mM Hepes pH7.6 and 15mM $MgCl_2$). Cells were subjected to 3 cycles of rapid freeze/thaw subsequent to the addition of EDTA-free protease inhibitor cocktails at the final concentration of 2 tablets/ml (Roche) and the debris was removed by centrifugation at 13,000xrpm, 4°C for 10min. The supernatant was used in subsequent CDP reductase activity assay. A typical assay mixture in a final volume of 135 µl contains, in final concentrations, 50mM Hepes pH7.6, 15mM $MgCl_2$, 3mM ATP, 10mM NaF, 0.5mM [5-^{3}H]-CDP, 2mM NADPH, 100µM *E. coli* Trx, 1µM *E. coli* TrxR, 6µM of human recombinant His_6-Rrm1 and freshly prepared lysate. The assay mixture was preincubated at 37°C for 1min, and the reaction was initiated by the addition of lysate. Four 30µl aliquots were removed and quenched with 30µl 2% HClO4 at the designated time points over 3.5min, followed by immediate neutralization with 0.4M 30µl KOH (Aye, Brignole et al. 2012). dCDP production was analyzed as described (Steeper and Steuart 1970). Briefly, the neutralized aliquots were treated with calf alkaline phosphatase according to manufacturer's protocol (Roche), and incubated for 2h at 37°C. Subsequent to the addition of 1mM dC as carrier, the dephosphorylated samples were applied to a borate column to separate ribonucleosides ([5-^{3}H]-Cyt) and deoxyribonucleosides ([5-^{3}H]-dC). Water was applied to the column to elute the [5-^{3}H]-dC product. The effluent was collected and [5-^{3}H]-dC was quantified by determining the radioactivity with liquid scintillation counter.

2.3.10 HPRT mutagenesis assay

Human osteosarcoma U2OS cells were pre-cleansed for existing HPRT mutation before the assay. U2OS cells were maintained in HAT media (standard culture media supplemented with 0.2mM sodium hypoxanthine, 0.4μM aminopterin, 0.02μM thymindine (GIBCO)) for two weeks. Cells were then recovered in HT media (standard culture media supplemented with 0.1mM sodium hypoxanthine, 0.016μM thymidine (GIBCO)) for one week. After that, cells were transfected with vector, Rrm2, Rrm2-Y177F, Rrm2-Y370F, Rrm2-Fe6, Rrm2-T33A, Rrm2-T33A-Y177F, Rrm2-T33A-Y370F and Rrm2-T33A-Fe6 plasmids using polyethylenimine (PEI) transfection reagent together with PGK-puro plasmid (Ehrhardt, Schmolke et al. 2006). Transfected U2OS cells were cultured in standard culture media as 3T3 cells in 2.3.2. 48 hours after transfection, standard media was replaced by selection media containing 2.0μg/ml puromycin, which was changed every 2 days. After 8 days, puromycin-resistant colonies were pooled together and expanded for HPRT mutagenesis assay as described (Xu, Page et al. 2008; D'Angiolella, Donato et al. 2012).

Basically, Rrm2 over-expressing U2OS cells were seeded at a density of 5 x 10^5 per 10cm culture dish with 10 dishes total for each cell line. Cells were kept in HPRT media (selection media supplemented with 5μg/ml 6-thioguanine (Sigma)) for two weeks. 6-thioguanian resistant colonies were stained by crystal violet and counted. Plating efficiency was determined by plating 100 cells per 10cm culture dish with 3 dishes total in selection media. After two weeks, colonies were stained by crystal violet and counted.

2.4 Results

2.4.1 Overexpression of R2 in cells leads to increased production of reactive oxygen species (ROS)

The small subunit R2 harbors di-nuclear iron centers that generate free radicals upon oxygen binding. To test whether elevated levels of R2 in cells affect their redox status, we measured superoxide levels as an indication of reactive oxygen species (ROS) production. Mouse 3T3 fibroblast cells overexpressing empty vector, Rrm1, Rrm2 and p53R2 were generated previously (Xu, Page et al. 2008) (see also Figure 2.1A). These cells were incubated with dihydroethidium (DHE) and imaged using confocal microscopy. Representative images of cells with red fluorescence are shown in Figure 2.1B. Fluorescence intensity was quantified by Image J and summarized in Figure 2.1C. As Figure 2.1 illustrated, overexpression of either small subunit, Rrm2 or p53R2, led to increased superoxide production in cells while overexpression of vector and the large subunit Rrm1 had no effect on cellular superoxide production.

2.4.2 Di-nuclear iron center of Rrm2 contributes to increased ROS in cells

To investigate the role of the di-nuclear iron center and the radical transfer pathway in Rrm2-induced ROS production in cells, a panel of Rrm2 mutants were generated and stably expressed in cells (Figure 2.2A). In Rrm2-Fe6 mutant, all six charged residues that coordinate the iron atom at the di-nuclear iron center were mutated to alanine (Strand, Karlsen et al. 2004). Rrm2-Y177F and Rrm2-Y370F had mutations in two essential tyrosine residues in the radical transfer pathway and could not produce free radicals at the corresponding tyrosine sites as shown *in vitro* with recombinant proteins (Potsch, Lendzian et al. 1999; Rova, Adrait et al. 1999). It is also shown *in vitro* that the Y370F mutation had no effect on free radical production at Y177 site

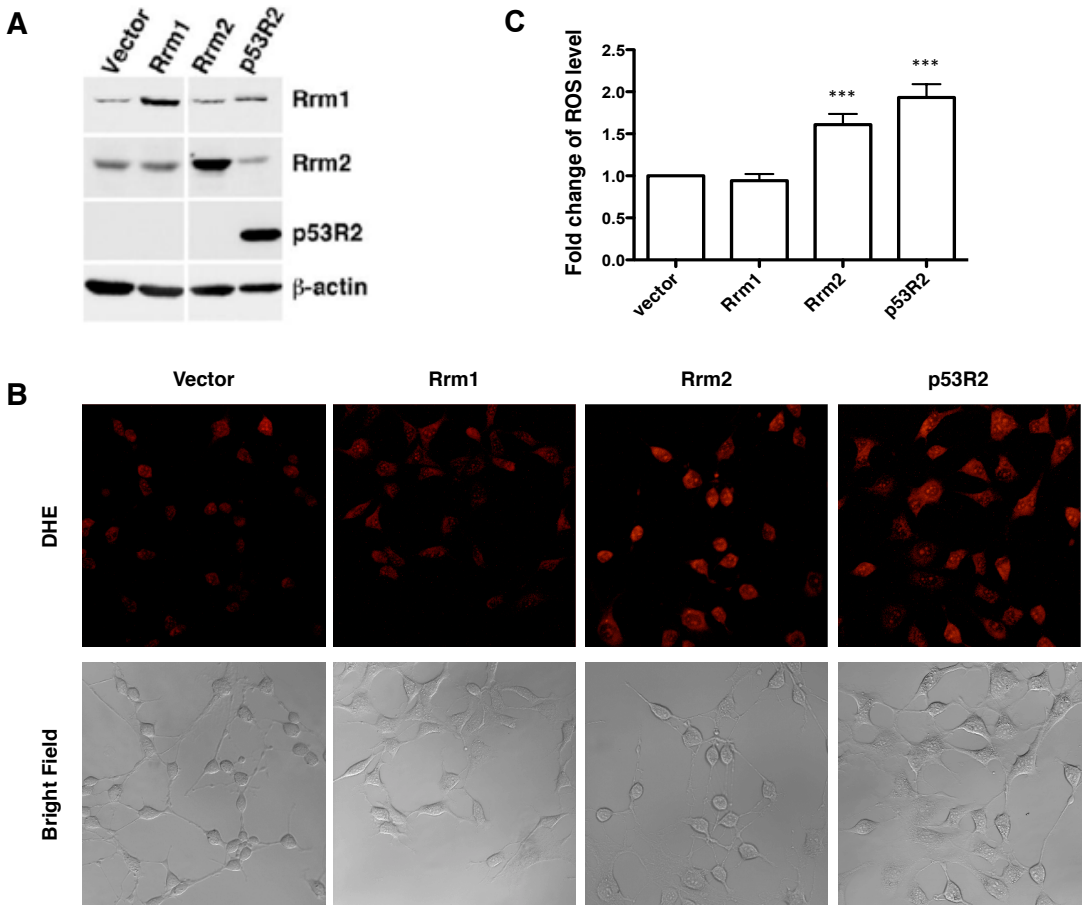

Figure 2.1 Overexpression of small subunit R2 leads to elevated levels of superoxide production in mouse fibroblasts. (A) Western blot showing the expression levels of RNR proteins in vector, Rrm1, Rrm2 and p53R2 transfected mouse cell lines. (Figure from Xu, Page et al. 2008). (B) Representative pictures showing red fluorescence of dihydroethidium (DHE) stained vector, Rrm1, Rrm2 and p53R2 expressing cells. Images were taken at 20x with 405nm excitation and 530nm emission. Corresponding bright field images were also shown. (C) Bar graph showing the fold change of superoxide levels in Rrm1, Rrm2 and p53R2 expressing cells as compared to the vector control. 175 cells for each cell line from 4 independent experiments were quantified and fluorescence levels were normalized against the vector control (*** $P<0.001$, two way ANOVA, error bars indicate standard deviation).

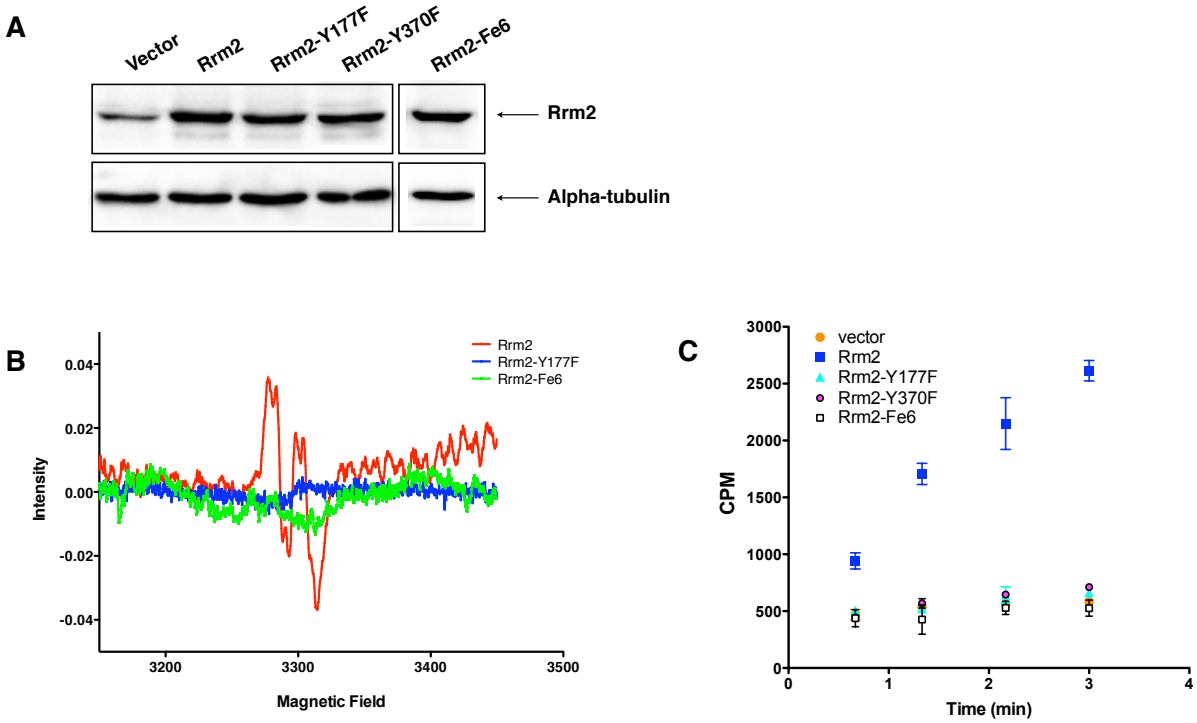

Figure 2.2 Enzymatic activity and EPR spectra in Rrm2 wild type and mutant expressing cells. (A) Western blot showing the expression levels of Rrm2-Y177F, Rrm2-Y370F and Rrm2-Fe6 in transfected mouse 3T3 cells. (B) EPR spectra of the Y177 site in Rrm2 wild type and mutant expressing 3T3 cells. Free radical production at Y177 site was detected in Rrm2 wild type and Rrm2-Y370F proteins while Rrm2-Y177F and Rrm2-Fe6 proteins were defective for free radical production. (C) Rrm2 wild type overexpressing 3T3 cells showed higher enzymatic activity than the vector control while Rrm2-Y177F, Rrm2-Y370F and Rrm2-Fe6 were all enzymatically inactive.

(Rova, Adrait et al. 1999). Due to the inability to transfer free radicals, recombinant Rrm2-Y177F and Rrm2-Y370F were shown to be enzymatically inactive *in vitro* (Potsch, Lendzian et al. 1999; Rova, Adrait et al. 1999).

Before we looked at ROS production in these mutants, we wanted to test whether the observations on radical production and enzyme activity in Rrm2-Y177F and Rrm2-Y370F held true in our *in vivo* cell culture system. We also wanted to investigate the effects of complete di-nuclear iron center disruption in Rrm2-Fe6 on radical production and RNR enzyme activity. Electron paramagnetic resonance (EPR) was used to track free radical production at the Y177 site in these mutants. As shown by Figure 2.2B, 3T3 cells overexpressing wild-type Rrm2 and Rrm2-Y370F had free radical production at Y177 site while cells overexpressing either Rrm2-Y177F or Rrm2-Fe6 had no free radical at Y177 site. These results correlated well with previously published *in vitro* data of Rrm2-Y177F and Rrm2-Y370F, and also demonstrated the importance of the di-nuclear iron center in free radical production in Rrm2.

Next, we measured RNR enzyme activity in cells expressing Rrm2-Y177F, Rrm2-Y370F and Rrm2-Fe6. As shown in Figure 2.2C, cells overexpressing wild-type Rrm2 showed increased RNR enzyme activity compared to cells with endogenous RNR expression. In contrast, cells overexpressing Rrm2-Y177F, Rrm2-Y370F and Rrm2-Fe6 showed minimal RNR enzyme activity. This result confirmed the *in vitro* observation of loss of enzyme activity in Rrm2-Y177F and Rrm2-Y370F. It also provided evidence on loss of activity in Rrm2-Fe6 mutant, indicating that free radical production and transfer are essential for RNR enzyme activity.

With the mutants behaving as expected in terms of Y177 radical production and enzyme activity, we then examined the levels of superoxide in cells over-expressing these mutants by DHE staining. Representative images in Figure 2.3A and 2.3B showed that increased superoxide

Figure 2.3 The effect of Rrm2 mutant overexpression in cells on superoxide production. (A) Representative pictures showing red fluorescence of DHE stained Rrm2-Y177F and Rrm2-Y370F expressing cells. Corresponding bright field images were also shown. Images were taken at 20x with 405nm excitation and 530nm emission. (B) Representative pictures showing red fluorescence of DHE stained Rrm2-Fe6 expressing cells. Corresponding bright field images were also shown. Images were taken at 40x with 405nm excitation and 530nm emission. (C) Bar graph showing the fold change of superoxide levels in Rrm2 wild type and mutant expressing cells as compared to the vector control. For staining with Rrm2-Y177F and Rrm2-Y370F, 285 cells for each cell line from 7 independent experiments were quantified; for staining with Rrm2-Fe6, 200 cells from 3 independent experiments were quantified. All fluorescence levels were normalized to the vector control (***$P<0.001$, two way ANOVA).

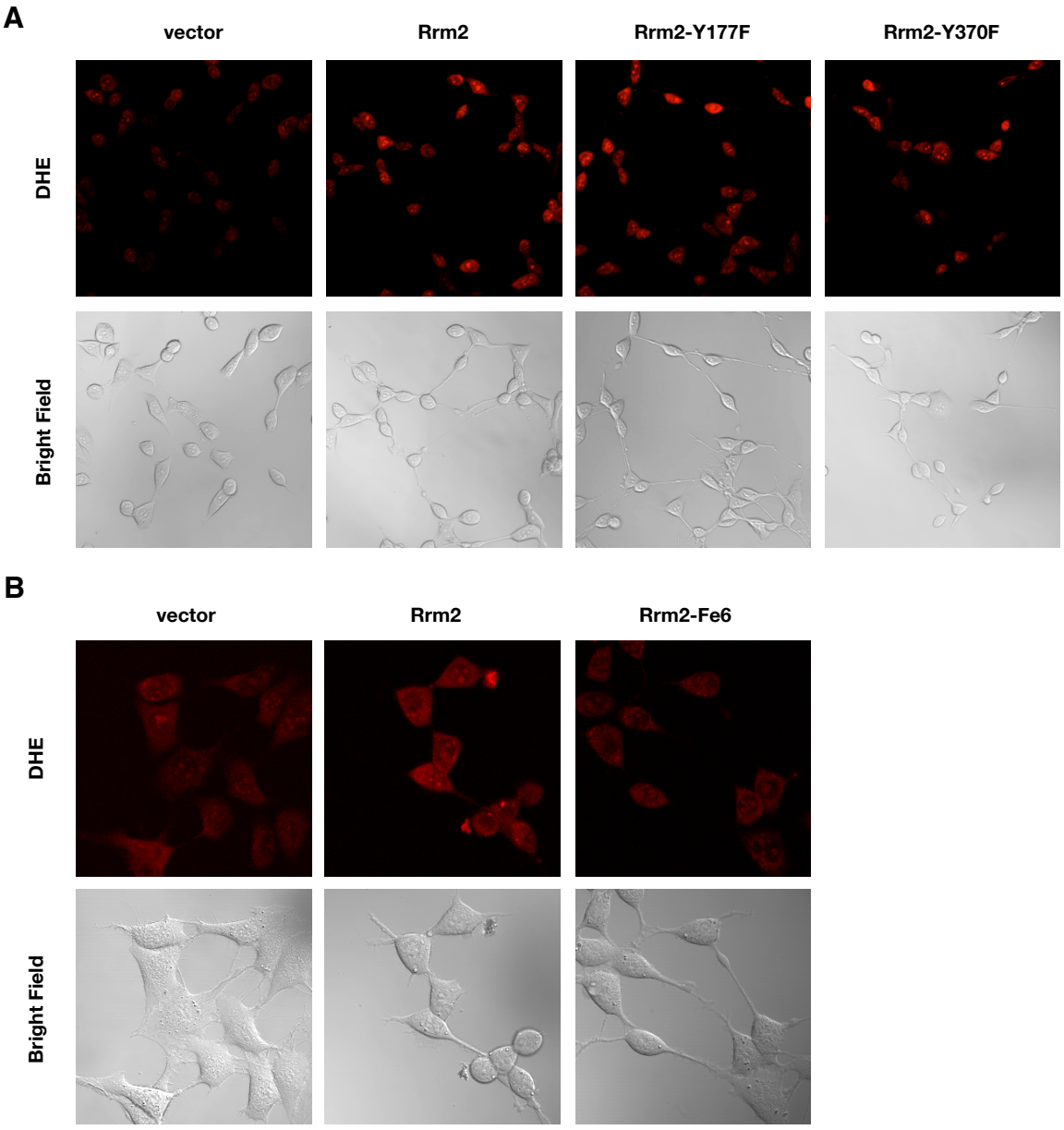
A
vector
Rrm2
Rrm2-Y177F
Rrm2-Y370F
DHE
Bright Field
B
vector
Rrm2
Rrm2-Fe6
DHE
Bright Field
C
Fold change of ROS level
2.0
1.5
1.0
0.5
0.0
***
***
***
vector
Rrm2
Rrm2-Y177F
Rrm2-Y370F
Fold change of ROS level
2.0
1.5
1.0
0.5
0.0
***
Vector
Rrm2
Rrm2-Fe6

was observed in Rrm2-Y177F and Rrm2-Y370F expressing cells while Rrm2-Fe6 expressing cells had basal level superoxide production. Image J quantification of red fluorescence further confirmed this observation (Figure 2.3C). Taken together, these results demonstrated that complete disruption of the di-nuclear iron center in Rrm2-Fe6 mutant resulted in loss of free radical production and rendered the levels of superoxide comparable to control cells, suggesting that increased superoxide in Rrm2 over-expressing cells resulted from free radical production at the di-nuclear iron center and was not affected by the status of the free radical transfer pathway.

2.4.3 Y177F and Y370F expressing cells have mild mitochondrial genome instability and mitochondrial redox imbalance

Although p53R2 is responsible for mitochondrial DNA (mtDNA) synthesis in resting cells, Rrm2 provides dNTPs for nuclear DNA and mtDNA synthesis in proliferating cells (Hakansson, Hofer et al. 2006; Pontarin, Ferraro et al. 2012). We were interested in whether introducing the Rrm2 mutants (Rrm2-Y177F, Rrm2-Y370F and Rrm2-Fe6) into cells would have dominant negative effects that may affect nuclear and mitochondrial DNA synthesis. Since mitochondria are a major source of cellular ROS (Kirkinezos and Moraes 2001), we were particularly interested in the effect of Rrm2 mutants on mitochondrial function and mitochondrial redox status. In order to examine this, we looked at the levels of mitochondrial DNA in Rrm2 mutant overexpressing cells. As shown in Figure 2.4A, Rrm2-Y177F and Rrm2-Y370F expressing cells showed about 50% depletion of mtDNA as compared to the vector control. In contrast, Rrm2-Fe6 had minimal effects on the levels of mtDNA in cells. In addition, there was a consistently slight, but not significant decrease of mtDNA in cells overexpressing wild type Rrm2.

Figure 2.4 Rrm2-Y177F and Rrm2-Y370F expression in cells leads to mitochondrial DNA depletion and excessive mitochondrial ROS production. (A) Mitochondrial DNA (mtDNA) levels in 3T3 cells transfected with vector, Rrm2, Rrm2-Y177F, Rrm2-Y370F and Rrm2-Fe6. Total DNAs from these cells were extracted and analyzed by qPCR. The level of cytochrome c oxidase subunit 1 (CO1) gene was used to assess the level of mtDNA and the level of GAPDH gene was used as the internal nuclear control. mtDNA levels from 4 independent experiments were analyzed (***P<0.001, **P<0.01, one way ANOVA). (B) Representative pictures showing red fluorescence of MitoSox Red stained Rrm2-Y177F and Rrm2-Y370F expressing cells. Corresponding bright field images were also shown. Images were taken at 40x with 514nm excitation and 575nm emission. (C) Bar graph showing the fold change of mitochondrial ROS levels in Rrm2 wild type, Rrm2-Y177F and Rrm2-Y370F expressing cells as compared to the vector control. 200 cells for each cell line from 4 independent experiments were quantified and all fluorescence levels were normalized to the vector control (***P<0.001, two way ANOVA).

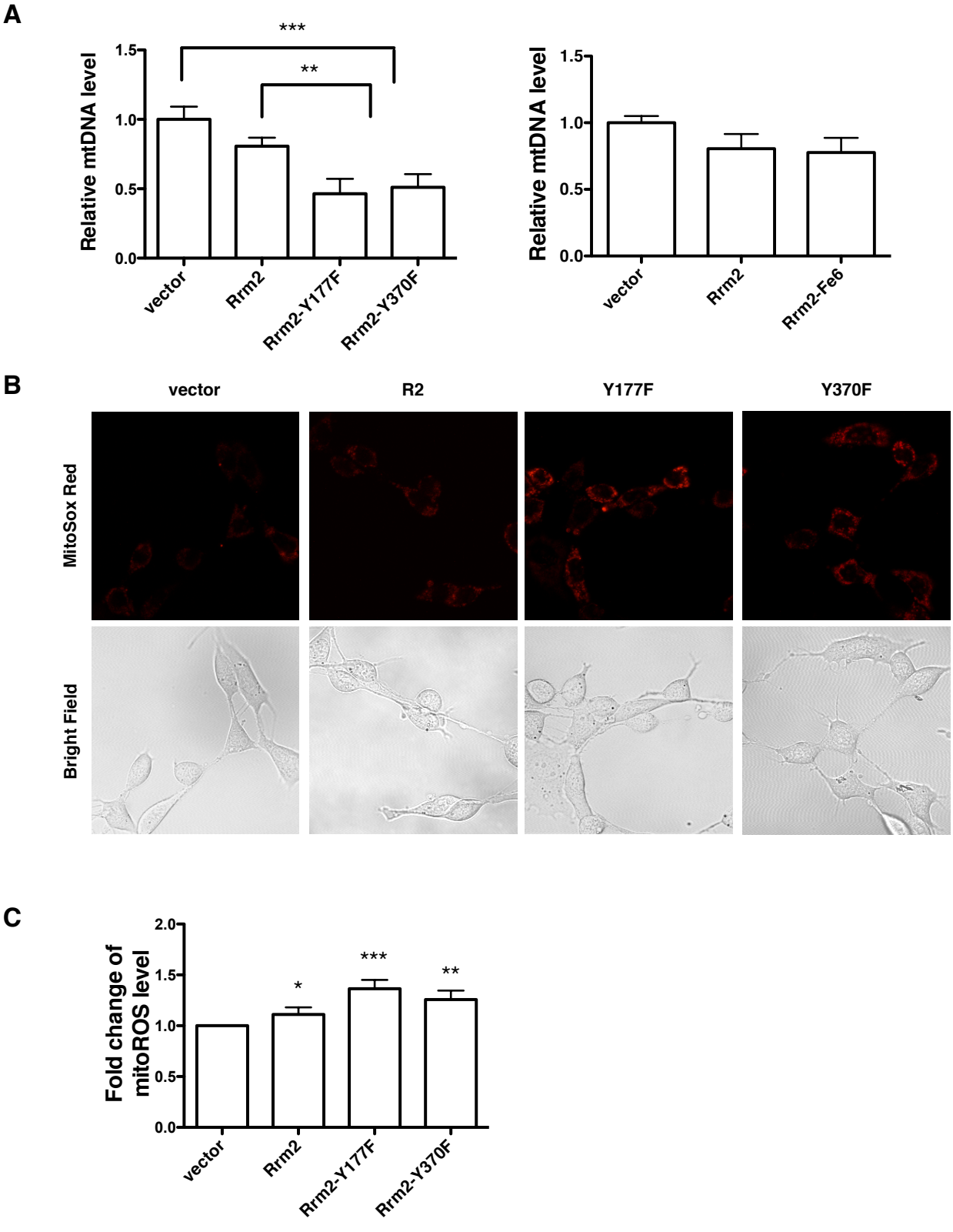
A
***
**
Relative mtDNA level
1.5
1.0
0.5
0.0
vector
Rrm2
Rrm2-Y177F
Rrm2-Y370F
Relative mtDNA level
1.5
1.0
0.5
0.0
vector
Rrm2
Rrm2-Fe6
B
vector
R2
Y177F
Y370F
MitoSox Red
Bright Field
C
Fold change of mitoROS level
2.0
1.5
1.0
0.5
0.0
*
***
**
vector
Rrm2
Rrm2-Y177F
Rrm2-Y370F

Next, we looked at the consequence of mtDNA depletion in Rrm2-Y177F and Rrm2-Y370F expressing cells. Previous studies have shown that mtDNA mutations and depletions led to altered mitochondrial redox homeostasis (Chomyn and Attardi 2003; Ishikawa, Takenaga et al. 2008; Lebedeva, Eaton et al. 2009). We then measured the levels of superoxide in mitochondria by staining Rrm2-Y177F and Rrm2-Y370F expressing cells with a mitochondria specific superoxide indicator MitoSox Red. As shown in Figure 2.4B and 2.4C, Rrm2-Y177F and Rrm2-Y370F expressing cells showed significant increase in mitochondrial superoxide production. In addition, there was a slight, but significant increase of mitochondrial superoxide in cells that overexpress wild type Rrm2. In conclusion, these data indicated that Rrm2-Y177F and Rrm2-Y370F mutants interfered with mitochondrial DNA synthesis in cells. Overexpression of these mutants led to mtDNA depletion and excessive superoxide production in cells.

2.4.4 Y177F and Y370F mutants lead to mitochondrial dysfunction by interfering with endogenous Rrm1

Y177F and Y370F over-expressing cells showed decreased mtDNA level and increased mitochondrial superoxide production. We hypothesized that these two mutants had dominant negative effects in cells by interfering with the endogenous Rrm1 large subunit. It was possible that Y177F and Y370F mutants bind to endogenous Rrm1 subunit and formed inactive RNR complex. As a consequence, the level of endogenous Rrm1 available for making wild type RNR was decreased, which could result in decreased levels of functional RNR, limited dNTP synthesis and compromised mtDNA replication. In order to test this hypothesis, we first generated Rrm2 mutants that could not bind to Rrm1. Rrm2 C terminus (either the last 7 or the last 20 C-terminal residues) had been shown to mediate the binding between Rrm1 and Rrm2 (Climent, Sjoberg et al. 1992; Lycksell, Ingemarson et al. 1994). We generated Rrm2Δ7,

Rrm2Δ20, Rm2-Y177FΔ7, Rrm2-Y177FΔ20 and Rrm2-Y370FΔ7 mutants by truncating the last 7 or the last 20 residues of the C-terminus.

In order to examine the interaction between Rrm2 C terminal truncation mutants and Rrm1, we made GST tagged proteins, GST-Rrm2, GST-Rrm2Δ7 and GST-Rrm2Δ20. After purification by glutathione beads, GST tagged Rrm2 proteins were incubated with 293 cell lysates and the binding to endogenous Rrm1 was assayed by western blot. As indicated by Figure 2.5A (left panel, while GST-Rrm2 successfully pulled down endogenous Rrm1, GST-Rrm2Δ7 and GST-Rrm2Δ20 were not able to interact with endogenous Rrm1. Since GST-Rrm2-Y177F and GST-Rrm2-Y370F were able to interact with endogenous Rrm1 (Figure2.5A right panel), this suggested that Y177F and Y370F mutations had no effect on Rrm2 and Rrm1 binding. Therefore, we expected that Rrm2-Y177FΔ7, Rrm2-Y177FΔ20 and Rrm2-Y370FΔ7 mutants were not able to bind endogenous Rrm1 as well. In addition, we were curious to see whether disruption of the di-nuclear iron center would change the overall structure of Rrm2 and affect binding to Rrm1. As shown in Figure 2.5A (right panel), complete disruption of the di-nuclear iron center in Rrm2-Fe6 had no effect on Rrm2 and Rrm1 binding.

After confirmation of loss of interaction between Rrm2 C-terminal truncation mutants and Rrm1, we generated 3T3 cells over-expressing these C-terminal truncation mutants (Figure 2.5B). When mtDNA and mitochondrial superoxide levels were studied, we observed normal mtDNA and mitochondrial superoxide levels in these cells (Figure 2.5E and 2.5F). These results suggested that in cells expressing Rrm2 C-terminal truncation mutants that could not interact with endogenous Rrm1, the dominant negative effect was disrupted, which brought the mtDNA and mitochondrial superoxide levels back to normal. We also examined the cellular superoxide levels in these Rrm2 C-terminal truncation mutants using DHE staining. As shown in Figure

Figure 2.5 Rrm2-Y177F and Rrm2-Y370F mutants cause mitochondrial dysfunction by interfering with endogenous Rrm1. (A) Left panel: pull-down assay showing the disruption of Rrm1 and Rrm2 interaction in Rrm2-Δ7 and Rrm2-Δ20. Right panel: pull-down assay showing normal interaction between Rrm2-Y177F, Rrm2-Y370F, Rrm2-Fe6 and Rrm1. GST tagged Rrm2 wild type and mutant proteins were bound to glutathione beads, incubated with 293 cell lysates and western blotted to detect the association with Rrm1. (B) Western blot showing the expression levels of Rrm2 C terminal truncation mutants, Rrm2-Δ7, Rrm2-Δ20, Rrm2-Y177F-Δ7, Rrm2-Y177F-Δ20 and Rrm2-Y370F-Δ7 in transfected mouse 3T3 cells. (C) Representative pictures showing red fluorescence of DHE stained Rrm2-Δ7, Rrm2-Δ20, Rrm2-Y177F-Δ7, Rrm2-Y177F-Δ20 and Rrm2-Y370F-Δ7 expressing cells. Corresponding bright field images were also shown. Images were taken at 20x with 405nm excitation and 530nm emission. (D) Bar graph showing the fold change of superoxide levels in Rrm2 wild type and mutant expressing cells as compared to the vector control. 150 cells for each cell line from 3 independent experiments were quantified. All fluorescence levels were normalized to the vector control (***$P<0.001$, two way ANOVA). (E) No changes in mtDNA levels were observed in 3T3 cells overexpressing Rrm2 C-terminal truncation mutants. mtDNA levels in these cell lines were measured using qPCR as in Figure 2.4A (3 independent experiments, one way ANOVA). (F) No change in mitochondrial superoxide levels were observed in 3T3 cells overexpressing Rrm2 C-terminal truncation mutants. Mitochondrial superoxide levels in these cell lines were measured using MitoSox Red staining and quantified using Image J as in Figure 2.4B and 2.4C. 100 cells from 2 independent experiments were analyzed (***$P<0.001$, two way ANOVA).

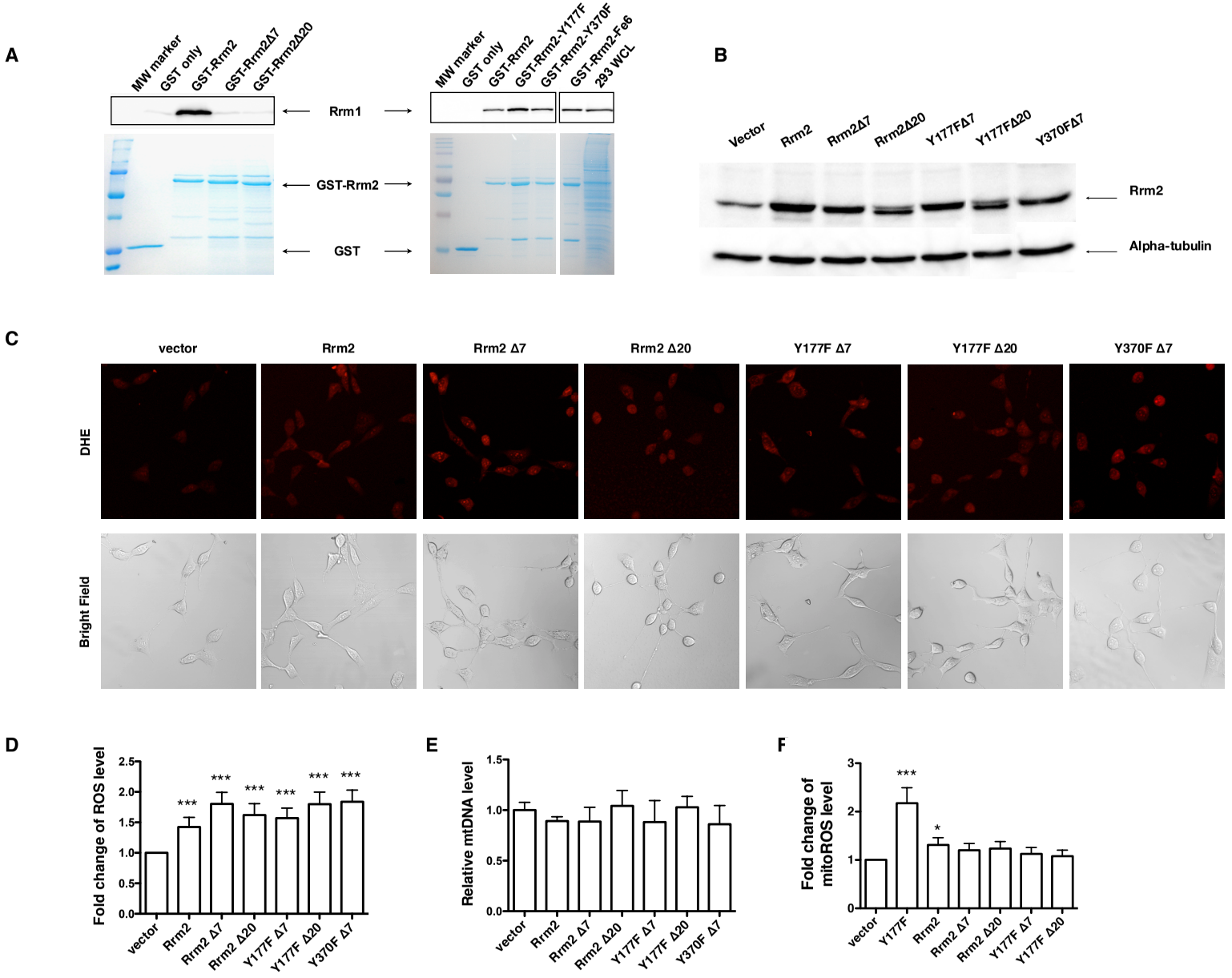
A
MW marker
GST only
GST-Rrm2
GST-Rrm2Δ7
GST-Rrm2Δ20
Rrm1
GST-Rrm2
GST
MW marker
GST only
GST-Rrm2
GST-Rrm2-Y177F
GST-Rrm2-Y370F
GST-Rrm2-Fe6
293 WCL
B
Vector
Rrm2
Rrm2Δ7
Rrm2Δ20
Y177FΔ7
Y177FΔ20
Y370FΔ7
Rrm2
Alpha-tubulin
C
vector
Rrm2
Rrm2 Δ7
Rrm2 Δ20
Y177F Δ7
Y177F Δ20
Y370F Δ7
DHE
Bright Field
D
Fold change of ROS level
E
Relative mtDNA level
F
Fold change of mitoROS level

2.5C and 2.5D, all Rrm2 C-terminal truncation mutants showed increased cellular superoxide levels. This further suggested that as long as the di-nuclear iron center was intact, there were increased cellular superoxide levels in Rrm2 and this superoxide production was not affected by the disruption of radical transfer and interaction between Rrm1 and Rrm2.

2.4.5 The role of ROS production in Rrm2-induced mutagenesis and tumorigenesis

It is shown that Rrm2 overexpression in 3T3 cells led to increased mutation frequency and Rrm2 overexpression in mice led to lung tumor development (Xu, Page et al. 2008). However, the molecular mechanism of R2-induced mutagenesis and tumorigenesis is not known. In this study, we showed that increased Rrm2 levels in cells led to increased RNR enzyme activity (Figure 2.3A) and increased ROS production (Figure 2.1B and 2.1C). Since preliminary dNTP measurement in Rrm2 overexpressing cells didn't show significant changes (Figure 2.6), we were interested in whether Rrm2-induced ROS production had a direct role in Rrm2-induced mutagenesis and tumorigenesis independent of RNR enzyme activity.

The panel of Rrm2 mutants generated in this study could be divided into two categories: one could not produce free radicals and had no enzyme activity such as Rrm2-Fe6; the other could produce free radicals but had no enzyme activity such as Rrm2-Y177F and Rrm2-Y370F. With these two types of Rrm2 mutants in hand, we were able to compare their effects on mutation frequency in cells and examine whether ROS production can lead to increased mutagenesis.

In order to study this, we generated U2OS cells that overexpressed vector, Rrm2, Rrm2-Fe6, Rrm2-Y177F and Rrm2-Y370F. HPRT assay was used to measure the mutation frequency in these cells. However, cells expressing wild type Rrm2 only showed slight increase in mutation frequency, making the comparison with mutation frequency in Rrm2 mutants hard (data not

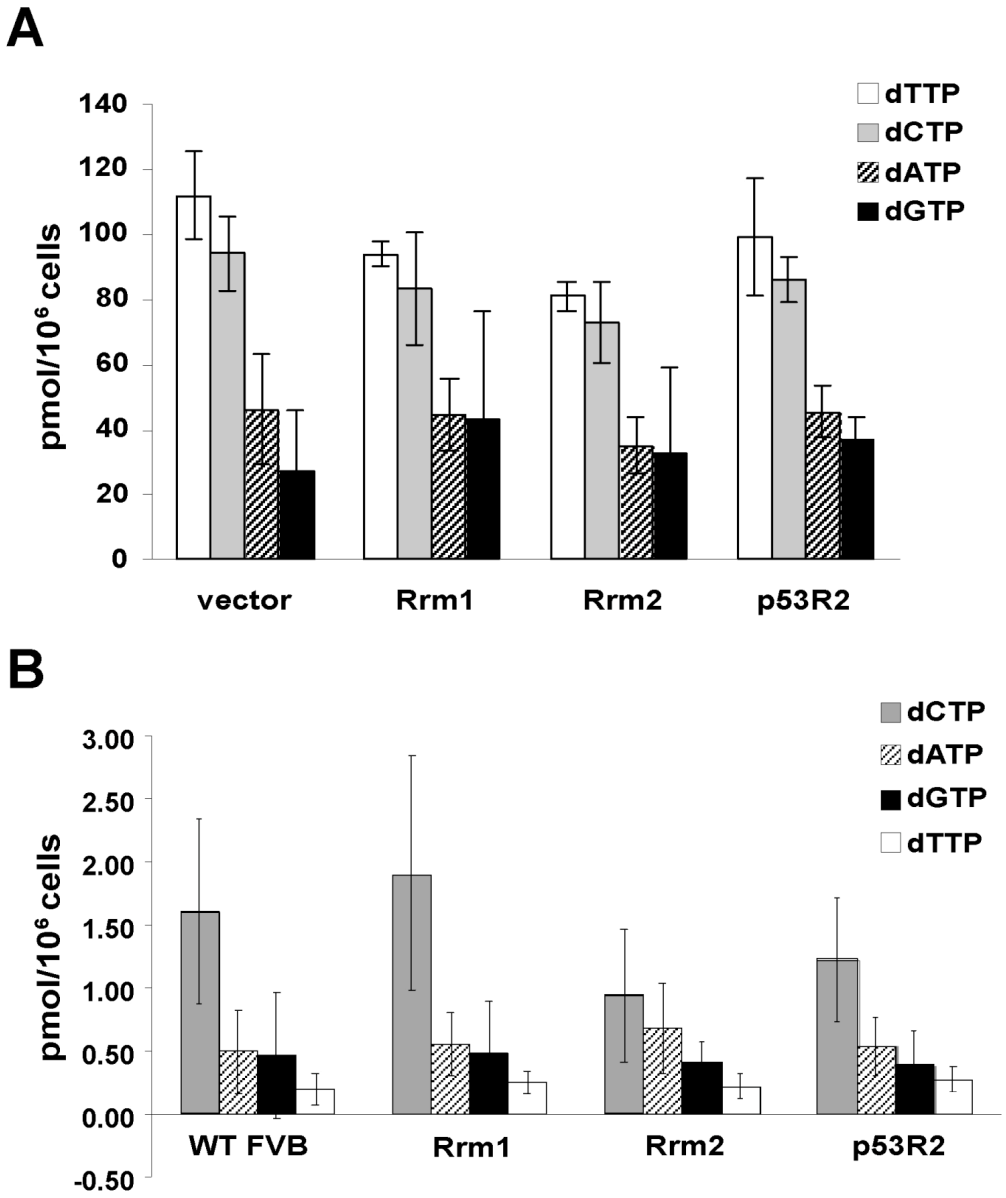

Figure 2.6 Total cellular dNTP levels in (A) proliferating Rrm2 and p53R2 expressing 3T3 cells and (B) RNR transgenic lung tissues. Total nucleotides were extracted from cells and each dNTP was measured by an indirect enzymatic assay. Each data point represents the mean of three independent experiments, with error bars representing the standard deviation. (Data collected and figure prepared by Dr. Xia Xu, 2008).

shown). In order to circumvent the problem, we decided to perform HPRT assay in a sensitized background, where we introduced Y177F, Y370F and Fe6 mutations into Rrm2-T33A mutant background. Rrm2-T33A is a non-degradable Rrm2 mutant and has been shown to cause more than 20x increase in mutation frequency in U2OS cells compared to control cells (D'Angiolella, Donato et al. 2012). By combining our Rrm2 mutants with Rrm2-T33A, we expect to establish a condition where we can analyze and compare mutation frequency in different Rrm2 mutants.

2.5 Discussion

In this study, we investigated the effect of the small subunit Rrm2 deregulation on redox homeostasis and mitochondrial function in cells. 3T3 cells overexpressing Rrm2 wild type showed increased levels of RNR enzyme activity, Y177 tyrosyl radical production and increased superoxide generation. Complete disruption of the di-nuclear iron center of Rrm2 in Rrm2-Fe6 mutant renders Rrm2 protein enzymatically inactive and Y177 radical production defective. As a consequence, Rrm2-Fe6 mutant has no effect on superoxide production in cells, indicating that functional di-nuclear iron center contributes to increase superoxide generation in Rrm2 wild type over-expressing cells. The discovery of Rrm2-induced superoxide production is consistent with published work where human recombinant Rrm2 showed increased hydrogen peroxide (H_2O_2) production *in vitro* (Liu, Xue et al. 2008). Since p53R2 has intact di-nuclear iron center as Rrm2, it is not surprising that p53R2 overexpressing cells also showed elevated superoxide levels in our study. However, this is opposite to published work. In the same paper that showed increased H_2O_2 production by Rrm2, human recombinant p53R2 was shown to have antioxidant activity *in vitro* (Liu, Xue et al. 2008). With inadequate information provided in the paper, we were not able to assess how much recombinant p53R2 and Rrm2 proteins were added to the assay system, whether these amounts reflected equal activity of the two subunits and how stable these subunits

were during the 30min assay period. Since Fe is required for R2 radical production, it is also not clear whether and how much Fe had been supplemented.

Two Rrm2 mutants, Rrm2-Y177F and Rrm2-Y370F that have mutations in the radical transfer pathway of Rrm2, caused increased superoxide production in cells (about 1.7-fold increase). These mutants also lead to about 1.3-fold increase in mitochondrial superoxide production through their dominant negative effects, suggesting that there are two sources for the observed overall increase in superoxide levels: the intact di-nuclear iron center and the dysfunctional mitochondria.

However, when the overall cellular superoxide levels were measured in cells with Rrm2 C-terminal truncation mutants that do not have dominant negative effect, no corresponding decrease in overall superoxide levels were observed. Instead, the levels of superoxide in these cells were comparable to those of Rrm2-Y177F and Rrm2-Y370F expressing cells where about 1.7-fold increase in overall superoxide was detected. This discrepancy could be due to the nature of the ROS indicator used. DHE is often used as an indicator of overall cellular superoxide levels. However, it only localizes in the cytosol and does not go to the mitochondria. It measures overall cellular superoxide because mitochondrial superoxide production can affect the cytosolic superoxide readout. As a result, the overall superoxide levels measured by DHE in the study may mainly reflect cytosolic superoxide changes. It is possible that the change in mitochondrial superoxide production is not strong enough to affect the cytosolic superoxide production and to be detected by DHE staining. This also suggests that increased mitochondrial superoxide production in Rrm2-Y177F and Rrm2-Y370F expressing cells only has minor contribution to the overall increased superoxide production observed in these cells.

Human p53R2 protein with truncation of the last 25 residues of the C-terminus leads to a disease called autosomal-dominant progressive external ophthalmoplegia (adPEO), which is a mitochondrial disorder that is characterized by accumulation of mtDNA deletions in postmitotic tissues. Because the mutant protein causes a dominant trait, it is hypothesized that this p53R2 truncation mutant can compete with the wild-type p53R2 in forming the heterotetramer, resulting in a gain of function or a dominant negative effect of RNR in cells (Tyynismaa, Ylikallio et al. 2009). Our Rrm2 C-terminal truncation mutants didn't show dominant negative effect and had normal mtDNA levels. This could be due to the fact that in cells overexpressing Rrm2 C-terminal truncation mutants, the p53R2 protein level is normal. Since the Rrm2 C-terminal truncation mutants cannot bind and interfere with endogenous Rrm1, there is enough Rrm1 subunits to form an active RNR with p53R2, which is the primary complex that is responsible for providing dNTPs for mtDNA replication. It would be interesting to introduce the p53R2 C-terminal truncation mutants into cells and investigate whether this will lead to mtDNA deletions as observed in human patients.

The dominant negative effect suggested here proposed that Rrm2-Y177F and Rrm2-Y370F mutants interfere with endogenous Rrm1 and decrease the level of functional RNR (both the Rrm1-Rrm2 and Rrm1-p53R2 form of RNR) in cells, resulting in limited dNTPs for mtDNA synthesis. dNTP pools in cells overexpressing Rrm2-Y177F and Rrm2-Y370F were assayed (Sherman and Fyfe 1989; Ferraro, Franzolin et al. 2010), but no depletion in dNTP pools was observed (Figure 2.7). Since these cells also didn't show any growth defects (Figure 2.8), this suggests that dNTP pool changes are small and our assay system may not be sensitive enough to detect such small changes.

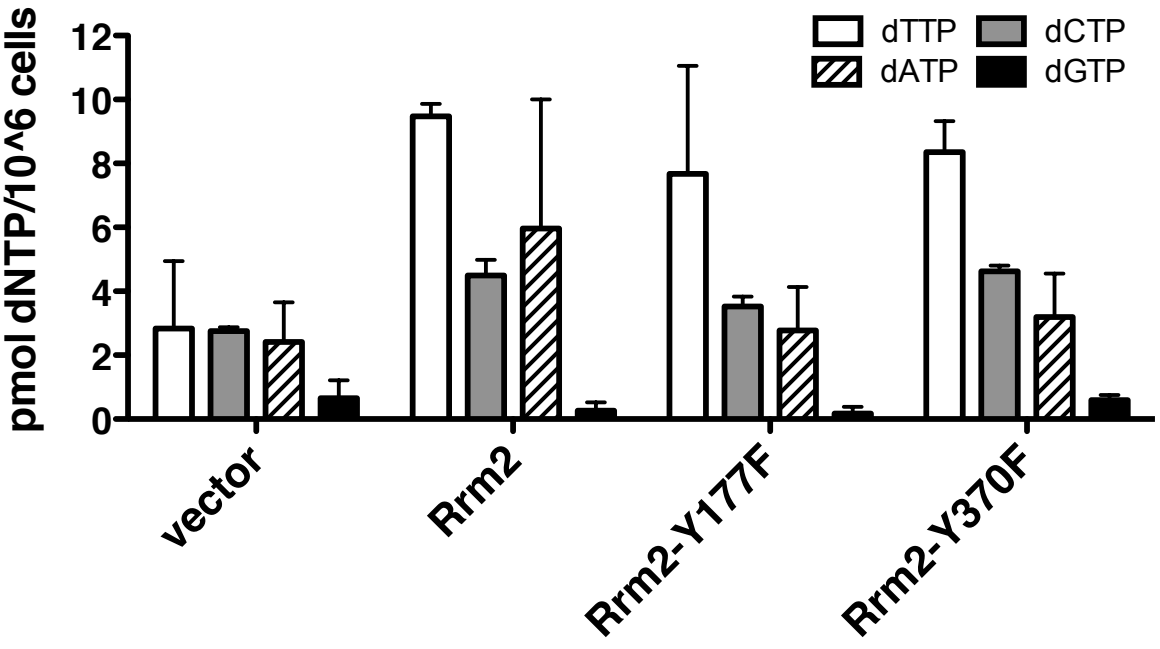

Figure 2.7 Total cellular dNTP levels in Rrm2-Y177F and Rrm2-Y370F overexpressing cells. Total nucleotides were extracted from cells and each dNTP was measured by an indirect enzymatic assay. Each data point represents the mean of two independent experiments, with error bars representing the standard deviation.

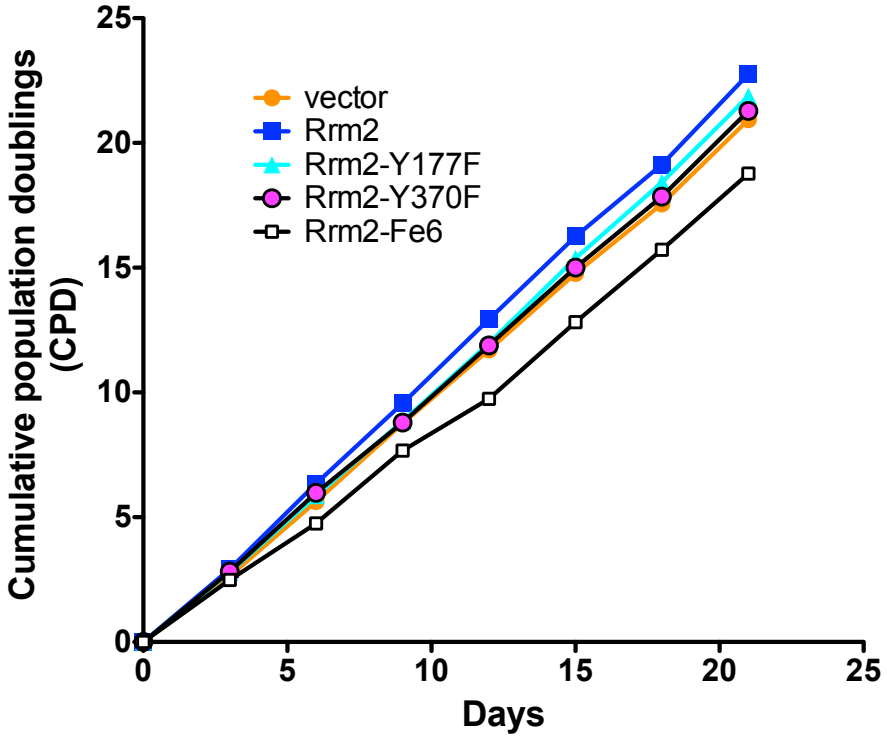

Figure 2.8 Proliferation of cells overexpressing Rrm2 WT and mutant proteins. Each cell line was cultured in standard culture media (see methods for details regarding the components of the media) and passed every 3 days with counting. Total population doublings were determined and plotted against time.

When mitochondrial superoxide levels were measured, besides the increased superoxide production in Rrm2-Y177F and Rrm2-Y370F cells, Rrm2 over-expressing cells also showed a slight, but significant increase in mitochondrial superoxide production. This could be due to the increased RNR activity and subsequent changes in dNTP pools in these cells. It has been shown that Rrm2 over-expressing transgenic mice had dNTP pool changes and progressive mtDNA depletion in skeletal muscle, supporting the idea that Rrm2 overexpression can lead to dNTP pool imbalance and affect mitochondria function (Ylikallio, Page et al. 2010). Again, our dNTP assay system may not be sensitive enough to detect such changes.

We showed that about 50% mtDNA depletion is associated with about 1.3-fold increase in mitochondrial superoxide production. This same mtDNA depletion level has been shown to cause significant disruption of cellular ROS homeostasis in p53 null cells. These cells are characterized by reduced mitochondrial and cellular superoxide levels (50% reduction) and increased cellular hydrogen peroxide (1.8-fold increase) (Lebedeva, Eaton et al. 2009). The opposite changes in superoxide levels in our R2-expressing cells and the p53 null cells could be due to following reasons. In the Lebedeva study, the concentration of DHE used to measure overall superoxide production was 40x more than that used in our study (80μM vs. 5μM, with 5μM commonly used). Too much loading of fluorescent dyes to cells can disrupt the redox status of cells in study as the probes can act as either antioxidants or prooxidants (Sen and Packer 2002). Furthermore, the Lebedeva study used p53 null cells. Since p53 is a transcription factor that is involved in many cellular processes, decreased mitochondrial superoxide production in p53 null cells may not be directly associated with mtDNA depletion. It has been shown that p53

represses activity of manganese superoxide dismutase (MnSOD), the mitochondrial enzyme responsible for the conversion of superoxide to hydrogen peroxide, in human cells (Drane, Bravard et al. 2001). As a result, knocking-out p53 could lead to decreased superoxide and increased hydrogen peroxide production independent of mtDNA levels.

Rrm2-Fe6 mutant binds to the large Rrm1 subunit, suggesting that disrupting the di-nuclear iron center does not affect the subunit interaction. It is surprising that Rrm2-Fe6 didn't show the same dominant negative effects as Rrm2-Y177F and Rrm2-Y370F. When culturing cells expressing Rrm2-Fe6, we noticed that these cells showed gradually decreased growth compared to Rrm2 wild type and other Rrm2 mutant cell lines (Figure 2.8). This observation suggests that Rrm2-Fe6 may have dominant negative effects in cells and may be selected against. This dominant negative effect could be the same as Rrm2-Y177F and Rrm2-Y370F where the mitochondrial function is affected. It could also be something different and more severe. For example, the dNTP pool balance may be more severely disrupted in Rrm2-Fe6 mutant, which affects not only the mitochondrial, but also the nuclear genome integrity. In the current study, all experiments performed on Rrm2-Fe6 mutant used early passage cells that grow normally and no defects in mtDNA synthesis was detected. It would be worth investigating the dNTP pools, mitochondrial and nuclear genome integrity and redox status in later slow-growing Rrm2-Fe6 mutant.

One important question we want to address is the downstream effect of R2-induced ROS production. Elevated ROS levels in cells have been shown to cause oxidative stress and promote mutagenesis and tumorigenesis (Droge 2002; Valko, Rhodes et al. 2006). Superoxide-generating proteins of the NADPH oxidase family have been shown *in vitro* to cause increased superoxide production and cell transformation when overexpressed alone or together with Ras (Irani, Xia et

al. 1997; Suh, Arnold et al. 1999; Mitsushita, Lambeth et al. 2004; Block and Gorin 2012). In addition, proteins that can sense oxidative stress and induce apoptosis help prevent ROS accumulation and thus their carcinogenic effects in cells (Dolado, Swat et al. 2007). We are currently investigating whether R2-induced ROS plays a direct role in mutagenesis and tumorigenesis. With the panel of Rrm2 mutants in hand, we are studying the mutagenic effect of Rrm2 mutants that can produce free radicals, but are enzymatically inactive (Rrm2-Y177F and Rrm2-Y370F), as well as Rrm2 mutant that is defective for both free radical production and enzyme activity (Rrm2-Fe6). If Rrm2-Y177F and Rrm2-Y370F show increased mutation frequency while Rrm2-Fe6 does not, this would suggest a role of R2-induced ROS in mutagenesis.

In conclusion, we showed that overexpression of the small subunit of RNR, R2, leads to increased ROS production in cells. The di-nuclear iron center of R2 produces free radicals and contributes to this increase in ROS. When charged residues critical for iron coordination were mutated in Rrm2-Fe6, there is no elevated ROS production in cells. Moreover, when critical tyrosine residues in the radical transfer pathway were mutated to non-hydrolysable residues in Rrm2-Y177F and Rrm2-Y370F mutants, they lost RNR enzyme activity. However, because the di-nuclear iron center is still intact, these mutants lead to increased ROS in cells. On top of this, they also have dominant negative effect by interfering with endogenous large R1 subunit, leading to mild mtDNA depletion and increased mitochondrial ROS production, which has a minor contribution to the increased overall ROS in cells. This panel of Rrm2 mutants gives us a great opportunity to study the role of RNR in redox homeostasis, mitochondrial function and the role of R2-induced ROS in mutagenesis and tumorigenesis.

2.6 Acknowledgment

We thank Dr. Xia Xu for generating Rrm2-Y177F and Rrm2-Y370F mutants, and for collecting data and making Figure 2.6, Dr. Yimon Aye and Dr. Yuan Fu for performing RNR enzyme activity and EPR assays for Figure 2.2B and C, Aaron Cohen for helping with ROS measurement and mitochondrial DNA analysis, Dr. David Infanger and Dr. Heinrich Lobe for helpful discussions on cellular and mitochondrial ROS measurement, and Dr. Hening Lin for suggestions on generating Rrm2 iron mutants and for allowing me to use their HPLC system.

CHAPTER 3 Identification of Exponential Growth Patterns for Murine Lung Neoplasms by Automated Quantification of micro-CT Images

Minxing Li[1*], Artit Jirapatnakul[2*], Alberto Biancardi[2], Mark L. Riccio[1], Robert S. Weiss[1, †], and Anthony P. Reeves[2, †]

[1]Department of Biomedical Sciences and [2]School of Electrical and Computer Engineering, Cornell University, Ithaca, New York 14853

* These authors contribute equally to the work

† Co-corresponding authors:

Weiss: Tel.: (607) 253-4443; Fax: (607) 253-4212; E-mail: rsw26@cornell.edu

Reeves: Tel.: (607) 255-2342; Fax: (607) 255-9072; E-mail: reeves@ece.cornell.edu

3.1 Abstract

Computed tomography (CT) is among the non-invasive imaging modalities for monitoring lung tumor growth in humans. Manual or semi-automated methods are used to calculate the tumor size, and an exponential growth model is used to predict tumor growth. However, current measurement methodologies are often time-consuming and lack consistency. In addition, knowledge of *in vivo* lung tumor growth patterns in humans is limited. Treatment of lung cancers in humans often involves surgical resection of the primary tumor, and individual patients rarely are subjected to multiple sequential CT scans because of the associated radiation exposure. In this study, we monitored lung tumor growth rate in a mouse model of lung cancer by micro-CT and developed an automated algorithm to measure tumor size at an early stage. Transgenic mice over-expressing the enzyme ribonucleotide reductase (RNR) develop non-small cell lung cancers at approximately 12 months of age and in this study were scanned four to six times with at least a three-week time interval in between the scans. Six tumors from four mice was analyzed and all showed an exponential growth pattern *in vivo.* The average tumor doubling time was about 71 days, while tumors of smaller initial size grew faster. These results establish automated algorithms to measure early stage lung tumor volume and confirm the exponential lung tumor growth model in humans. The improved computational methods developed here, as well as a better understanding of mouse lung tumor growth patterns, are expected to serve as a resource that will aid efforts to improve lung cancer diagnosis and the evaluation of therapeutic responses.

3.2 Introduction

Lung cancer is the leading cause of cancer death among both men and women worldwide. The five-year survival rate for lung cancer is only 16%, as compared to 89% and 100% for breast and prostate cancers, respectively. If lung cancers are detected and treated in their earliest stages, the survival rate can be improved to 92% (Jemal, Siegel et al. 2010). Not only is the detection of lung tumors critical, but measuring disease progression and treatment response is also important for improving patient care. Such clinical data can be collected using non-invasive imaging techniques, such as X-ray computed tomography (CT). CT images are generated based on X-ray attenuation by tissues, with the degree of attenuation proportional to the tissue density. CT instruments generate a series of 2D X-ray images, which are stacked together to produce a 3D image. Based on these images, clinicians can identify and measure potential lung neoplasms.

Tumor size and growth rate are key criteria for cancer staging and can be used to evaluate the effectiveness of therapies. Measurement of these parameters must be highly accurate in order for CT scans to be useful for clinical purposes. Accurate quantification of tumor growth requires optimization of CT scan parameters and measurement software using extensive data sets with growing tumors. However, these data sets are not readily available for human patients because of the large number of repeated CT scans required and the associated X-ray dosage concerns. Furthermore, human patients are subjected to clinical interventions that include surgical resection or therapies that impair growth. As a result, much of the research on evaluating measurement methods has relied on the use of repeat "coffee break" scans, in which patients are scanned twice over a short period of time (Goodman, Gulsun et al. 2006; Gietema, Schaefer-Prokop et al. 2007; Zhao, James et al. 2009; Oxnard, Zhao et al. 2011); or the use of repeat scans obtained during

image-guided biopsy of pulmonary nodules (Reeves, Jirapatnakul et al. 2009). These studies have reported repeat scan variability of around 25% volume change. However, it is unclear whether these data can be extrapolated to the measurement of growing tumors.

One approach to quantify tumor growth is to combine an empirical tumor volume measurement with a mathematical model for tumor growth rate. The two most commonly used growth models are the exponential growth model, where the growth rate is proportional to the current value and continues indefinitely, and the Gompertzian growth model, which resembles the exponential growth model initially but reduces the growth rate as time progresses. However, due to the reasons noted above, the *in vivo* growth of human lung tumors has not been extensively studied. Another complication for accurately measuring tumor growth is the variance in ground truth. Several studies have suggested that manual measurements of tumor size by radiologists are inconsistent (Marten, Auer et al. 2006; Reeves, Biancardi et al. 2007; Ross, Miller et al. 2007) and should not be relied upon to provide ground truth. In order to circumvent the limitations of human CT cans, we used a mouse model of lung cancer to develop automated methods for accurate tumor growth rate and growth pattern determination. Because we examined early lung tumor growth where the nutrients and space are not constrained for tumor cells, we hypothesized that an exponential growth pattern would be observed.

Mouse models have great value for the study of lung cancer, and micro-CT has been used to detect and measure tumors (Cavanaugh, Cody et al. 2004; Veldhuizen, Ford et al. 2007). Investigation of disease progression and therapeutic responses are of particular interest in these animal models, and require accurate and consistent methods for tumor growth measurements. Currently, most tumor measurements on murine micro-CT scans are performed using basic tools. Haines *et al.* applied thresholds to CT images and separated lung parenchyma from soft tissue

structures by region growing and manual contouring. The change in soft tissue volume was used as a measure of tumor burden (Haines, Bettano et al. 2009). Fushiki *et al.* used a similar method with additional manual and semi-automated segmentation to select only neoplastic tissue (Fushiki, Kanoh-Azuma et al. 2009). A more advanced method applied a semi-automated tool which presented a preliminary automated tumor boundary. However, manual modification of the boundary was required to produce an acceptable segmentation (Cody, Nelson et al. 2005). All of these methods require extensive user interaction with the system, which is time-consuming and may result in measurement variability among different users.

In this study, we utilized a mouse lung tumor model based on overexpression of the small subunit of the enzyme ribonucleotide reductase (RNR) (Xu, Page et al. 2008). RNR catalyzes the rate-limiting step in deoxyribonucleotide biosynthesis, and plays an essential role in the maintenance of genome integrity. RNR-overexpressing mice develop lung adenomas and adenocarcinomas that histopathologically resemble human papillary adenocarcinomas, the most common form of human non-small cell lung cancer. RNR-induced lung tumors arise via a mutagenic mechanism and frequently contain K-ras mutations, which also occur in approximately 30% of human lung adenocarcinomas (Reynolds and Anderson 1991; Reynolds, Wiest et al. 1992). In combination with deletion of the DNA mismatch repair gene Msh6, RNR overexpression results in lung neoplasms in 100% of mice by 6 months of age (Xu, Page et al. 2008).

Micro-CT images of RNR-induced murine lung neoplasms were measured using an automated algorithm adapted from tools for the measurement of pulmonary nodules on human chest CT scans. Initial imaging studies in mice were performed to optimize scan parameters and refine computational algorithms for tumor volume measurement. Four lung tumor-bearing mice

were then sequentially scanned for tumor growth rate determination by curve fitting. Our results indicate that the tumors demonstrated exponential growth, a finding that is consistent with modeling of growth patterns for human lung cancers. This study provided better tools for lung tumor measurements, as well as better insights into lung tumor growth, which can improve early detection and facilitate therapeutic evaluation of human lung cancers.

3.3 Material and methods

3.3.1 Animals, necropsy and histology analyses

Rrm2 and p53R2 transgenic mice ($Rrm2^{Tg}$ and $p53R2^{Tg}$) were described previously (Xu, Page et al. 2008). $Msh6^{+/-}$ mice (Edelmann, Yang et al. 1997) were obtained from the Mouse Models of Human Cancers Consortium and interbred with $Rrm2^{Tg}$ mice to generate $Msh6^{-/-}R2^{Tg}$ experimental mice. All mice were maintained identically, following guidelines approved by the Cornell University Institutional Animal Care and Use Committee.

After the final micro-CT scan, mice were euthanized by asphyxiation using carbon dioxide and necropsied. Lungs were imaged using a Canon digital camera and were inflated and fixed with 10% neutral-buffered formalin, embedded in paraffin, sectioned, and stained with hematoxylin and eosin (H&E). H&E sections of the lungs were scanned using the Aperio ScanScope and physical measurements of lung neoplasms were made using the Aperio software. Lung neoplasms were classified based on guidelines endorsed by the Mouse Models of Human Cancers Consortium (Nikitin, Alcaraz et al. 2004).

3.3.2 Micro-CT imaging

3.3.2.1 Post-mortem imaging

Preliminary scans of mice following euthanasia were used for initial development and verification of the algorithm. Nine mice were scanned after they were euthanized by carbon dioxide asphyxiation. These scans were acquired using a GE eXplore CT 120 micro-CT scanner. Scan parameters that varied in current, voltage, number of projections, number of frames to average, and reconstruction resolution were tested (Table 3.1). Three of the nine euthanized mice had visible tumors, which were used to test the automated tumor measurement methods.

3.3.2.2 Live imaging

In the live study scans, mice were first put in the induction chamber and anesthetized with a continuous flow of 4% isoflurane/oxygen mixture. When the animals stopped moving and their breathing slowed down, the isoflurane/oxygen mixture was reduced to 1-3% and maintained at this range during the duration of the micro-CT scan (Hung, Dodson et al. 2009). Scans of the thoracic region were acquired using the same micro-CT scanner with a current of 50 mA and voltage of 100 kV. Each scan consisted of 720 projections in a single full rotation of the gantry. Two frames were acquired at each position of the gantry and averaged prior to being transferred to the workstation for reconstruction. Respiratory gating of the mice was achieved using the BioVet physiological monitoring and triggering system by m2m imaging corporation. A small external force by taping a piece of paper tower to the back of the mouse was applied in order for the mouse to activate the pressure sensor used for respiratory gating. Micro-CT images were reconstructed at 50 μm^3 voxel dimensions. The final image volume varied according to the selected region of interest, but typically ranged from 400 x 400 x 500 slices to 800 x 550 x 1000

Table 3.1[a]. Different scanner acquisition parameters tested in this study.

#	Current (mA)	Voltage (kVp)	Exposure time (ms)	# of Views/scan	Frame averaging	SD (HU)
1	32	70	32	220	1	53.3
2	50	70	32	220	1	80.4
3	32	80	32	220	1	45.6
4	50	80	32	220	1	41.1
5	50	100	32	220	1	39.2
6	50	100	20	360	2	30.5

[a] The intensities of small regions within the lung parenchyma were sampled and used to compute the standard deviation (SD). Higher standard deviation values indicate higher noise.

slices. Half of the total live scans had calibration phantoms included. Scans were converted from the manufacturer's proprietary format to DICOM and then imported into research software.

3.3.3 Automated volumetric analysis

The volume of the murine lung tumors was computed from the segmentation result produced by an automated algorithm. The algorithm was adapted from previous work on automated segmentation of lung tumors in whole lung CT scans of humans (Kostis, Reeves et al. 2003). An overview of the algorithm, which consists of several stages, is presented in Figure 3.1. The user initiates the algorithm by drawing a line across the nodule indicating the nodule's extent. The algorithm uses the provided information to extract a region of interest to analyze. After pre-processing the image, an adaptive threshold is applied, followed by filtering to remove attached pulmonary vessels. If the nodule is juxtapleural, an additional step is performed to separate the nodule from the chest wall. The final result is a binary image containing only those voxels belonging to the nodule. The steps of the algorithm are described in further detail in the following sections.

3.3.3.1 Region of interest pre-processing

The endpoints of the line drawn by the user are used to estimate the location and size of the nodule. A large region of interest (ROI) corresponding to 5x5x5 cm cube is extracted from the whole micro-CT scan around the estimated center of the nodule. This large region of interest is analyzed to determine if the nodule is juxtapleural. A threshold is applied to the image and the connected component that contains the estimated nodule is kept. A nodule is considered juxtapleural if this connected component occupies more than 15% of the ROI. Depending on the outcome, different parameters are used to separate attached structures and an additional step to separate the nodule from the chest wall is performed.

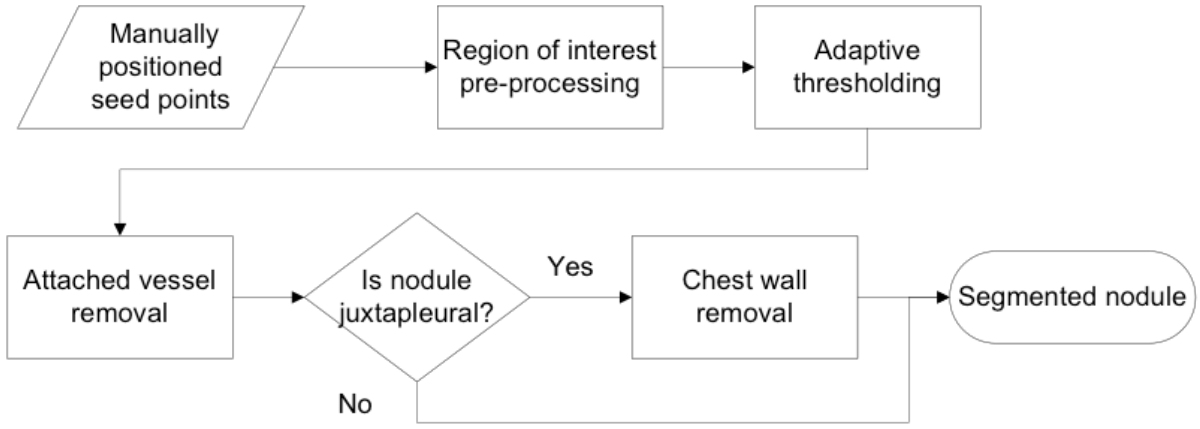

Figure 3.1. Flowchart showing the major steps of the automated segmentation algorithm.

The next pre-processing step is to further refine the estimated nodule location and size in order to ensure consistency if the manually specified points are altered slightly. By modeling a pulmonary nodule as a sphere, we can use a 3D Laplacian of Gaussian (LoG) template to localize the nodule and a 3D Gaussian template to estimate the size. A LoG template is used to locate the nodule to account for nodules with attached structures. An iterative process is used to optimize the location and size using the LoG and Gaussian templates respectively. A sample result from this step is shown in Figure 3.2.

The estimated nodule location and size are used to establish a tight region of interest around the nodule, which is set to twice the estimated size of the nodule. In the case of scans obtained in a longitudinal study, the ROI size is fixed to the same value for all scans in the study. This tight ROI is then resampled to provide subvoxel accuracy to help reduce the effects of partial voxels (Kostis, Reeves et al. 2003; Reeves, Chan et al. 2006). At the end of the pre-processing step, we have a refined estimation of the nodule size and location and a tight region of interest both before and after resampling.

3.3.3.2 Adaptive thresholding

The next step in the segmentation algorithm is to threshold the region of interest to separate the soft tissue from the lung parenchyma. While the use of an adaptive threshold does not provide much benefit for segmenting nodules from human CT scans compared to a fixed threshold (Reeves, Chan et al. 2006), the murine micro-CT scans exhibited significant variation in the intensity of the lung parenchyma from one scan to another. To compensate for this variation, an adaptive threshold was selected for each scan. A histogram of the small region of interest, prior to resampling, was generated. A threshold was established based on the assumption that the histogram would be bi-modal, with one peak corresponding to the lung

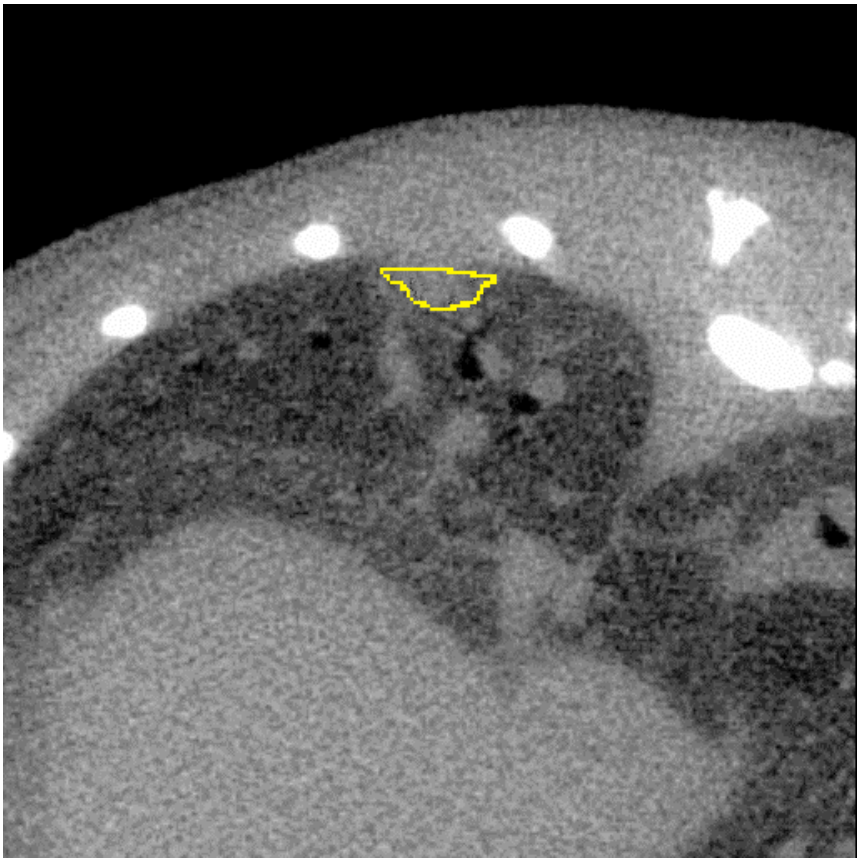

Figure 3.2. A representative image showing size and location estimation of a nodule by the automated algorithm. Micro-CT image of an RNR transgenic mouse lung (transverse view) is shown, with a nodule highlighted in yellow by the algorithm. The image was derived from a scan taken at 50μm with 720 projections. The size of this nodule was estimated by the automated algorithm to be 1.41 mm in diameter, 1.46 mm^3 in volume.

parenchyma and another to the soft tissue. The threshold was selected to be the midpoint of the two peaks, as shown by the plot in Figure 3.3. After the adaptive threshold was determined, the threshold was applied to the resampled ROI image to generate a binary image, with all soft tissue structures labeled.

3.3.3.3 Pulmonary vessel removal

To separate the nodule from attached structures such as pulmonary vessels, iterative morphological filtering is performed. A morphological opening is performed using a large spherical kernel to remove the vessel attachments, followed by a series of dilation operations with increasingly larger spherical kernels to regrow some of the fine surface features. This process is described in further detail by Kostis *et al* (Kostis, Reeves et al. 2003). Figure 3.4A, 3.4B and 3.4C illustrate the effect of this step on a 3D reconstruction of the nodule region, showing the region before and after applying the vessel removal step.

3.3.3.4 Chest wall removal

Finally, if the nodule is juxtapleural, a surface-fitting approach is used to estimate the 3D shape of the chest wall or pleural surface in order to remove it from the segmentation. The pleural surface has low curvature and few inflection points, which suggests a model using a second or third degree polynomial function. A more detailed description of the work can be found in Jirapatnakul, A.C. *et al* (Jirapatnakul, Mulman et al. 2011).

The nodule and pleural surface points were first extracted from the image by a morphological erosion and binary exclusive-OR (XOR) operation. Given two binary images, the XOR operation produces a binary image showing where the two input images differed. The surface points are those points belonging to either the nodule or pleural surface but having a lung parenchyma voxel as a neighbor. The average normal was computed from these surface points

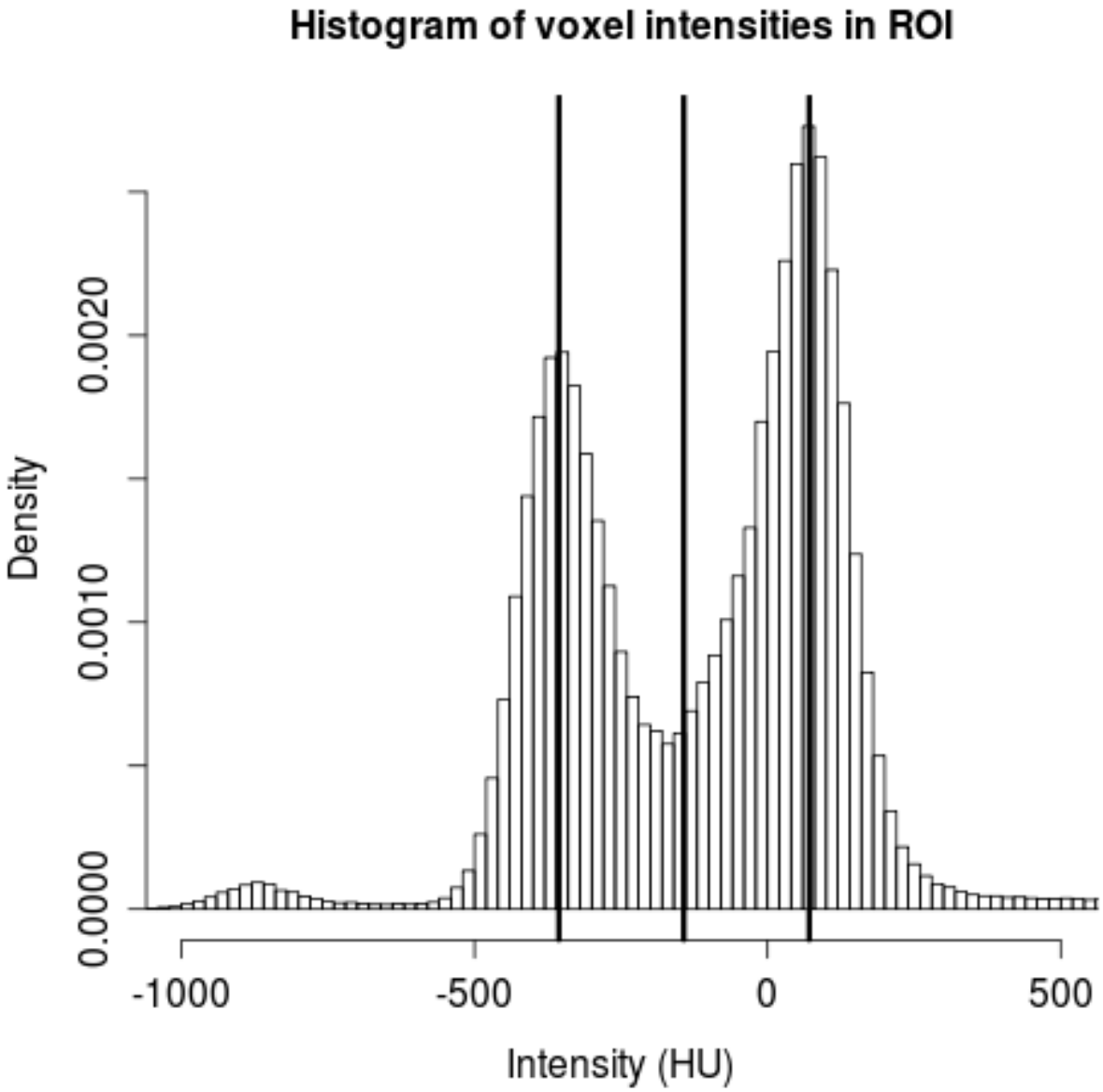

Figure 3.3. Histogram showing voxel intensities of the lung parenchyma and soft tissue in a region of interest. Voxel intensities of a region of lung from an RNR transgenic mouse including a nodule were sampled and used to create the histogram. Bins were set at 10 HU. The peak on the left represents the lung parenchyma and the peak on the right represents the soft tissue. The line in the middle indicates the calculated adaptive threshold by the automated algorithm. The data shown were from a scan taken at 50μm with 720 projections.

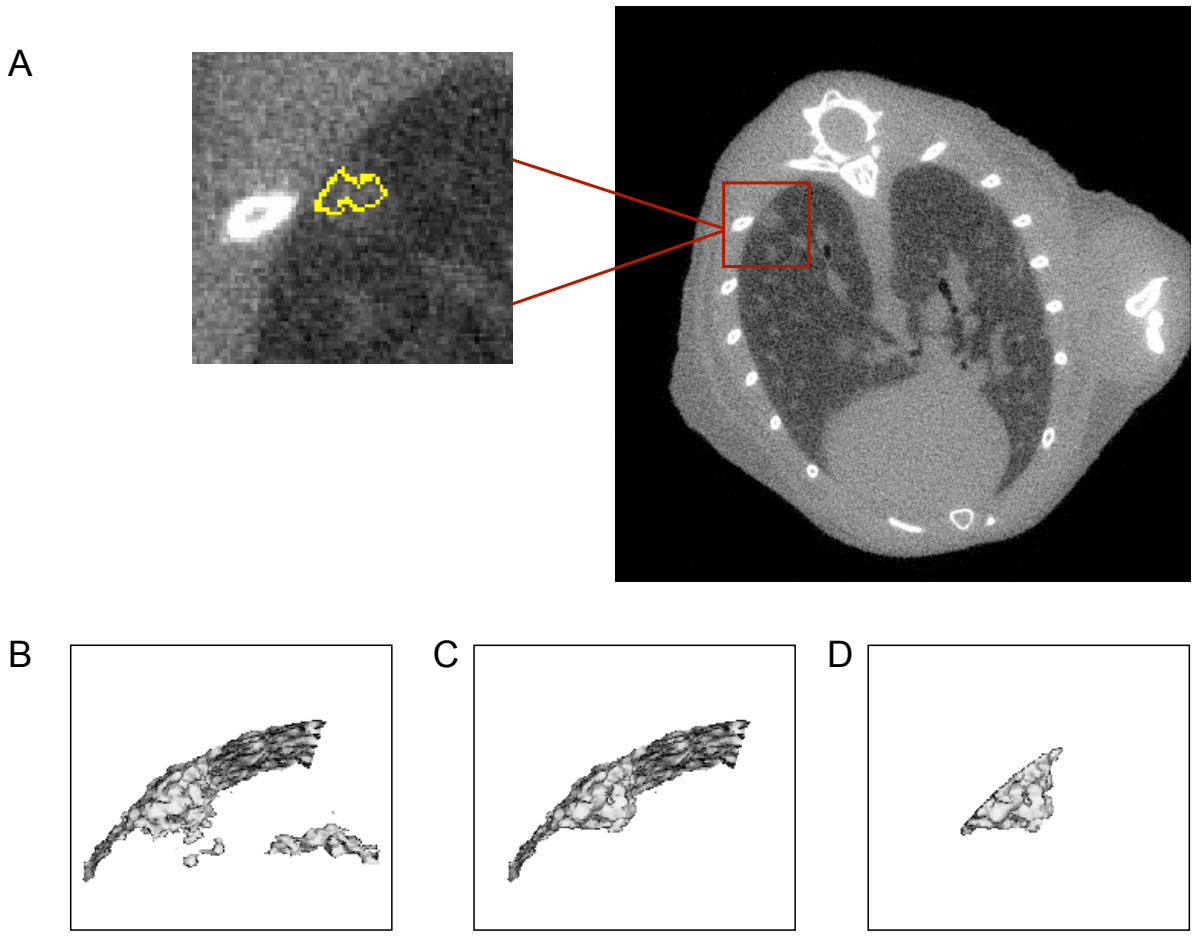

Figure 3.4. 3D visualization of the lung showing the steps of removing vessels and the chest wall from the segmented nodule. (A) Micro-CT image of a whole lung (transverse view) from an RNR transgenic mouse with a zoom-in image showing a nodule (yellow circle outlined by automated algorithm). 3D visualization of the lung from the same mouse with a nodule was created from the segmentation after (B) adaptive thresholding, (C) vessel removal, and (D) removal of the chest wall by the automated algorithm. The final result in (D) shows a successful segmentation of the nodule free of vessels and the chest wall. The 3D visualization was created based on a scan taken at 50µm with 720 projections.

and used to orient a coordinate system to simplify the calculation of the error in the estimated surface. The surface points were then mapped into this coordinate system.

To estimate the surface, a hill climbing optimization method was used to search for the best parameters of a third degree polynomial function with the goal of minimizing the error of the estimated surface to the actual surface points. However, one important task is to distinguish the points belonging to the pleural surface from the points belonging to the nodule surface or other nearby structures. This is accomplished by first using only those surface points located far from the nodule and iteratively evaluating larger subsets of surface points until there is a large change in the estimated surface. A 3D reconstruction of the nodule is shown after juxtapleural segmentation in Figure 3.4D.

3.3.3.5 Volume computation

The result of the segmentation algorithm is a binary image, with the voxels belonging to the nodule labeled as 1 and all other voxels labeled as 0. The volume is computed by summing the number of voxels in the nodule segmentation and multiplying by the voxel size. If the removal of the chest wall is not complete, which is the most common problem of a non-satisfactory segmentation, several parameters can be adjusted to change the segmentation: size of the morphological filter used for attachment removal, size of the volume of interest, and whether the nodule is juxtapleural, for nodules where the algorithm fails to correctly detect that the nodule is juxtapleural.

3.3.4 Manual tumor measurements

The growth measured by the automated algorithm was compared to the growth measured by an observer. The observer measured each tumor by selecting the axial slice through the tumor with the largest cross-sectional area and marking the largest diameter. This diameter was

converted to a volume measurement, assuming a spherical model, and this volume was compared to the volume measured by the algorithm. This closely mirrors the measurement method used in RECIST (Eisenhauer, Therasse et al. 2009).

3.3.5 Growth analysis

In this study, each mouse was scanned several times. Tumors were identified and their volumes were measured for each scan. Tumor growth can be determined from the tumor volume and time interval between scans. Exponential growth can be modeled by the following equation:

$$V_2 = V_1 e^{r\cdot(t_2 - t_1)}$$

where V_1 is the volume at time t_1, V_2 is the volume at time t_2, and r is the growth rate. After taking the natural log and rearranging the equation, we obtain the linear expression:

$$r = \frac{\ln(V_2/V_1)}{(t_2 - t_1)}$$

When we plotted ln (volume) versus time and obtained the best-fit line, the slope of the line equals *r* in the growth equation.

We calculated the tumor doubling time (DT, defined as ln2/r), as well as the growth index (GI) of tumors observed in the scans. We define GI, the percent tumor growth per month, as follows:

$$GI = 100\left[(V_2/V_1)^{(30.4375/(t_2 - t_1)} - 1\right]$$

Rearranging this equation gives a GI value that can be calculated using the slope r of the best-fit line:

$GI = 100[e^{30.4375r}-1]$

In contrast to DT where a lower value indicates faster growth, a higher GI represents faster growth. DT can be converted to GI by the following equation:

$GI = 100[2^{30.4375 / DT}-1]$

3.4 Results

In this study, we used micro-CT to monitor the progression of murine lung tumors *in vivo*. Prior to performing imaging of live animals, we first performed post-mortem imaging of nice mice, three of which had lung neoplasms, in order to optimize micro-CT methods, scan parameters, and measurement algorithms. Figure 3.5A shows the micro-CT image of the lung from a euthanized mouse scanned with 360 projections and the image was reconstructed at 50 micron resolution. The neoplasm identified in the micro-CT scan was also identified on the histological slide of the corresponding lung lobe (Figure 3.5B). The neoplasm is an adenoma, with a clear border between the solid tumor mass and the surrounding lung parenchyma. Higher magnification images of the histological section clearly showed that the tumor region is much denser than the surrounding lung parenchyma, hence the different densities of these tissues observed in micro-CT. The diameter of this tumor was measured to be 2mm at necropsy. The automated algorithm was used to measure the volume of the same tumor. The region of interest including the tumor is illustrated in Figure 3.5C, with every third image from the tumor segmentation shown. A 3D visualization of this segmented tumor was then generated with axial, sagittal and coronal views shown in Figure 3.5D. Consistent with the physical measurement at necropsy, the diameter computed by the algorithm was 1.82mm. Physical and computed measurements for three additional tumors from two tumor-bearing mice were compared and also found to be highly similar with the difference in tumor diameter between the two methods ranges from 3.8% to 32% (Table 3.2). Together, these results validate our computational methods for automated lung tumor measurement from micro-CT images of mice.

The GE eXplore CT 120 micro-CT scanner was a newly released scanner at the time of this study. Therefore we tested different scan parameters to optimize the tradeoffs between

Figure 3.5. Micro-CT and histological analyses of an RNR transgenic mouse lung tumor. (A) Micro-CT image of lung (sagittal view) from an RNR transgenic mouse with a tumor (red circle generated manually). Image was derived from a scan taken at 50μm with 220 projections. (B) Hematoxylin and eosin stained lung tissue of the same mouse (scale bar 1000μm). Normal and tumor tissues are also shown at a higher magnification (scale bar 40μm). Diameter of the tumor was measured to be 2mm at necropsy. (C) Upper panel: Several slices (every 4th slice shown) through a small region of interest including the tumor in (A). Lower panel: The same tumor separated by the automated segmentation algorithm from other soft tissue structures such as blood vessels and the chest wall. The result is shown with the tumor in red and other soft tissue structures in green. (D) A 3D visualization of the segmented tumor in (C) showing axial, sagittal, and coronal views. The volume equivalent diameter of the tumor is calculated to be 1.82 mm.

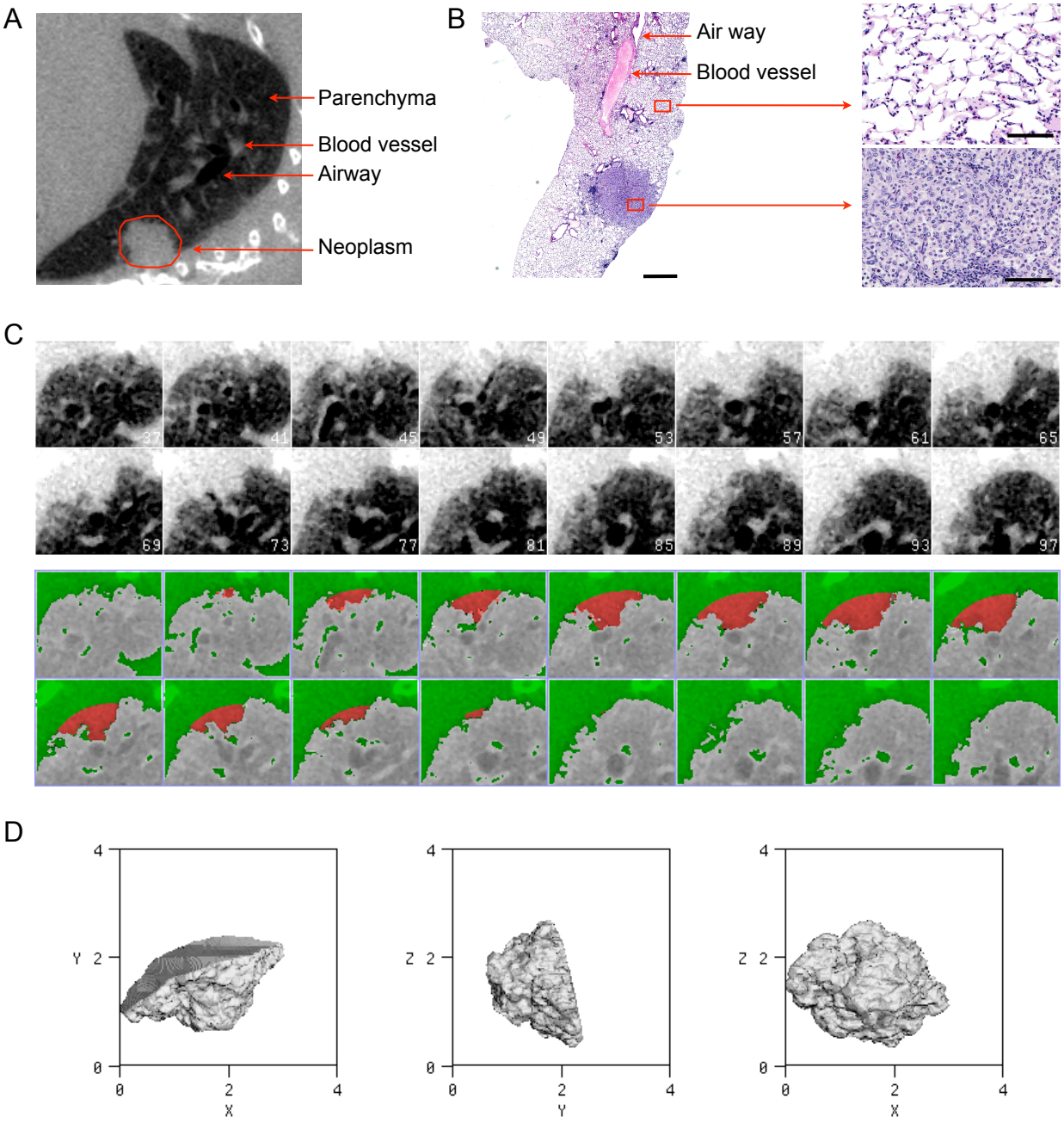
A
Parenchyma
Blood vessel
Airway
Neoplasm
B
Air way
Blood vessel
C
37
41
45
49
53
57
61
65
69
73
77
81
85
89
93
97
D
Y 2
Z 2
Z 2
X
Y
X

Table 3.2. Comparison of tumor sizes determined by physical measurement from histological slides or by automated analysis of post-mortem micro-CT scans

Mouse (tumor)	Diameter by physical measurement (mm)	Diameter by automated algorithm[a] (mm)	Percent difference between two methods
Mouse 1 (tumor A)	1.94	2.03	4.5%
Mouse 1 (tumor B)	1.89	1.82	3.8%
Mouse 2	2.60	3.02	14.9%
Mouse 3	2.39	1.73	32%

[a] The automated algorithm is not designed for diameter measurement. Rather, for ease of comparison, the volume measured by the algorithm was converted to an equivalent diameter assuming the tumor is a sphere.

speed, image quality, and radiation dosage of this particular scanner. In order to do this, one mouse was repeatedly scanned with six different sets of parameters. The noise of the scans was quantified by measuring the standard deviation of five local regions in the lung parenchyma (Table 3.1). The scan with the lowest noise was produced with the following parameters: 100 kVp, 50 mA, 360 projections, and 2 frame averaging. To increase image quality and resolution, the parameters used for subsequent live imaging were 100 kVp, 50 mA, 720 projections and 2 frame averaging with reconstruction at 50μm resolution. All live scans were acquired using these optimized parameters with the exception of two scans (Table 3.3).

Live micro-CT scanning was performed on four lung tumor-bearing mice. These mice were scanned a minimum of four times, with at least three weeks between scans. Each scan was examined to identify potential nodules. For each mouse, at least one tumor was visible in every scan over the course of the study and could be tracked sequentially for growth rate analysis. The volume of each nodule was computed by the automated algorithm at each time point and recorded for growth analysis (Figure 3.6A and Figure 3.7). Two observers independently verified the segmentation of the tumors by the algorithm.

Mice were euthanized following the last live scan, and necropsy and histological analyses were performed for further characterization of the tumors identified in micro-CT scans (Figure 3.6B, 3.6C and Figure 3.7). The growth of each nodule over time is illustrated in Figure 3.6D. In this graph, natural log of the tumor volume was plotted against time and a line of best fit was used to model the tumor measurements for each mouse. The slopes of the straight lines were then converted to growth index (GI) and tumor doubling time (DT) to indicate the growth rates of the tumors (Table 3.4). The initial tumor volume for each tumor varied from $0.050mm^3$ to $0.898mm^3$. Tumors that had smaller initial volumes tended to grow slightly faster, with the

Table 3.3. Scanner acquisition parameters used for live scans

	Current (mA)	Voltage (kVp)	Exposure Time (ms)	# of Views/scan	Frame averaging
All except	50	100	20	720	2
Mouse 1 (time point 3)	50	100	20	720	1
Mouse 2 (time point 1)	50	100	20	440	2

Figure 3.6. Sequential micro-CT scans over time to measure lung tumor growth rate in four RNR transgenic mice. (A) Micro-CT image of sequential scans of an RNR transgenic mouse (mouse #3 tumor A) (Manually generated red circle indicates the tumor). Images were acquired at 50μm with 720 projections. (B) Gross image of the lungs at necropsy showing the tumor (black arrow) after the last scan. (C) Hematoxylin and eosin stained section from lungs shown in (B) (scale bar 1000μm). Normal and tumor tissues are also shown at a higher magnification (scale bar 40μm). (D) Growth curves of lung tumors from four RNR transgenic mice. Natural log of the tumor volume was plotted against time from the first micro-CT scan. A straight line of best fit was used to model the growth of each tumor.

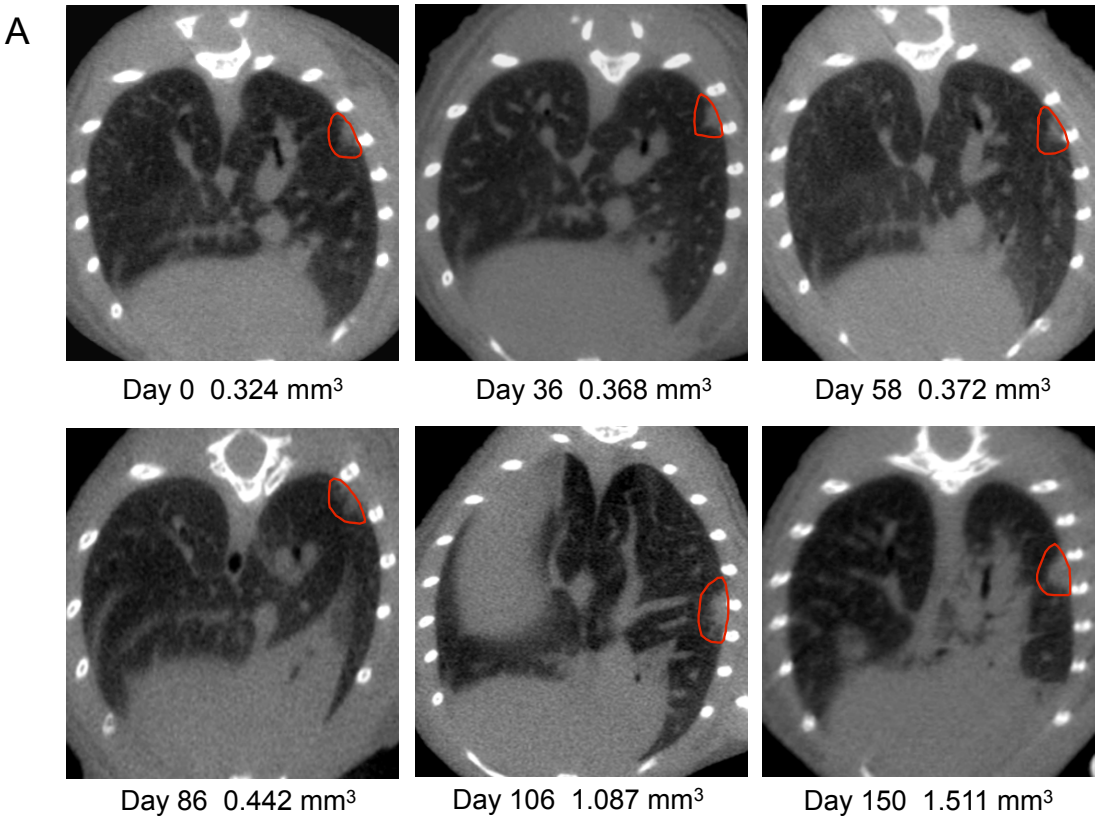
A
Day 0 0.324 mm3
Day 36 0.368 mm3
Day 58 0.372 mm3
Day 86 0.442 mm3
Day 106 1.087 mm3
Day 150 1.511 mm3
B
C
D
Ln (tumor volume) (ln mm3)
Interval (day)
mouse 1
mouse 2
mouse 3 (A)
mouse 3 (B)
mouse 4 (A)
mouse 4 (B)

Figure 3.7. Analysis of lung tumor growth in RNR transgenic mice by sequential micro-CT scanning. Micro-CT imaging was performed on RNR transgenic mice and representative 2-D micro-CT images are shown for each imaging session (A) mouse #1; (B) mouse #2; (C) mouse #3 tumor B; (D) mouse #4 tumor A; (E) mouse #4 tumor B. All images were acquired at 50μm with 720 projections. The time point of the scan and calculated tumor volume are indicated. Manually generated red outlines highlight the tumor analyzed in each image. H&E stained sections were generated for each sample following the final imaging session. Scale bar represents 1000μm.

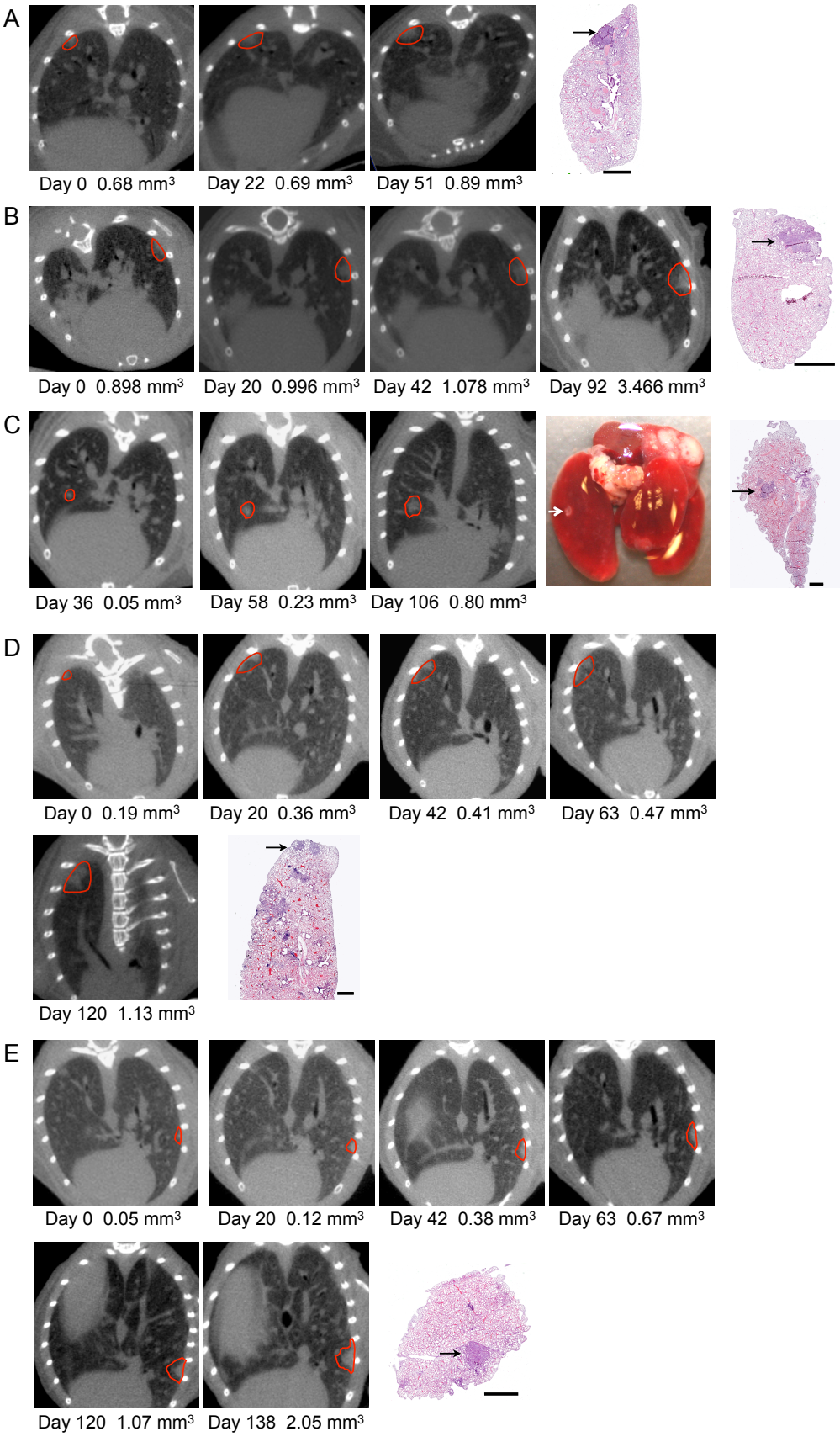
A
Day 0 0.68 mm3
Day 22 0.69 mm3
Day 51 0.89 mm3
B
Day 0 0.898 mm3
Day 20 0.996 mm3
Day 42 1.078 mm3
Day 92 3.466 mm3
C
Day 36 0.05 mm3
Day 58 0.23 mm3
Day 106 0.80 mm3
D
Day 0 0.19 mm3
Day 20 0.36 mm3
Day 42 0.41 mm3
Day 63 0.47 mm3
Day 120 1.13 mm3
E
Day 0 0.05 mm3
Day 20 0.12 mm3
Day 42 0.38 mm3
Day 63 0.67 mm3
Day 120 1.07 mm3
Day 138 2.05 mm3

Table 3.4 Tumor volume doubling time and growth index of tumors detected in RNR transgenic mice by micro-CT.

Mouse (Tumor)	Age at first scan (month)	Initial tumor volume (mm^3)	Growth curve slope	Tumor volume doubling time (=ln2/slope) (days)	Growth index [=100($e^{30.4375*slope}$-1)] (% increase per month)
1	11	0.685	0.0053	130.8	17.51
2	12	0.898	0.0151	45.90	58.35
3 (A)	12	0.324	0.0111	62.44	40.19
(B)		0.052	0.0368	18.84	206.5
4 (A)	11	0.190	0.0136	50.97	51.28
(B)		0.050	0.0237	29.25	105.7

NOTE: mice were first micro-CT scanned at the indicated age and then subjected to a series of sequential scans to monitor tumor growth. The slope of the growth curve was converted to tumor doubling time and growth index to indicate the rate of tumor growth.

exception for the tumor in mouse 2 (Table 3.4). The GI values of the tumors ranged from 17.51 to 105.7% per month.

The growth curves of the tumors in Figure 3.6D followed an exponential growth pattern, although there was deviation from a perfect exponential model. The deviation could be due to several factors. To assess whether the deviation was caused by variation from the micro-CT scanner due to alterations in calibration from scan to scan, phantoms of known density were scanned together with the mice. The intensities of the voxels within the phantom were sampled and the mean and standard deviation of the distribution was computed. Histograms for the distribution of intensities for air, water, and bone phantoms were plotted for two scans of the same mouse (Figure 3.8A and 3.8B), with the mean and standard deviations reported in Table 3.5. While the mean intensity of the air phantom did not vary much (4.2 HU difference), the means for the water and bone phantoms differed by 25.7 HU and 20.6 HU, respectively. The noise of the scans, which is quantified by the standard deviation of the distribution of pixel values in the phantoms, also differed from scan to scan. The greatest difference occurred with the air phantom, where there was a 30.9 HU difference. The difference decreased as the mean intensity increased, with the standard deviations for water and bone being 24.7 HU and 3.4 HU respectively. In addition to phantoms, we also measured the voxel intensities of the lung parenchyma and soft tissue from different scans to see whether they were consistent. Figure 3.8C and 3.8D shows the distribution of voxel intensities for the lung parenchyma and soft tissue from two different scans on the same mouse (mouse 4). The value that best separated the lung parenchyma from soft tissue varied by 35 HU from one scan to the other. These data show that alterations in calibration and tissue intensities from scan to scan can contribute to variations of the measurements and deviation from a perfect exponential growth curve.

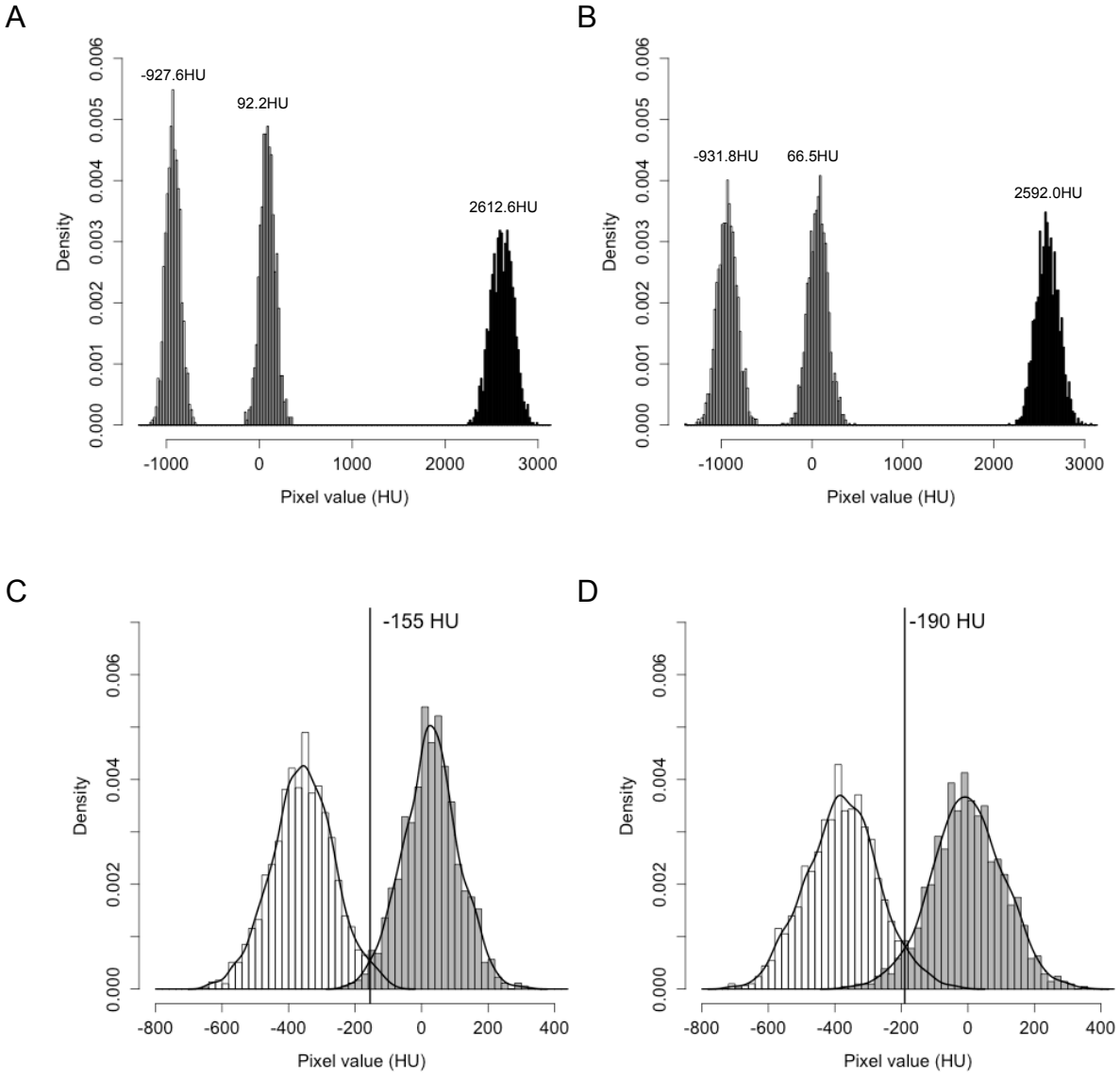

Figure 3.8. Phantoms and tissues show variation in intensities across different scans. (A) Distribution of intensities of three phantoms, air, water, and bone (left to right peaks), with mean intensities -927.6HU, 92.2HU, and 2612.6HU, respectively, in one scan. (B) Distribution of intensities of the same phantoms as in (A) in a repeated scan six weeks later with mean intensities -931.8HU, 66.5HU, and 2592.0HU, respectively. (C) Distribution of intensities in the lung parenchyma (white) and soft tissue (gray) from one mouse in one scan with an adaptive threshold at -155HU. (D) Distribution of intensities of the same tissues as in (C) of the same mouse in a repeated scan six weeks later with an adaptive threshold at -190HU. All scans were acquired at 50μm with 720 projections. Variations in the intensity distribution of the phantoms and tissues were observed in repeated scans.

Table 3.5[a]. Descriptive statistics for the intensities of the histogram plots in Figure 3.8A and 3.8B.

	Air		Water		Bone	
Scan	**Mean (HU)**	**SD (HU)**	**Mean (HU)**	**SD (HU)**	**Mean (HU)**	**SD (HU)**
Mouse 4 (Time point 2)	-927.6	77.8	92.2	82.3	2612.6	120.6
Mouse 4 (Time point 4)	-931.8	108.7	66.5	107.0	2592.0	124.0

[a] The standard deviation (SD) is a measure of the noise in the scan, with higher values indicating more noise.

Next, we investigated whether changes in the nodule morphology could contribute to variations of the measurements. We suspected that the slight variability in the position of the mouse during each scan might affect the shape of the lung, which in turn could affect the lung volume and tumor morphology. In addition, as lung tumor burden increased over time, mice at later time points sometimes had breathing problems due to disease progression. This resulted in incomplete expansion of the lung tissue during inhalation and could affect measured lung and tumor volumes. To measure whether there were changes in lung volume from scan to scan, we applied the threshold found during the adaptive thresholding step of the algorithm to the lung total area and performed morphological filtering and connected component analysis to isolate the lungs. We measured the lung volume in each scan for all the mice and found that the change from the maximum lung volume to the minimum lung volume for a mouse ranged from 28% to 61%. This suggests that changes in the lung volume and nodule morphology due to changes in mouse positions and disease burden are factors that could contribute to variations in tumor volume measurements.

Deviation from a perfect exponential growth model also could be due to inaccurate measurements by the automated algorithm, such as when it fails to separate the boundary between the nodule and its attached structures. In order to address this, we compared the tumor volumes measured by the automated algorithm with those measured manually by an observer. As shown in Figure 3.9 and Figure 3.10, even when there were differences between the absolute values measured, the two methods give very similar trends for tumor growth, indicating that the automated algorithm can separate the nodules well from attached structures and give accurate measurement of tumor volumes.

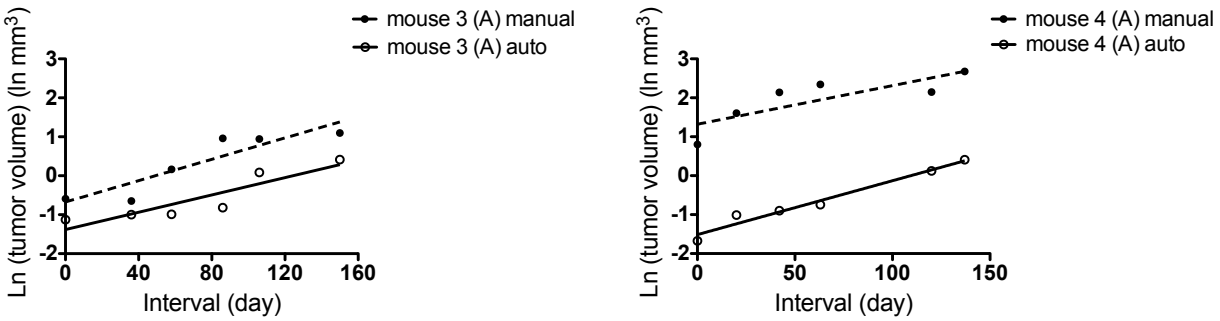

Figure 3.9. Comparison of lung tumor growth measured manually by an observer and by the automated algorithm. Growth curves were plotted for tumors from mouse 3 tumor A (left) and mouse 4 tumor A (right) based on measurements by an observer and by the automated algorithm. The slopes of the manual and automated measurements were compared by Student's t-test and no statistically significant differences were observed between the two slopes (P=0.54 for mouse 3 tumor A and P=0.32 for mouse 4 tumor A), indicating that there was good correlation between the measurements from the two methods.

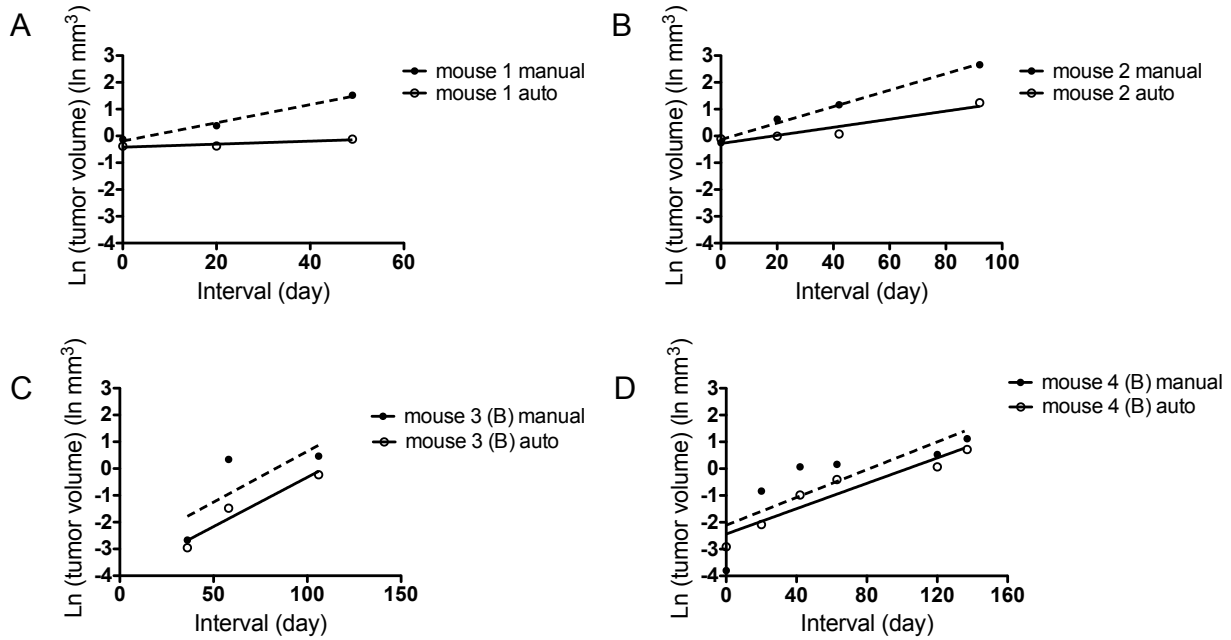

Figure 3.10. Comparison of lung tumor volume values determined manually by an observer and by the automated algorithm. Four tumor-bearing mice were subjected to sequential micro-CT imaging, and tumor volume measurements were determined manually by an observer or by the automated algorithm. (A) mouse #1, (B) mouse #2, (C) mouse #3 tumor B and (D) mouse #4 tumor B. The slopes of the manual and automated measurements were compared by Student's t-test and no statistically significant differences between the two slopes were observed for mouse 3 tumor B and mouse 4 tumor B (P=0.98 and P=0.83 respectively), indicating that there is good correlation between the measurements by the two methods. The slopes of the manual and automated measurements for mouse 1 and mouse 2 showed significant differences (P=0.024 and P=0.020 respectively). This may due to the different scan parameters used for mouse 1 (time point 3) and mouse 2 (time point 1) (see Table 3.3). In addition, for these early scans, the micro-CT machine was not calibrated for every the scan, which also may have contributed to measurement inaccuracies.

3.5 Discussion

The development of micro-CT has provided an opportunity to monitor disease progression and therapeutic responses over time in mouse models of human diseases. To take advantage of this opportunity, we developed an automated method to measure tumor volume in a mouse model of lung cancer using micro-CT scans. Prior to developing the automated algorithm, parameters used for the micro-CT scans were optimized on scans of euthanized mice. There were several trade-offs when optimizing the parameters. To obtain the highest resolution and best image quality, long time scans were required. However, we were constrained by the radiation dose that could be given to the mouse and the amount of time the mouse could be kept under anesthesia. The optimal parameters chosen in this study has the lowest noise level given the constraints of live animal scans, though the noise was still higher than what is typically obtained using low-dose whole lung human CT scans for which the algorithm was originally designed. This is due to the scale at which micro-CT operates – the image noise is inversely proportional to the spacing between the voxels, if X-ray exposure is held constant (Holdsworth and Thornton 2002). The micro-CT scans in this study were acquired with a voxel size of 0.05 mm x 0.05 mm x 0.05 mm compared to typical human CT scans of 0.6 mm x 0.6 mm x 1.0 mm. Table 3.1 shows the tested parameters in the study and the noise measurements. In general, higher voltage tended to produce less noise, and noise could be further reduced by the use of frame averaging and additional projections. Figure 3.11 shows a single snapshot of a typical low-dose human CT scan obtained from the Public Lung Database to Address Drug Response as well as a micro-CT scan obtained in this study. Visually, the micro-CT scan has a noisier appearance, as evidenced by the texture pattern of the lung parenchyma compared to that of the human CT scan (Figures 3.11C and 3.11D). The increase in noise is reflected in the histogram shown in Figure 3.11A, in which

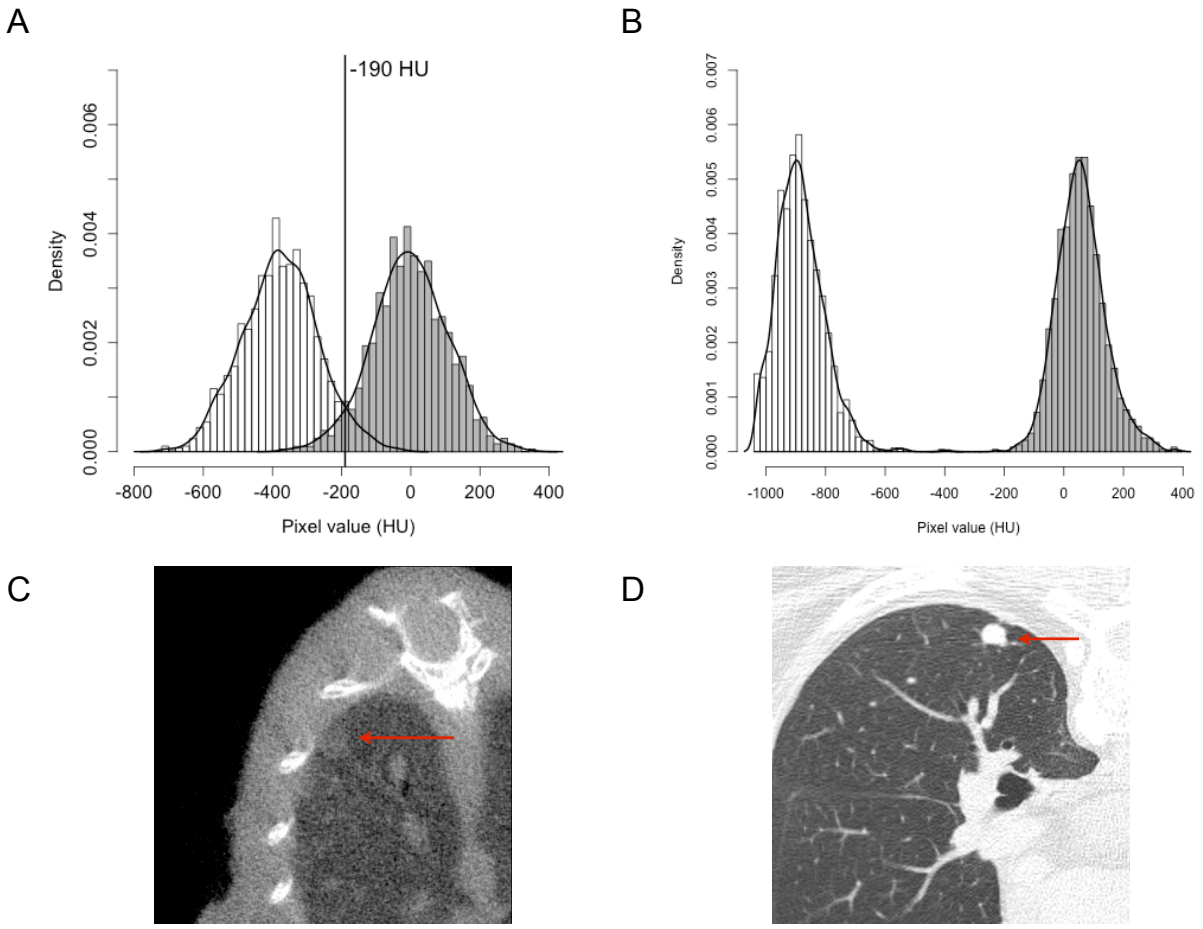

Figure 3.11. Comparison of soft tissue and lung parenchyma intensities in a micro-CT scan and a human whole lung CT scan. Distribution of intensities in the lung parenchyma (white) and soft tissue (gray) in (A) a mouse micro-CT scan with adaptive threshold of -190 HU and (B) a human whole lung CT scan with no need for adaptive threshold. The mouse micro-CT scan was obtained at 50μm with 720 projections. The human whole lung CT scan was from the Weill Cornell Medical College Lung CT database. It was obtained using a GE LightSpeed Ultra scanner at 120kVp and 80mA, with 0.7 x 0.7 x 1.25mm resolution. The peaks in (A) were not as sharp as those in (B), indicating that the mouse micro-CT scans were noisier than human CT scans. Magnified regions of the lung from (C) a micro-CT scan (yellow circle indicates tumor) and (D) a whole-lung CT scan (red arrow points to tumor) were shown to visualize the difference in scan quality. No scaling was done to the images and each image was windowed for viewing.

the micro-CT scan has much wider distribution of intensities than the human CT scan shown in Figure 3.11B. The mean and standard deviation of the distributions are given in Table 3.6. Nevertheless, the automated algorithm developed in this study is able to cope with the noise level found in micro-CT scans, as shown by the successful segmentation of tumors in Figure 3.5D.

The growth curves of the tumors followed an exponential pattern, which is consistent with modeling of tumor growth patterns for human lung cancer (Schwartz 1961; Spratt, Meyer et al. 1995). It is also consistent with a recent CT study that shows exponential growth in early stage pancreatic cancers (Haeno, Gonen et al. 2012). Therefore, the exponential growth model of lung tumors is validated for mice *in vivo* and can be used in tumor measurement algorithms to monitor disease progression and therapeutic responses. However, the growth curves obtained in this study showed deviations from an ideal exponential model, although it remains unknown whether this accurately reflects the actual growth behavior of the tumors. We showed that alterations in scanner calibration and changes in mouse lung volumes are factors that could contribute to this deviation, while inaccuracy of the automated algorithm appears to play less of a role.

One characteristic of CT is that the scale is calibrated. Air has a density of -1000 HU and water has a density of 0 HU. Thus, materials of the same density should have a consistent intensity on a CT scan, both across time and instruments. This allows for the use of a fixed threshold to separate different tissue types, in this case for the lung parenchyma and soft tissue. However, in this study, we found up to a 26 HU difference in the mean intensity of the same phantom imaged at different times and up to a 30 HU difference in the standard deviation, indicating inconsistencies in calibration and noise characteristics for the scanner. As a result, instead of a fixed threshold, an adaptive threshold estimated from the local region of interest was

Table 3.6[a]. Descriptive statistics for the intensities of the histogram plots in Figure 3.11.

	Parenchyma		Soft tissue	
	Mean	SD	Mean	SD
Micro-CT	-376.9	110.2	-1.6	109.4
Human CT	-883.8	79.0	57.9	82.3

[a] The standard deviation (SD) is a measure of the noise in the scan, with higher values indicating more noise.

used. These findings additionally suggest that the micro-CT scanner should be calibrated prior to each scan using density phantoms that expand the entire range of densities to be observed in the scan.

We also observed changes in lung volume between scans for individual mice. The lung volume of the same mouse varied up to 60% from one scan to another. Slight differences in mouse positioning between scans could contribute to observed differences in lung volume. In addition, as lung disease progressed, the increased tumor burden resulted in reduced respiratory capacity, which might be another factor contributing to changes in observed lung volume. Furthermore, in order for the mouse to activate the pressure sensor used for respiratory gating during live scans, a small external force was applied on the back of the mouse, which could lead to slight compression of the lungs. An alternative method for respiratory gating is to use a ventilator to control the respiratory cycle of the mouse. This would eliminate the need for a pressure sensor and provide better control of the degree and rate of inspiration.

To verify that measurement accuracy of the automated algorithm does not significantly contribute to deviations from the ideal exponential growth model, an observer performed manual uni-dimensional measurements for all the tumors from all scans. Although the absolute tumor volumes were likely to be different between the manual and automated methods, of greater importance was that the growth patterns determined by the two methods were very similar. As shown in Figures 3.9 and 3.10, a similar trend indicted that the measured exponential growth was the result of actual changes in nodule volume and not the inaccuracy of the measuring method. The manual measurements of the tumor volume tended to be larger than those of the automated measurements. This is because the manual measurements assume a spherical shape for the tumor and use the uni-dimensional measurement of the longest diameter to calculate tumor volume. For

non-spherical shapes, this tends to exaggerate the volume compared to the automated method that measures the volume directly. There were only two measurements where the manual uni-dimensional volume was smaller than the volume measured by the algorithm. These nodules were both very small (0.5 mm and 1.2 mm in diameter) and may not be accurately measured manually. The automated algorithm does have one limitation in terms of segmenting tumors that have complicated morphology. One assumption made during the development of the algorithm was that the tumor would only touch the outer chest wall. As a result, tumors located in the lower lung near the diaphragm and touching both the chest wall and the diaphragm could not be successfully segmented (Figure 3.12).

The neoplasms analyzed in this study were all adenomas. The growth index (GI) values for these tumors ranged from 17.51 to 105.7% per month, which is much greater than the GI of 5.4% per month reported for human lung tumors (Yankelevitz, Reeves et al. 2000), indicating that the murine tumors grow faster. This likely is due to the fact that the tumors in mice were detected at an early stage when they experience preferential growth conditions relative to larger human tumors, including greater nutrient access, oxygenation and less spatial constraint. For the same reason, tumors with smaller initial volumes in this study tended to grow faster. In support of this, Haeno *et al.* (Haeno, Gonen et al. 2012) reported in their study that primary pancreatic tumors that were larger at diagnosis grew slower. The tumor in mouse 2 was an exception in our study, as it had a bigger initial volume and also grew faster than some of the smaller neoplasms. This may be because this tumor appeared to be at a more advanced stage, as evidenced histologically by the lack of a well-defined boundary (Figure 3.7B). Tumor volume doubling time (VDT) for the tumors analyzed in this study ranged from 29.25 to 130.8 days (Table 3.4) with an average of 70.8 days. Oliver *et al.* (Oliver, Mercer et al.) reported an average mouse lung

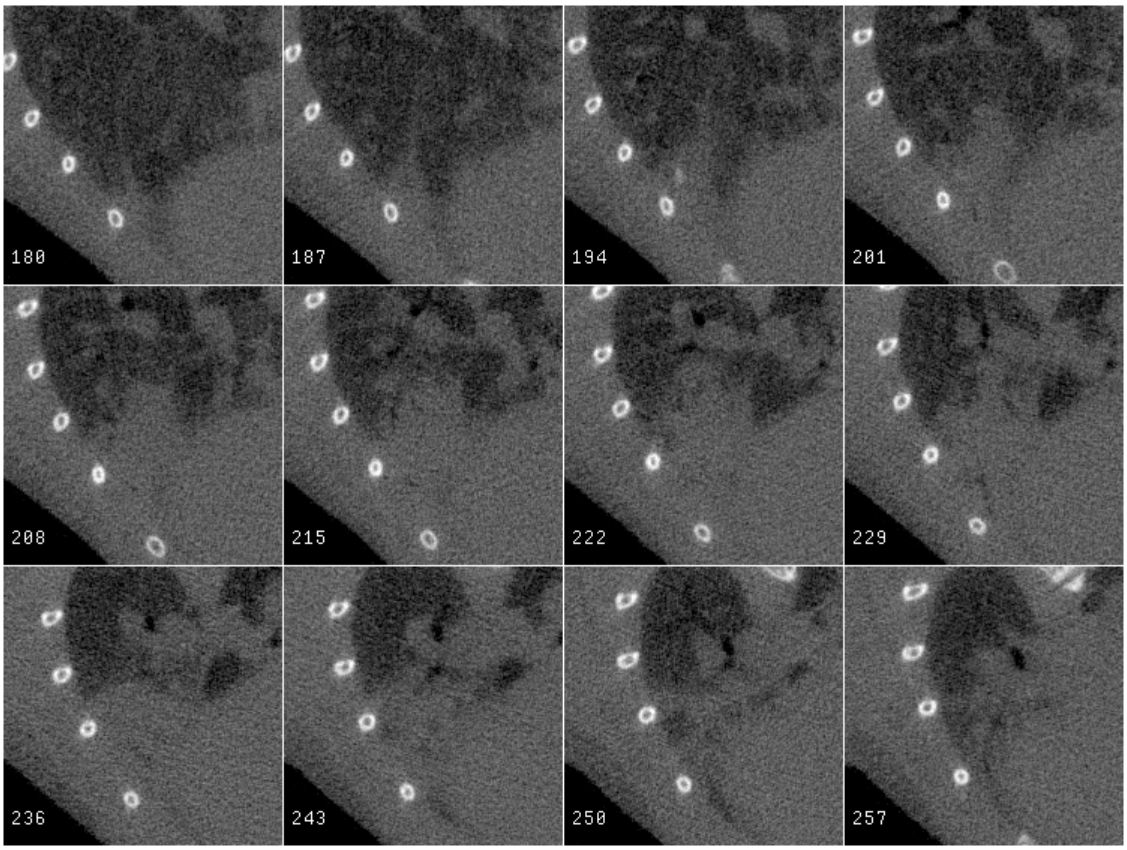

Figure 3.12. Representative micro-CT images showing a nodule that is attached to both the chest wall and diaphragm. Micro-CT images of a nodule from mouse #3 that abuts the chest wall and diaphragm are shown. This nodule could not be successfully segmented by the automated algorithm because it violates the assumption of the algorithm that the nodule can only have one major attachment. These images were windowed to enhance the contrast for viewing and representative segmentations that are seven slices apart are shown. This scan was acquired at 50μm with 720 projections.

tumor VDT of 35 days (with high variation). Haines *et al.* (Haines, Bettano et al. 2009) and Fushiki *et al.* (Fushiki, Kanoh-Azuma et al. 2009) showed an average VDT for murine lung tumors of around 42 days. These values are within the range of our tumor VDT and are comparable to our average number. These studies all used the K-as$^{LSL-G12D}$ mouse model, where the activation of the oncogene K-ras is induced by Adeno-Cre virus infection (Jackson, Willis et al. 2001). In comparison, the mouse model used in this study develops lung tumors through a stochastic process associated with mutations in the K-ras oncogene. The different mouse models used may contribute to the observed difference in the average tumor VDT. Moreover, a recent study in human lung cancer patients revealed an average tumor VDT of 136 days for 111 lung cancer cases (Henschke, Yankelevitz et al. 2012). 110 of the 111 cases had lung tumors diagnosed at screening rather than by symptoms, suggesting that the average VDT of 136 days reflects tumor growth at an early stage and therefore is comparable to the average VDT of 70.8 days in our mouse model.

The automated pulmonary nodule segmentation algorithm for measuring murine tumors imaged by micro-CT reported here was capable of accurate measurements of tumor volumes and was used to monitor disease progression over time. Tumor volume measurements from micro-CT have the potential to be used as an imaging biomarker in preclinical studies. With future improvements to handle nodules with more difficult morphology this automated algorithm holds promise for use in monitoring disease progression following treatment with candidate drugs and evaluation of therapeutic responses.

3.6 Acknowledgements

This research was funded by NIH grant R01 CA108773 (RSW) and an Innovation Grant from the Cornell University Institute for Biotechnology & Life Science Technologies (RSW and APR). The authors additionally thank the Cornell University Center for Vertebrate Genomics for supporting the purchase of anesthesia equipment and the micro-CT instrument. Minxing Li coordinated this study and contributed to animal maintenance, live mice scanning, micro-CT data collection and post-mortem tumor analysis. Artit Jirapatnakul contributed to automated algorithm development, phantom analysis and lung tumor volume measurements. Both contributed to text writing, figure preparation and data analysis.

CHAPTER 4 Summary and Future Directions

4.1 RNR deregulation, ROS imbalance and genome instability

Ribonucleotide reductase (RNR) plays an essential role in organismal survival and genome maintenance by providing dNTPs for DNA synthesis. Deregulation of RNR has been shown to cause mutagenesis and tumorigenesis. A major focus of the mechanism of RNR-induced mutagenesis is on how RNR deregulation affects the dNTP pool balance. As an enzyme that produces free radicals during its catalytic cycle, the effect of RNR deregulation on the redox homeostasis in cells is less well studied. The first part of this dissertation (chapter two) was aiming to elucidate the effect of RNR deregulation on cellular redox status.

In order to do this, we generated 3T3 cells that overexpress Rrm1, Rrm2 and p53R2 and showed that expression of the small subunits Rrm2 and p53R2 lead to elevated reactive oxygen species (ROS) in cells. By generating a series of Rrm2 mutants, we demonstrated that the di-nuclear iron center of Rrm2 contributes to increased ROS while the radical transfer pathway has no effect on ROS production. In addition, some of the Rrm2 mutants have dominant negative effects in cells, leading to mitochondrial DNA depletion and mitochondrial redox imbalance. These findings indicate the importance of RNR regulation in maintaining cellular ROS levels and suggest the possibility that R2-induced ROS may play a role in mutagenesis and tumorigenesis.

With the panel of Rrm2 mutants generated in this study, we are able to investigate whether R2-induced ROS plays a direct role in mutagenesis (Figure 4.1). By comparing the mutation frequency in the three groups of Rrm2 proteins, if Rrm2-radical transfer mutants show increased mutation frequency while Rrm2-iron mutant does not, we can conclude that R2 can lead to mutagenesis through ROS production independent of RNR enzyme activity.

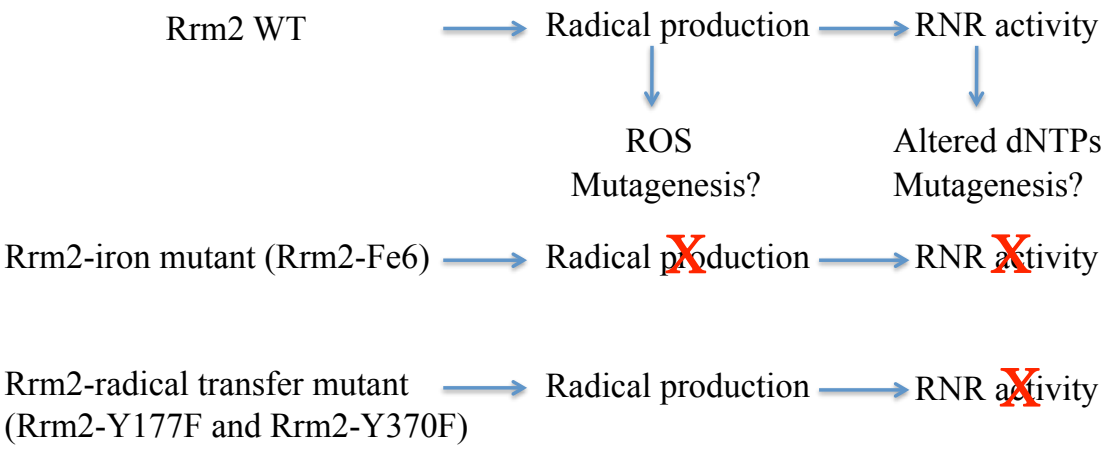

Figure 4.1 Rrm2 mutants in studying the role of ROS in mutagenesis. Cells overexpressing WT Rrm2 have increased mutation frequency, which could result from increased enzyme activity and/or free radical production. Comparing the mutation frequency in Rrm2-Fe6 and Rrm2-Y177F/Rrm2-Y370F can tell us whether ROS plays a direct role in Rrm2-induced mutagenesis.

One important question we want to address is the molecular mechanism of R2-induced mutagenesis and lung tumorigenesis in mice. In this study, we showed that Rrm2 overexpression in cells leads to increased RNR enzyme activity and elevated ROS production, both of which could be mutagenic. However, dNTP measurements using Rrm2 overexpressing lung and 3T3 cells didn't show significant change, suggesting that increased RNR enzyme activity may not cause dNTP alterations due to the multilayered regulation of RNR *in vivo*. Alternatively, it could be that the method used to measure dNTP is not sensitive enough to detect small overall or local changes. On the other hand, R2 overexpression in cells leads to increased ROS. It would be very interesting to look at whether this increased ROS leads to oxidative stress and mutagenesis in cells. Oxidative stress can be addressed by measuring the levels of 8-oxoG (a major DNA oxidation product) and mutation frequency can be studied by HPRT assay. It is important to keep in mind that these two different mutagenic mechanisms of RNR may not be mutually exclusive. Instead, both may contribute to mutation accumulation and lead to tumorigenesis (Figure 4.2).

In this study, we provided some evidence on RNR deregulation and ROS imbalance. In fact, there are a lot more to explore in this direction. For example, we can measure ROS levels in lung tissues from R2 transgenic mice. ROS levels in tumor tissues (with different tumor stages) and adjacent normal lung tissues can be measured and compared. This would give us a more direct look at ROS in lung tumor initiation and progression. On the other hand, R2 overexpressing cells and R2 transgenic mice can be treated with antioxidant such as N-Acetyl Cysteine (NAC) and see whether this brings down the ROS levels and decreases mutation frequency and lung tumor incidences. It is also worth investigating the antioxidant defense systems, including the levels and dynamics of superoxide dismutase, catalase and glutathione/glutathione peroxidase in R2 overexpressing cells and R2 transgenic mice.

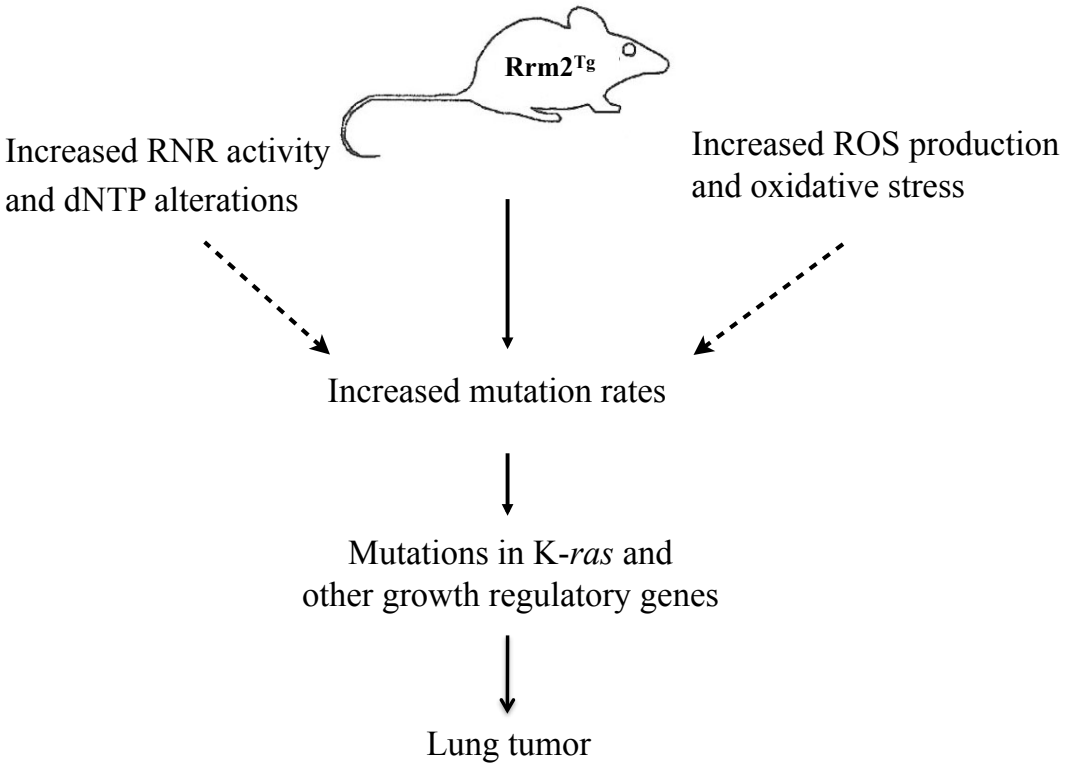

Figure 4.2 Model of the molecular mechanism of RNR-induced lung tumorigenesis. Overexpression of Rrm2 can lead to increased enzyme activity and ROS production in cells, both of which could be mutagenic and contribute to mutagenesis and tumorigenesis.

Furthermore, since misincorporation of 8-oxoG into DNA is primarily repaired by the base excision repair pathway (Robertson, Klungland et al. 2009), R2 transgenic mice can be bred with mice that are defective for base excision repair and see whether this leads to synergistic acceleration of tumorigenesis.

Another research area that worth looking into is RNR deregulation and mitochondrial function. p53R2 mutations have been identified in several human mitochondrial diseases and have been shown to cause mtDNA depletion ((Bourdon, Minai et al. 2007; Kollberg, Darin et al. 2009; Shaibani, Shchelochkov et al. 2009). It would be interesting to obtain patient cell lines and/or make clones of these p53R2 mutants and study their effect on mitochondrial function. For example, we can examine whether mtDNA depletion in these cells leads to respiratory defects and mitochondrial ROS imbalance, and whether this increase in ROS further leads to oxidative damage in cells (a vicious cycle). We can introduce WT p53R2/Rrm2 back to these mutant cells and see whether mtDNA depletion and mitochondrial ROS imbalance can be rescued.

Reactive oxygen species (ROS) are important cell signaling molecules and it is important to maintain their homeostasis. Increased ROS production and subsequent oxidative stress has been associated with many disease conditions, but their exact roles are still not clear. It remains puzzling whether ROS or disease comes first, whether ROS is required for disease initiation or it potentiates disease progression, and whether ROS can be exploited therapeutically. Recently, there is more discussion on targeting ROS and their downstream pathways in cancer cells (Trachootham, Alexandre et al. 2009; Raj, Ide et al. 2011). However, the study of ROS is difficult due to their numerous roles in cellular processes and their labile nature. Advances in understanding ROS biology require methodology that can accurately monitor cellular ROS

concentrations. With the development of biological assays, we hope to further elucidate the relationship between ROS and diseases.

4.2 RNR mouse model of lung cancer and translational imaging studies

R2 transgenic mice develop lung tumors that histopathologically resemble human papillary adenocarcinomas (Xu, Page et al. 2008) and therefore can be used as an authentic lung tumor model in translational studies. Lung caner has high mortality rate and this is largely due to the fact that the tumors are often detected at late and advanced stages where treatments are rarely effective. Therefore, early detection of lung cancer is critical for improving survival of this disease. The second part of this dissertation (chapter 3) was aiming to improve early lung tumor detection and study lung tumor growth rate by micro-computed tomography (micro-CT) using R2 transgenic mice as a model.

In order to do this, we adapted an automated algorithm from tools for the measurement of pulmonary nodules on human chest CT scans and used it to measure mouse lung tumors. Euthanized mice were first imaged to optimize scan parameters and refine computational algorithms for tumor volume measurement. Four live lung tumor-bearing mice were then scanned sequentially for tumor growth rate determination. Findings from this study establish automated algorithms to measure early stage lung tumor and confirm the exponential lung tumor growth model in humans.

As a good lung tumor model in imaging studies, R2 transgenic mice can be used to explore more imaging options. Positron emission tomography (PET) is a noninvasive, three-dimensional imaging technique that depicts physiologic processes. Recently, PET and CT have been combined (PET/CT) in a single scanner where metabolic and anatomic information can be revealed simultaneously (Bybel, Brunken et al. 2006). Different PET tracers can be used to

depict specific physiologic processes. Since tumor cells metabolize glucose at a high rate (Warburg 1956), a glucose analogue [18F] fluorodeoxyglucose (FDG) has been used in PET/CT to diagnose and stage neoplasms such as lung cancers (Bruzzi and Munden 2006). Besides [18F] FDG, other tracers have been proposed to monitor different physiologic processes in tumor development such as [18F] Fluorothymidine in cell proliferation, [18F] Fluoromisonidazole in tumor hypoxia and [18F] Arginine glycine aspartic acid in angiogenesis (Bybel, Brunken et al. 2006). Studies in small animal models would be extremely helpful to test these tracers and establish working protocols that can be applied to humans. In this context, our R2 mice can serve as a great model to study non-small cell lung cancer (NSCLC) in PET/CT imaging. In addition to tumor diagnosis and staging, PET/CT can also be used to test drug efficacy. For instance, R2 mice can be treated with anticancer drugs and tumor sizes and metabolism can be monitored by PET/CT scanning on a regular basis. A reduction in tumor size and metabolic activity would be an indication of effective treatment and better survival.

The use of PET/CT imaging brings both refinements and greater complexity in tumor imaging. Interpretation of PET/CT images requires multidisciplinary collaboration between oncologists, basic researchers, radiologists and engineers. By using R2 mice as a model of NSCLC for imaging, we can help improve tumor diagnosis and staging, as well as protocols and algorithms used in tumor measurements and quantifications.

REFERENCES

Akerblom, L., A. Ehrenberg, et al. (1981). "Overproduction of the free radical of ribonucleotide reductase in hydroxyurea-resistant mouse fibroblast 3T6 cells." Proceedings of the National Academy of Sciences of the United States of America **78**(4): 2159-2163.

Akita, H., Z. Zheng, et al. (2009). "Significance of RRM1 and ERCC1 expression in resectable pancreatic adenocarcinoma." Oncogene **28**(32): 2903-2909.

Arner, E. S. and S. Eriksson (1995). "Mammalian deoxyribonucleoside kinases." Pharmacology & therapeutics **67**(2): 155-186.

Aye, Y., E. J. Brignole, et al. (2012). "Clofarabine targets the large subunit (alpha) of human ribonucleotide reductase in live cells by assembly into persistent hexamers." Chemistry & biology **19**(7): 799-805.

Aye, Y., M. J. Long, et al. (2012). "Mechanistic Studies of Semicarbazone Triapine Targeting Human Ribonucleotide Reductase in Vitro and in Mammalian Cells: TYROSYL RADICAL QUENCHING NOT INVOLVING REACTIVE OXYGEN SPECIES." The Journal of biological chemistry **287**(42): 35768-35778.

Aye, Y. and J. Stubbe (2011). "Clofarabine 5'-di and -triphosphates inhibit human ribonucleotide reductase by altering the quaternary structure of its large subunit." Proceedings of the National Academy of Sciences of the United States of America **108**(24): 9815-9820.

Baldauf, H. M., X. Pan, et al. (2012). "SAMHD1 restricts HIV-1 infection in resting CD4(+) T cells." Nature medicine **18**(11): 1682-1689.

Bebenek, K., J. D. Roberts, et al. (1992). "The effects of dNTP pool imbalances on frameshift fidelity during DNA replication." The Journal of biological chemistry **267**(6): 3589-3596.

Bennett, C. N., C. C. Tomlinson, et al. (2012). "Cross-species genomic and functional analyses identify a combination therapy using a CHK1 inhibitor and a ribonucleotide reductase inhibitor to treat triple-negative breast cancer." Breast cancer research : BCR **14**(4): R109.

Bepler, G., I. Kusmartseva, et al. (2006). "RRM1 modulated in vitro and in vivo efficacy of gemcitabine and platinum in non-small-cell lung cancer." Journal of clinical oncology : official journal of the American Society of Clinical Oncology **24**(29): 4731-4737.

Bepler, G., S. Sharma, et al. (2004). "RRM1 and PTEN as prognostic parameters for overall and disease-free survival in patients with non-small-cell lung cancer." Journal of clinical oncology : official journal of the American Society of Clinical Oncology **22**(10): 1878-1885.

Bergman, A. M., P. P. Eijk, et al. (2005). "In vivo induction of resistance to gemcitabine results in increased expression of ribonucleotide reductase subunit M1 as the major determinant." Cancer research **65**(20): 9510-9516.

Bester, A. C., M. Roniger, et al. (2011). "Nucleotide deficiency promotes genomic instability in early stages of cancer development." Cell **145**(3): 435-446.

Bjorklund, S., S. Skog, et al. (1990). "S-phase-specific expression of mammalian ribonucleotide reductase R1 and R2 subunit mRNAs." Biochemistry **29**(23): 5452-5458.

Block, K. and Y. Gorin (2012). "Aiding and abetting roles of NOX oxidases in cellular transformation." Nature reviews. Cancer **12**(9): 627-637.

Bouffard, D. Y., J. Laliberte, et al. (1993). "Kinetic studies on 2',2'-difluorodeoxycytidine (Gemcitabine) with purified human deoxycytidine kinase and cytidine deaminase." Biochemical pharmacology **45**(9): 1857-1861.

Bourdon, A., L. Minai, et al. (2007). "Mutation of RRM2B, encoding p53-controlled

ribonucleotide reductase (p53R2), causes severe mitochondrial DNA depletion." Nature genetics **39**(6): 776-780.

Bradley, M. O. and N. A. Sharkey (1978). "Mutagenicity of thymidine to cultured Chinese hamster cells." Nature **274**(5671): 607-608.

Bristow, R. G. and R. P. Hill (2008). "Hypoxia and metabolism. Hypoxia, DNA repair and genetic instability." Nature reviews. Cancer **8**(3): 180-192.

Bruzzi, J. F. and R. F. Munden (2006). "PET/CT imaging of lung cancer." Journal of thoracic imaging **21**(2): 123-136.

Burkhalter, M. D., S. A. Roberts, et al. (2009). "Activity of ribonucleotide reductase helps determine how cells repair DNA double strand breaks." DNA repair **8**(11): 1258-1263.

Buss, J. L., B. T. Greene, et al. (2004). "Iron chelators in cancer chemotherapy." Current topics in medicinal chemistry **4**(15): 1623-1635.

Bybel, B., R. C. Brunken, et al. (2006). "PET and PET/CT imaging: what clinicians need to know." Cleveland Clinic journal of medicine **73**(12): 1075-1087.

Caras, I. W. and D. W. Martin, Jr. (1988). "Molecular cloning of the cDNA for a mutant mouse ribonucleotide reductase M1 that produces a dominant mutator phenotype in mammalian cells." Molecular and cellular biology **8**(7): 2698-2704.

Cavanaugh, D., D. D. Cody, et al. (2004). "In vivo respiratory-gated micro-CT imaging in small-animal oncology models." Mol Imaging **3**: 55-62.

Ceppi, P., M. Volante, et al. (2006). "ERCC1 and RRM1 gene expressions but not EGFR are predictive of shorter survival in advanced non-small-cell lung cancer treated with cisplatin and

gemcitabine." Annals of oncology : official journal of the European Society for Medical Oncology / ESMO **17**(12): 1818-1825.

Chabes, A., B. Georgieva, et al. (2003). "Survival of DNA damage in yeast directly depends on increased dNTP levels allowed by relaxed feedback inhibition of ribonucleotide reductase." Cell **112**(3): 391-401.

Chabes, A. and B. Stillman (2007). "Constitutively high dNTP concentration inhibits cell cycle progression and the DNA damage checkpoint in yeast Saccharomyces cerevisiae." Proceedings of the National Academy of Sciences of the United States of America **104**(4): 1183-1188.

Chabes, A. and L. Thelander (2000). "Controlled protein degradation regulates ribonucleotide reductase activity in proliferating mammalian cells during the normal cell cycle and in response to DNA damage and replication blocks." The Journal of biological chemistry **275**(23): 17747-17753.

Chabes, A. L., S. Bjorklund, et al. (2004). "S Phase-specific transcription of the mouse ribonucleotide reductase R2 gene requires both a proximal repressive E2F-binding site and an upstream promoter activating region." The Journal of biological chemistry **279**(11): 10796-10807.

Chabes, A. L., C. M. Pfleger, et al. (2003). "Mouse ribonucleotide reductase R2 protein: a new target for anaphase-promoting complex-Cdh1-mediated proteolysis." Proceedings of the National Academy of Sciences of the United States of America **100**(7): 3925-3929.

Chang, L., B. Zhou, et al. (2008). "ATM-mediated serine 72 phosphorylation stabilizes ribonucleotide reductase small subunit p53R2 protein against MDM2 to DNA damage." Proceedings of the National Academy of Sciences of the United States of America **105**(47): 18519-18524.

Chomyn, A. and G. Attardi (2003). "MtDNA mutations in aging and apoptosis." Biochemical and biophysical research communications **304**(3): 519-529.

Climent, I., B. M. Sjoberg, et al. (1992). "Site-directed mutagenesis and deletion of the carboxyl terminus of Escherichia coli ribonucleotide reductase protein R2. Effects on catalytic activity and subunit interaction." Biochemistry **31**(20): 4801-4807.

Cody, D. D., C. L. Nelson, et al. (2005). "Murine lung tumor measurement using respiratory-gated micro-computed tomography." Investigative radiology **40**: 263-269.

D'Angiolella, V., V. Donato, et al. (2012). "Cyclin F-mediated degradation of ribonucleotide reductase M2 controls genome integrity and DNA repair." Cell **149**(5): 1023-1034.

Davidson, J. D., L. Ma, et al. (2004). "An increase in the expression of ribonucleotide reductase large subunit 1 is associated with gemcitabine resistance in non-small cell lung cancer cell lines." Cancer research **64**(11): 3761-3766.

Deng, Z. L., D. W. Xie, et al. (2005). "Novel genetic variations of the p53R2 gene in patients with colorectal adenoma and controls." World journal of gastroenterology : WJG **11**(33): 5169-5173.

Dolado, I., A. Swat, et al. (2007). "p38alpha MAP kinase as a sensor of reactive oxygen species in tumorigenesis." Cancer cell **11**(2): 191-205.

Domkin, V., L. Thelander, et al. (2002). "Yeast DNA damage-inducible Rnr3 has a very low catalytic activity strongly stimulated after the formation of a cross-talking Rnr1/Rnr3 complex." The Journal of biological chemistry **277**(21): 18574-18578.

Drane, P., A. Bravard, et al. (2001). "Reciprocal down-regulation of p53 and SOD2 gene expression-implication in p53 mediated apoptosis." Oncogene **20**(4): 430-439.

Droge, W. (2002). "Free radicals in the physiological control of cell function." Physiological reviews **82**(1): 47-95.

Duxbury, M. S., H. Ito, et al. (2004). "Retrovirally mediated RNA interference targeting the M2 subunit of ribonucleotide reductase: A novel therapeutic strategy in pancreatic cancer." Surgery **136**(2): 261-269.

Edelmann, W., K. Yang, et al. (1997). "Mutation in the mismatch repair gene Msh6 causes cancer susceptibility." Cell **91**(4): 467-477.

Ehrhardt, C., M. Schmolke, et al. (2006). "Polyethylenimine, a cost-effective transfection reagent." Signal Transduction **6**(3): 179-184.

Eisenhauer, E. A., P. Therasse, et al. (2009). "New response evaluation criteria in solid tumours: revised RECIST guideline (version 1.1)." European journal of cancer (Oxford, England : 1990) **45**: 228-247.

Eklund, H., U. Uhlin, et al. (2001). "Structure and function of the radical enzyme ribonucleotide reductase." Progress in biophysics and molecular biology **77**(3): 177-268.

Elford, H. L., M. Freese, et al. (1970). "Ribonucleotide reductase and cell proliferation. I. Variations of ribonucleotide reductase activity with tumor growth rate in a series of rat hepatomas." The Journal of biological chemistry **245**(20): 5228-5233.

Elledge, S. J., Z. Zhou, et al. (1993). "DNA damage and cell cycle regulation of ribonucleotide reductase." BioEssays : news and reviews in molecular, cellular and developmental biology **15**(5): 333-339.

Engstrom, Y., S. Eriksson, et al. (1985). "Cell cycle-dependent expression of mammalian ribonucleotide reductase. Differential regulation of the two subunits." The Journal of biological

chemistry **260**(16): 9114-9116.

Engstrom, Y. and B. Rozell (1988). "Immunocytochemical evidence for the cytoplasmic localization and differential expression during the cell cycle of the M1 and M2 subunits of mammalian ribonucleotide reductase." The EMBO journal **7**(6): 1615-1620.

Eriksson, S., A. Graslund, et al. (1984). "Cell cycle-dependent regulation of mammalian ribonucleotide reductase. The S phase-correlated increase in subunit M2 is regulated by de novo protein synthesis." The Journal of biological chemistry **259**(19): 11695-11700.

Fairman, J. W., S. R. Wijerathna, et al. (2011). "Structural basis for allosteric regulation of human ribonucleotide reductase by nucleotide-induced oligomerization." Nature structural & molecular biology **18**(3): 316-322.

Fan, H., A. Huang, et al. (1997). "The R1 component of mammalian ribonucleotide reductase has malignancy-suppressing activity as demonstrated by gene transfer experiments." Proceedings of the National Academy of Sciences of the United States of America **94**(24): 13181-13186.

Fan, H., C. Villegas, et al. (1998). "The mammalian ribonucleotide reductase R2 component cooperates with a variety of oncogenes in mechanisms of cellular transformation." Cancer research **58**(8): 1650-1653.

Fan, H., C. Villegas, et al. (1996). "Ribonucleotide reductase R2 component is a novel malignancy determinant that cooperates with activated oncogenes to determine transformation and malignant potential." Proceedings of the National Academy of Sciences of the United States of America **93**(24): 14036-14040.

Fasullo, M., O. Tsaponina, et al. (2010). "Elevated dNTP levels suppress hyper-recombination in Saccharomyces cerevisiae S-phase checkpoint mutants." Nucleic acids research **38**(4): 1195-1203.

Feig, D. I., T. M. Reid, et al. (1994). "Reactive oxygen species in tumorigenesis." Cancer research **54**(7 Suppl): 1890s-1894s.

Ferraro, P., E. Franzolin, et al. (2010). "Quantitation of cellular deoxynucleoside triphosphates." Nucleic acids research **38**(6): e85.

Filatov, D., S. Bjorklund, et al. (1996). "Induction of the mouse ribonucleotide reductase R1 and R2 genes in response to DNA damage by UV light." The Journal of biological chemistry **271**(39): 23698-23704.

Fushiki, H., T. Kanoh-Azuma, et al. (2009). "Quantification of mouse pulmonary cancer models by microcomputed tomography imaging." Cancer science: 1-6.

Gautam, A. and G. Bepler (2006). "Suppression of lung tumor formation by the regulatory subunit of ribonucleotide reductase." Cancer research **66**(13): 6497-6502.

Gautam, A., Z. R. Li, et al. (2003). "RRM1-induced metastasis suppression through PTEN-regulated pathways." Oncogene **22**(14): 2135-2142.

Gietema, H. A., C. M. Schaefer-Prokop, et al. (2007). "Pulmonary nodules: Interscan variability of semiautomated volume measurements with multisection CT-- influence of inspiration level, nodule size, and segmentation performance." Radiology **245**: 888-894.

Gon, S., R. Napolitano, et al. (2011). "Increase in dNTP pool size during the DNA damage response plays a key role in spontaneous and induced-mutagenesis in Escherichia coli." Proceedings of the National Academy of Sciences of the United States of America **108**(48): 19311-19316.

Gong, W., X. Zhang, et al. (2012). "RRM1 expression and clinical outcome of gemcitabine-containing chemotherapy for advanced non-small-cell lung cancer: a meta-analysis." Lung

cancer **75**(3): 374-380.

Goodman, L. R., M. Gulsun, et al. (2006). "Inherent variability of CT lung nodule measurements in vivo using semiautomated volumetric measurements." American journal of roentgenology **186**: 989-994.

Graff, P., O. Amellem, et al. (2002). "Role of ribonucleotide reductase in regulation of cell cycle progression during and after exposure to moderate hypoxia." Anticancer research **22**(1A): 59-68.

Guittet, O., P. Hakansson, et al. (2001). "Mammalian p53R2 protein forms an active ribonucleotide reductase in vitro with the R1 protein, which is expressed both in resting cells in response to DNA damage and in proliferating cells." The Journal of biological chemistry **276**(44): 40647-40651.

Haeno, H., M. Gonen, et al. (2012). "Computational modeling of pancreatic cancer reveals kinetics of metastasis suggesting optimum treatment strategies." Cell **148**(1-2): 362-375.

Haines, B. B., K. A. Bettano, et al. (2009). "A quantitative volumetric micro-computed tomography method to analyze lung tumors in genetically engineered mouse models." Neoplasia **11**: 39-47.

Hakansson, P., L. Dahl, et al. (2006). "The Schizosaccharomyces pombe replication inhibitor Spd1 regulates ribonucleotide reductase activity and dNTPs by binding to the large Cdc22 subunit." The Journal of biological chemistry **281**(3): 1778-1783.

Hakansson, P., A. Hofer, et al. (2006). "Regulation of mammalian ribonucleotide reduction and dNTP pools after DNA damage and in resting cells." The Journal of biological chemistry **281**(12): 7834-7841.

Heinemann, V., Y. Z. Xu, et al. (1990). "Inhibition of ribonucleotide reduction in CCRF-CEM

cells by 2',2'-difluorodeoxycytidine." Molecular pharmacology **38**(4): 567-572.

Henschke, C. I., D. F. Yankelevitz, et al. (2012). "Lung Cancers Diagnosed at Annual CT Screening: Volume Doubling Times." Radiology **263**(2): 578-583.

Ho, S. N., H. D. Hunt, et al. (1989). "Site-directed mutagenesis by overlap extension using the polymerase chain reaction." Gene **77**(1): 51-59.

Holdsworth, D. W. and M. M. Thornton (2002). "Micro-CT in small animal and specimen imaging." Trends in Biotechnology **20**(8): S34-S39.

Hu, C. M., M. T. Yeh, et al. (2012). "Tumor cells require thymidylate kinase to prevent dUTP incorporation during DNA repair." Cancer cell **22**(1): 36-50.

Hung, C. S., K. W. Dodson, et al. (2009). "A murine model of urinary tract infection." Nat Protoc **4**(8): 1230-1243.

Hurta, R. A. and J. A. Wright (1992). "Alterations in the activity and regulation of mammalian ribonucleotide reductase by chlorambucil, a DNA damaging agent." The Journal of biological chemistry **267**(10): 7066-7071.

Irani, K., Y. Xia, et al. (1997). "Mitogenic signaling mediated by oxidants in Ras-transformed fibroblasts." Science **275**(5306): 1649-1652.

Ishikawa, K., K. Takenaga, et al. (2008). "ROS-generating mitochondrial DNA mutations can regulate tumor cell metastasis." Science **320**(5876): 661-664.

Jackson, E. L., N. Willis, et al. (2001). "Analysis of lung tumor initiation and progression using conditional expression of oncogenic K-ras." Genes & development **15**(24): 3243-3248.

Jemal, A., R. Siegel, et al. (2010). "Cancer statistics, 2010." CA: a cancer journal for clinicians **60**(5): 277-300.

Jiang, R., J. L. Zhang, et al. (2004). "Mechanism for induction of hydroxyurea resistance and loss of latent EBV genome in hydroxyurea-treated Burkitt's lymphoma cell line Raji." Journal of medical virology **73**(4): 589-595.

Jirapatnakul, A. C., Y. D. Mulman, et al. (2011). "Segmentation of juxtapleural pulmonary nodules using a robust surface estimate." International journal of biomedical imaging **2011**: 632195.

Johansson, E., K. Hjortsberg, et al. (1998). "Two YY-1-binding proximal elements regulate the promoter strength of the TATA-less mouse ribonucleotide reductase R1 gene." The Journal of biological chemistry **273**(45): 29816-29821.

Jordan, A. and P. Reichard (1998). "Ribonucleotide reductases." Annual review of biochemistry **67**: 71-98.

Jordheim, L. P., O. Guittet, et al. (2005). "Increased expression of the large subunit of ribonucleotide reductase is involved in resistance to gemcitabine in human mammary adenocarcinoma cells." Molecular cancer therapeutics **4**(8): 1268-1276.

Jordheim, L. P., P. Seve, et al. (2011). "The ribonucleotide reductase large subunit (RRM1) as a predictive factor in patients with cancer." The lancet oncology **12**(7): 693-702.

Julias, J. G. and V. K. Pathak (1998). "Deoxyribonucleoside triphosphate pool imbalances in vivo are associated with an increased retroviral mutation rate." Journal of virology **72**(10): 7941-7949.

Kaelin, W. G., Jr., W. Krek, et al. (1992). "Expression cloning of a cDNA encoding a

retinoblastoma-binding protein with E2F-like properties." Cell **70**(2): 351-364.

Kaufman, E. R. and R. L. Davidson (1979). "Bromodeoxyuridine mutagenesis in mammalian cells is stimulated by purine deoxyribonucleosides." Somatic cell genetics **5**(5): 653-663.

Kauppi, B., B. B. Nielsen, et al. (1996). "The three-dimensional structure of mammalian ribonucleotide reductase protein R2 reveals a more-accessible iron-radical site than Escherichia coli R2." Journal of molecular biology **262**(5): 706-720.

Ke, P. Y., Y. Y. Kuo, et al. (2005). "Control of dTTP pool size by anaphase promoting complex/cyclosome is essential for the maintenance of genetic stability." Genes & development **19**(16): 1920-1933.

Kimura, T., S. Takeda, et al. (2003). "Impaired function of p53R2 in Rrm2b-null mice causes severe renal failure through attenuation of dNTP pools." Nature genetics **34**(4): 440-445.

Kirkinezos, I. G. and C. T. Moraes (2001). "Reactive oxygen species and mitochondrial diseases." Seminars in cell & developmental biology **12**(6): 449-457.

Kochanowski, N., F. Blanchard, et al. (2006). "Intracellular nucleotide and nucleotide sugar contents of cultured CHO cells determined by a fast, sensitive, and high-resolution ion-pair RP-HPLC." Analytical biochemistry **348**(2): 243-251.

Kolberg, M., K. R. Strand, et al. (2004). "Structure, function, and mechanism of ribonucleotide reductases." Biochimica et biophysica acta **1699**(1-2): 1-34.

Kollberg, G., N. Darin, et al. (2009). "A novel homozygous RRM2B missense mutation in association with severe mtDNA depletion." Neuromuscular disorders : NMD **19**(2): 147-150.

Kostis, W. J., A. P. Reeves, et al. (2003). "Three-dimensional segmentation and growth-rate

estimation of small pulmonary nodules in helical CT images." IEEE Trans Med Imaging **22**(10): 1259-1274.

Kumar, D., A. L. Abdulovic, et al. (2011). "Mechanisms of mutagenesis in vivo due to imbalanced dNTP pools." Nucleic acids research **39**(4): 1360-1371.

Kumar, D., J. Viberg, et al. (2010). "Highly mutagenic and severely imbalanced dNTP pools can escape detection by the S-phase checkpoint." Nucleic acids research **38**(12): 3975-3983.

Kunz, B. A. and S. E. Kohalmi (1991). "Modulation of mutagenesis by deoxyribonucleotide levels." Annual review of genetics **25**: 339-359.

Lahouassa, H., W. Daddacha, et al. (2012). "SAMHD1 restricts the replication of human immunodeficiency virus type 1 by depleting the intracellular pool of deoxynucleoside triphosphates." Nature immunology **13**(3): 223-228.

Lassmann, G., L. Thelander, et al. (1992). "EPR stopped-flow studies of the reaction of the tyrosyl radical of protein R2 from ribonucleotide reductase with hydroxyurea." Biochemical and biophysical research communications **188**(2): 879-887.

Lebedeva, M. A., J. S. Eaton, et al. (2009). "Loss of p53 causes mitochondrial DNA depletion and altered mitochondrial reactive oxygen species homeostasis." Biochimica et biophysica acta **1787**(5): 328-334.

Lee, Y. D. and S. J. Elledge (2006). "Control of ribonucleotide reductase localization through an anchoring mechanism involving Wtm1." Genes & development **20**(3): 334-344.

Lee, Y. D., J. Wang, et al. (2008). "Dif1 is a DNA-damage-regulated facilitator of nuclear import for ribonucleotide reductase." Molecular cell **32**(1): 70-80.

Lis, E. T., B. M. O'Neill, et al. (2008). "Identification of pathways controlling DNA damage induced mutation in Saccharomyces cerevisiae." DNA repair **7**(5): 801-810.

Liu, X., L. Lai, et al. (2011). "Ribonucleotide reductase small subunit M2B prognoses better survival in colorectal cancer." Cancer research **71**(9): 3202-3213.

Liu, X., L. Xue, et al. (2008). "Redox property of ribonucleotide reductase small subunit M2 and p53R2." Methods in molecular biology **477**: 195-206.

Liu, X., H. Zhang, et al. (2012). "Ribonucleotide Reductase Small Subunit M2 serves as a prognostic biomarker and prognoses poor survival of colorectal cancers." Clinical science.

Liu, X., B. Zhou, et al. (2006). "Metastasis-suppressing potential of ribonucleotide reductase small subunit p53R2 in human cancer cells." Clinical cancer research : an official journal of the American Association for Cancer Research **12**(21): 6337-6344.

Logan, D. T. (2011). "Closing the circle on ribonucleotide reductases." Nature structural & molecular biology **18**(3): 251-253.

Lu, A. G., H. Feng, et al. (2012). "Emerging roles of the ribonucleotide reductase M2 in colorectal cancer and ultraviolet-induced DNA damage repair." World journal of gastroenterology : WJG **18**(34): 4704-4713.

Lycksell, P. O., R. Ingemarson, et al. (1994). "1H NMR studies of mouse ribonucleotide reductase: the R2 protein carboxyl-terminal tail, essential for subunit interaction, is highly flexible but becomes rigid in the presence of protein R1." Biochemistry **33**(10): 2838-2842.

Ma, X. J., R. Salunga, et al. (2003). "Gene expression profiles of human breast cancer progression." Proceedings of the National Academy of Sciences of the United States of America **100**(10): 5974-5979.

Mandel, H., R. Szargel, et al. (2001). "The deoxyguanosine kinase gene is mutated in individuals with depleted hepatocerebral mitochondrial DNA." Nature genetics **29**(3): 337-341.

Mann, G. J., E. A. Musgrove, et al. (1988). "Ribonucleotide reductase M1 subunit in cellular proliferation, quiescence, and differentiation." Cancer research **48**(18): 5151-5156.

Marten, K., F. Auer, et al. (2006). "Inadequacy of manual measurements compared to automated CT volumetry in assessment of treatment response of pulmonary metastases using RECIST criteria." European radiology **16**: 781-790.

Martin, K. R. and J. C. Barrett (2002). "Reactive oxygen species as double-edged swords in cellular processes: low-dose cell signaling versus high-dose toxicity." Human & experimental toxicology **21**(2): 71-75.

Martinez, M. A., J. P. Vartanian, et al. (1994). "Hypermutagenesis of RNA using human immunodeficiency virus type 1 reverse transcriptase and biased dNTP concentrations." Proceedings of the National Academy of Sciences of the United States of America **91**(25): 11787-11791.

Mathews, C. K. (2006). "DNA precursor metabolism and genomic stability." FASEB journal : official publication of the Federation of American Societies for Experimental Biology **20**(9): 1300-1314.

Mathews, C. K. and S. Song (2007). "Maintaining precursor pools for mitochondrial DNA replication." FASEB journal : official publication of the Federation of American Societies for Experimental Biology **21**(10): 2294-2303.

Matsushita, S., R. Ikeda, et al. (2012). "p53R2 is a prognostic factor of melanoma and regulates proliferation and chemosensitivity of melanoma cells." Journal of dermatological science **68**(1): 19-24.

Mendelman, L. V., J. Petruska, et al. (1990). "Base mispair extension kinetics. Comparison of DNA polymerase alpha and reverse transcriptase." The Journal of biological chemistry **265**(4): 2338-2346.

Mitic, N., M. D. Clay, et al. (2007). "Spectroscopic and electronic structure studies of intermediate X in ribonucleotide reductase R2 and two variants: a description of the FeIV-oxo bond in the FeIII-O-FeIV dimer." Journal of the American Chemical Society **129**(29): 9049-9065.

Mitsushita, J., J. D. Lambeth, et al. (2004). "The superoxide-generating oxidase Nox1 is functionally required for Ras oncogene transformation." Cancer research **64**(10): 3580-3585.

Morikawa, T., R. Hino, et al. (2010). "Expression of ribonucleotide reductase M2 subunit in gastric cancer and effects of RRM2 inhibition in vitro." Human pathology **41**(12): 1742-1748.

Morikawa, T., D. Maeda, et al. (2010). "Ribonucleotide reductase M2 subunit is a novel diagnostic marker and a potential therapeutic target in bladder cancer." Histopathology **57**(6): 885-892.

Moss, J., H. Tinline-Purvis, et al. (2010). "Break-induced ATR and Ddb1-Cul4(Cdt)(2) ubiquitin ligase-dependent nucleotide synthesis promotes homologous recombination repair in fission yeast." Genes & development **24**(23): 2705-2716.

Murphy, M. P. (2009). "How mitochondria produce reactive oxygen species." The Biochemical journal **417**(1): 1-13.

Nakahira, S., S. Nakamori, et al. (2007). "Involvement of ribonucleotide reductase M1 subunit overexpression in gemcitabine resistance of human pancreatic cancer." International journal of cancer. Journal international du cancer **120**(6): 1355-1363.

Nakano, K., E. Balint, et al. (2000). "A ribonucleotide reductase gene is a transcriptional target of p53 and p73." Oncogene **19**(37): 4283-4289.

Niida, H., Y. Katsuno, et al. (2010). "Essential role of Tip60-dependent recruitment of ribonucleotide reductase at DNA damage sites in DNA repair during G1 phase." Genes & development **24**(4): 333-338.

Nikitin, A. Y., A. Alcaraz, et al. (2004). "Classification of proliferative pulmonary lesions of the mouse: recommendations of the mouse models of human cancers consortium." Cancer research **64**(7): 2307-2316.

Nordlund, P. and H. Eklund (1995). "Di-iron-carboxylate proteins." Current opinion in structural biology **5**(6): 758-766.

Nordlund, P. and P. Reichard (2006). "Ribonucleotide reductases." Annual review of biochemistry **75**: 681-706.

Nordlund, P., B. M. Sjoberg, et al. (1990). "Three-dimensional structure of the free radical protein of ribonucleotide reductase." Nature **345**(6276): 593-598.

Nutting, C. M., C. M. van Herpen, et al. (2009). "Phase II study of 3-AP Triapine in patients with recurrent or metastatic head and neck squamous cell carcinoma." Annals of oncology : official journal of the European Society for Medical Oncology / ESMO **20**(7): 1275-1279.

Ocean, A. J., P. Christos, et al. (2011). "Phase II trial of the ribonucleotide reductase inhibitor 3-aminopyridine-2-carboxaldehydethiosemicarbazone plus gemcitabine in patients with advanced biliary tract cancer." Cancer chemotherapy and pharmacology **68**(2): 379-388.

Ohtaka, K., N. Kohya, et al. (2008). "Ribonucleotide reductase subunit M1 is a possible chemoresistance marker to gemcitabine in biliary tract carcinoma." Oncology reports **20**(2): 279-

286.

Okumura, H., S. Natsugoe, et al. (2006). "Expression of p53R2 is related to prognosis in patients with esophageal squamous cell carcinoma." Clinical cancer research : an official journal of the American Association for Cancer Research **12**(12): 3740-3745.

Oliver, T. G., K. L. Mercer, et al. "Chronic cisplatin treatment promotes enhanced damage repair and tumor progression in a mouse model of lung cancer." Genes Dev **24**(8): 837-852.

Oxnard, G. R., B. Zhao, et al. (2011). "Variability of lung tumor measurements on repeat computed tomography scans taken within 15 minutes." Journal of clinical oncology : official journal of the American Society of Clinical Oncology **29**(23): 3114-3119.

Perrino, F. W. and L. A. Loeb (1989). "Differential extension of 3' mispairs is a major contribution to the high fidelity of calf thymus DNA polymerase-alpha." The Journal of biological chemistry **264**(5): 2898-2905.

Petruska, J., M. F. Goodman, et al. (1988). "Comparison between DNA melting thermodynamics and DNA polymerase fidelity." Proceedings of the National Academy of Sciences of the United States of America **85**(17): 6252-6256.

Pontarin, G., P. Ferraro, et al. (2012). "Mammalian ribonucleotide reductase subunit p53R2 is required for mitochondrial DNA replication and DNA repair in quiescent cells." Proceedings of the National Academy of Sciences of the United States of America **109**(33): 13302-13307.

Pontarin, G., P. Ferraro, et al. (2007). "p53R2-dependent ribonucleotide reduction provides deoxyribonucleotides in quiescent human fibroblasts in the absence of induced DNA damage." The Journal of biological chemistry **282**(23): 16820-16828.

Pontarin, G., A. Fijolek, et al. (2008). "Ribonucleotide reduction is a cytosolic process in

mammalian cells independently of DNA damage." Proceedings of the National Academy of Sciences of the United States of America **105**(46): 17801-17806.

Potsch, S., F. Lendzian, et al. (1999). "The iron-oxygen reconstitution reaction in protein R2-Tyr-177 mutants of mouse ribonucleotide reductase. Epr and electron nuclear double resonance studies on a new transient tryptophan radical." The Journal of biological chemistry **274**(25): 17696-17704.

Probst, H., H. Schiffer, et al. (1989). "Oxygen dependent regulation of mammalian ribonucleotide reductase in vivo and possible significance for replicon initiation." Biochemical and biophysical research communications **163**(1): 334-340.

Qiu, W., B. Zhou, et al. (2006). "Characterization of enzymatic properties of human ribonucleotide reductase holoenzyme reconstituted in vitro from hRRM1, hRRM2, and p53R2 subunits." Biochemical and biophysical research communications **340**(2): 428-434.

Rahman, M. A., A. R. Amin, et al. (2012). "Systemic delivery of siRNA nanoparticles targeting RRM2 suppresses head and neck tumor growth." Journal of controlled release : official journal of the Controlled Release Society **159**(3): 384-392.

Raj, L., T. Ide, et al. (2011). "Selective killing of cancer cells by a small molecule targeting the stress response to ROS." Nature **475**(7355): 231-234.

Rampazzo, C., C. Miazzi, et al. (2010). "Regulation by degradation, a cellular defense against deoxyribonucleotide pool imbalances." Mutation research **703**(1): 2-10.

Reeves, A. P., A. M. Biancardi, et al. (2007). "The Lung Image Database Consortium (LIDC): a comparison of different size metrics for pulmonary nodule measurements." Academic radiology **14**: 1475-1485.

Reeves, A. P., A. B. Chan, et al. (2006). "On measuring the change in size of pulmonary nodules." IEEE Transactions on Medical Imaging **25**: 435-450.

Reeves, A. P., A. C. Jirapatnakul, et al. (2009). The VOLCANO'09 Challenge: Preliminary Results. Second International Workshop on Pulmonary Image Analysis, London, MICCAI.

Reichard, P. (1988). "Interactions between deoxyribonucleotide and DNA synthesis." Annual review of biochemistry **57**: 349-374.

Reichard, P. and A. Ehrenberg (1983). "Ribonucleotide reductase--a radical enzyme." Science **221**(4610): 514-519.

Reichard, P., R. Eliasson, et al. (2000). "Cross-talk between the allosteric effector-binding sites in mouse ribonucleotide reductase." The Journal of biological chemistry **275**(42): 33021-33026.

Reynolds, C., C. Obasaju, et al. (2009). "Randomized phase III trial of gemcitabine-based chemotherapy with in situ RRM1 and ERCC1 protein levels for response prediction in non-small-cell lung cancer." Journal of clinical oncology : official journal of the American Society of Clinical Oncology **27**(34): 5808-5815.

Reynolds, S. H. and M. W. Anderson (1991). "Activation of proto-oncogenes in human and mouse lung tumors." Environmental health perspectives **93**: 145-148.

Reynolds, S. H., J. S. Wiest, et al. (1992). "Protooncogene activation in spontaneously occurring and chemically induced rodent and human lung tumors." Progress in clinical and biological research **376**: 303-320.

Rhodes, D. R., J. Yu, et al. (2004). "ONCOMINE: a cancer microarray database and integrated data-mining platform." Neoplasia **6**(1): 1-6.

Robert, T., F. Vanoli, et al. (2011). "HDACs link the DNA damage response, processing of double-strand breaks and autophagy." Nature **471**(7336): 74-79.

Robertson, A. B., A. Klungland, et al. (2009). "DNA repair in mammalian cells: Base excision repair: the long and short of it." Cellular and molecular life sciences : CMLS **66**(6): 981-993.

Rodriguez, J., V. Boni, et al. (2011). "Association of RRM1 -37A>C polymorphism with clinical outcome in colorectal cancer patients treated with gemcitabine-based chemotherapy." European journal of cancer **47**(6): 839-847.

Rofougaran, R., M. Vodnala, et al. (2006). "Enzymatically active mammalian ribonucleotide reductase exists primarily as an alpha6beta2 octamer." The Journal of biological chemistry **281**(38): 27705-27711.

Ross, J. C., J. V. Miller, et al. (2007). "An analysis of early studies released by the Lung Imaging Database Consortium (LIDC)." Academic radiology **14**: 1382-1388.

Rova, U., A. Adrait, et al. (1999). "Evidence by mutagenesis that Tyr(370) of the mouse ribonucleotide reductase R2 protein is the connecting link in the intersubunit radical transfer pathway." The Journal of biological chemistry **274**(34): 23746-23751.

Saada, A., A. Shaag, et al. (2001). "Mutant mitochondrial thymidine kinase in mitochondrial DNA depletion myopathy." Nature genetics **29**(3): 342-344.

Sabouri, N., J. Viberg, et al. (2008). "Evidence for lesion bypass by yeast replicative DNA polymerases during DNA damage." Nucleic acids research **36**(17): 5660-5667.

Sanvisens, N., M. C. Bano, et al. (2011). "Regulation of ribonucleotide reductase in response to iron deficiency." Molecular cell **44**(5): 759-769.

Schwartz, M. (1961). "A biomathematical approach to clinical tumor growth." Cancer **14**: 1272-1294.

Sen, C. K. and L. Packer (2002). Redox cell biology and genetics. Part A. San Diego, Calif., Academic Press.

Shaibani, A., O. A. Shchelochkov, et al. (2009). "Mitochondrial neurogastrointestinal encephalopathy due to mutations in RRM2B." Archives of neurology **66**(8): 1028-1032.

Shao, J., B. Zhou, et al. (2006). "Ribonucleotide reductase inhibitors and future drug design." Current cancer drug targets **6**(5): 409-431.

Shao, J., B. Zhou, et al. (2004). "In vitro characterization of enzymatic properties and inhibition of the p53R2 subunit of human ribonucleotide reductase." Cancer research **64**(1): 1-6.

Sherman, P. A. and J. A. Fyfe (1989). "Enzymatic assay for deoxyribonucleoside triphosphates using synthetic oligonucleotides as template primers." Analytical biochemistry **180**(2): 222-226.

Simon, G., A. Sharma, et al. (2007). "Feasibility and efficacy of molecular analysis-directed individualized therapy in advanced non-small-cell lung cancer." Journal of clinical oncology : official journal of the American Society of Clinical Oncology **25**(19): 2741-2746.

Smeds, J., R. Kumar, et al. (2001). "Polymorphic insertion of additional repeat within an area of direct 8 bp tandem repeats in the 5'-untranslated region of the p53R2 gene and cancer risk." Mutagenesis **16**(6): 547-550.

Sneeden, J. L. and L. A. Loeb (2004). "Mutations in the R2 subunit of ribonucleotide reductase that confer resistance to hydroxyurea." The Journal of biological chemistry **279**(39): 40723-40728.

Spratt, J. S., J. S. Meyer, et al. (1995). "Rates of growth of human solid neoplasms: Part I." Journal of surgical oncology **60**(2): 137-146.

Steeper, J. R. and C. D. Steuart (1970). "A rapid assay for CDP reductase activity in mammalian cell extracts." Analytical biochemistry **34**: 123-130.

Strand, K. R., S. Karlsen, et al. (2004). "Crystal structural studies of changes in the native dinuclear iron center of ribonucleotide reductase protein R2 from mouse." The Journal of biological chemistry **279**(45): 46794-46801.

Suh, Y. A., R. S. Arnold, et al. (1999). "Cell transformation by the superoxide-generating oxidase Mox1." Nature **401**(6748): 79-82.

Tanaka, H., H. Arakawa, et al. (2000). "A ribonucleotide reductase gene involved in a p53-dependent cell-cycle checkpoint for DNA damage." Nature **404**(6773): 42-49.

Thelander, L. (2007). "Ribonucleotide reductase and mitochondrial DNA synthesis." Nature genetics **39**(6): 703-704.

Trachootham, D., J. Alexandre, et al. (2009). "Targeting cancer cells by ROS-mediated mechanisms: a radical therapeutic approach?" Nature reviews. Drug discovery **8**(7): 579-591.

Traynor, A. M., J. W. Lee, et al. (2010). "A phase II trial of triapine (NSC# 663249) and gemcitabine as second line treatment of advanced non-small cell lung cancer: Eastern Cooperative Oncology Group Study 1503." Investigational new drugs **28**(1): 91-97.

Tyynismaa, H., E. Ylikallio, et al. (2009). "A heterozygous truncating mutation in RRM2B causes autosomal-dominant progressive external ophthalmoplegia with multiple mtDNA deletions." American journal of human genetics **85**(2): 290-295.

Uhlin, U. and H. Eklund (1994). "Structure of ribonucleotide reductase protein R1." Nature **370**(6490): 533-539.

Ullman, B., S. M. Clift, et al. (1980). "Alterations in deoxyribonucleotide metabolism in cultured cells with ribonucleotide reductase activities refractory to feedback inhibition by 2'-deoxyadenosine triphosphate." The Journal of biological chemistry **255**(17): 8308-8314.

Uppsten, M., M. Farnegardh, et al. (2006). "The first holocomplex structure of ribonucleotide reductase gives new insight into its mechanism of action." Journal of molecular biology **359**(2): 365-377.

Uramoto, H., K. Sugio, et al. (2006). "P53R2, p53 inducible ribonucleotide reductase gene, correlated with tumor progression of non-small cell lung cancer." Anticancer research **26**(2A): 983-988.

Valko, M., C. J. Rhodes, et al. (2006). "Free radicals, metals and antioxidants in oxidative stress-induced cancer." Chemico-biological interactions **160**(1): 1-40.

Vartanian, J. P., A. Meyerhans, et al. (1994). "G-->A hypermutation of the human immunodeficiency virus type 1 genome: evidence for dCTP pool imbalance during reverse transcription." Proceedings of the National Academy of Sciences of the United States of America **91**(8): 3092-3096.

Veldhuizen, R. A. W., N. L. Ford, et al. (2007). "In vivo characterization of lung morphology and function in anesthetized free-breathing mice using micro-computed tomography." Journal of applied physiology (Bethesda, Md. : 1985) **102**: 2046-2055.

Wang, L. M., F. F. Lu, et al. (2012). "Overexpression of catalytic subunit M2 in patients with ovarian cancer." Chinese medical journal **125**(12): 2151-2156.

Warburg, O. (1956). "On the origin of cancer cells." Science **123**(3191): 309-314.

Weber, G. (1980). "Recent advances in the design of anticancer chemotherapy." Oncology **37 Suppl 1**: 19-24.

Weinberg, G., B. Ullman, et al. (1981). "Mutator phenotypes in mammalian cell mutants with distinct biochemical defects and abnormal deoxyribonucleoside triphosphate pools." Proceedings of the National Academy of Sciences of the United States of America **78**(4): 2447-2451.

Wheeler, L. J., I. Rajagopal, et al. (2005). "Stimulation of mutagenesis by proportional deoxyribonucleoside triphosphate accumulation in Escherichia coli." DNA repair **4**(12): 1450-1456.

Wong, A., R. A. Soo, et al. (2009). "Clinical pharmacology and pharmacogenetics of gemcitabine." Drug metabolism reviews **41**(2): 77-88.

Wonganan, P., W. G. Chung, et al. (2012). "Silencing of ribonucleotide reductase subunit M1 potentiates the antitumor activity of gemcitabine in resistant cancer cells." Cancer biology & therapy **13**(10): 908-914.

Wu, X. and M. Huang (2008). "Dif1 controls subcellular localization of ribonucleotide reductase by mediating nuclear import of the R2 subunit." Molecular and cellular biology **28**(23): 7156-7167.

Xie, C. and W. Plunkett (1995). "Metabolism and actions of 2-chloro-9-(2-deoxy-2-fluoro-beta-D- arabinofuranosyl)-adenine in human lymphoblastoid cells." Cancer research **55**(13): 2847-2852.

Xie, K. C. and W. Plunkett (1996). "Deoxynucleotide pool depletion and sustained inhibition of ribonucleotide reductase and DNA synthesis after treatment of human lymphoblastoid cells with

2-chloro-9-(2-deoxy-2-fluoro-beta-D-arabinofuranosyl) adenine." Cancer research **56**(13): 3030-3037.

Xu, X., J. L. Page, et al. (2008). "Broad overexpression of ribonucleotide reductase genes in mice specifically induces lung neoplasms." Cancer Res **68**(8): 2652-2660.

Xue, L., B. Zhou, et al. (2007). "Ribonucleotide reductase small subunit p53R2 facilitates p21 induction of G1 arrest under UV irradiation." Cancer research **67**(1): 16-21.

Xue, L., B. Zhou, et al. (2006). "Structurally dependent redox property of ribonucleotide reductase subunit p53R2." Cancer research **66**(4): 1900-1905.

Yamaguchi, T., K. Matsuda, et al. (2001). "p53R2-dependent pathway for DNA synthesis in a p53-regulated cell cycle checkpoint." Cancer research **61**(22): 8256-8262.

Yanamoto, S., G. Kawasaki, et al. (2009). "Ribonucleotide reductase small subunit p53R2 promotes oral cancer invasion via the E-cadherin/beta-catenin pathway." Oral oncology **45**(6): 521-525.

Yanamoto, S., G. Kawasaki, et al. (2003). "Expression of p53R2, newly p53 target in oral normal epithelium, epithelial dysplasia and squamous cell carcinoma." Cancer letters **190**(2): 233-243.

Yankelevitz, D. F., A. P. Reeves, et al. (2000). "Small Pulmonary Nodules: Volumetrically Determined Growth Rates Based on CT Evaluation." Radiology **217**: 251-256.

Ylikallio, E., J. L. Page, et al. (2010). "Ribonucleotide reductase is not limiting for mitochondrial DNA copy number in mice." Nucleic acids research **38**(22): 8208-8218.

Yoshida, Y., T. Tsunoda, et al. (2011). "KRAS-mediated up-regulation of RRM2 expression is essential for the proliferation of colorectal cancer cell lines." Anticancer research **31**(7): 2535-

2539.

Zhang, K., S. Hu, et al. (2009). "Overexpression of RRM2 decreases thrombspondin-1 and increases VEGF production in human cancer cells in vitro and in vivo: implication of RRM2 in angiogenesis." Molecular cancer **8**: 11.

Zhang, Y., L. Liu, et al. (2011). "Investigation of in vivo diferric tyrosyl radical formation in Saccharomyces cerevisiae Rnr2 protein: requirement of Rnr4 and contribution of Grx3/4 AND Dre2 proteins." The Journal of biological chemistry **286**(48): 41499-41509.

Zhang, Z., X. An, et al. (2006). "Nuclear localization of the Saccharomyces cerevisiae ribonucleotide reductase small subunit requires a karyopherin and a WD40 repeat protein." Proceedings of the National Academy of Sciences of the United States of America **103**(5): 1422-1427.

Zhao, B., L. P. James, et al. (2009). "Evaluating variability in tumor measurements from same-day repeat CT scans of patients with non-small cell lung cancer." Radiology **252**: 263-272.

Zhao, X., B. Georgieva, et al. (2000). "Mutational and structural analyses of the ribonucleotide reductase inhibitor Sml1 define its Rnr1 interaction domain whose inactivation allows suppression of mec1 and rad53 lethality." Molecular and cellular biology **20**(23): 9076-9083.

Zhao, X., E. G. Muller, et al. (1998). "A suppressor of two essential checkpoint genes identifies a novel protein that negatively affects dNTP pools." Molecular cell **2**(3): 329-340.

Zhao, X. and R. Rothstein (2002). "The Dun1 checkpoint kinase phosphorylates and regulates the ribonucleotide reductase inhibitor Sml1." Proceedings of the National Academy of Sciences of the United States of America **99**(6): 3746-3751.

Zheng, Z., T. Chen, et al. (2007). "DNA synthesis and repair genes RRM1 and ERCC1 in lung

cancer." The New England journal of medicine **356**(8): 800-808.

Zhou, B. S., N. Y. Hsu, et al. (1995). "Overexpression of ribonucleotide reductase in transfected human KB cells increases their resistance to hydroxyurea: M2 but not M1 is sufficient to increase resistance to hydroxyurea in transfected cells." Cancer research **55**(6): 1328-1333.

Zhou, B. S., P. Tsai, et al. (1998). "Overexpression of transfected human ribonucleotide reductase M2 subunit in human cancer cells enhances their invasive potential." Clinical & experimental metastasis **16**(1): 43-49.

APPENDIX 1 The Physiological Effect of Disrupting Two Primary Regulatory Mechanisms of Mouse Ribonucleotide Reductase

Introduction

Mammalian Ribonucleotide Reductase (RNR) is regulated by two primary regulatory mechanisms: one is the cell cycle regulation of the R2 protein level and the other is the feedback inhibition of RNR activity through the activity site of the R1 subunit (Nordlund and Reichard 2006). During the cell cycle, the R1 protein level is constant while the R2 protein level fluctuates. R2 protein peaks during S phase and is undetectable outside of S phase (Engstrom, Eriksson et al. 1985). As a result, the R2 protein level acts as a limiting factor for RNR enzyme activity. It has previously been shown that disruption of the cell cycle regulation of R2 by overexpressing this subunit in mice leads to lung tumorigenesis through a mutagenic mechanism (Xu, Page et al. 2008). RNR activity is also regulated through the activity site of R1. This site senses the ratio of dATP and ATP in cells. dATP binding at the activity site of R1 inhibits RNR enzyme activity while ATP binding stimulates enzyme activity (Kolberg, Strand et al. 2004). Disruption of the activity site in R1 by the D57N (aspartic acid to asparagine) point mutation results in an enzyme that cannot be inhibited by dATP binding and leads to perturbations in dNTP pools and increased mutation rate in cells (Weinberg, Ullman et al. 1981; Caras and Martin 1988). Mice that are heterozygous for the D57N mutation ($Rrm1^{+/D57N}$) were grossly normal while mice that are homozygous for the mutation ($Rrm1^{D57N/D57N}$) were embryonic lethal (Page, JL and Weiss, RS, unpublished data).

We are interested in the physiological consequences of simultaneous disruption of both the regulatory mechanisms of RNR. We hypothesized that this interruption would result in significant dNTP pool disturbances and mutagenesis. In order to do this, I crossed $Rrm1^{+/D57N}$

heterozygous mice with $Rrm2^{Tg}$/$p53R2^{Tg}$ mice and aged the desired $Rrm2^{Tg}Rrm1^{+/D57N}$ and $p53R2^{Tg}Rrm1^{+/D57N}$ experimental mice till 15-months old. These mice were born at expected frequency and had limited phenotypes.

Materials and Methods

Mice

$Rrm2^{Tg}$ and $p53R2^{Tg}$ transgenic mice and $Rrm1^{D57N}$ knock in (KI) mice were generated previously (Xu, Page et al. 2008) (Page, JL and Weiss, RS, unpublished data). $Rrm2^{Tg}$ and $p53R2^{Tg}$ mice were interbred with $Rrm1^{+/D57N}$ mice to generate $Rrm2^{Tg}Rrm1^{+/D57N}$ and $p53R2^{Tg}Rrm1^{+/D57N}$ experimental mice. All mice were maintained identically and aged till moribund for 15-month old.

Pathological assessment

Mice terminated according to schedule were euthanized by asphyxiation using carbon dioxide and necropsied. The weight of the whole mouse and tissues including kidney, testis, heart, and skeletal muscle (right quadriceps) were measured at necropsy. Lung, spleen, thymus, kidney, testis, ovary, uterus, heart, diaphragm, liver and skeletal muscle (right quadriceps) tissues were fixed with 10% neutral-buffered formalin, embedded in paraffin and 5μm thick sections were stained with hematoxylin and eosin.

Results

$Rrm2^{Tg}Rrm1^{+/D57N}$ and $p53R2^{Tg}Rrm1^{+/D57N}$ mice were born at expected frequency

$Rrm2^{Tg}$ and $p53R2^{Tg}$ mice were intercrossed with $Rrm1^{+/D57N}$. Offspring were genotyped at weaning by PCR. The total numbers of mice of each genotype observed are listed in Table 1 and Table 2. χ^2 test indicated that there is no difference among the four different genotypes.

Table 1 Number of offspring obtained from $Rrm2^{Tg}$ and $Rrm1^{+/D57N}$ intercrosses.

Genotype	# Expected	# Observed
Wild type	29.25	34
$Rrm1^{+/D57N}$	29.25	21
$Rrm2^{Tg}$	29.25	32
$Rrm2^{Tg}Rrm1^{+/D57N}$	29.25	30
Total		117 (P=0.61[a])

[a] χ^2 test is done among the four different genotypes and no statistical significance is observed.

Table 2 Number of offspring obtained from p53R2^{Tg} and Rrm1$^{+/D57N}$ intercrosses.

Genotype	# Expected	# Observed
Wild type	26	42
Rrm1$^{+/D57N}$	26	29
p53R2^{Tg}	26	19
p53R2^{Tg}Rrm1$^{+/D57N}$	26	15
Total		104 (P_1=0.047[a]; P_2=0.66[b])

[a] χ^2 test is done among the four different genotypes and statistical significance is observed. However, this is due to the fact that p53R2^{Tg} single mutant mice were underrepresented (Xu, X, Page, JL, Li, M and Weiss, RS, unpublished data).

[b] χ^2 test is done between p53R2^{Tg} and p53R2^{Tg}Rrm1$^{+/D57N}$ mice and this time no statistical significance is observed.

$Rrm2^{Tg}Rrm1^{+/D57N}$ and $p53R2^{Tg}Rrm1^{+/D57N}$ mice were grossly normal

A cohort of $Rrm2^{Tg}Rrm1^{+/D57N}$ and $p53R2^{Tg}Rrm1^{+/D57N}$ mice were maintained and monitored till 15-month old. All mice survived the 15-month period and were grossly normal. Since $Rrm2^{Tg}$ and $p53R2^{Tg}$ mice develop lung tumors and $Rrm1^{+/D57N}$ heterozygous mice were grossly normal (with slight increase in lung tumorigenesis), we were interested in whether $Rrm2^{Tg}Rrm1^{+/D57N}$ and $p53R2^{Tg}Rrm1^{+/D57N}$ mice have synergistic increase in lung tumorigenesis and whether they develop new pathological phenotypes. However, as summarized in Table 3, $Rrm2^{Tg}Rrm1^{+/D57N}$ and $p53R2^{Tg}Rrm1^{+/D57N}$ mice have limited phenotypes.

Discussion

It is somewhat surprising that $Rrm2^{Tg}Rrm1^{+/D57N}$ and $p53R2^{Tg}Rrm1^{+/D57N}$ mice were grossly normal and didn't have synergistic phenotypes even if they have disruptions in the two primary RNR regulatory pathways. Besides the $Rrm1^{+/D57N}$ and $Rrm1^{D57N/D57N}$ KI mice, the Weiss lab also generated Rrm1-$D57N^{Tg}$ transgenic mice that overexpress the Rrm1-D57N mutant protein. The Rrm1-$D57N^{Tg}$ mice were also grossly normal and had no significant increased in total cellular dNTP pools (Page, JL and Weiss, RS, unpublished data). When Rrm1-$D57N^{Tg}$ mice were intercrossed with $Rrm2^{Tg}$ and $p53R2^{Tg}$ mice, the resulting bitransgenic Rrm1-$D57N^{Tg}Rrm2^{Tg}$ and Rrm1-$D57N^{Tg}p53R2^{Tg}$ mice showed embryonic and neonatal lethality, as well as huge increases in cellular dNTP pools (Page, JL and Weiss, RS, unpublished data). Several recent studies indicate that when RNR activity is inhibited by allosteric effector binding at the activity site, the large R1 subunit is converted into persistent inactive hexamers (Aye and Stubbe 2011; Fairman, Wijerathna et al. 2011; Aye, Brignole et al. 2012). Based on this information, we propose the following model to explain the observations with Rrm1-$D57N^{Tg}$,

Table 3 Pathological analyses of 15-month old $Rrm2^{Tg}Rrm1^{+/D57N}$ and $p53R2^{Tg}Rrm1^{+/D57N}$ mice

Genotype	Sex	Weight (g)	Lung	Lymph node (near thymus)	Heart (mg)	Uterine or testis (mg)	Kidney (mg)	Skeletal muscle (mg)
$p53R2^{Tg}$ $Rrm1^{+/D57N}$	M	40.12	Tumor		156	93	317	118
$p53R2^{Tg}$ $Rrm1^{+/D57N}$	M	34.79	Tumor	Enlarged	183	94 (moderate degeneration)	306	175
$p53R2^{Tg}$ $Rrm1^{+/D57N}$	M	37.65	Tumor		214	116	360	194
$Rrm1^{+/D57N}$	M	37.62			192	128	341	212
$p53R2^{Tg}$	M	42.36		Enlarged	209	127	362	112
Wild type	M	37.57			197	121 (moderate degeneration)	364	190
$Rrm2^{Tg}$ $Rrm1^{+/D57N}$	F	41.34	Tumor		175		260	179
$Rrm2^{Tg}$ $Rrm1^{+/D57N}$	F	31.86	Tumor	Enlarged	146		218	181
$Rrm2^{Tg}$ $Rrm1^{+/D57N}$	F	42.94	Tumor		158	Dilated lumen	189	132
$Rrm2^{Tg}$ $Rrm1^{+/D57N}$	F	35.03	Tumor		163		214	163
$p53R2^{Tg}$ $Rrm1^{+/D57N}$	F	41.31			153		213	135
$Rrm2^{Tg}$	F	41.59	Tumor		180		242	183
Wild type	F	49.73			162		235	179
Wild type	F	44.33			148	Dilated lumen	241	179

$Rrm1^{+/D57N}$, $Rrm1^{D57N/D57N}$, Rrm1-$D57N^{Tg}Rrm2^{Tg}$, Rrm1-$D57N^{Tg}p53R2^{Tg}$, $Rrm2^{Tg}Rrm1^{+/D57N}$ and $p53R2^{Tg}Rrm1^{+/D57N}$ mice (Figure 1).

Figure 1 Hypothetical model of RNR deregulation in various RNR mouse models. (A) In wide type mice, dATP binding to Rrm1 locks Rrm1 subunits in homohexamer confirmation and inhibits RNR activity to maintain balanced dNTP pools in cells. (B) In Rrm1-D57N^{Tg} and Rrm1$^{+/D57N}$ mice, there are Rrm1 WT and Rrm1-D57N mutant proteins. There could be two scenarios: (i) there could be heterohexamer formation of Rrm1 WT and Rrm1-D57N upon dATP inhibition. Even if Rrm1-D57N cannot respond to dATP inhibition, Rrm1 WT in the heterohexamer can respond and lead to inactive RNR complex; (ii) R2 subunit is the limiting factor for RNR enzyme activity. Even if there is Rrm1-D57N present, there is no excess R2 subunit to form a functional RNR complex. As a result, these mice are grossly normal and have limited phenotypes. (C) In Rrm1$^{D57N/D57N}$ mice, there is no Rrm1 WT protein, all Rrm1-D57N proteins complex with R2 and form RNR enzymes that cannot respond to dATP inhibition any more, leading to increased dNTP pools and embryonic lethality in mice. (D) In Rrm1$^{+/D57N}$Rrm2^{Tg} and Rrm1$^{+/D57N}$p53R2^{Tg} mice, half of the R1 protein is WT and half is Rrm1-D57N. Even if the R2 subunit is overexpressed, there is a big chance that Rrm1-D57N is locked in the heterohexamer with Rrm1 WT. Since Rrm1 WT can respond to dATP inhibition, these mice have inactive RNR complexes and limited phenotypes. In Rrm1-D57N^{Tg}Rrm2^{Tg} and Rrm1-D57N^{Tg}p53R2^{Tg} mice, majority of the R1 protein is Rrm1-D57N. These Rrm1-D57N mutants can complex with R2 and form active RNR proteins that do not respond to dATP inhibition, resulting in increased dNTP pools and embryonic and neonatal lethality in mice.

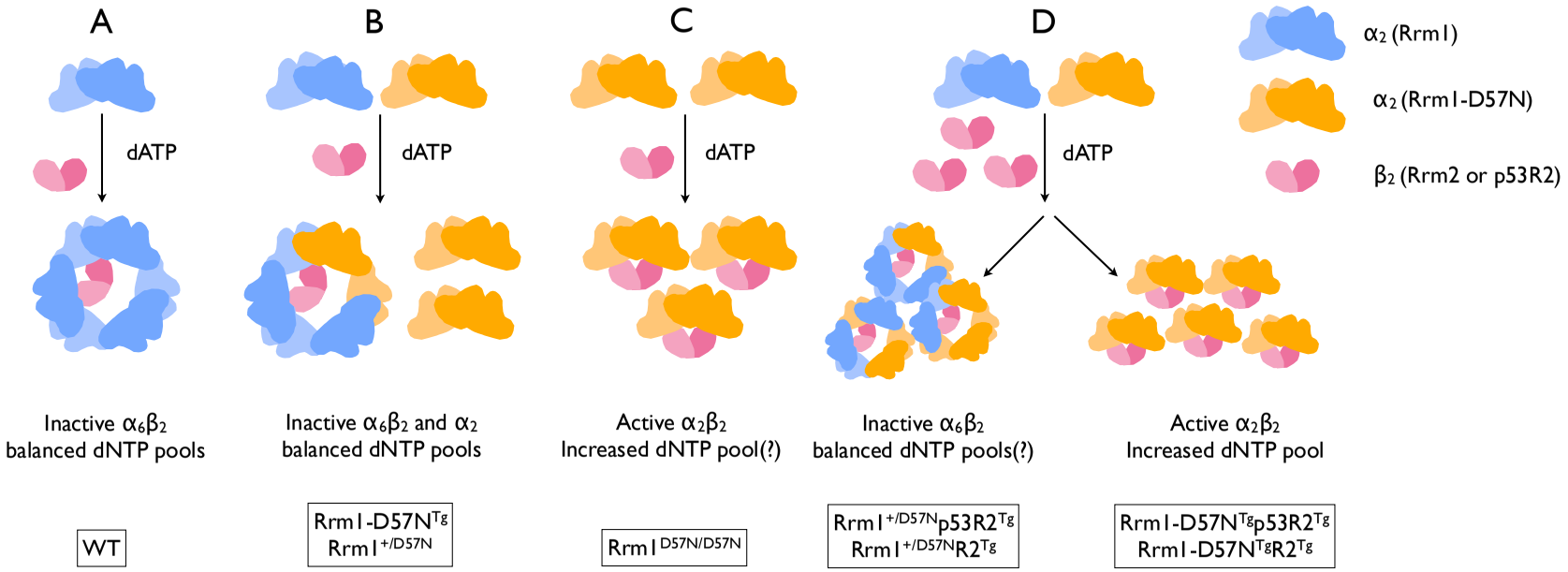
A
B
C
D
dATP
dATP
dATP
dATP
α2 (Rrm1)
α2 (Rrm1-D57N)
β2 (Rrm2 or p53R2)
Inactive α6β2
balanced dNTP pools
Inactive α6β2 and α2
balanced dNTP pools
Active α2β2
Increased dNTP pool(?)
Inactive α6β2
balanced dNTP pools(?)
Active α2β2
Increased dNTP pool
WT
Rrm1-D57NTg
Rrm1+/D57N
Rrm1D57N/D57N
Rrm1+/D57Np53R2Tg
Rrm1+/D57NR2Tg
Rrm1-D57NTgp53R2Tg
Rrm1-D57NTgR2Tg

APPENDIX 2 Mammalian Ribonucleotide Reductase is Governed by Two Primary Regulatory Mechanisms that Prevent Lethal Alterations in Nucleotide Levels

Jennifer L. Page[1], Minxing Li[1], Emil Ylikallio[2], Gabriel Balmus[1], Xia Xu[1], Joshua Levy[1], Henna Tyynismaa[2], Rachel M. Peters[1], Teresa Southard[1], Anu Suomalainen[2], and Robert S. Weiss[1*]

[1]Department of Biomedical Sciences, Cornell University, Ithaca, New York 14853 [2]Research Programs Unit, Molecular Neurology, Biomedicum Helsinki, University of Helsinki, Finland

Correspondent footnote:

Robert S. Weiss

Department of Biomedical Sciences

Cornell University

T2-006C Veterinary Research Tower

Ithaca, New York 14853

Telephone: (607) 253-4443

Fax: (607) 253-4212

E-mail: rsw26@cornell.edu

Note: this appendix is presented as a draft manuscript. Minxing Li contributed to embryo dissection, analysis and genotyping of all embryos presented in Figure 2. She contributed partially to embryo data collection in Table 3 and Table 4, as well as embryo and neonatal dNTP measurements in Figure 4.

SUMMARY (250 words max)

Background: Regulation of RNR is accomplished through multiple mechanisms which include control of R2 subunit protein levels and negative feedback regulation through the activity site within the R1 subunit. The D57N mutation within the activity site disables feedback inhibition and results in a mutator phenotype in cultured cells.

Results: We generated a mouse model featuring a hyperactive mutant form of the enzyme. We crossed mice overexpressing the *Rrm1-D57N*^{Tg} mutant to *Rrm2*- or *p53R2*-overexpressing mice. Combining overexpression of the mutant form of the large subunit, but not the wild type large subunit, with either small subunit caused synthetic lethality. The extent of *Rrm1*^{D57N} overexpression affected the dNTP output in tissues expressing the RNR transgenes most highly, with higher RNR expression correlating with elevated and unbalanced nucleotide pools. Moreover, the dNTP pool alterations correlated with the onset of phenotypes in the mice. Mice that survived to adulthood were underrepresented and displayed severe skeletal muscle degeneration and premature aging phenotypes.

Conclusions: We propose a mechanism in which simultaneously overriding two primary RNR regulatory mechanisms results in greatly elevated RNR activity, producing abnormal dNTP pools that interfere with genome maintenance and function. These experiments provide insights into how the control of nucleotide levels through regulation of RNR catalytic activity impacts genomic stability and survival in mammals.

HIGHLIGHTS (85 characters each)

- Disabling both main regulatory mechanisms of RNR causes synthetic lethality
- Increased RNR activity correlates to increased dNTPs and to timing of lethality
- Deregulating RNR leads to premature aging phenotypes and degeneration of multiple tissues

INTRODUCTION

Proper genome maintenance is critical for survival. In addition to the nuclear genome, which is comprised of approximately 3.4 gigabases of DNA and encoding roughly 28,000 genes in mice, eukaryotic cells maintain a mitochondrial genome, which is multicopy, comprised of 16,569 bp of DNA and only encodes 37 genes. One of the key determinants in the maintenance of these genomes is the availability of dNTPs for DNA synthesis. Efficient and faithful replication by the three main replicative polymerases, the nuclear DNA polymerases d and e, and the mitochondrial DNA Pol g, relies on adequate and balanced nucleotide pools. All three polymerases contain exonucleolytic proofreading domains that prevent DNA mismatches under ideal conditions, but all three make increased replication errors in perturbed nucleotide pools (1-4). In particular, elevated nucleotide pools increase the error rate of all three polymerases and result in increased mutation rates(5). Conversely, elevated nucleotide pools have also been shown to aid survival following DNA damage, by promoting lesion by-pass(6). This suppresses potentially deleterious repair mechanisms such as sister chromatid exchange and hyperrecombination, stabilizing the genome at the cost of potentially increased point mutations(7).

Non-elevated but unbalanced nucleotide pools are also highly mutagenic(8, 9). During DNA synthesis, excessive amounts of an incorrect nucleotide at the site of elongation can dramatically increase mismatches(1), and also can promote frame-shift errors by yeast Pol a and in HeLa cell extracts(10). At the most extreme, severely unbalanced dNTP pools, particularly those that deplete one or more specific nucleotides, can trigger activation of the S-phase check point(9).

Another significant effect of unbalanced nucleotide pools is instability of mitochondrial

DNA, which can manifest as mtDNA depletion, large scale deletions, or point mutations in mtDNA. Mitochondrial DNA maintenance syndromes are a set of heterogeneous disorders that can present in almost any tissue at any age (Reviewed in (12), (13)). Homozygous or compound heterozygous mutations in the ribonucleotide reductase small subunit p53R2 are important causes of mtDNA depletion syndrome(15-17), mimicking the phenotypes of inactivating mutations in thymidine kinase and deoxyguanosine kinase (18-21). In contrast, a dominant truncating mutation in the p53R2 gene causes multiple mtDNA deletions in their skeletal muscle but normal mtDNA copy number(22). Therefore, perturbed nucleotide pools are known to cause diverse forms of mtDNA instability.

Control over nucleotide abundance and pool balance is accomplished in part through the cytosolic enzyme ribonucleotide reductase (RNR)(26). RNR catalyzes the rate-limiting step in *de novo* dNTP biosynthesis(27). The mammalian enzyme is composed of two subunits, a large R1 subunit encoded by a single gene, *Rrm1*, and a small R2 subunit, encoded by either *Rrm2* or *Rrm2b* (a.k.a. *p53R2*)(28). Control of RNR activity in mammals is primarily accomplished through two main partially redundant mechanisms; limitation of small subunit availability and allosteric feedback control.

The S-phase R2 gene, *Rrm2*, is not expressed in mammalian cells during quiescent stages of the cell cycle(30), but is strongly induced in S-phase to complex with *Rrm1* and synthesize dNTPs for DNA synthesis(31). The *Rrm2* protein is targeted for proteolytic degradation at the G2/M transition by the APC^{Cdh1} complex(32), limiting the bulk of RNR activity to S-phase. The *p53R2* protein is expressed at low levels throughout the cell cycle and a complex of *Rrm1* and *p53R2* is continually active(30).

We previously described the generation of mice which overexpress individual RNR

subunits(33). Modest dNTP pool alterations were observed in the skeletal muscle of mice expressing individual RNR transgenes(34), suggesting that overexpression of single RNR subunits caused limited net increases in enzyme activity. We also generated mice that feature simultaneous overexpression of *Rrm1* and either small RNR subunit. Combined overexpression of both wild-type RNR subunits caused even greater increases in nucleotide pools and age-dependent mtDNA depletion(34).

In addition to control of RNR protein levels, a second regulatory mechanism governing RNR activity is allosteric feedback control. The $Rrm1^{D57N}$ mutation disables allosteric feedback control and was shown in yeast and in mammalian cell culture models to be mutagenic(6, 37). Further experiments in yeast which involved overexpression of *rnr1-D57N* simultaneously disrupted both main regulatory mechanisms controlling RNR activity. This more thorough deregulation resulted in constitutively elevated dNTP pools that were able to inhibit origin firing in S-phase and cause a slow-growth phenotype. To date, no studies have been performed to test the physiological effect of the $Rrm1^{D57N}$ mutation in an *in vivo* animal model. We therefore generated transgenic mice that broadly overexpress the $Rrm1^{D57N}$ mutant to a high degree.

Here we report on the first model of loss of allosteric feedback control of RNR in mice, as well as the effect of simultaneous disruption of multiple regulatory modes of RNR. Whereas mice that overexpressed *Rrm1*-D57N alone were grossly normal, combined overexpression of *Rrm1*-D57N with either small subunit caused synthetic lethality. We show that simultaneous overexpression of Rrm1-D57N and either small subunit leads to both increased and unbalanced dNTP pools, and the extent of the dNTP pool perturbation correlates with the onset of lethality. These manipulations will allow us to study the effects of various degrees of RNR deregulation in mice, and more completely understand the complex control of this critical enzyme.

MATERIALS AND METHODS

Plasmids. An expression plasmid encoding mouse *Rrm1* was constructed in the pCaggs expression vector as described previously (Xu, et al.). Relative to the previously reported Rrm1 transgene construct, UTR sequences were removed in order to improve expression. The *Rrm1* open reading frame (ORF) was amplified from pCaggs-*Rrm1* with primers:

F: 5'-CTCGTCGACATGCATGTGATCAAGCGAGA*TG*GC-3'

R: 5'-TCAGGATCCACACATCAGGCACTC-3'

The PCR product was cloned into pCR2.1 with the Topo-TA cloning kit (Strategene). Following sequencing analysis of the insertion fragment ends to confirm the absence of PCR-induced mutations, the PCR-amplified *Rrm1* sequence was digested out with StuI and replaced by the non-amplified StuI fragment from pCaggs-*Rrm1*. Fragment orientation was confirmed by SphI and EcoRI digestion. The *Rrm1* ORF was then excised from pCR2.1 with SalI/XhoI and ligated into XhoI-linearized pCaggs. Fragment orientation was confirmed by BamHI and SalI/XhoI digests. The *Rrm1*-D57N mutation was inserted by site-directed mutagenesis. Briefly, primers

D57N (5'-CCACAGTGGAACTGAACACCCTGGCTGCT-3')

D57N-AS (5'-AGCAGCCAGGGTCAGTTCCACTGTGG-3')

were used to amplify the entire pCaggs-*Rrm1* plasmid. Following DpnI digestion, products were transformed into DH5a and cultured on NZY^{+} medium. The presence of the mutation was confirmed by XcmI digest, as the D57N mutation destroys an XcmI site. The pCaggs-*Rrm1*-D57N clone was confirmed to be free of other mutations by sequencing.

Transgenic mice. Transgenic mice were generated by microinjection of linear plasmid DNA into the male pronucleus of FVB/N zygotes. The pCaggs-*Rrm1*-D57N plasmid was linearized by SalI digestion. Transgenic founder mice were identified by Southern blot analysis. Transgenic

mice were maintained as hemizygotes on the FVB/N inbred background strain. Genotyping of mice expected to carry a single RNR transgene was performed as previously described (33). In crosses between *Rrm1* or *Rrm1*-D57N and Rrm2 or p53R2, mice were genotyped by Southern blot as described below.

Southern blot analysis. DNA extracted from tails of adult mice or yolk sacs of embryos was subjected overnight to transgene-specific restriction digest and separated on 0.8% agarose gel. The *Rrm1* and *Rrm1*-D57N transgenes were detected by digestion with *BamHI* (Fermentas) and the p53R2 transgene was detected by digestion with EcoRV (Fermentas). Following alkaline transfer to a nylon membrane (GeneScreen Plus, Perkin Elmer), the presence of transgene DNA was detected with a transgene-specific radiolabeled probe.

Northern blot analysis. Total RNA was extracted from mouse cells with RNAStat-60 (TelTech, Inc) and separated on agarose/formaldehyde gel. RNA was transferred to a nylon membrane (GeneScreen, Perkin Elmer) and detected with *Rrm1*- or *Gapdh*-specific radiolabeled probe.

Immunoblot analysis. Tissue extracts were prepared by lysis in RIPA buffer (150mM NaCl, 50mM NaF, 1% NP-40, 0.8% DOC, 0.1% SDS, 50 mM Tris pH 8.0, and 50 mM EDTA) supplemented with protease inhibitors (apropinin, 2mg/mL; leupeptin 2mg/mL, and PMSF, 20 mg/mL) and sodium orthovanadate (400 mM) as a phosphatase inhibitor. Extracts were separated on 10% polyacrylamide gel and transferred to PVDF membrane (Perkin Elmer). R1 protein was detected by AD203, mouse monoclonal anti-R1 (InRo Biomedtek), and loading was assessed by detection of a-tubulin with mouse monoclonal anti-a-tubulin (Sigma). To quantify overexpression in *Rrm1*-D57N transgenic mice, serial dilutions were prepared in RIPA buffer. The same sample volume necessary for 25 mg of total protein from undiluted lysate was used for

the dilution samples. Chemiluminescent signal was detected on a VersaDoc Imaging system and quantified using Quantity One software (Bio-Rad Laboratories). Band intensity was determined for each dilution series sample and plotted following subtraction of background signal. The measured intensity for each undiluted wild-type band was fitted to the generated line for the corresponding *Rrm1*-D57N^{Tg} dilution series. Fold overexpression values were corrected for loading by standardization based on α-tubulin signal.

Histology. Adult mice were euthanized by overdose with carbon dioxide. Neonates (mice ages P10 and younger) were euthanized by decapitation. Tissues for histological analysis were excised and fixed overnight at room temperature in 10% buffered formalin. Tissues were sectioned at 5mm thickness prior to staining with hematoxylin and eosin (H&E), Masson's trichrome stain (MT), or Periodic Acid Schiff's stain (PAS). Adult and neonate sample dehydration, embedding, sectioning, and staining were conducted by the Core Histology Lab in the College of Veterinary Medicine at Cornell University. Embryos were fixed overnight in 4% paraformaldehyde at 4°C, after which time they were transferred to 70% ethanol and kept at 4°C during genotyping of yolk sacs. Processed and embedded embryos were sectioned at 5mm thickness and were stained with H&E, or Feulgen-Schiff's.

Neonate survival assays. *Rrm1*-D57N(low)^{Tg} female mice were set up in timed matings with *Rrm2*^{Tg} or *p53R2*^{Tg} males. Females were monitored until pups were born, at which time the pups were counted and weighed. Mice were counted and weighed daily until P21. Pups were genotyped by Southern blot at weaning or when found dead. Only litters in which the fate of all pups was known and in which all control littermates survived the full 21 days or died naturally were used in this analysis. Survival plots were generated with SPSS software.

Southern blotting for mtDNA copy number determination.

Total DNA was isolated from tissues by proteinase K digestion and standard phenol-chloroform extraction. Southern blotting was performed essentially as described (39). Briefly, three micrograms total DNA was digested with SacI overnight at 37°C, samples were then separated by electrophoresis in an agarose gel and blotted by alkaline transfer onto a Hybond N+ membrane (Amersham Biosciences). The membrane was hybridized overnight at 68°C in a roller hybridizer using 5 μCi/ml ^{32}P-dCTP labeled (PCR-generated) mouse mtDNA probe, and 18S rDNA probe in pBR322 plasmid. Phosphoimager analysis was done with Typhoon 9400 (Amersham Biosciences) and mtDNA was quantified against the 18S rDNA signal using ImageQuant v5.0 software (Amersham Biosciences).

Real time PCR.

For mtDNA quantification, the quantitative real-time (Q)PCR reactions were done with 25 ng total DNA used as template and normalizing the *mt-Cytb* gene amplification level (primer sequences: 5'-GCTTTCCACTTCATCTTACCATTTA-3' and 5'-^{TG}T^{TG}GGT^{TG}TT^{TG}ATCC^{TG}-3') against the amplification level of *Rbm15,* which was used as a nuclear DNA control (primer sequences:5'- GGACACTTTTCTTGGGCAAC -3' and 5'-AGTTTGGCCCTGTGAGACAT-3'). Samples were run on an Abi Prism SDS 7000 machine (Applied Biosystem). Amplification conditions were: 95°C for 7 minutes followed by 35 cycles of 95°C for 10 seconds and 60°C for 30 seconds. Dissociation curves were checked to ensure the existence of a single PCR product. Each sample was run in duplicate, and samples with significant variation between duplicates were excluded. QPCR data were analyzed using 7000 System Sequence Detection Software version 1.2.3 (Applied Biosystems).

Long PCR.

Long PCR to amplify the entire mitochondrial genome or selectively deleted mtDNA molecules was done using the Expand Long Template PCR System (Roche). 25 ng total DNA was used as template. Cycling conditions were: 92°C for 2 minutes followed by 30 cycles of 92°C for 10 seconds and 68°C for 12 minutes. PCR products were separated by electrophoresis on 1% agarose gels and visualized with a Typhoon 9400 scanner (Amersham Biosciences). Primers hybridized to the control region of mtDNA located at nucleotide positions 1953-1924 and 2473-2505 (primer sequences 5'- GAG GTG ATG TTT TTG GTA AAC AGG CGG GGT -3' and 5'-GGT TCG TTT GTT CAA CGA TTA AAG TCC TAC GTG -3').

Extraction of nucleotides from neonate skeletal muscle and embryos.

Total nucleotides were extracted from neonatal skeletal muscle using the method described in (34) with the following modifications: Neonates were euthanized by decapitation and immediately dissected in order to prevent nucleotide degradation. Skeletal muscle harvested from all four limbs was pooled together and immediately chilled on dry ice. The sample was weighed and snap-frozen in liquid nitrogen. Samples were stored at -80°C until nucleotides were extracted. Samples were homogenized in cold 10% trichloroacetic acid+15mM $MgCl_2$ for 1 minute in a Qiagen TissueLyser. Halfway through, samples were incubated on ice for 30 sec.

Embryos at e10.5 were removed from the uterus and yolk sac in cold 1x PBS and immediately ground in 100mL of cold 0.4N perchloric acid using a microcentrifuge tube-fitting pestle. Following homogenization, samples were incubated on ice for 20 minutes. The rest of the extraction was performed as previously described(34).

RESULTS

Generation of *Rrm1*-D57N transgenic mice and expression analyses

We previously showed(33) that mice overexpressing either small RNR subunit, Rrm2 or p53R2, develop lung neoplasms at a high frequency, but the effect of hyperactive RNR in mammals has not been addressed. To assess the effect of loss of RNR allosteric feedback control, we generated mice that overexpress a mutant form of the large subunit. The previously identified *Rrm1*^{D57N} mutant harbors a point mutation in the activity site of the large subunit that disables feedback control(37). The *Rrm1*^{D57N} mutation was shown in both yeast and in a mammalian cell culture model to be mutagenic(6, 37), but the effect of loss of allosteric feedback control in an *in vivo* mammalian model has yet to be determined. To generate transgenic mice overexpressing *Rrm1*-D57N, we modified the previously-generated pCaggs-*Rrm1* construct. Two independent transgenic founder animals were obtained (Fig 1A, lanes 6 and 12). The founder animal in lane 12 showed greater transgene signal and the presence of two different transgene bands whereas the founder in lane 6 showed a single band of lower relative intensity; the resulting strains are referred to hereafter as *Rrm1*-D57N(low)^{Tg} (lane 6) and *Rrm1*-D57N(high)^{Tg} (lane 12). The strains were maintained on a pure FVB/N background.

Endogenous and transgenic expression was assessed in a variety of tissues in *Rrm1*-D57N(high)^{Tg} and wild-type FVB mice by Northern blot analysis (Fig 1B). In wild type FVB mice, *Rrm1* was detected most strongly in the most proliferative tissues, the testis and thymus (Fig 1B, left). Northern blot analysis of *Rrm1*-D57N(high)^{Tg} mice revealed two bands corresponding to *Rrm1* transcript, the upper band from the endogenous locus was the predominant band in the spleen and thymus, while the lower band from the transgene predominated in lung, liver, kidney, and skeletal muscle.

Figure 1. Generation of *Rrm1*-D57N overexpressing mice. *A.* Southern blot analysis of DNA from potential *Rrm1*-D57N^{Tg} founder animals. Tail DNA from potential founder animals was subjected to hybridization with *Rrm1*-specific radiolabeled probe. Arrows indicate bands corresponding to endogenous *Rrm1* gene and *Rrm1*-D57N transgene. Asterisks denote founder DNA showing presence of *Rrm1*-D57N transgene. Note that the founder in lane 12 [referred to as *Rrm1*-D57N(high)] shows an additional transgene band, indicating integration of a greater amount of the transgene DNA than the founder in lane 6 [*Rrm1*-D57N(low)]. *B.* Northern blot analysis of *Rrm1* expression in wild type and *Rrm1*-D57N(high) mice. Total RNA was extracted from the indicated tissues of wild type FVB (left panel) and *Rrm1*-D57N(high) transgenic mice (right panel) and subjected to Northern blot analysis with a radiolabeled *Rrm1*-specific probe. Positions of endogenous- and *Rrm1*-D57N-derived transcripts are indicated. Total RNA is shown as a loading control. Note that skeletal muscle lane in right panel was intentionally underloaded. Wild type FVB panel is reprinted from Xu *et al*.(33) *C.* Immunoblot analysis of *Rrm1* protein expression in the indicated tissues of wild type (wt), *Rrm1*-D57N(low)^{Tg} (L), and *Rrm1*-D57N(high)^{Tg} (H) transgenic mice. Total protein from the indicated tissues was detected with R1-specific antibody. The same membrane was probed with an antibody specific to a-tubulin as a loading control. *D*. Measurement of dNTP pools in the skeletal muscle of adult wild type, Rrm1^{Tg} and Rrm1-D57N(high)^{Tg} mice. Total nucleotides were extracted from the skeletal muscle of mice of the indicated genotypes and were assayed using the indirect enzymatic method of Sherman and Fyfe, with modifications by Ferraro, *et al*.

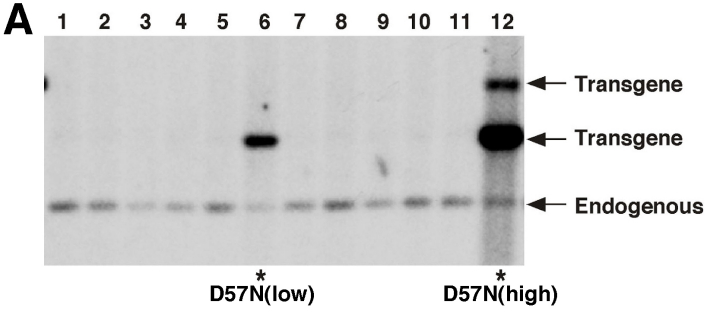
A
1 2 3 4 5 6 7 8 9 10 11 12
Transgene
Transgene
Endogenous
D57N(low)
D57N(high)

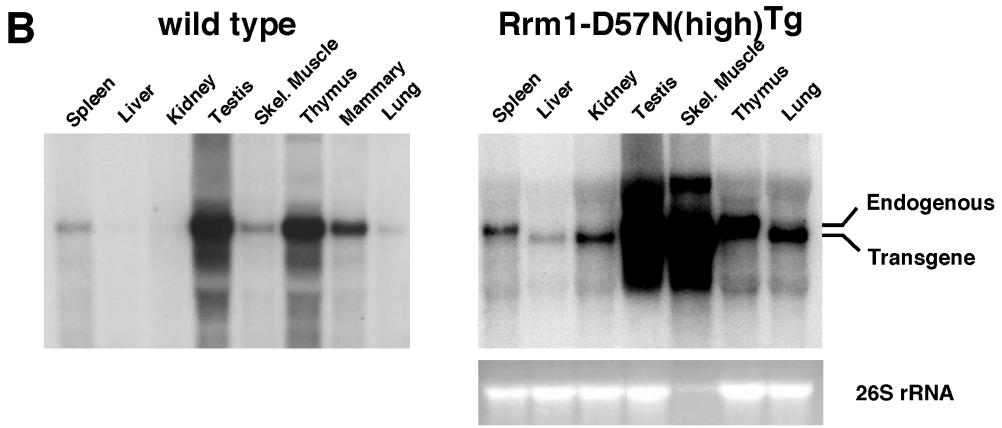
B
wild type
Rrm1-D57N(high)Tg
Spleen
Liver
Kidney
Testis
Skel. Muscle
Thymus
Mammary
Lung
Endogenous
Transgene
26S rRNA

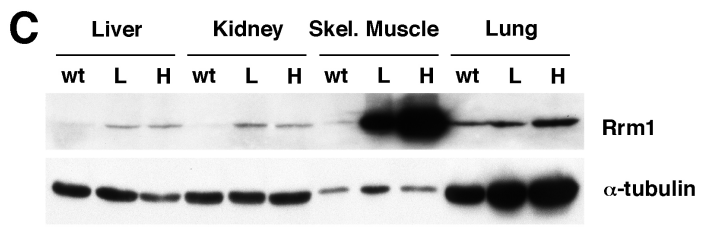
C
Liver
Kidney
Skel. Muscle
Lung
wt L H wt L H wt L H wt L H
Rrm1
α-tubulin

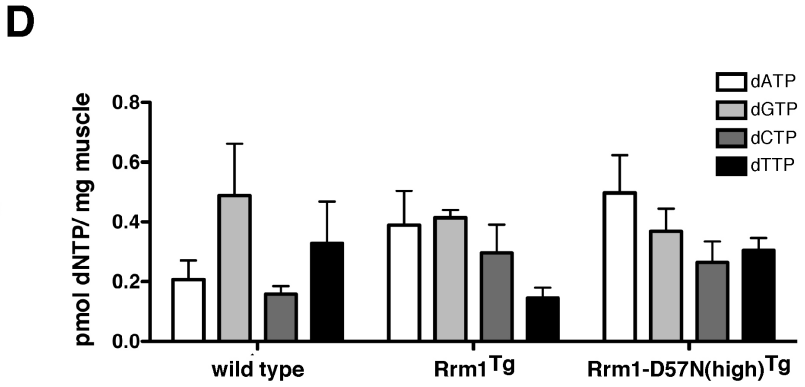
D
pmol dNTP/ mg muscle
0.0
0.2
0.4
0.6
0.8
dATP
dGTP
dCTP
dTTP
wild type
Rrm1Tg
Rrm1-D57N(high)Tg

The expression results obtained by Northern blot analysis were confirmed by immunoblot (Fig 1C). We assessed total R1 protein levels in tissues obtained from wild type FVB mice (wt), *Rrm1*-D57N(low)^{Tg} mice (L), and *Rrm1*-D57N(high)^{Tg} (H) mice. In agreement with the Southern blot in Fig 1A, *Rrm1*-D57N(high)^{Tg} mice showed higher R1 protein levels than *Rrm1*-D57N(low)^{Tg} mice, which were intermediate between wild type and *Rrm1*-D57N(high)^{Tg} levels. To obtain a more precise value for *Rrm1*-D57N overexpression in tissues from transgenic mice, we utilized the serial dilution method reported previously(34). Because pCaggs drives the greatest expression in skeletal and cardiac muscle, we assessed the level of D57N overexpression in these two tissues (Supplementary Figure 1). We found that the D57N(low)^{Tg} was expressed roughly 94-fold (93.99x) in the skeletal muscle while the D57N(high)^{Tg} was expressed over 600-fold (608.41x).

We next wanted to address whether overexpression of Rrm1-D57N in mice would cause changes to the dNTP pools. We previously reported that mice that overexpress either of the small RNR subunits, Rrm2 or p53R2, show elevated and unbalanced dNTP pools in the skeletal muscle, the tissue with the highest level of overexpression. We therefore measured dNTPs from the skeletal muscle of wild type, Rrm1^{Tg}, and Rrm1-D57N(high)^{Tg} aged 3-6 months (Figure 1D). We found no dNTP pool elevations in the Rrm1^{Tg} mice compared to wild type mice, consistent with our findings from a previous study(34). We found modest elevations in the skeletal muscle from Rrm1-D57N(high)^{Tg} (2.4-fold over wild type), but these were not statistically significant when compared to either wild type or Rrm1^{Tg} mice.

Even with the high levels of Rrm1-D57N overexpression, mice harboring the transgenes appeared grossly normal and were obtained at expected frequencies (Table 1). In crosses between wild type FVB mice and Rrm1-D57N(low)^{Tg} mice, 256 wild type and 231 transgenic

Table 1: Rrm1-D57N transgenic mice are obtained at expected frequencies.[a]

cross			genotype	# offspring
wt FVB	x	Rrm1-D57N(low)^{Tg}	wild type	256 (243.5)
			R1^{Tg}	231 (243.5)
wt FVB	x	Rrm1-D57N(high)^{Tg}	wild type	275 (260.5)
			R1^{Tg}	246 (260.5)

[a] Mice harboring *Rrm1*-D57N(low)^{Tg} or *Rrm1*-D57N(high)^{Tg} were crossed to wild type FVB mice. Progeny were genotyped at weaning by PCR. Observed numbers of animals of each genotype are indicated with expected number in parentheses.

mice were obtained (p=0.26, c^2). Likewise, crosses between wild type FVB and Rrm1-D57N(high)^{Tg} mice yielded 275 wild type and 246 transgenic mice (p=0.20, c^2). In order to assess the phenotypic effects of loss of RNR allosteric regulatory control in mice, we generated a cohort of Rrm1-D57N(low)^{Tg}, Rrm1-D57N(high)^{Tg}, and transgene-negative control mice and aged them to a maximum age of 18 months. Necropsy of these mice revealed that mice harboring either D57N transgene were grossly normal relative to wild type control animals. We found a modest increase in the lung tumor incidence in both Rrm1-D57N(low)^{Tg} (36.73%, n=49) and Rrm1-D57N(high)^{Tg} (34.62%, n=26) mice compared to wild type mice (27.27%, n=44). Mean tumor size, tumor multiplicity, and histopathological grade were not altered by overexpression of Rrm1-D57N.

The Rrm1-D57N mutation has been previously reported to be mutagenic in both yeast(6) and mammalian cells(37). To assess the mutagenic potential of Rrm1-D57N overexpression, we used the Big Blue mutation detection system to measure the mutant frequency in the lungs of Rrm1-D57N(low)^{Tg} and Rrm1-D57N(high)^{Tg} mice, and also combined overexpression of Rrm1-D57N^{Tg} with a mismatch repair deficiency caused by loss of *Msh6*. We found no difference in the mutation frequency in either Rrm1-D57N^{Tg} strain compared to wild type mice. Rrm1-D57N overexpression also failed to synergize with mismatch repair deficiency to significantly shorten lifespan or accelerate tumor development. These results suggest that overexpression of an RNR mutant defective for allosteric feedback control has limited effects in mice.

Simultaneous overexpression of *Rrm1*-D57N and either small RNR subunit causes synthetic lethality

We previously reported (34) that combined overexpression of *Rrm1* and either small RNR subunit resulted in viable mice which developed late-onset mitochondrial DNA (mtDNA)

depletion. In crosses between Rrm1^{Tg} and Rrm2^{Tg}, roughly 49 bitransgenic mice were expected and 46 were observed; similarly, in crosses between Rrm1^{Tg} and p53R2^{Tg}, 33 bitransgenic mice were observed of about 38 expected. However, those mice only exhibited disruption of one RNR regulatory mechanism, control of RNR activity through limitation of small subunit protein levels. As previously stated, mice overexpressing *Rrm1*-D57N alone were also obtained at expected frequencies and were grossly normal. In order to assess the effect of simultaneous disruption of multiple RNR regulatory modes, we crossed mice overexpressing either small RNR subunit with mice overexpressing *Rrm1*-D57N. We used each *Rrm1*-D57N strain individually in these crosses, resulting in four possible overexpression combinations. We found that mice with either level of *Rrm1*-D57N overexpression and either small RNR subunit were not viable (Table 2). Specifically, of an expected 30 *Rrm1*-D57N(high)^{Tg} + *p53R2*^{Tg} bitransgenic mice, 0 were obtained. Likewise, 51.25 *Rrm1*-D57N(low)^{Tg} + *p53R2*^{Tg} bitransgenic mice were expected and 0 were observed, and 26.5 *Rrm1*-D57N(high)^{Tg} + *Rrm2*^{Tg} bitransgenic mice were expected and 0 were obtained. Interestingly, of 69.75 expected *Rrm1*-D57N(low)^{Tg} + *Rrm2*^{Tg} bitransgenic mice expected, 5 were obtained that survived to adulthood. Of the five surviving bitransgenic adults, two survived only 21 days and one only 25 days. The last two mice were littermates, one female surviving 90 days and one male surviving 102 days. These results suggest that simultaneous disruption of multiple regulatory mechanisms of RNR is incompatible with survival in mice.

Lethality manifests at different stages depending on cross

While rare surviving adult *Rrm1*-D57N(low)^{Tg} + *Rrm2*^{Tg} mice were obtained, no other cross produced any surviving offspring. To determine the exact stage of lethality, we dissected embryos from *Rrm1*-D57N(high)^{Tg} x *p53R2*^{Tg} mice (Fig 2A). Through embryonic day 10.5 (e10.5), bitransgenic embryos were observed at the expected frequencies, and most were grossly

Table 2. Synthetic lethality upon simultaneous overexpression of *Rrm1*-D57N and either small RNR subunit.

cross	genotype	*Rrm1*^{Tg} (wt)	*Rrm1*-	*Rrm1*-
R1^{Tg} x *Rrm2*^{Tg}	wild type	57 (48.75)	96 (69.75)	33 (26.5)
	R1^{Tg}	54 (48.75)	93 (69.75)	35 (26.5)
	Rrm2^{Tg}	38 (48.75)	85 (69.75)	38 (26.5)
	R1^{Tg} + *Rrm2*^{Tg}	46 (48.75)	5 (69.75)[a]	0 (26.5)[a]
R1^{Tg} x *p53R2*^{Tg}	wild type	29 (37.25)	77 (51.25)	51 (30)
	R1^{Tg}	52 (37.25)	68 (51.25)	40 (30)
	p53R2^{Tg}	35 (37.25)	60 (51.25)	29 (30)
	R1^{Tg} + *p53R2*^{Tg}	33 (37.25)	0 (51.25)[a]	0 (30)[a]

Note: Mice harboring *Rrm1*^{Tg}, *Rrm1*-D57N(low)^{Tg} , or *Rrm1*-D57N(high)^{Tg} were crossed to mice carrying either the Rrm2 or p53R2 transgene. Progeny were genotyped at weaning by Southern blot. Observed numbers of animals of each genotype are indicated with expected number in parentheses.

[a] $p<0.05$, c^2 test.

Figure 2. **Gross morphology of *Rrm1*-D57N(high)^{Tg} + *Rrm2*^{Tg} or *p53R2*^{Tg} bitransgenic embryos.** *A*. *Rrm1*-D57N(high)^{Tg} + *p53R2*^{Tg} bitransgenic embryos. Bitransgenics are grossly normal through 11.5 dpc. At 12.5 dpc, dead bitransgenic embryos were observed. *B*. *Rrm1*-D57N(high)^{Tg} + *Rrm2*^{Tg} bitransgenic embryos and controls. Bitransgenics are found dead as early as 13.5 dpc. Some normal embryos are observed at e14.5.

A

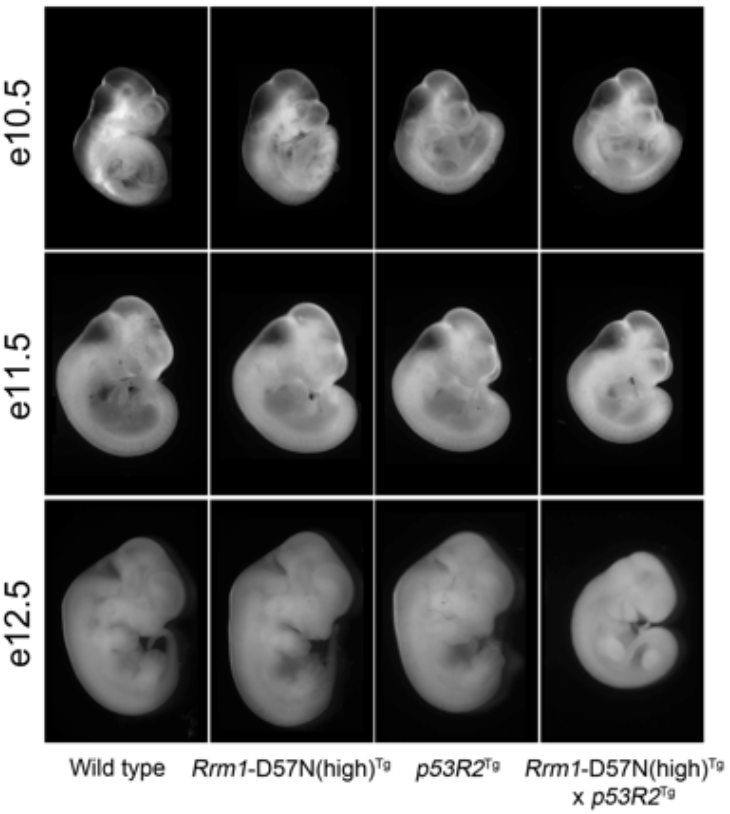
e10.5
e11.5
e12.5
Wild type
Rrm1-D57N(high)Tg
p53R2Tg
Rrm1-D57N(high)Tg
x p53R2Tg

B

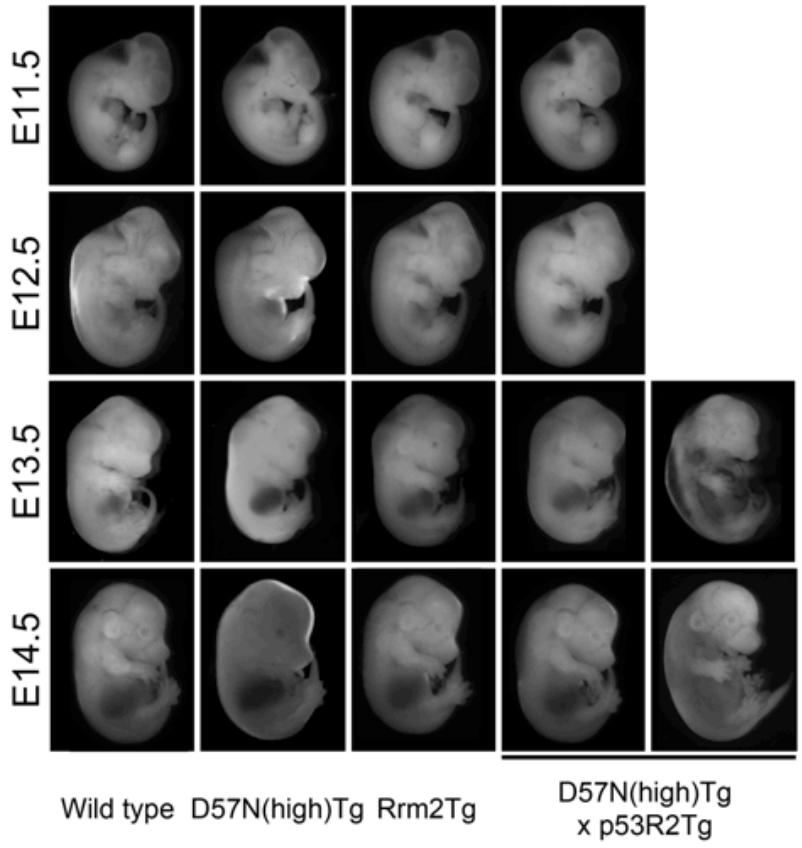
E11.5
E12.5
E13.5
E14.5
Wild type
D57N(high)Tg
Rrm2Tg
D57N(high)Tg
x p53R2Tg

normal. After e12.5, only dead bitransgenic embryos were observed, and were fewer than expected. These embryos lacked blood within the vessels of the yolk sac (data not shown). The frequency of resorbed embryos increased over the time frame analyzed, with few resorptions being observed before e10.5, but 8, 19 and 9 resorptions at e10.5, e11.5 and e12.5, respectively. Life span of *Rrm1*-D57N(high)^{Tg} + *p53R2*^{Tg} mice was summarized in Table 2.

Bitransgenic embryos derived from crosses between *Rrm1*-D57N(high)^{Tg} and *Rrm2*^{Tg} mice displayed great variability in lifespan. As early as e10.5, abnormal bitransgenic embryos were observed. Normal bitransgenic embryos were observed through e17.5 but at lower than expected frequencies, and two bitransgenic mice were observed that had survived gestation but died immediately after birth. Life span of *Rrm1*-D57N(high)^{Tg} + *Rrm2*^{Tg} mice was summarized in Table 3.

The lifespan of *Rrm1*-D57N(low)^{Tg} + *p53R2*^{Tg} bitransgenic mice was intermediate between that of *Rrm1*-D57N(high)^{Tg} + *Rrm2*^{Tg} mice and *Rrm1*-D57N(low)^{Tg} + *Rrm2*^{Tg} mice (Figure 3). *Rrm1*-D57N(low)^{Tg} + *p53R2*^{Tg} bitransgenic mice survived birth and developed normally through approximately 4 days. However, survival of these bitransgenics decreased rapidly at P5, with all bitransgenics observed dying between P5 and P8 (Fig 3D). The frequency of *Rrm1*-D57N^{Tg} + *p53R2*^{Tg} and *Rrm1*-D57N^{Tg} + *Rrm2*^{Tg} mice at weaning age is summarized in Table 2. Overall, higher levels of expression of Rrm1-D57N cause a shorter lifespan, while overexpression of p53R2 has more severe effects when combined with Rrm1-D57N than does overexpression of Rrm2.

Altered dNTP pools in the skeletal muscle of Rrm1-D57N(low)^{Tg} + Rrm2^{Tg} bitransgenic mice

We hypothesized that simultaneously removing both main regulatory mechanisms

Table 3. Lifespan of *Rrm1*-D57N(high)^{Tg} + *p53R2*^{Tg} bitransgenic embryos.[a]

	Rrm1-D57N(high)^{Tg} x p53R2^{Tg}								
	wild type		Rrm1-D57N^{Tg}		p53R2^{Tg}		bitransgenic		
stage	# obs	(#exp)	# obs	(#exp)	# obs	(#exp)	# obs	(#exp)	resorptions
9.5	5	4.5	6	4.5	3	4.5	4(1)	4.5	2
10.5	37(3)	26.75	24	26.75	14	26.75	32(1)	26.75	8
11.5	54	30.5	29	30.5	36	30.5	13(3)	30.5	19
12.5	25	16.5	14	16.5	16	16.5	11(11)	16.5	9
13.5	12	10.25	17(2)	10.25	10(1)	10.25	2(2)	10.25	1
14.5	7	4	5	4	4	4	0	4	0

[a] Females harboring the *Rrm1*-D57N(high) transgene were mated to males harboring the p53R2 transgene. At the indicated time points (in days post coitus or dpc) females were euthanized by CO_2 asphyxiation and the embryos analyzed. DNA isolated from the yolk sacs was genotyped by Southern blot analysis. Total numbers of embryos of each genotype observed are indicated with expected numbers. Numbers in parentheses indicate dead and abnormal embryos.

Table 4. Lifespan of *Rrm1*-D57N(high)^{Tg} + *Rrm2*^{Tg} bitransgenic embryos.[a]

	Rrm1-D57N(high)^{Tg} x Rrm2^{Tg}								
	wild type		Rrm1-D57N^{Tg}		Rrm2^{Tg}		bitransgenic		
stage	# obs	(#exp)	# obs	(#exp)	# obs	(#exp)	# obs	(#exp)	resorptions
9.5	3	4	5	4	3	4	5	4	0
10.5	7	7.25	3	7.25	11	7.25	8(1)	7.25	3
11.5	6	6	6	6	7	6	5	6	9
12.5	8	10	7(1)	10	16	10	9(1)	10	2
13.5	2	8.25	7	8.25	13(1)	8.25	11(6)	8.25	1
14.5	2	4	2	4	7	4	5(3)	4	1
15.5	7	9.25	9(1)	9.25	11(1)	9.25	10(7)	9.25	1
16.5	1	4	3	4	7	4	5(1)	4	0
17.5	7	7	6	7	12(1)	7	4(3)	7	0
18.5	11(1)	8.75	7	8.75	17	8.75	0	8.75	7
19.5	4	2.75	4(1)	2.75	3	2.75	0	2.75	0
P0	9	4.5	3	4.5	4	4.5	2(2)	4.5	0

[a] Females harboring the *Rrm1*-D57N(high) transgene were mated to males harboring the Rrm2 transgene. At the indicated time points (in days post coitus or dpc) females were euthanized by CO_2 asphyxiation and the embryos analyzed. DNA isolated from the yolk sacs was genotyped by Southern blot analysis. Total numbers of embryos of each genotype observed are indicated with expected numbers. Numbers in parentheses indicate dead and abnormal embryos.

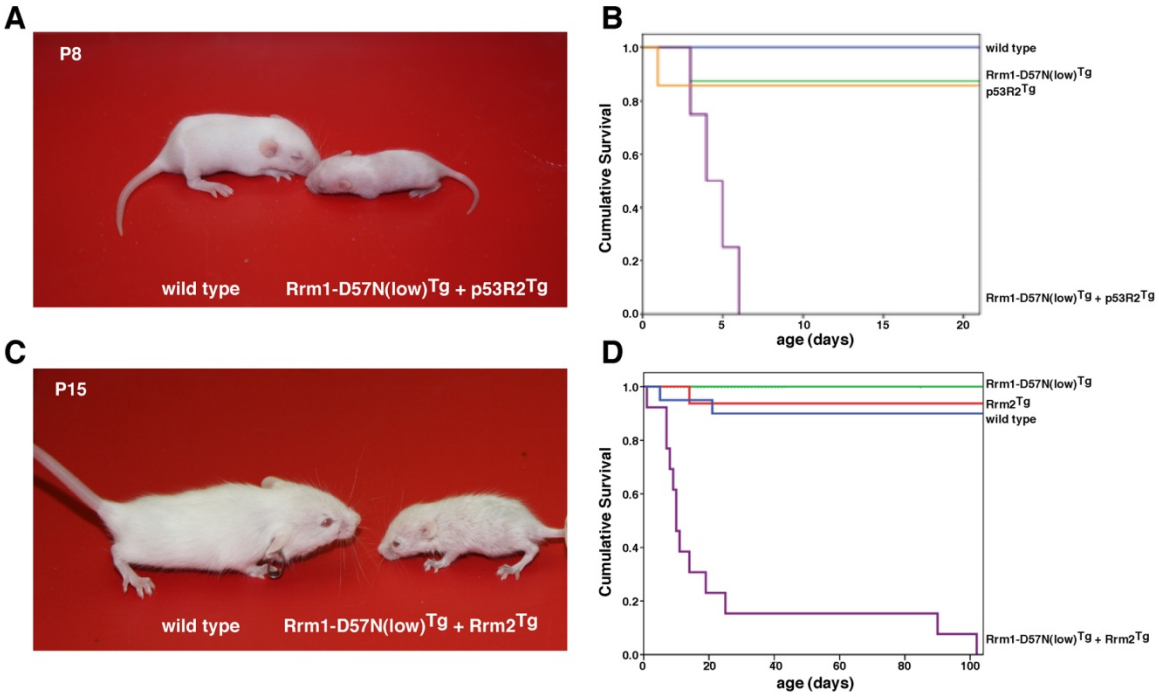

Figure 3. Reduced survival of bitransgenic mice. *A*. Gross morphology of *Rrm1*-D57N(low)^{Tg} + *p53R2*^{Tg} bitransgenic mice. *B*. Reduced survival of bitransgenic mice derived from *Rrm1*-D57N(low)^{Tg} x *p53R2*^{Tg} cross. Pups were counted on P0 (day of birth) and monitored daily. Pups were genotyped by Southern blot analysis of tail DNA at 21 days of age or when found dead. Bitransgenic mice (purple line) have a 50% survival rate of 5 days. *C*. Gross morphology of *Rrm1*-D57N(low)^{Tg} + *Rrm2*^{Tg} bitransgenic mice. Bitransgenic mice are runted and show alopecia and decreased activity. A bitransgenic mouse (right) is pictured at P15 with a wild type littermate (left). *D*. Survival of *Rrm1*-D57N(low)^{Tg} + *Rrm2*^{Tg} bitransgenic mice. Pups were genotyped by Southern blot analysis of tail DNA at 21 days of age or when found dead. Bitransgenics surviving past 21 days of age were housed with sex-matched littermates and monitored frequently, and euthanized when moribund.

governing RNR activity would lead to elevated and/or unbalanced nucleotide pools, which may have consequences for genomic stability and survival. We next wanted to test whether RNR deregulation in mice caused lethality through alterations to dNTP pools. In order to test this, we extracted total nucleotides from the skeletal muscle of Rrm1-D57N(low)^{Tg} + Rrm2^{Tg} bitransgenic neonates at P5. The total amount of each dNTP was measured using the indirect enzymatic assay described by Sherman and Fyfe with modifications(34, 40, 41). Remarkably, the level of dATP in Rrm1-D57N(low)^{Tg} + Rrm2^{Tg} bitransgenic muscle tissue was increased over 300-fold over wild type (Figure 4A). This increase in dATP actually interfered with the assays to measure dGTP, dCTP, and dTTP by competing with the radiolabeled dATP for incorporation into the DNA product. We therefore measured dNTPs in the bitransgenics by preparing 10- or 100-fold dilutions and compared the dNTP level to undiluted control samples. Levels of each nucleotide were increased in the bitransgenics relative to wild type mice; dATP was increased 335-fold, dGTP was increased 2.55-fold, dCTP was increased 8.78-fold, and dTTP was increased 12.57-fold. The data are summarized in Figure 4A. These results suggest that simultaneous disruption of multiple regulatory modes of RNR dramatically elevates RNR activity and leads to significant increases in dNTP levels.

Of the four RNR transgene combinations that result in synthetic lethality, the Rrm1-D57N(low)^{Tg} + Rrm2^{Tg} bitransgenic mice display the least severe phenotype and the longest lifespan, yet show dramatic dNTP pool alterations within the skeletal muscle. We therefore hypothesized that the combination which produces the most severe phenotype, Rrm1-D57N(high)^{Tg} x p53R2^{Tg}, would show a more dramatic increase in dNTPs, which would correlate with the early lethality. We tested this hypothesis by extracting nucleotides from the skeletal muscle from Rrm1-D57N(low)^{Tg} + p53R2^{Tg} neonates (Figure 4B) and from whole

Figure 4. dNTP pool alterations in bitransgenic embryos and neonates. *A*. dNTP pools in Rrm1-D57N(low)^{Tg} + Rrm2^{Tg} bitransgenic neonates. Total nucleotides were extracted from the skeletal muscle of bitransgenic and control littermates at P5. Each dNTP was measured by an indirect enzymatic assay. Results are normalized for total amount of tissue used. *B*. dNTP pools in Rrm1-D57N(low)^{Tg} + p53R2^{Tg} bitransgenic neonates at P3 or P5. *C*. dNTP pools from whole embryos derived from the Rrm1-D57N(high)^{Tg} x p53R2^{Tg} cross at e10.5. *D*. dNTP pools from whole embryos derived from the Rrm1-D57N(low)^{Tg} x Rrm2^{Tg} cross at e10.5. *E*. NDP precursor pools in Rrm1-D57N(low)^{Tg} + Rrm2^{Tg} bitransgenic neonate skeletal muscle. Nucleotides are measured by HPLC and compared to standard curves.

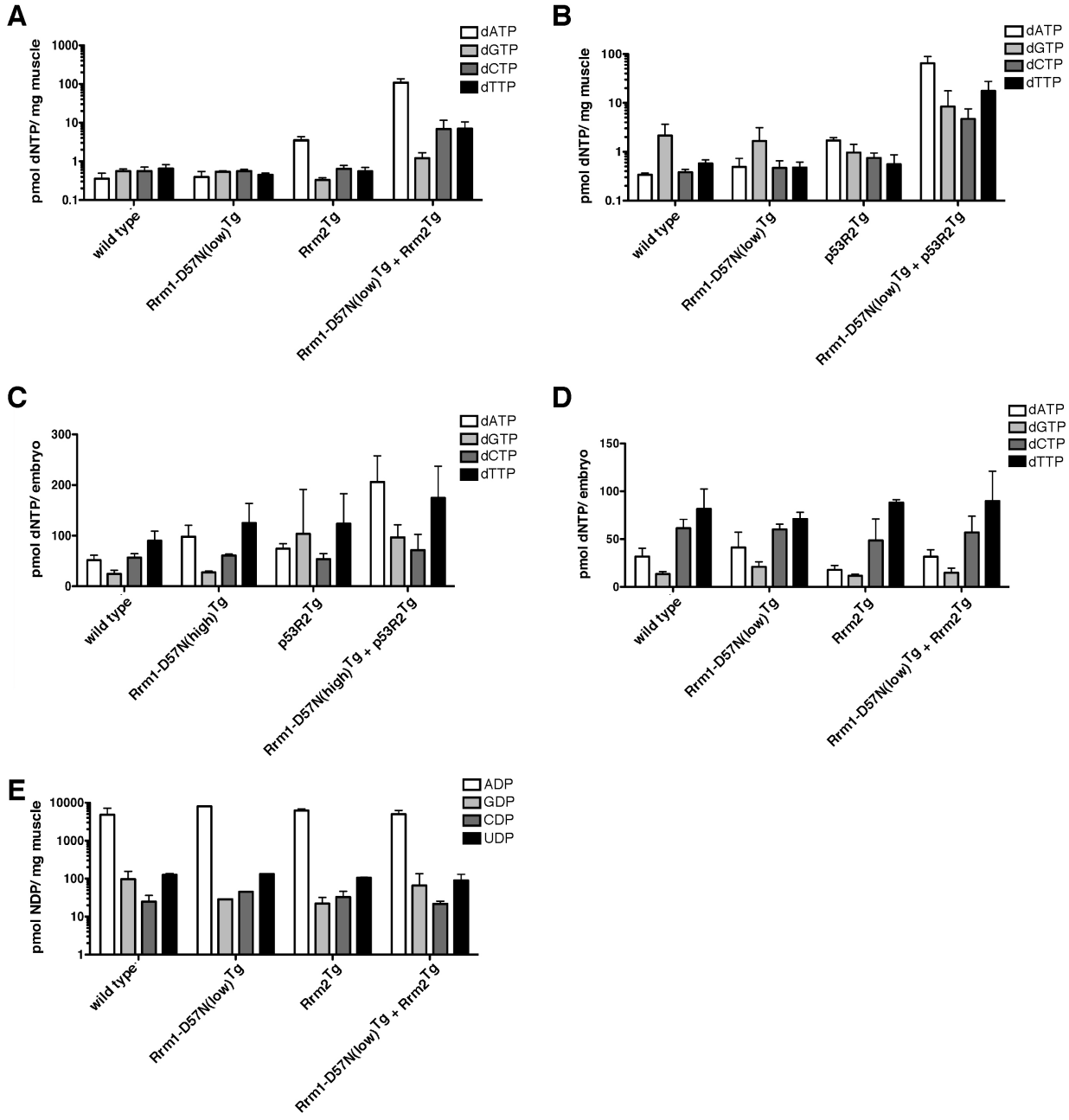
A
pmol dNTP/ mg muscle
1000
100
10
1
0.1
dATP
dGTP
dCTP
dTTP
wild type
Rrm1-D57N(low)Tg
Rrm2Tg
Rrm1-D57N(low)Tg + Rrm2Tg
B
pmol dNTP/ mg muscle
100
10
1
0.1
dATP
dGTP
dCTP
dTTP
wild type
Rrm1-D57N(low)Tg
p53R2Tg
Rrm1-D57N(low)Tg + p53R2Tg
C
pmol dNTP/ embryo
300
200
100
0
dATP
dGTP
dCTP
dTTP
wild type
Rrm1-D57N(high)Tg
p53R2Tg
Rrm1-D57N(high)Tg + p53R2Tg
D
pmol dNTP/ embryo
150
100
50
0
dATP
dGTP
dCTP
dTTP
wild type
Rrm1-D57N(low)Tg
Rrm2Tg
Rrm1-D57N(low)Tg + Rrm2Tg
E
pmol NDP/ mg muscle
10000
1000
100
10
1
ADP
GDP
CDP
UDP
wild type
Rrm1-D57N(low)Tg
Rrm2Tg
Rrm1-D57N(low)Tg + Rrm2Tg

embryos derived from the Rrm1-D57N(high)^{Tg} x p53R2^{Tg} cross at e10.5 (Figure 4C).

While dNTP pools were again elevated and unbalanced in the Rrm1-D57N(low)^{Tg} + p53R2^{Tg} neonatal skeletal muscle, they were not perturbed to the same extent as in Rrm1-D57N(low)^{Tg} + Rrm2^{Tg} neonates.

We were surprised to find that dNTP pools were only moderately altered in Rrm1-D57N(high)^{Tg} + p53R2^{Tg} bitransgenic embryos relative to wild type embryos. dATP showed a 3.99-fold increase, while dGTP was increased 3.91-fold, dCTP was increased 1.26-fold, and dTTP was increased 1.94-fold. The increases in dATP and dGTP are statistically significant ($p=0.02$ and $p=0.01$, respectively, Student's t-test), while the changes in dCTP and dTTP are not. However, these results suggest the simultaneous overexpression of Rrm1-D57N(high)^{Tg} and p53R2^{Tg} generate altered dNTP pools in developing embryos.

These results suggested that the timing of lethality is dictated in part by dNTP pool alterations during embryonic development. We hypothesized that if Rrm1-D57N(high)^{Tg} + p53R2^{Tg} bitransgenic embryos show only minor dNTP pool changes yet die during mid-gestation, then perhaps embryos carrying the Rrm1-D57N(low) transgene are able to survive gestation because they exhibit no dNTP pool changes as embryos, and show dramatic increases in dNTP pools later as the transgenes become highly expressed within the skeletal muscle. We tested this hypothesis by extracting and measuring dNTPs in whole embryos derived from the Rrm1-D57N(low)^{Tg} + Rrm2^{Tg} cross at e10.5. We found no difference in any of the dNTPs between the genotypes, supporting our hypothesis. The data are summarized in Figure 4D.

Extreme RNR hyperactivity could not only elevate dNTP pools to toxic levels, but could conceivably also deplete the pools of precursors. In order to test whether this was occurring in our bitransgenic neonates, we measured the levels of the NDPs (CDP, UDP, GDP, and ADP) by

HPLC (Figure 4E). We again found no differences between genotypes. These data suggest that elevated RNR activity causes increased and unbalanced dNTP pools, but not depleted precursor pools.

Mitochondrial genome instability does not cause synthetic lethality in the bitransgenics

We previously reported age-dependent mtDNA depletion in wild-type *Rrm1*^{Tg} + *Rrm2*^{Tg} or *p53R2*^{Tg} mice, to levels of approximately 40% compared to wild-type (42). Furthermore, mtDNA depletion to <1-10 % in mice is known to be lethal during embryonic development (43) and after birth (15). Therefore, we asked if the synthetic lethality of *Rrm1*-D57N^{Tg} + *Rrm2*^{Tg} or *p53R2*^{Tg} bitransgenic mice was caused by mtDNA instability. We measured mtDNA copy number in Rrm1-D57N(low)^{Tg} + Rrm2^{Tg} bitransgenic mice at juvenile (P4 and P8), young adult (P19 and P25), and aged adult (P90 and P102) mice (Figure 5A). We found that the bitransgenic mice had normal mtDNA copy numbers in the skeletal muscle at P4 and P8. However, while mtDNA copy number in skeletal muscle of control mice increased with age, mtDNA copy number in the skeletal muscle of bitransgenic mice failed to expand to the same level throughout development. At P19, mtDNA copy number in bitransgenic mice was ~50% of the wild type level. In the two mice that survived to 90 and 102 days, mtDNA copy numbers in skeletal muscle were 30 % and 62 % of the wild-type levels, respectively. Therefore, as the mice aged beyond P19, the mtDNA levels remained lower in the Rrm1-D57N(low)^{Tg} + Rrm2^{Tg} bitransgenic mice than in wild-type mice, but the depletion did not appear to progress below the levels present at P19. The data are summarized in Figure 5A.

We measured mtDNA copy numbers also in other tissues of the Rrm1-D57N(low)Tg + Rrm2Tg bitransgenic mice. In heart, the mtDNA level remained similar to wild-type both at P8 and P25. In liver and kidney, the mtDNA copy numbers were normal at P8, and showed a

Figure 5. **mtDNA integrity in bitransgenic mice.** *A*. mtDNA copy number in bitransgenic mice from the *Rrm1*-D57N(low)^{Tg} x *Rrm2*^{Tg} cross. Total DNA was extracted from skeletal muscle of bitransgenic and control mice at different stages of development: juvenile=P4, P8; young adult= P19, P25; aged adult=P90, P102.mtDNA is quantified by qPCR and normalized to the nuclear 18S rRNA. *B*. Long PCR on mtDNA from skeletal muscle of *Rrm1*-D57N(low)^{Tg} + *Rrm2*^{Tg} bitransgenic and wild type littermate at P25. Only the full 16 kb mtDNA is detected. *C.* Activity of respiratory chain complexes in skeletal muscle of *Rrm1*-D57N(low)^{Tg} + *Rrm2*^{Tg} bitransgenic and wild type littermate at P25. Tissues are stained for activity of the mtDNA-encoded complex IV (COX, brown), the nDNA-encoded complex II (SDH, blue), or both.

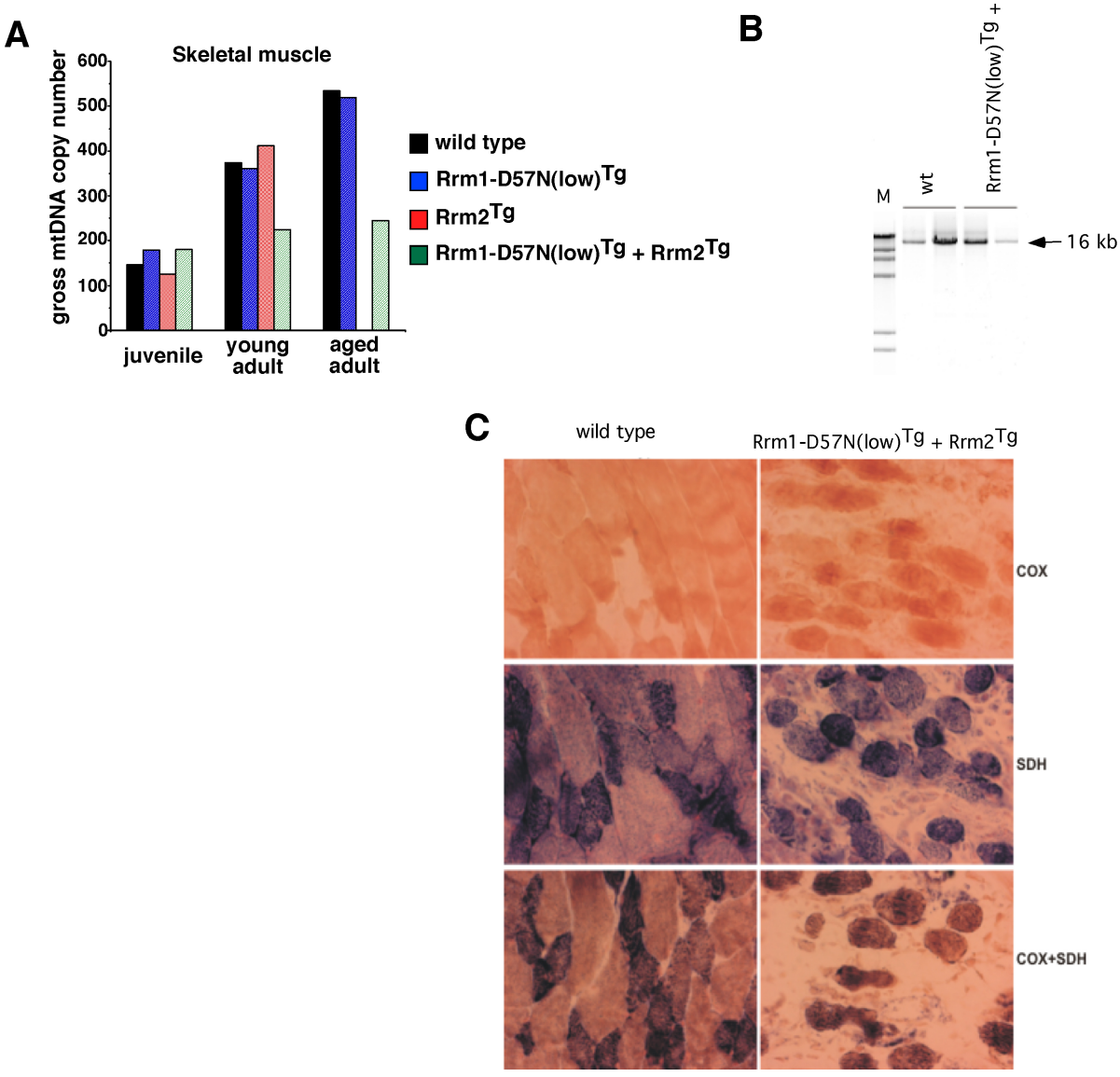
A
Skeletal muscle
gross mtDNA copy number
600
500
400
300
200
100
0
juvenile
young adult
aged adult
wild type
Rrm1-D57N(low)Tg
Rrm2Tg
Rrm1-D57N(low)Tg + Rrm2Tg
B
M
wt
Rrm1-D57N(low)Tg + Rrm2Tg
16 kb
C
wild type
Rrm1-D57N(low)Tg + Rrm2Tg
COX
SDH
COX+SDH

tendency to decrease at P19 and P25 but this difference was not statistically significant (data not shown). These results suggest that simultaneous overexpression of Rrm1-D57N(low)^{Tg} and Rrm2^{Tg} delays the developmental amplification of mtDNA, but the residual mtDNA is higher than the minimum threshold reported to escape pathogenic mtDNA depletion in mice.

In addition to quantitative mtDNA defects, alterations to dNTP pools have been suggested to cause mtDNA point mutations and large scale mtDNA deletions in humans (Tyynismaa et al. Am J Hum Genet. 2009 Aug;85(2):290-5, Nishino et al. Science. 1999 Jan 29;283(5402):689-92,, Nishigaki et al. J Clin Invest. 2003 Jun;111(12):1913-21.). We sequenced mtDNA in the hypervariable control region and the cytochrome *b* gene regions but found no increase in mtDNA point mutations in skeletal muscle of D57N(low)Tg + Rrm2Tg bitransgenic mice at P25 (data not shown). To determine whether mtDNA deletions were present, we performed long PCR to assess the total size of the mtDNA in P25 bitransgenic mice. In both wild type and *Rrm1*-D57N(low)^{Tg} + *Rrm2*^{Tg} bitransgenic mice, we detected only the full-length mtDNA (16kb) in skeletal muscle (Figure 5B), kidney and heart (data not shown), indicating that no deletions were formed in the mtDNA of Rrm1-D57N(low)^{Tg} + Rrm2^{Tg} bitransgenic mice.

A clinically significant defect of mtDNA maintenance leads to dysfunction of respiratory chain complex IV (cytochrome *c* oxidase, COX) that is partially encoded by mtDNA. Compensatory hyperproliferation of mitochondria, which can be observed as increased activity of the nuclear encoded complex II (succinate dehydrogenase, SDH), is also frequently observed. We performed the COX/SDH assay on frozen skeletal muscle from the P25 bitransgenic, which displayed ~50% mtDNA, and a wild type littermate (Figure 5C). We found normal COX activity in the muscle of the bitransgenic mouse, and no increase in SDH signal.

Taken together, these results showed that extreme upregulation of dNTP pools in

bitransgenic D57N(low)Tg + Rrm2Tg mice caused age-dependent mtDNA depletion in skeletal muscle, but no point mutations or deletions. The mice were born with normal mtDNA copy numbers, suggesting that mtDNA maintenance was not impaired during embryonic development. Finally, the mtDNA depletion was not deep enough to impair respiratory chain function, as determined by the COX/SDH activity assay.

Bitransgenic neonates display pleural effusion, hepatocellular swelling, and kidney degeneration.

The aforementioned muscle defects were only observed in Rrm1-D57N(low)^{Tg} + Rrm2^{Tg} bitransgenic mice that survived to adulthood, but do not account for the earlier lethality observed in this and the other synthetic lethal crosses. We therefore sought to determine the defects that arise in the more severely-affected mice via histological staining of a wide range of tissues at earlier time points. Mice were monitored and weighed daily from birth in order to be able to predict when the bitransgenics might expire; at that time the entire litter was culled for histological analysis. Liver, kidneys, and muscle tissues were all examined by H&E staining for changes in morphology.

We first noticed upon necropsy that Rrm1-D57N(low)^{Tg} + Rrm2^{Tg} bitransgenic mice, but not control mice, showed pleural effusion. Fluid accumulation affected the entire pleural cavity, and in mice surviving 8 days or later, was also observed within the abdomen. Pleural effusion was observed in roughly 50% of all Rrm1-D57N(low)^{Tg} + Rrm2^{Tg} neonates as early as P4. At P5 and later, all bitransgenic neonates displayed the fluid accumulation. However, effusion was not observed in the mice surviving 19 days or longer. In order to determine the type of the pleural effusion, we collected the fluid and analyzed the constituents. Total fluid albumin content among three bitransgenic neonates averaged 1.1 g/dL; the total fluid protein content averaged 1.67 g/dL.

Pleural effusions with less than 1.6g/dL albumin and less than 2.0 g/dL total protein are considered transudative.

In order to determine the cause of the pleural effusions, we analyzed liver, intestine, spleen, kidney, heart, lung, skeletal muscle, and brain via H&E staining. Rrm1-D57N(low)^{Tg} + Rrm2^{Tg} bitransgenic mice surviving to 9 or 11 days of age showed kidney degeneration. Kidneys exhibited degeneration of renal tubules, edema, dilated tubules, and fibrosis (Figure 6A). This phenotype was not observed in the kidneys of 3-month-old bitransgenic mice.

We also found that bitransgenic neonates displayed hepatocellular swelling at p6 (n=4), p7 (n=5), p8 (n=2), p9 (n=1), and p11 (n=1) (Figure 6C and data not shown). Examination of the liver isolated from bitransgenic mice surviving 3 months of age did not show the same phenotype (DNS). Hepatocytes can accumulate either glycogen or lipid to show the swollen phenotype. To distinguish between these two possibilities, we performed periodic acid Schiff's (PAS) staining on liver samples from selected bitransgenics and control animals. Liver from a bitransgenic neonate at P11 showed a lack of red staining, indicating lipid accumulation in those cells (DNS). However, a bitransgenic neonate aged P9 showed hepatocytes with lipid accumulation as well as hepatocytes with glycogen (Figure 6D).

Severe muscle degeneration in *Rrm1*-D57N(low)^{Tg} + *Rrm2*^{Tg} bitransgenic mice

Of approximately 70 *Rrm1*-D57N(low)^{Tg} + *Rrm2*^{Tg} bitransgenic adults expected, only 5 were observed. The few surviving *Rrm1*-D57N(low)^{Tg} + *Rrm2*^{Tg} bitransgenic mice were runted compared to littermates. Throughout life, bitransgenic mice were hunched, inactive, and displayed small muscles and alopecia. All bitransgenic mice showed a significant loss of body weight prior to death. Upon necropsy, we found that bitransgenic mice which survived 90 days or longer exhibited severe skeletal and cardiac muscle degeneration. H&E staining of

Figure 6. Spectrum of phenotypes in *Rrm1*-D57N^{Tg} + *Rrm2*^{Tg} bitransgenic neonates. *A.* Kidney degeneration in bitransgenic animals. Tissues were harvested from bitransgenic and control littermates at P11 and fixed overnight in 10% formalin. Sections were stained with H&E. The bitransgenic shows degeneration of cortical tubules (arrows), dilated tubules in the medulla (arrowheads), and fibrosis (thick arrows). *B.* Hepatocellular swelling in bitransgenic liver. Tissues were harvested from bitransgenic and control littermates at P9 and fixed, sectioned, and H&E stained as previously. Arrow indicates focus of hepatocytes with abnormal accumulations of lipid or glycogen, leading to swollen appearance. *C.* Periodic acid Schiff's stain of neonate livers from (*B*). Hepatocytes with glycogen accumulation stain fuschia, while hepatocytes with lipid accumulation remain mostly white. Glycogen is abundant in the wild type liver but does not accumulate within hepatocytes.

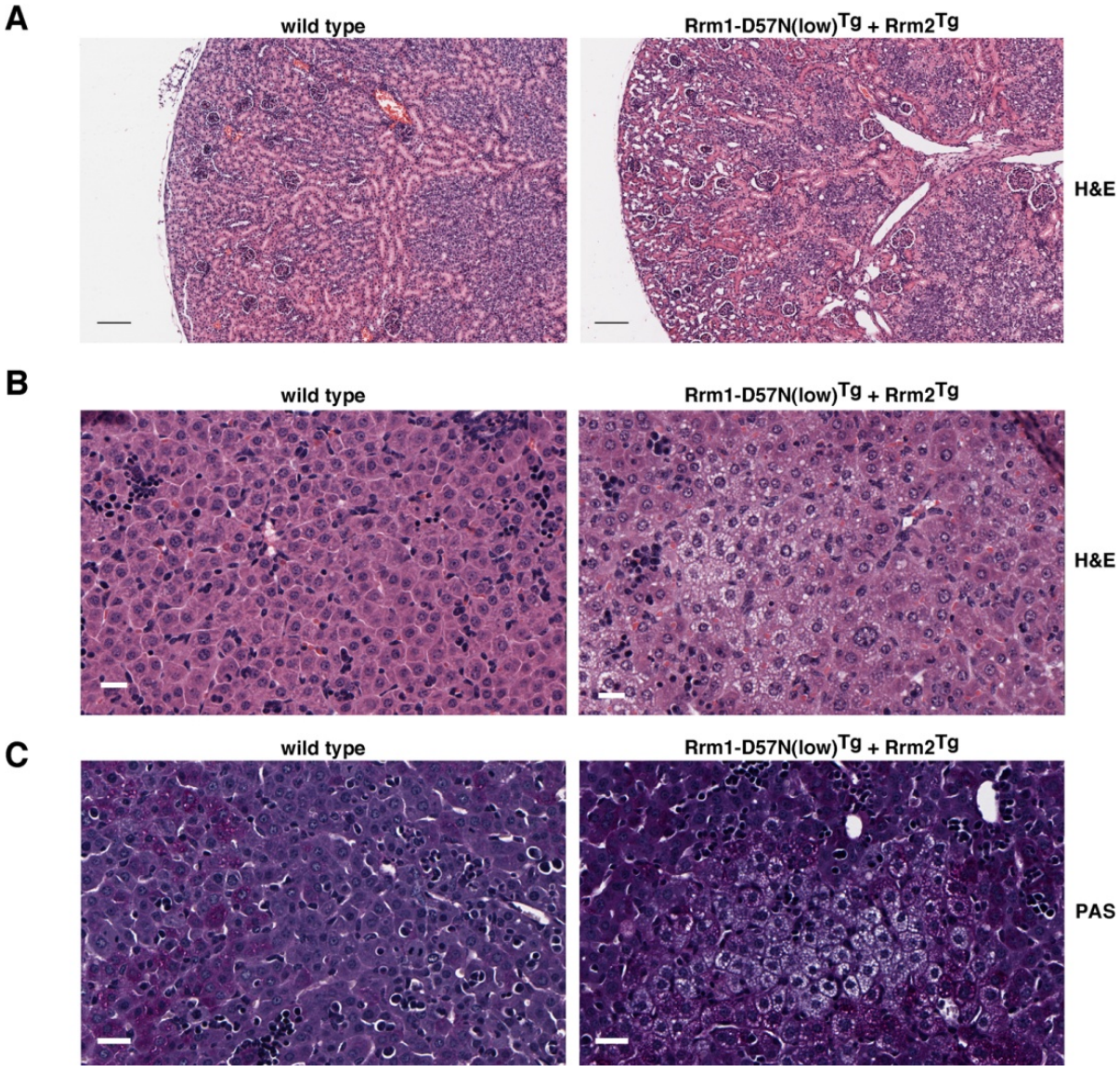
A
wild type
Rrm1-D57N(low)Tg + Rrm2Tg
H&E
B
wild type
Rrm1-D57N(low)Tg + Rrm2Tg
H&E
C
wild type
Rrm1-D57N(low)Tg + Rrm2Tg
PAS

bitransgenic and control skeletal muscle samples reveals disorganized fibers and large, open nuclei, in the bitransgenic (Fig 7A). To further investigate the degree of muscle degeneration, we performed Masson's trichrome staining on duplicate sections of the same samples. Staining with Masson's trichrome stain also revealed severe degeneration in the bitransgenic, as demonstrated by vacuoles appearing within the skeletal muscle fibers and extensive fibrosis developing between muscle fibers (Fig 7A). Histological analysis of cardiac muscle tissue also revealed severe degeneration (Fig 7B). Analysis of a wider range of tissues did not reveal marked degenerative changes, suggesting that degeneration was limited to skeletal and cardiac muscle tissues. Taken together, these results suggest that high-level overexpression and deregulation of RNR leads to elevated dNTP pools that correlate with overexpression levels and cause tissue-specific degeneration.

DISCUSSION

Previously works have analyzed the results of disabling RNR via small subunit overexpression or by mutation of the allosteric activity site. Because deregulating RNR by disabling allosteric feedback control had limited phenotypes, we sought to further deregulate the enzyme by simultaneously disrupting both main regulatory modes. In yeast, simultaneous disruption of the two main regulatory mechanisms caused constitutively elevated dNTP pools, which resulted in proliferation defects(38). In order to determine if mice would have a similar phenotype, we crossed mice overexpressing either *Rrm1*-D57N transgene to mice overexpressing either small RNR subunit. In mice, cell proliferation defects would be expected to lead to embryonic lethality, as cell division is required for embryogenesis. Our first observation was that the combination of *Rrm1*-D57N and either small RNR subunit causes synthetic lethality in mice, which would be predicted by the previous model. We next found that the timing of the lethality

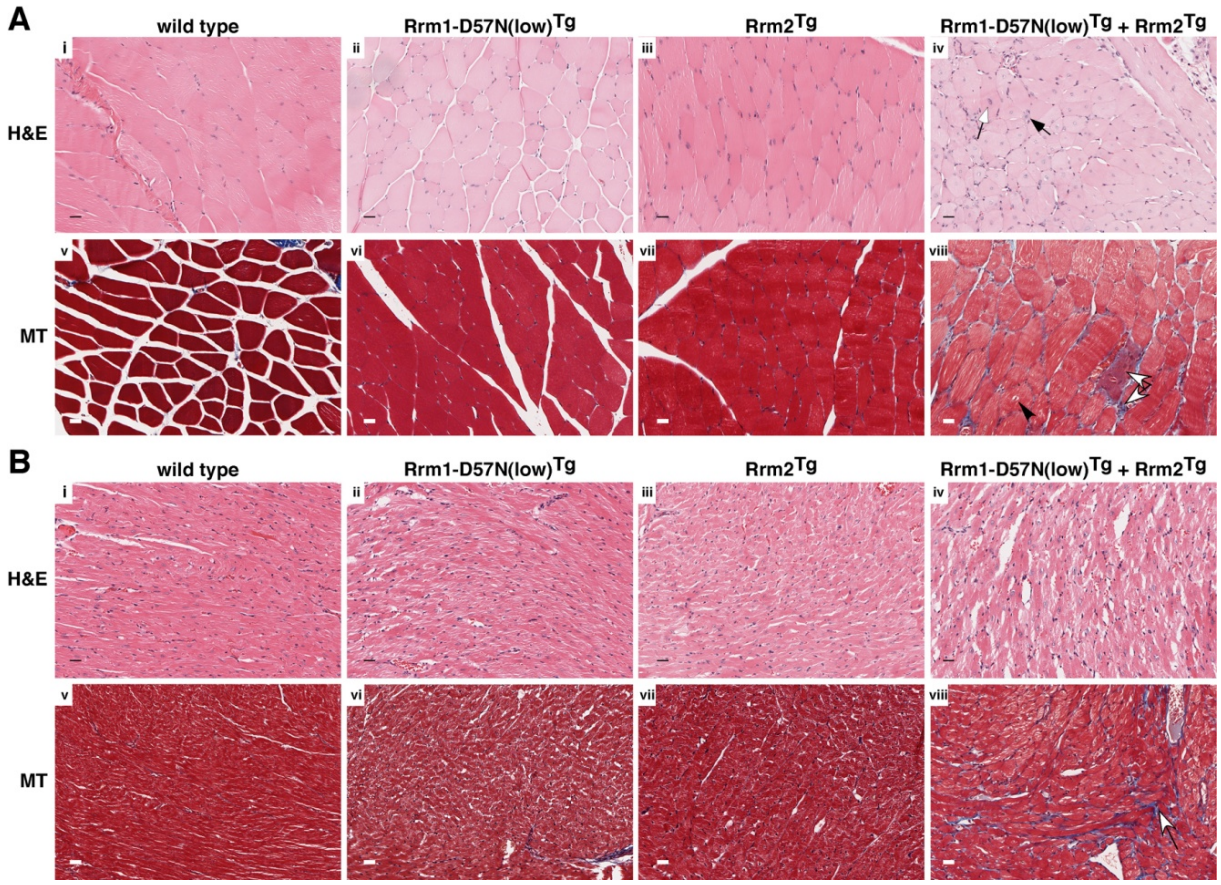

Figure 7. Muscle degeneration in *Rrm1*-D57N(low)^{Tg} + *Rrm2*^{Tg} bitransgenic adult mice. Degeneration of skeletal muscle (*A.*) and cardiac muscle (*B.*) in bitransgenic adults. Tissues from 90-day old mice were fixed overnight in formalin at room temperature prior to embedding and sectioning. Tissues were stained with H&E (i-iv) or Masson's trichrome (v-viii). Both skeletal and cardiac muscle from bitransgenic mice (*A*: iv, viii, *B*: iv, viii) display irregular fiber size and shape, large internal nuclei (white arrows), interstitial replacement fibrosis (white arrowheads), and vacuoles within muscle fibers (black arrowheads).

was determined by which specific transgenic combination was expressed. Combination of *Rrm1*-D57N(high)^{Tg} with either small subunit caused embryonic lethality. The *Rrm1*-D57N(low)^{Tg} strain, when paired with *Rrm2*^{Tg} or *p53R2*^{Tg}, was able to survive longer, through gestation, but the lifespan is still significantly shortened and lasts a matter of days. In both cases the presence of the *p53R2*^{Tg} makes the phenotype more severe than having *Rrm2*^{Tg}. This may be due to the differential patterns of expression of Rrm2 and p53R2. p53R2 is expressed at very low levels throughout the cell cycle, while during S-phase, Rrm2 is expressed very highly. High-level overexpression of p53R2 would then be expected to cause a more significant deregulation of RNR than overexpression of Rrm2. That some bitransgenic mice are able to survive through gestation contradicted our hypothesis. These findings indicate that while RNR is deregulated to a lethal extent in these mice, it is not sufficiently altered to cause cellular defects.

In order to explain the lethality caused by simultaneous disruption of both main regulatory modes of RNR, it was necessary to determine whether nucleotide pools were altered in bitransgenic mice, and to what extent. We hypothesized that if the least-severe combination resulted in altered nucleotide pools, then the other three combinations must also alter nucleotide pools, and may provide for a mechanism by which severe RNR deregulation results in lethality. We therefore measured nucleotides from the skeletal muscle of Rrm1-D57N(low)^{Tg} + Rrm2^{Tg} bitransgenic mice and control littermates at P5 and P6. We found that dNTP pools were dramatically elevated and unbalanced, resulting in a greater than 300-fold increase in dATP, while dCTP and dTTP were increased about 10-fold, and dGTP was increased 50%. This was consistent with our previous findings that both the Rrm1-D57N(low)^{Tg} and Rrm2^{Tg} transgenes are highly overexpressed within the skeletal muscle. These significant changes support a role for RNR hyperactivity in causing synthetic lethality.

We also found support for the hypothesis that the extent of dNTP pool alteration determines lifespan. We found that dNTP pools were significantly altered in the Rrm1-D57N(high)^{Tg} + p53R2^{Tg} bitransgenic embryos, which die around e12.5, but not in the Rrm1-D57N(low)^{Tg} + Rrm2^{Tg} bitransgenic embryos, which survive gestation and die about 1 week after birth. This indicates that any dNTP pool alteration has severe consequences for developing embryos, while a tissue-specific increase in dNTPs can be tolerated for a short time.

Rrm1-D57N(low)^{Tg} + *Rrm2*^{Tg} bitransgenic mice, the least severe combination, were severely underrepresented in adulthood, most having succumbed to illness within the first 2 weeks of life. Rare surviving bitransgenic adults displayed severe skeletal and cardiac muscle degeneration. In addition to muscle degeneration, they also displayed a general wasting phenotype, kyphosis, and alopecia. Taken together, these phenotypes are consistent with premature aging. Mice harboring a proofreading-deficient DNA Pol g with an increased rate of mtDNA point mutations also display premature aging (48), suggesting that destabilization of the mitochondrial genome may play a role in this synthetic lethality. Indeed, altered dNTP pools are thought to underlie mtDNA instability in several mitochondrial disorders in humans, and in mouse models. For instance, knock-out mice lacking p53R2 developed post-natal mtDNA depletion leading to early death{Bourdon, 2007 #166},{Kimura, 2003 #165}. We also previously noted that mice overexpressing *Rrm1*^{Tg} and *Rrm2*^{Tg} or *p53R2*^{Tg} displayed age-dependent mtDNA depletion, which was associated with altered dNTP pools in the skeletal muscle (34, 42). These results showed that mtDNA maintenance in mice is dependent on dNTP balance. Therefore, we hypothesized that synthetic lethality and premature aging in *Rrm1*-D57N(low)^{Tg} + *Rrm2*^{Tg} bitransgenic mice may be mediated through mitochondrial genome instability. However, our analyses of *Rrm1*-D57N(low)^{Tg} + *Rrm2*^{Tg} mice showed that mtDNA

was surprisingly intact, despite the highly disordered dNTP pool. We did observe age-related mtDNA depletion, but found no signs of increased rate of mtDNA point mutations or deletions. The mtDNA depletion is unlikely to account for the lethal phenotype for the following reasons: First, the earliest age at which mtDNA depletion in skeletal muscle was observed was P19, although the other phenotypes developed much earlier. Second, the residual level of mtDNA was similar to that of other mouse models that have mtDNA depletion but no overt muscle degeneration ({Akman, 2008 #143}., {Zhou, 2008 #145}. Furthermore, it must be noted that severe muscle degeneration and deposition of connective tissue could cause the measured mtDNA level to be lower than the actual mtDNA level within the muscle fibers. The normal result from the COX/SDH activity assay confirmed that mitochondrial dysfunction is not a cause of muscle degeneration in these mice. Therefore, while the mtDNA depletion in bitransgenic mice supports the notion that mtDNA replication is sensitive to the dNTP balance, it does not explain the early lethality of these animals.

A hypothesis to explain the particular phenotypes observed in the *Rrm1*-D57N(low)^{Tg} + *Rrm2*^{Tg} bitransgenic mice links cellular control of nucleotide levels and hypertension. A cellular defense against unbalanced nucleotide pools is through nucleotide degradation, in which dNTPs are cleaved by deaminases and nucleoside phosphorylases and either returned to the substrate cycles or excreted(49). For purines especially, elevated degradation products in the bloodstream of mice or humans can have adverse effects. The products of purine nucleotide degradation, xanthine, hypoxanthine, and uric acid, are elevated in the blood of hypertensive patients(50) and elevating uric acid causes hypertension in rats(51). Among other phenotypes, hypertension causes pleural effusion(52) and glaucoma(53), which are either observed in Rrm1-D57N(low)^{Tg} + Rrm2^{Tg} bitransgenic mice or are similar to phenotypes observed in these mice. Therefore, we

hypothesize that simultaneous disruption of both main RNR regulatory pathways in *Rrm1*-D57N(low)^{Tg} + *Rrm2*^{Tg} bitransgenic mice elevates nucleotide pools, which are rapidly degraded in an attempt to keep levels balanced. The increase in nucleotide degradation products in the blood triggers hypertension, which results in pleural effusion and eventually suffocates the bitransgenic mice at a young age. Further work is necessary in order to link elevated nucleotide pools with the observed phenotypes.

Deregulation of RNR in mice by small subunit overexpression causes lung tumorigenesis and moderately elevated dNTP pools, while overexpression of the feedback-resistant mutant *Rrm1*-D57N had limited phenotypes. Only when these two regulatory modes were simultaneously disabled were phenotypes observed, suggesting that these two mechanisms are partially redundant. The timing of the lethality is dependent on the degree of RNR deregulation, with higher-level overexpression of *Rrm1-D57N*^{Tg} or either small subunit resulting in more severe defects and earlier lethality. In yeast, simultaneous loss of both regulatory modes caused proliferation defects, while the cells were able to survive. All together, we conclude that severe deregulation of RNR in multicellular organisms has hazardous consequences, and further work will allow us to explore the ability of cells to maintain their genomes in the presence of deregulated RNR.

ACKNOWLEDGMENTS

We would like to thank Dr. Patrick Stover and Dr. Hening Lin for allowing use of the UPLC and for technical advice. We would also like to thank Christina Cota for valuable suggestions regarding embryonic phenotypes. This work was supported by Cornell University Center for Vertebrate Genomics Scholar Awards [J.P. and X.X.]; and National Institutes of Health training grant T32GM07617 [J.P.].

References

1. Kunkel T (2004) DNA replication fidelity. *Journal of Biological Chemistry* 279(17):16895.
2. Kunkel T & Mosbaugh D (1989) Exonucleolytic proofreading by a mammalian DNA polymerase. gamma. *Biochemistry* 28(3):988-995.
3. Song S*, et al.* (2005) DNA precursor asymmetries in mammalian tissue mitochondria and possible contribution to mutagenesis through reduced replication fidelity. *Proceedings of the National Academy of Sciences of the United States of America* 102(14):4990.
4. Byrnes JJ, Downey KM, Black VL, & So AG (1976) A new mammalian DNA polymerase with 3' to 5' exonuclease activity: DNA polymerase delta. (Translated from eng) *Biochemistry* 15(13):2817-2823 (in eng).
5. Meuth M (1989) The molecular basis of mutations induced by deoxyribonucleoside triphosphate pool imbalances in mammalian cells. *Experimental cell research* 181(2):305-316.
6. Chabes A*, et al.* (2003) Survival of DNA damage in yeast directly depends on increased dNTP levels allowed by relaxed feedback inhibition of ribonucleotide reductase. (Translated from eng) *Cell* 112(3):391-401 (in eng).
7. Fasullo M, Tsaponina O, Sun M, & Chabes A (2010) Elevated dNTP levels suppress hyper-recombination in Saccharomyces cerevisiae S-phase checkpoint mutants. (Translated from eng) *Nucleic Acids Res* 38(4):1195-1203 (in eng).
8. Kunz B & Kohalmi S (1991) Modulation of mutagenesis by deoxyribonucleotide levels. *Annual review of genetics* 25(1):339-359.
9. Kumar D, Viberg J, Nilsson AK, & Chabes A (2010) Highly mutagenic and severely

imbalanced dNTP pools can escape detection by the S-phase checkpoint. (Translated from Eng) *Nucleic Acids Res* (in Eng).

10. Bebenek K, Roberts J, & Kunkel T (1992) The effects of dNTP pool imbalances on frameshift fidelity during DNA replication. *Journal of Biological Chemistry* 267(6):3589.
11. Hastak K*, et al.* (2008) DNA synthesis from unbalanced nucleotide pools causes limited DNA damage that triggers ATR-CHK1-dependent p53 activation. (Translated from eng) *Proc Natl Acad Sci U S A* 105(17):6314-6319 (in eng).
12. Copeland WC (2008) Inherited mitochondrial diseases of DNA replication. (Translated from eng) *Annu Rev Med* 59:131-146 (in eng).
13. McFarland R, Taylor RW, & Turnbull DM (2010) A neurological perspective on mitochondrial disease. (Translated from eng) *Lancet Neurol* 9(8):829-840 (in eng).
14. Suomalainen A & Isohanni P (2010) Mitochondrial DNA depletion syndromes - Many genes, common mechanisms. (Translated from Eng) *Neuromuscul Disord* (in Eng).
15. Bourdon A*, et al.* (2007) Mutation of RRM2B, encoding p53-controlled ribonucleotide reductase (p53R2), causes severe mitochondrial DNA depletion. (Translated from eng) *Nat Genet* 39(6):776-780 (in eng).
16. Kollberg G*, et al.* (2009) A novel homozygous RRM2B missense mutation in association with severe mtDNA depletion. (Translated from eng) *Neuromuscul Disord* 19(2):147-150 (in eng).
17. Kimura T*, et al.* (2003) Impaired function of p53R2 in Rrm2b-null mice causes severe renal failure through attenuation of dNTP pools. (Translated from eng) *Nat Genet* 34(4):440-445 (in eng).
18. Akman HO*, et al.* (2008) Thymidine kinase 2 (H126N) knockin mice show the essential

role of balanced deoxynucleotide pools for mitochondrial DNA maintenance. (Translated from eng) *Hum Mol Genet* 17(16):2433-2440 (in eng).

19. Gotz A*, et al.* (2008) Thymidine kinase 2 defects can cause multi-tissue mtDNA depletion syndrome. (Translated from eng) *Brain* 131(Pt 11):2841-2850 (in eng).
20. Lee W & Sokol R (2007) Liver disease in mitochondrial disorders. (New York: Thieme-Stratton, c1981-), pp 259-273.
21. Mandel H*, et al.* (2001) The deoxyguanosine kinase gene is mutated in individuals with depleted hepatocerebral mitochondrial DNA. (Translated from eng) *Nat Genet* 29(3):337-341 (in eng).
22. Tyynismaa H*, et al.* (2009) A heterozygous truncating mutation in RRM2B causes autosomal-dominant progressive external ophthalmoplegia with multiple mtDNA deletions. (Translated from eng) *Am J Hum Genet* 85(2):290-295 (in eng).
23. Nishino I, Spinazzola A, & Hirano M (1999) Thymidine phosphorylase gene mutations in MNGIE, a human mitochondrial disorder. (Translated from eng) *Science* 283(5402):689-692 (in eng).
24. Hirano M, Nishigaki Y, & Marti R (2004) Mitochondrial neurogastrointestinal encephalomyopathy (MNGIE): a disease of two genomes. (Translated from eng) *Neurologist* 10(1):8-17 (in eng).
25. Lopez LC*, et al.* (2009) Unbalanced deoxynucleotide pools cause mitochondrial DNA instability in thymidine phosphorylase-deficient mice. (Translated from eng) *Hum Mol Genet* 18(4):714-722 (in eng).
26. Pontarin G*, et al.* (2008) Ribonucleotide reduction is a cytosolic process in mammalian cells independently of DNA damage. (Translated from eng) *Proc Natl Acad Sci U S A*

105(46):17801-17806 (in eng).

27. Kolberg M, Strand KR, Graff P, & Andersson KK (2004) Structure, function, and mechanism of ribonucleotide reductases. (Translated from eng) *Biochim Biophys Acta* 1699(1-2):1-34 (in eng).

28. Tanaka H*, et al.* (2000) A ribonucleotide reductase gene involved in a p53-dependent cell-cycle checkpoint for DNA damage. (Translated from eng) *Nature* 404(6773):42-49 (in eng).

29. Engstrom Y, Rozell B, Hansson HA, Stemme S, & Thelander L (1984) Localization of ribonucleotide reductase in mammalian cells. (Translated from eng) *EMBO J* 3(4):863-867 (in eng).

30. Hakansson P, Hofer A, & Thelander L (2006) Regulation of mammalian ribonucleotide reduction and dNTP pools after DNA damage and in resting cells. (Translated from eng) *J Biol Chem* 281(12):7834-7841 (in eng).

31. Chabes AL, Bjorklund S, & Thelander L (2004) S Phase-specific transcription of the mouse ribonucleotide reductase R2 gene requires both a proximal repressive E2F-binding site and an upstream promoter activating region. (Translated from eng) *J Biol Chem* 279(11):10796-10807 (in eng).

32. Chabes AL, Pfleger CM, Kirschner MW, & Thelander L (2003) Mouse ribonucleotide reductase R2 protein: a new target for anaphase-promoting complex-Cdh1-mediated proteolysis. (Translated from eng) *Proc Natl Acad Sci U S A* 100(7):3925-3929 (in eng).

33. Xu X*, et al.* (2008) Broad overexpression of ribonucleotide reductase genes in mice specifically induces lung neoplasms. (Translated from eng) *Cancer Res* 68(8):2652-2660 (in eng).

34. Ylikallio E*, et al.* (2010) Ribonucleotide reductase is not limiting for mitochondrial DNA copy number in mice. (Translated from Eng) *Nucleic Acids Res* (in Eng).

35. Ingemarson R & Thelander L (1996) A Kinetic Study on the Influence of Nucleoside Triphosphate Effectors on Subunit Interaction in Mouse Ribonucleotide ReductaseÜ. *Biochemistry* 35(26):8603-8609.

36. Uppsten M, Farnegardh M, Domkin V, & Uhlin U (2006) The first holocomplex structure of ribonucleotide reductase gives new insight into its mechanism of action. *Journal of molecular biology* 359(2):365-377.

37. Caras IW & Martin DW, Jr. (1988) Molecular cloning of the cDNA for a mutant mouse ribonucleotide reductase M1 that produces a dominant mutator phenotype in mammalian cells. (Translated from eng) *Mol Cell Biol* 8(7):2698-2704 (in eng).

38. Chabes A & Stillman B (2007) Constitutively high dNTP concentration inhibits cell cycle progression and the DNA damage checkpoint in yeast Saccharomyces cerevisiae. (Translated from eng) *Proc Natl Acad Sci U S A* 104(4):1183-1188 (in eng).

39. Tyynismaa H*, et al.* (2005) Mutant mitochondrial helicase Twinkle causes multiple mtDNA deletions and a late-onset mitochondrial disease in mice. *Proc Natl Acad Sci U S A* 102(49):17687-17692.

40. Sherman PA & Fyfe JA (1989) Enzymatic assay for deoxyribonucleoside triphosphates using synthetic oligonucleotides as template primers. (Translated from eng) *Anal Biochem* 180(2):222-226 (in eng).

41. Ferraro P, Franzolin E, Pontarin G, Reichard P, & Bianchi V (2010) Quantitation of cellular deoxynucleoside triphosphates. (Translated from eng) *Nucleic Acids Res* 38(6):e85 (in eng).

42. Ylikallio E*, et al.* (2010) Ribonucleotide reductase is not limiting for mitochondrial DNA copy number in mice. (Translated from eng) *Nucleic Acids Res* 38(22):8208-8218 (in eng).

43. Larsson NG*, et al.* (1998) Mitochondrial transcription factor A is necessary for mtDNA maintenance and embryogenesis in mice. (Translated from eng) *Nat Genet* 18(3):231-236 (in eng).

44. Chabes A, Domkin V, & Thelander L (1999) Yeast Sml1, a protein inhibitor of ribonucleotide reductase. *Journal of Biological Chemistry* 274(51):36679.

45. Chabes A & Thelander L (2000) Controlled protein degradation regulates ribonucleotide reductase activity in proliferating mammalian cells during the normal cell cycle and in response to DNA damage and replication blocks. (Translated from eng) *J Biol Chem* 275(23):17747-17753 (in eng).

46. Elledge SJ, Zhou Z, & Allen JB (1992) Ribonucleotide reductase: regulation, regulation, regulation. (Translated from eng) *Trends Biochem Sci* 17(3):119-123 (in eng).

47. Goodman M, Creighton S, Bloom L, Petruska J, & Kunkel T (1993) Biochemical basis of DNA replication fidelity. *Critical reviews in biochemistry and molecular biology* 28(2):83-126.

48. Trifunovic A*, et al.* (2004) Premature ageing in mice expressing defective mitochondrial DNA polymerase. *Nature* 429(6990):417-423.

49. Rampazzo C*, et al.* (2010) Regulation by degradation, a cellular defense against deoxyribonucleotide pool imbalances. (Translated from Eng) *Mutat Res* (in Eng).

50. Nagaya N*, et al.* (1999) Serum uric acid levels correlate with the severity and the mortality of primary pulmonary hypertension. *American journal of respiratory and*

critical care medicine 160(2):487.

51. Mazzali M*, et al.* (2001) Elevated uric acid increases blood pressure in the rat by a novel crystal-independent mechanism. (Translated from eng) *Hypertension* 38(5):1101-1106 (in eng).

52. Zocchi L (2002) Physiology and pathophysiology of pleural fluid turnover. (Translated from eng) *Eur Respir J* 20(6):1545-1558 (in eng).

53. Langman M, Lancashire R, Cheng K, & Stewart P (2005) Systemic hypertension and glaucoma: mechanisms in common and co-occurrence. *British Journal of Ophthalmology* 89(8):960.